Search for the Decay $K_L \to \pi^0 \nu\bar{\nu}$ at the J-PARC KOTO Experiment

Department of Physics, Graduate School of Science, Kyoto University

Kota Nakagiri

February 19, 2019

Abstract

The $K_L \to \pi^0\nu\overline{\nu}$ is a CP-violating decay process of the neutral K meson with a longer lifetime, K_L. It is an excellent probe to search for new physics beyond the Standard Model (SM), because new physics can contribute to the process and this decay is highly suppressed in the SM.

The KOTO experiment is designed to search for the $K_L \to \pi^0\nu\overline{\nu}$ decay. In KOTO, we identify the $K_L \to \pi^0\nu\overline{\nu}$ signal by detecting two photons from a π^0 without any extra visible particles. The KOTO experiment is also sensitive to the $K_L \to \pi^0 X^0$ decay, where X^0 is an invisible light boson, because it has the same final state as the $K_L \to \pi^0\nu\overline{\nu}$ decay. In this thesis, we report the results of a search for the $K_L \to \pi^0\nu\overline{\nu}$ and $K_L \to \pi^0 X^0$ decays based on the data collected in 2015.

We learned from the data taken in 2013 that the background caused by a neutron hitting an electromagnetic calorimeter, which is called "hadron-cluster background", is crucial. We collected a control sample for the hadron-cluster background in 2015. We developed new analysis methods to separate hadronic showers from electromagnetic showers.

We found a new background source caused by an η meson production close to the calorimeter. A new analysis method was developed to eliminate this background.

Finally, we achieved a single event sensitivity of $(1.30 \pm 0.01_{\rm stat} \pm 0.14_{\rm syst}) \times 10^{-9}$ for the $K_L \to \pi^0\nu\overline{\nu}$ decay and no signal candidate events were observed. We set an upper limit of 3.0×10^{-9} for the branching fraction of the $K_L \to \pi^0\nu\overline{\nu}$ decay at the 90% confidence level, which improves the previous limit by an order of magnitude. We also set an upper limit for the branching fraction of the $K_L \to \pi^0 X^0$ decay to be 2.4×10^{-9} at the 90% confidence level with the X^0 mass of 135 MeV/c^2.

Acknowledgments

The work in this thesis was accomplished thanks to the tremendous support of many people. I would like to express my gratitude to them on this occasion.

First of all, I would like to express my sincere gratitude to Prof. Tsuyoshi Nakaya, who gave me a wonderful opportunity for the research of high energy physics. I am always impressed by his deep insight into physics. I would like to express heartfelt gratitude to my supervisor Prof. Hajime Nanjo for his continuous support. He has taught me physics and experimental methods from the basic level. It is not too much to say that a large part of me as a physicist was given by him. I am cordially thankful to Prof. Atsuko Ichikawa. She has been my roommate in our laboratory for five years. Although she is not a member of the KOTO collaboration, she gave me comments and advice on my study (and also on this thesis !). Her viewpoints were very impressive to me.

I would like to express my gratitude to all the KOTO collaborators. I am deeply thankful to Prof. Taku Yamanaka, the spokesperson of the KOTO experiment. I respect his attitude toward physics to enjoy experiments. I am grateful to Prof. Tadashi Nomura and Prof. Koji Shiomi. I learned a lot about KOTO from them. They always showed me the correct way when I was lost in my study. I would like to show my great appreciation to Prof. Takeshi Komatsubara, especially for his strong readership as a chairman of the internal paper-review committee for the KOTO 2015 run paper. Without him, I could not have prepared the draft of the paper in just one month. Especially I would like to give special thanks to Mr. Ichinori Kamiji, who has been my colleague since we were undergraduate students. I am quite happy that I spent my research life with him. He has been one of my most reliable colleagues. I am grateful to Prof. G. Y. Lim and Prof. H. Watanabe for the detector construction and environmental supports at J-PARC. I would like to thank Prof. M. Campbell, Prof. M. Tecchio, Dr. B. Beckford, Dr. S. Su, Ms. M. Hutcheson, Prof. Y. W. Wah, Mr. M. Bogdan, Prof. J. Comfort, Prof. Y. Tajima, and Prof. Y. Sugiyama for their great work for the complicated DAQ system. I am grateful to KOTO colleagues who worked together in J-PARC and/or discussed the analysis together: Dr. Y. C. Tung, Mr. Y. Luo, Mr. Q. Lin, Prof. Y. B. Hsiung, Mr. C. Lin, Mr. S. H. Chen, Mr. J. L. Kim, Prof. M. Togawa, Dr. K. Sato, Dr. J. W. Lee, Ms. R. Murayama, Mr. K. Miyazaki, Dr. K. Kotera, Dr. N. Shimizu, Prof. S. Suzuki, and Prof. T. Matsumura. I would like to appreciate a lot of discussion with and cooperation from the members of the Kyoto Kaon group: Prof. N. Sasao, Prof. T. Masuda, Mr. N. Kawasaki, Prof. D. Naito, Dr. Y. Maeda, Mr. S. Seki, Mr. T. Hineno, Mr. S. Shinohara. I learned a lot from the discussion with them.

I would like to thank all the members of the High Energy Physics Group in Kyoto University: Prof. M. Ishino, Prof. R. Wendell, Prof. O. Tajima, Prof. T. Sumida, Prof. A. Minamino, Prof. T. Kikawa, Prof. C. Bronner, Dr. N. Patel, Dr. S. V. Cao, Dr. B. Quilain, Dr. K. D. Nakamura, Dr. S. Obara, Dr. S. Adachi, Dr. S. Honda, Mr. H. Kubo, Dr. K. Ieki, Prof. K. Suzuki, Dr. K. Huang, Mr. S. Takahashi, Dr. T. Hiraki, Prof. S. Hirota, Dr. T. Tashiro, Mr. T. Nagasaki, Mr. N. Kamo, Mr. S. Akiyama, Dr. K. G. Nakamura, Mr. T. Hayashino, Dr. T. Kunigo, Mr. Y. Ishiyama, Mr. K. Yoshida, Mr. M. Jiang, Ms. S. Yanagita, Mr. S. Ban, Ms. M. Yamamoto, Mr. R. Monden, Mr. K. Kondo, Mr. S. Akatsuka, Mr. Y. Ashida, Mr. S. Tanaka, Mr. Y. Noguchi, Ms. A. Hiramoto, Ms. Y. Nakanishi, Mr. W. Uno, Mr. Y. Okazaki, Mr. K. Nakamura, Mr. M. Mori, Mr. M. Yoshida, Mr. K. Kuniyoshi, Mr. J. Komine, Mr. K. Yasutome, Mr. T. Abe, Mr. T. Ikemitsu, Mr. T. Odagawa, Mr. S. Kuribayashi, Mr. M. Tajima, Mr. M. Hatano, Mr. Y. Mino, Ms. I. Sanjana, Ms. E. Hayashi, Ms. S. Yamashita, Ms. H. Sekiguchi, and Ms. M. Sasaki. I really enjoyed discussions and casual conversations with them.

It always relaxed, encouraged, and stimulated me.

I am deeply thankful to *izakaya* Waya in Ichijoji, Kyoto and the Waya friends for relaxing me in my Ph.D. life.

Finally, I would like to express my deepest appreciation to my family, especially to my parents Akira Nakagiri and Asami Nakagiri for their unconditional support and love throughout my life.

Kota Nakagiri
Kyoto, Japan
February, 2019

Contents

Chapter 1

Introduction

At the beginning of the universe, particles and anti-particles (matter and anti-matter) should be created in equal amounts. However, the universe today is filled with matter whereas anti-matter has almost disappeared. A. Sakharov pointed out [1] that this baryon asymmetry of the universe can be understood if the following three conditions are met:

- the processes which violate baryon-number symmetry exist
- the processes which violate CP symmetry exist
- baryon-number violating processes occur in non-thermal equilibrium.

As for CP symmetry, which is the symmetry between particles and anti-particles, the violation of the symmetry, "CP violation", was first discovered in the decay of neutral K meson [2] and explained by the Cabibbo-Kobayashi-Maskawa (CKM) model [3, 4] within the framework of the Standard Model (SM). However, the size of the violation in the CKM model is too small to explain the matter dominant universe [5]. We thus believe the existence of new physics beyond the SM that breaks CP symmetry.

The decay of the long-lived neutral K meson, $K_L \to \pi^0\nu\overline{\nu}$, is a highly suppressed direct CP-violating process in the framework of the SM, and hence one of the most sensitive probes to search for new physics which breaks CP symmetry [6, 7]. This decay does not so suffer from hadronic interactions in the decay, and has small theoretical uncertainties. Any deviation of the branching fraction of $K_L \to \pi^0\nu\overline{\nu}$ from the SM prediction would strongly imply the contributions of new physics.

The J-PARC KOTO experiment [8, 9] is dedicated to studying the $K_L \to \pi^0\nu\overline{\nu}$ decay. We performed the first physics run in 2013 [10] and achieved a sensitivity comparable to that of the KEK E391a experiment [11], which set the best upper limit for the branching fraction of the $K_L \to \pi^0\nu\overline{\nu}$ decay. In 2015, we again conducted data taking. In this thesis, we present the results of the $K_L \to \pi^0\nu\overline{\nu}$ decay search with the KOTO 2015 data. The search for the $K_L \to \pi^0 X^0$ decay [12, 13] is also described, where X^0 is an invisible neutral light boson.

1.1 CP violation in the Cabbibo-Kobayashi-Maskawa model

In the SM, the Lagrangian of the charged current in the weak interaction of quarks is written as

$$\mathcal{L}_{CC} = \frac{-g}{\sqrt{2}} \left[\bar{u_i} V_{ij} d_j W^- + \bar{d_j} V_{ij}^* u_i W^+ \right], \tag{1.1}$$

where $i, j = 1, 2, 3$ indicate generation numbers, u_i and d_i represent left-handed up-type (u, c, t) and down-type (d, s, b) quark, respectively, $W^\pm$ denotes the weak boson, and V_{ij} represents the matrix element of the Cabbibo-Kobayashi-Maskawa (CKM) matrix, V_{CKM}, which connects the mass eigenstates (d, s, b) and weak eigenstates (d', s', b'):

$$\begin{pmatrix} d' \\ s' \\ b' \end{pmatrix} = \begin{pmatrix} V_{ud} & V_{us} & V_{ub} \\ V_{cd} & V_{cs} & V_{cb} \\ V_{td} & V_{ts} & V_{tb} \end{pmatrix} \begin{pmatrix} d \\ s \\ b \end{pmatrix} = V_{\mathrm{CKM}} \begin{pmatrix} d \\ s \\ b \end{pmatrix}. \tag{1.2}$$

The CP conjugation of the Lagrangian is then given as

$$\mathcal{L}_{CC}^{CP} = \frac{-g}{\sqrt{2}} \left[\bar{d}_i V_{ij} u_j W^+ + \bar{u}_j V_{ij}^* d_i W^- \right]. \tag{1.3}$$

From Eq. 1.1 and Eq. 1.3, the CP violation occurs when $V_{ij} \neq V_{ij}^*$, which means that the complex phase in the CKM matrix plays an essential role in the CP violation.

The CKM matrix can be parametrized by three mixing angles θ_{12}, θ_{23}, θ_{13}, and a CP-violating phase δ as

$$V_{\mathrm{CKM}} = \begin{pmatrix} 1 & 0 & 0 \\ 0 & c_{23} & s_{23} \\ 0 & -s_{23} & c_{23} \end{pmatrix} \begin{pmatrix} c_{13} & 0 & s_{13}e^{-i\delta} \\ 0 & 1 & 0 \\ -s_{13}e^{i\delta} & 0 & c_{13} \end{pmatrix} \begin{pmatrix} c_{12} & s_{12} & 0 \\ -s_{12} & c_{12} & 0 \\ 0 & 0 & 1 \end{pmatrix} \tag{1.4}$$

$$= \begin{pmatrix} c_{12}c_{13} & s_{12}c_{13} & s_{13}e^{-i\delta} \\ -s_{12}c_{23} - c_{12}s_{23}s_{13}e^{i\delta} & c_{12}c_{23} - s_{12}s_{23}s_{13}e^{i\delta} & s_{23}c_{13} \\ s_{12}s_{23} - c_{12}c_{23}s_{13}e^{i\delta} & -c_{12}s_{23} - s_{12}c_{23}s_{13}e^{i\delta} & c_{23}c_{13} \end{pmatrix}, \tag{1.5}$$

where $s_{ij} = \sin\theta_{ij}$ and $c_{ij} = \cos\theta_{ij}$. It also can be expressed with Wolfenstein parameterization [14] as

$$V_{\mathrm{CKM}} = \begin{pmatrix} 1 - \lambda^2/2 & \lambda & A\lambda^3(\rho - i\eta) \\ -\lambda & 1 - \lambda^2/2 & A\lambda^2 \\ A\lambda^3(1 - \rho - i\eta) & -A\lambda^2 & 1 \end{pmatrix} + \mathcal{O}(\lambda^4), \tag{1.6}$$

where

$$\lambda = s_{12} = \frac{|V_{us}|}{\sqrt{|V_{ud}|^2 + |V_{us}|^2}} \sim 0.23, \tag{1.7}$$

$$A\lambda^2 = s_{23} = \lambda \left| \frac{V_{cb}}{V_{us}} \right|, \tag{1.8}$$

$$A\lambda^3(\rho + i\eta) = s_{13}e^{i\delta} = V_{ub}^* = \frac{A\lambda^3(\bar{\rho} + i\bar{\eta})\sqrt{1 - A^2\lambda^4}}{\sqrt{1 - \lambda^2}[1 - A^2\lambda^4(\bar{\rho} + i\bar{\eta})]}, \tag{1.9}$$

$$\bar{\rho} + i\bar{\eta} = \frac{V_{ud}V_{ub}^*}{V_{cd}V_{cb}^*}. \tag{1.10}$$

The parameter η (or $\bar{\eta} \sim \eta(1 - \lambda^2/2)$) represents the imaginary part of the CKM matrix, which causes the CP violation.

The unitarity of the CKM matrix gives

$$V_{ud}V_{ub}^* + V_{cd}V_{cb}^* + V_{td}V_{tb}^* = 0, \tag{1.11}$$

and thus

$$\frac{V_{ud}V_{ub}^*}{V_{cd}V_{cb}^*} + 1 + \frac{V_{td}V_{tb}^*}{V_{cd}V_{cb}^*} = 0. \tag{1.12}$$

Consequently a unitarity triangle is obtained as shown in Fig. 1.1. The vertexes of the triangle on the complex plane are $(0, 0)$, $(1, 0)$, and $(\bar{\rho}, \bar{\eta})$ from Eq. 1.10. The parameters of the unitarity triangle has been measured by various measurements. The global fit for the Wolfenstein parameters gives [15]

$$\lambda = 0.22453 \pm 0.00044, \tag{1.13}$$

$$A = 0.836 \pm 0.015, \tag{1.14}$$

$$\bar{\rho} = 0.122^{+0.018}_{-0.017}, \tag{1.15}$$

$$\bar{\eta} = 0.355^{+0.012}_{-0.011}. \tag{1.16}$$

and constraints on the parameters on the $\bar{\rho}$-$\bar{\eta}$ plane are shown in Fig. 1.2.

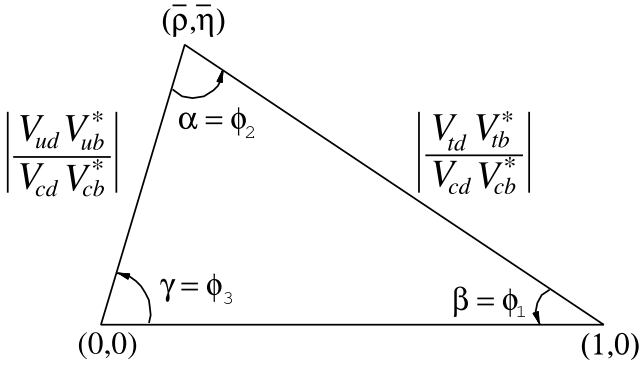

Figure 1.1: Unitarity triangle (quoted from Ref. [15]).

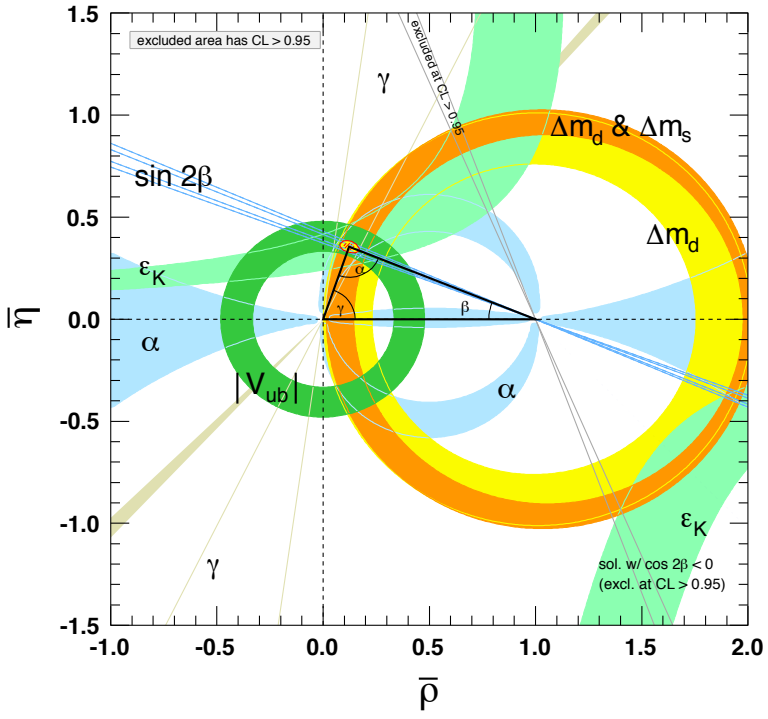

Figure 1.2: Constraints of the Wolfenstein parameters on the $\bar{\rho}$-$\bar{\eta}$ plane (quoted from Ref. [15]). The shaded areas represent the 95% C.L. allowed regions.

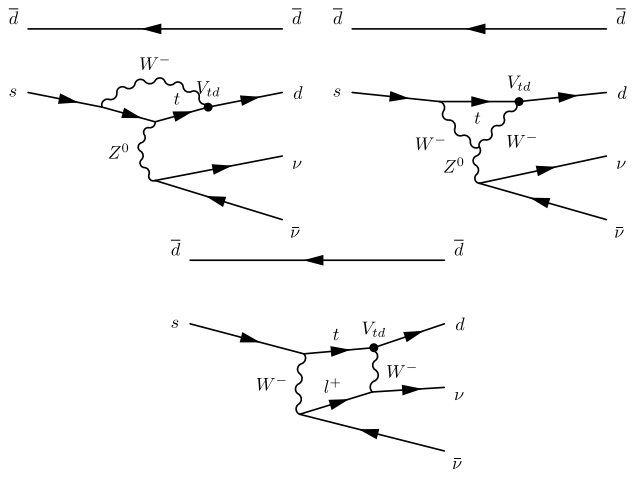

Figure 1.3: Examples of Feynman diagrams of the $K_L \to \pi^0 \nu\overline{\nu}$ decay in the SM (quoted from Ref. [16]). Top two (bottom) diagrams are called Z-penguin (box) diagrams.

1.2 $K_L \to \pi^0 \nu\overline{\nu}$ Decay

1.2.1 $K_L \to \pi^0 \nu\overline{\nu}$ Decay in the Standard Model

The $K_L \to \pi^0 \nu\overline{\nu}$ decay is a rare decay which violates the CP symmetry. Examples of Feynman diagrams of this decay are shown in Fig. 1.3. This decay is caused via an $s \to d$ Flavor Changing Neutral Current (FCNC) process. Since FCNC process at a tree level is prohibited in the SM [17], the lowest order processes are the loop processes involving internal W boson exchanges, which are called "Z-penguin" and "box" diagrams, and they highly suppress the decay.

The quark level amplitude of this process $\mathcal{A}(s \to d\nu\bar{\nu})$ has the structure [7]

$$\mathcal{A}(s \to d\nu\bar{\nu}) \sim \frac{m_t^2}{M_W^2}\lambda_t + \frac{m_c^2}{M_W^2}\ln\frac{M_W}{m_c}\lambda_c + \frac{\Lambda_{\rm QCD}^2}{M_W^2}\lambda_u, \tag{1.17}$$

where $\lambda_q = V_{qs}^* V_{qd}$, $x_q = m_q^2/M_W^2$, $\Lambda_{\rm QCD} \sim 200$ MeV is QCD energy scale, and $M_W = 80.4$ GeV/c^2, $m_c = 1.28$ GeV/c^2, $m_t = 173$ GeV/c^2 are the masses of W boson, charm-quark, and top-quark, respectively. This implies that the contribution of top-quark, which carries a large CP-violating phase via V_{td}, is large ($\sim 68\%$), while that of charm-quark and up-quark are small ($\sim 29\%$ and $\sim 3\%$, respectively). In other words, this amplitude is dominated by short-distance contribution and the long-distance contribution is strongly suppressed; this makes it possible to predict the branching fraction of the $K_L \to \pi^0 \nu\overline{\nu}$ decay with good precision. Furthermore, as one can find from the following expressions of the amplitude of the $K_L \to \pi^0 \nu\overline{\nu}$ decay, contributions from charm-quark and up-quark are canceled out in the first order, with the charm-quark contribution well below 1%, and the $K_L \to \pi^0 \nu\overline{\nu}$ decay is fully dominated by the top-quark contribution:

$$\begin{aligned} A\left(K_L \to \pi^0 \nu\bar{\nu}\right) &\sim \frac{1}{\sqrt{2}}\left(A\left(K^0 \to \pi^0 \nu\bar{\nu}\right) - A\left(\bar{K}^0 \to \pi^0 \nu\bar{\nu}\right)\right) \\ &\propto V_{ts}V_{td}^* - V_{ts}^* V_{td} \\ &\sim -A\lambda^2(A\lambda^3(1-\rho+i\eta) - A\lambda^3(1-\rho-i\eta)) \\ &= -i2A^2\lambda^5\eta \\ &\propto \eta. \end{aligned} \tag{1.18}$$

This implies that the branching fraction of the $K_L \to \pi^0 \nu\overline{\nu}$ decay is proportional to η^2 and this decay is induced by the CP-violating phase in the weak interaction. The measurement of the $K_L \to \pi^0 \nu\overline{\nu}$

decay thus corresponds to the measurement of the "height" of the unitarity triangle shown in Fig. 1.1 and Fig. 1.2.

The branching fraction of the $K_L \to \pi^0 \nu\bar{\nu}$ in the SM is predicted to be [18]

$$\mathcal{B}(K_L \to \pi^0 \nu\bar{\nu}) = (3.00 \pm 0.30) \times 10^{-11}. \tag{1.19}$$

Most part of the uncertainty comes from the uncertainty of the input parameters of the calculation, $|V_{ub}|$, $|V_{cb}|$, and γ (ϕ_3), and the theoretical uncertainty is only 2%. This small branching fraction and the small uncertainty allow the $K_L \to \pi^0 \nu\bar{\nu}$ decay to be an excellent probe to examine the SM and to search for new physics beyond the SM (BSM) because small BSM effects can be seen via this decay.

1.2.2 $K^+ \to \pi^+ \nu\bar{\nu}$ Decay and Grossman-Nir bound

The $K^+ \to \pi^+ \nu\bar{\nu}$ decay is also a rare decay induced by the quark level amplitude of $s \to d\nu\bar{\nu}$. The branching fraction of this decay is predicted in the SM to be

$$\mathcal{B}(K^+ \to \pi^+ \nu\bar{\nu}) = (9.11 \pm 0.72) \times 10^{-11}. \tag{1.20}$$

Y. Grossman and Y. Nir pointed out [19] the following model-independent relation between the decay width (Γ) of the $K_L \to \pi^0 \nu\bar{\nu}$ and $K^+ \to \pi^+ \nu\bar{\nu}$ decays considering isospin symmetry:

$$r_{is} \times \frac{\Gamma(K_L \to \pi^0 \nu\bar{\nu})}{\Gamma(K^+ \to \pi^+ \nu\bar{\nu})} = \sin^2\theta, \tag{1.21}$$

where θ is the relative CP-violating phase between the K^0-$\bar{K^0}$ mixing amplitude and the $s \to d\nu\bar{\nu}$ decay amplitude, and $r_{is} = 0.954$ is the isospin breaking factor [20]. Using the lifetime ratio of K_L and K^+, $\tau_{K_L}/\tau_{K^+} = 4.13$ [15] and $\sin\theta \leq 1$, we obtain an upper limit for the ratio of the branching fraction of $K_L \to \pi^0 \nu\bar{\nu}$ and $K^+ \to \pi^+ \nu\bar{\nu}$ as

$$\frac{\mathcal{B}(K_L \to \pi^0 \nu\bar{\nu})}{\mathcal{B}(K^+ \to \pi^+ \nu\bar{\nu})} < \frac{\tau_{K_L}}{\tau_{K^+}} \frac{1}{r_{is}} \sim 4.3, \tag{1.22}$$

which gives

$$\mathcal{B}(K_L \to \pi^0 \nu\bar{\nu}) < 4.3 \times \mathcal{B}(K^+ \to \pi^+ \nu\bar{\nu}). \tag{1.23}$$

This "Grossman-Nir bound" gives a model-independent upper limit for the $K_L \to \pi^0 \nu\bar{\nu}$ decay from the $K^+ \to \pi^+ \nu\bar{\nu}$ measurements and new physics effects on the $K_L \to \pi^0 \nu\bar{\nu}$ decay is limited by this bound.

The branching fraction of the $K^+ \to \pi^+ \nu\bar{\nu}$ decay was measured by the E787 and E949 experiments [21] at Brookhaven National Laboratory (BNL) to be

$$\mathcal{B}(K^+ \to \pi^+ \nu\bar{\nu}) = (17.3^{+11.5}_{-10.5}) \times 10^{-11}, \tag{1.24}$$

based on the seven observed events. Recently the NA62 experiment at the CERN SPS has started a measurement of the $K^+ \to \pi^+ \nu\bar{\nu}$ decay and they released their first result based on the data taken in 2016 [22], which corresponds to 2% of the full statistics accumulated during the 2016 - 2018 data-taking period. They set an upper limit of 14×10^{-10} for the $K^+ \to \pi^+ \nu\bar{\nu}$ branching fraction at the 95% C.L., which is consistent with the E787 and E949 measurements. Based on Eq. 1.24, the Grossman-Nir bound is obtained to be

$$\mathcal{B}(K_L \to \pi^0 \nu\bar{\nu}) < 1.5 \times 10^{-9} \quad (90\%\ \text{C.L.}). \tag{1.25}$$

1.2.3 $K_L \to \pi^0 \nu\bar{\nu}$ Decay in Beyond the Standard Models

The SM predicts the branching fraction of the $K_L \to \pi^0 \nu\bar{\nu}$ to be 3×10^{-11}. The actual value can be larger if there are BSM physics processes (e.g. Refs. [23, 24, 25, 26, 27, 28, 29, 30]).

Figure 1.4 shows the correlation between the branching fraction of $K_L \to \pi^0 \nu\bar{\nu}$ and $K^+ \to \pi^+ \nu\bar{\nu}$ in some types of BSM physics models. In the models with a CKM-like structure of flavor interactions,

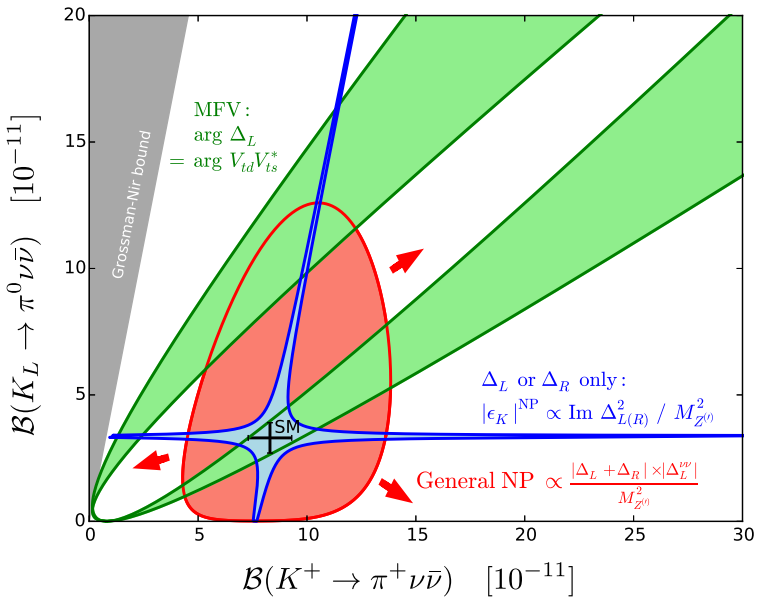

Figure 1.4: Correlations of BSM physics effects in the plane of $\mathcal{B}(K^+ \to \pi^+ \nu\bar{\nu})$ versus $\mathcal{B}(K_L \to \pi^0 \nu\bar{\nu})$. The figure is quoted from Ref. [23].

such as minimal flavor violation (MFV) models, $\mathcal{B}(K^+ \to \pi^+ \nu\bar{\nu})$ and $\mathcal{B}(K_L \to \pi^0 \nu\bar{\nu})$ will lie along the green band in Fig. 1.4. Note that due to stringent correlations with other flavor observables, the size of deviations of the branching fractions from the SM predictions is limited within about 10% [31, 32]. In the models with only left-handed or right-handed couplings to the quark currents, such as the littlest-Higgs models with T-parity (LHT) [33] and the models with flavor changing Z or Z' with pure left-handed or right-handed couplings [34, 35], $\mathcal{B}(K^+ \to \pi^+ \nu\bar{\nu})$ and $\mathcal{B}(K_L \to \pi^0 \nu\bar{\nu})$ will lie along the blue branches in Fig. 1.4. The two-branch structure is due to the constraint from the indirect CP-violation parameter, ϵ_K [36]; BSM effects are limited from the good agreement of the measurements and the SM prediction of ϵ_K. The horizontal branch represents the case that the BSM contribution to the $K \to \pi\nu\bar{\nu}$ amplitude is real and thus there are no effects on $\mathcal{B}(K_L \to \pi^0 \nu\bar{\nu})$. On the other hand, the other branch represents the case that the BSM contribution is imaginary. Detailed descriptions of this structure can be found in Ref. [37]. In the models with both left-handed and right-handed couplings or the models in which the correlation between ϵ_K and $K \to \pi\nu\bar{\nu}$ is weak or absent, such as the general minimum supersymmetric standard models (MSSM) [32] and the Randall-Sundrum models with custodial protection (RSc) [38], the two-branch structure is absent and $\mathcal{B}(K^+ \to \pi^+ \nu\bar{\nu})$ and $\mathcal{B}(K_L \to \pi^0 \nu\bar{\nu})$ will have the structure as shown in the red region in Fig. 1.4.

As an example of a BSM physics model, Fig. 1.5 shows the correlation between $\mathcal{B}(K_L \to \pi^0 \nu\bar{\nu})$ and $\mathcal{B}(K^+ \to \pi^+ \nu\bar{\nu})$ in a model with a 50 TeV Z' with purely left-handed couplings to quarks [34]. The value of $\mathcal{B}(K_L \to \pi^0 \nu\bar{\nu})$ can be as large as 15×10^{-11}, five times larger than that of the SM prediction.

1.2.4 $K_L \to \pi^0 X^0$ Decay

The existence of a light neutral boson, X^0, is motivated from a viewpoint of the muon g-2 anomaly [39]; a light Z' boson as X^0 associated with a new force gauging the difference between the μ and τ numbers, $L_\mu - L_\tau$, [40] can explain the anomaly [12]. In this model, $s \to dZ'$ transition occurs through the mixing of up-type quarks and vector-like U quark in a W boson loop as shown in Fig. 1.6. It can be probed with the $K_L \to \pi^0 X^0$ and $K^+ \to \pi^+ X^0$ decays. These decays can be detected by the experiments to search for the $K_L \to \pi^0 \nu\bar{\nu}$ and $K^+ \to \pi^+ \nu\bar{\nu}$ decays since the signal signatures are similar if the X^0 decays into invisible particles e.g. $X^0 (= Z') \to \nu\bar{\nu}$, or it has a lifetime long enough to escape the experimental system without decaying.

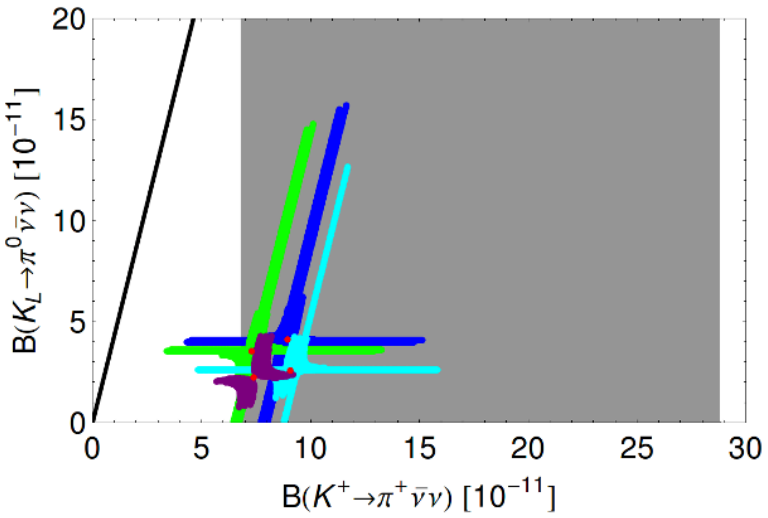

Figure 1.5: $\mathcal{B}(K^+ \to \pi^+ \nu\bar{\nu})$ versus $\mathcal{B}(K_L \to \pi^0 \nu\bar{\nu})$ in a model with a 50 TeV Z' with purely left-handed couplings to quarks. The figure is quoted from Ref. [34]. The four colors represent four scenarios with different $|V_{ub}|$ and $|V_{cb}|$ values as input variables determined from inclusive ($|V_{ub}| = (4.3 \pm 0.1) \times 10^{-3}$, $|V_{cb}| = (42.0 \pm 0.5) \times 10^{-3}$) and exclusive ($|V_{ub}| = (3.4 \pm 0.1) \times 10^{-3}$, $|V_{cb}| = (39.0 \pm 0.5) \times 10^{-3}$) decays. The four red points correspond to the SM predictions for four $(|V_{ub}|, |V_{cb}|)$ scenarios. The black solid line represents the Grossman-Nir bound and the region above this line is excluded at the 90% C.L. The gray region indicates the 1σ arrowed region from the $K^+ \to \pi^+ \nu\bar{\nu}$ measurements.

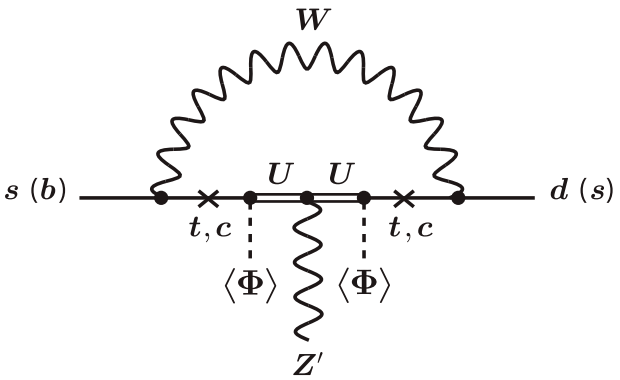

Figure 1.6: Feynman diagram of the $s \to dZ'$ transition (quoted from Ref. [12]). The Z' boson couples to a vector-like U quark which mixes with c and t. "$\times$" denotes the flip of chirality. Φ represents a scalar field with an extra $U(1)$ charge.

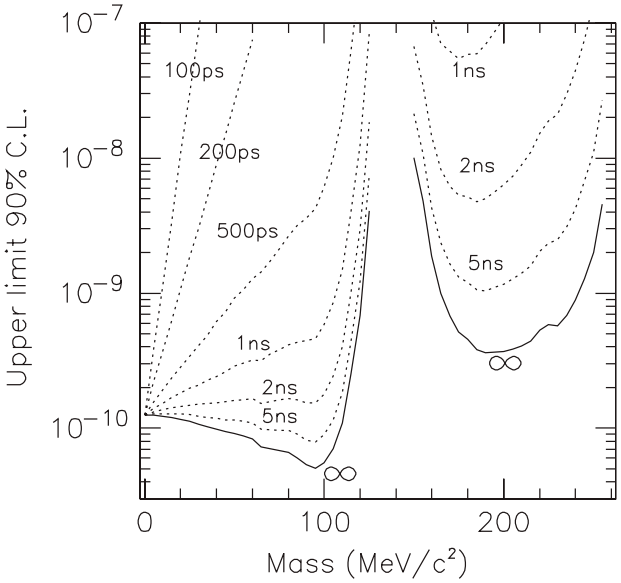

Figure 1.7: Upper limit for the $\mathcal{B}(K^+ \to \pi^+ X^0)$ at 90% C.L. as a function of X^0 mass (solid lines). The dashed lines represent the upper limit in the cased that X^0 is unstable and it decays to detectable particles with given lifetimes. The figure is quoted from Ref. [21].

The upper limits for the branching fraction of the $K^+ \to \pi^+ X^0$ decay as a function of the mass of X^0 (m_{X^0}) were set by the E787 and E949 experiments [21], which measured the branching fraction of the $K^+ \to \pi^+ \nu\overline{\nu}$ decay, as shown in Fig. 1.7. They observed the K^+ decay at rest, and detected the emitted π^+, but nothing else. However, they excluded the kinematic region where the missing mass or the X^0 mass $m_{\rm miss} = m_{X^0} = \sqrt{P_{K^+} - P_{\pi^+}}$, where P_{K^+} and P_{π^+} are the four-momenta of the decay K^+ and the emitted π^+, respectively, is calculated to be around the π^0 mass, namely $116 \lesssim m_{\rm miss} \lesssim 152$ MeV/c^2, so as to avoid the contamination from the $K^+ \to \pi^+ \pi^0$ decay. This decay has a large branching fraction of $\mathcal{B}(K^+ \to \pi^+ \pi^0) \sim 21\%$ and can be a background event if two photons from a π^0 decay are not detected. The above kinematical exclusion made the upper limit line missing in the region $m_{X^0} \sim m_{\pi^0}$.

Let us consider the $K_L \to \pi^0 X^0$ decay. As with the $K_L \to \pi^0 \nu\overline{\nu}$ and $K^+ \to \pi^+ \nu\overline{\nu}$ decays, the branching fractions of the $K_L \to \pi^0 X^0$ and $K^+ \to \pi^+ X^0$ decays has the Grossman-Nir relation :

$$\mathcal{B}(K_L \to \pi^0 X^0) < 4.3 \times \mathcal{B}(K^+ \to \pi^+ X^0). \tag{1.26}$$

In the search for the $K_L \to \pi^0 X^0$ decay, a large part of the X^0 mass region is limited by the $K^+ \to \pi^+ X^0$ search with the Grossman-Nir relation. The region $m_{X^0} \sim m_{\pi^0}$, however, is not limited because there are no upper limits from the $K^+ \to \pi^+ X^0$ decay; this is the "experimental loophole" in the indirect limits for the $K_L \to \pi^0 X^0$ decay [12]. On the other hand, the $K_L \to \pi^0 X^0$ decay with $m_{X^0} \sim m_{\pi^0}$ is detectable by the $K_L \to \pi^0 \nu\overline{\nu}$ searches because such kinematical exclusion is not adopted.

A large part of the loophole was covered by the $K_L \to \pi^0 \nu\overline{\nu}$ search at the first run of the KOTO experiment [10], even though the $K_L \to \pi^0 \nu\overline{\nu}$ sensitivity was worse than the Grossman-Nir bound.

1.3 History of the experimental $K_L \to \pi^0 \nu\overline{\nu}$ search

Various experimental searches for the $K_L \to \pi^0 \nu\overline{\nu}$ decay has been performed so far, although they have never observed the $K_L \to \pi^0 \nu\overline{\nu}$ signal events yet. The history of the upper limit for the branching fraction of the $K_L \to \pi^0 \nu\overline{\nu}$ decay is shown in Fig. 1.8 [6, 41, 42, 43, 44, 45, 46, 11, 10]. We will introduce the recent experiments, namely the KEK E391a experiment [11] and the J-PARC KOTO experiment [9, 8], in the following sections.

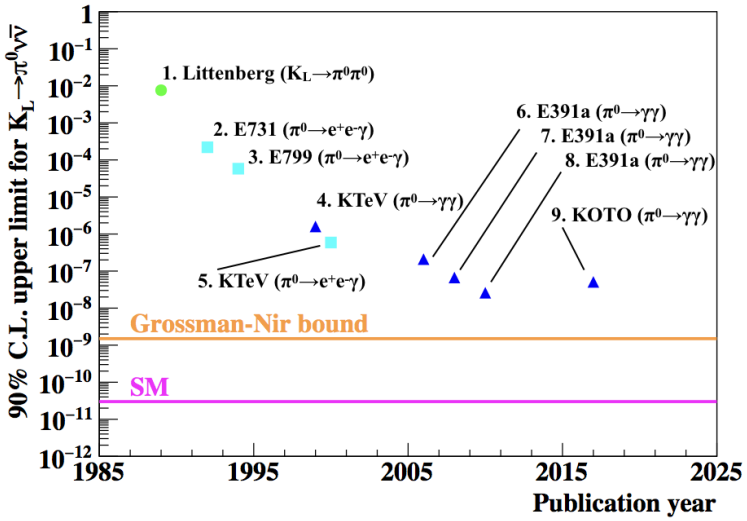

Figure 1.8: History of the upper limit for the branching fraction of the $K_L \to \pi^0\nu\overline{\nu}$ decay. The green point indicates the first study performed by L. S. Littenberg. The cyan square (blue triangle) points represent the results based on the final state of $\pi^0 \to e^+e^-\gamma$ ($\pi^0 \to 2\gamma$). The magenta (orange) line indicate the SM prediction (Grossman-Nir bound at 90% C.L.).

1.3.1 KEK E391a Experiment

The KEK E391a experiment [11] was the first dedicated experiment to search for the $K_L \to \pi^0\nu\overline{\nu}$ decay conducted at the High Energy Accelerator Research Organization (KEK) in Japan. The goal of E391a is to achieve the sensitivity of the branching ratio predicted in the SM with a beam delivered from the 12 GeV proton synchrotron. The experiment was designed to detect two photons from a π^0 decay without any extra detectable particles. Data taking was performed from 2004 to 2005, and the final result is

$$\mathcal{B}(K_L \to \pi^0\nu\overline{\nu}) < 2.6 \times 10^{-8} \quad (90\%\ \text{C.L.}). \tag{1.27}$$

1.3.2 J-PARC KOTO Experiment

The J-PARC KOTO experiment [8, 9], which has been conducted at the Japan Proton Accelerator Research Complex (J-PARC) [47], in Tokai Village, Ibaraki Prefecture, is the successor of the KEK E391a experiment. The KOTO adopts the same experimental method as the E391a experiment, which will be explained in Sec. 2.1. The goal of the KOTO experiment is to achieve the sensitivity for the $K_L \to \pi^0\nu\overline{\nu}$ decay to the level of the SM prediction (SM sensitivity).

The first data taking was performed in 2013 (hereinafter referred to as "2013 run"). Although the data taking was unfortunately terminated due to an accident in the experimental facility, sensitivity comparable to that of the E391a experiment was achieved only with a 100 hours of data taking period. As a result, one event was observed as a $K_L \to \pi^0\nu\overline{\nu}$ signal candidate and it was consistent with the background estimation of 0.34 ± 0.16 events [10]. The upper limit for the $K_L \to \pi^0\nu\overline{\nu}$ decay was set to be

$$\mathcal{B}(K_L \to \pi^0\nu\overline{\nu}) < 5.1 \times 10^{-8} \quad (90\%\ \text{C.L.}). \tag{1.28}$$

1.4 Purpose and outline of this thesis

We collected approximately 20 times more data in 2015 (hereinafter referred to as "2015 run") than in 2013. Since the expected number of background events was already 0.34 ± 0.16 in the 2013 run, it

is essential to suppress the background level to search for the $K_L \to \pi^0 \nu\overline{\nu}$ and $K_L \to \pi^0 X^0$ decays with the 2015 run data.

The purpose of this thesis is to report a search for the $K_L \to \pi^0 \nu\overline{\nu}$ and $K_L \to \pi^0 X^0$ decays based on the 2015 data with new analysis methods we developed to suppress the backgrounds.

The outline of this thesis is as follows. In Chapter 2, the experimental methodologies and apparatus of the KOTO experiment are described. The trigger and data taking condition in the 2015 run are summarized in Chapter 3, and the event reconstruction procedure is described in Chapter 4. In Chapter 5, production schemes of Monte Carlo (MC) simulations are explained. The analysis procedures and the results of the search for $K_L \to \pi^0 \nu\overline{\nu}$ and $K_L \to \pi^0 X^0$ are described in Chapter 6. In Chapter 7, we discuss the obtained results, future prospects and possible measures to reach better sensitivity. We conclude this thesis in Chapter 8.

Chapter 2

The KOTO Experiment

The KOTO experiment [8, 9] is dedicated to studying the $K_L \to \pi^0\nu\overline{\nu}$ decay. In this chapter, the experimental methodologies for detecting $K_L \to \pi^0\nu\overline{\nu}$ and the apparatus of the KOTO experiment are explained.

2.1 Experimental Methods

2.1.1 Signal Identification

In the KOTO experiment, we use decay in-flight K_L's and identify the signal with the concept of "*two photons + nothing else*"; we measure two photons from a π^0 decay and ensure the absence of extra particles associated with the π^0 decay since neutrinos are undetectable.

The schematic view of the signal identification is shown in Fig. 2.1. In the $K_L \to \pi^0\nu\overline{\nu}$ decay, the π^0 decays immediately[*1] to two photons with a branching fraction of 98.8% [15]. These two photons are detected by an electromagnetic calorimeter. The calorimeter consists of CsI crystals and the energies and positions of two photons are measured. Using the four-momentum of two photons $(E_1, \boldsymbol{p}_1)$, $(E_2, \boldsymbol{p}_2)$, the invariant mass of a π^0 is given by

$$(E_1 + E_2)^2 - (\boldsymbol{p}_1 + \boldsymbol{p}_1)^2 = 2E_1E_2(1 - \cos\theta), \tag{2.1}$$

where θ is the opening angle of the two photons. We calculate the opening angle with the nominal π^0 mass, M_{π^0}, as

$$\cos\theta = 1 - \frac{M_{\pi^0}^2}{2E_1E_2}. \tag{2.2}$$

Assuming the decay vertex is on the beam axis, corresponding to the z-axis in our detector coordinate system, we obtain the decay z position Z_{vtx} as shown in Fig. 2.2 and then the transverse momentum of the π^0, P_t.

One signature of the $K_L \to \pi^0\nu\overline{\nu}$ decay is that there are no other detectable particles associated with the π^0 decay. We ensure that there are no other detectable particles associated with the π^0 decay by having hermetic veto counters around the decay volume. A beam hole is needed in the calorimeter to allow intense K_L beam pass through. Thus in the downstream, veto counters in-beam is required. If there are any activities in the veto counters, such events are discarded ("*veto cuts*"). By imposing the veto cuts, we can reject the background from other K_L decays as described in the following subsection.

Another signature of the $K_L \to \pi^0\nu\overline{\nu}$ decay is that the reconstructed π^0 has a non-zero P_t since the neutrinos carry away momentum. We define the signal region on the P_t versus Z_{vtx} plane (Fig. 2.3), and regard the remaining events in the signal region after imposing all the selection criteria ("*cuts*") including other π^0 kinematic cuts, as signal candidates. In this analysis, we performed a blind analysis, in which we decided all the cuts without observing events inside the signal region.

[*1] $c\tau_{\pi^0} \sim 2.5 \times 10^{-8}$ m [15].

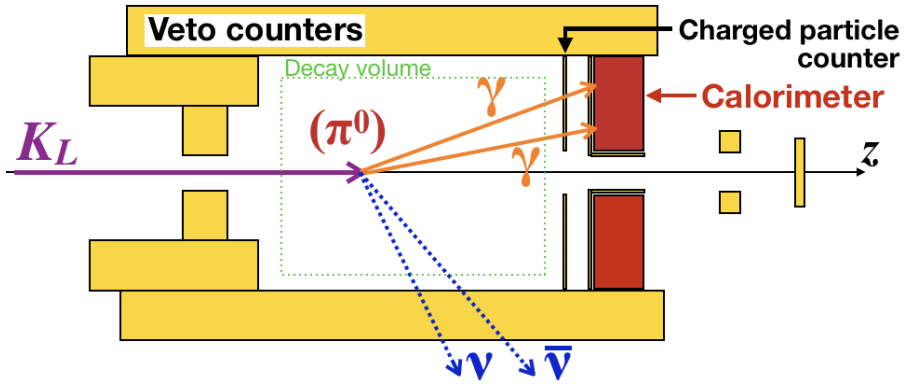

Figure 2.1: Schematic explanation of the signal detection in KOTO. Red boxes represent an electromagnetic calorimeter and yellow boxes represent veto counters. Two photons from a π^0 decay are measured with the calorimeter and the absence of extra particles is ensured with the hermetic veto counters surrounding the decay volume. Backgrounds from other K_L decay modes are rejected by imposing veto cuts.

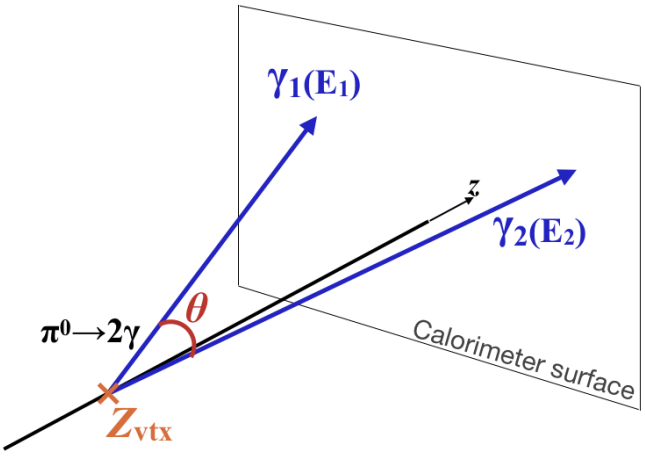

Figure 2.2: z vertex (Z_{vtx}) reconstruction of a π^0.

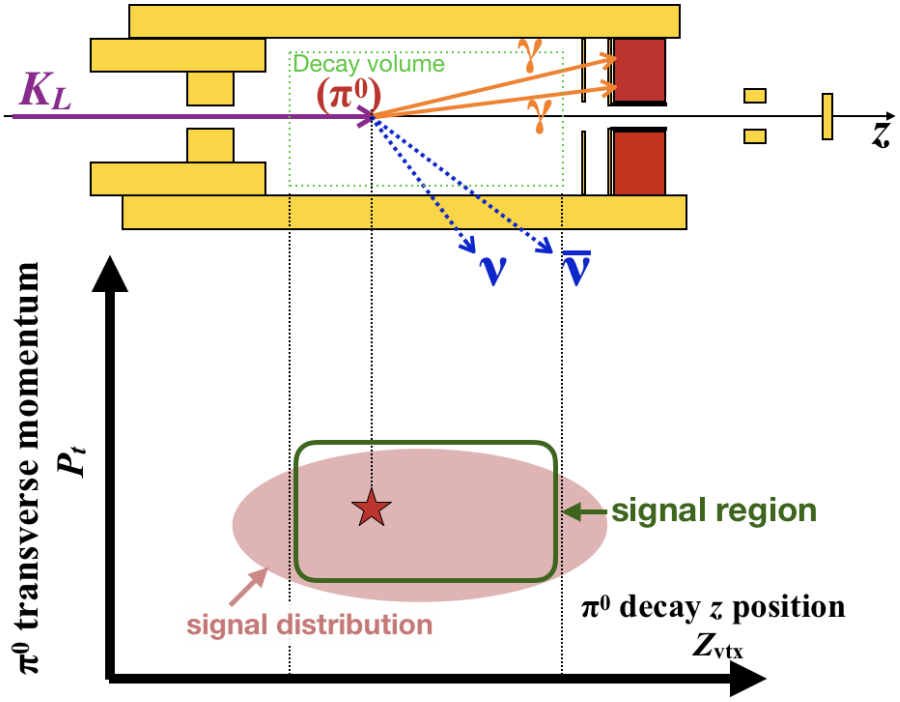

Figure 2.3: P_t versus $Z_{\rm vtx}$ plane (bottom) and schematic signal event display (top). The green box represents the signal region.

2.1.2 Background

The backgrounds in the $K_L \to \pi^0\nu\overline{\nu}$ search in the KOTO experiment are categorized into two groups: K_L decay background and neutron-induced background.

2.1.2.1 K_L Decay Background

The K_L decay background is caused by other K_L decay modes. The main K_L decay modes and their branching fractions are summarized in Table 2.1.

The $K_L \to \pi^\pm e^\mp \nu_e$, $K_L \to \pi^\pm \mu^\mp \nu_\mu$, and $K_L \to \pi^+\pi^-$ decays can make two clusters in the CsI calorimeter, but they can be vetoed with a charged veto counter located in front of the CsI calorimeter (see Fig. 2.1). Decays associated with π^0('s) are the main sources of the background. The $K_L \to \pi^+\pi^-\pi^0$ and $K_L \to 2\pi^0$ are serious sources in particular because only two extra particles can be used to veto the event.

In the case of the $K_L \to 2\gamma$ decay, the particles in the final state are identical to that of $K_L \to \pi^0\nu\overline{\nu}$. The background from this decay mode is rejected by kinematic cuts, not by veto cuts; reconstructed two photons from $K_L \to 2\gamma$ has no P_t because there are no extra particles in this decay.

2.1.2.2 Neutron-Induced Background

The neutron-induced background is caused by "*halo-neutrons*". The halo-neutrons, explained in Sec. 2.2.3, are the neutrons distributing around the beam core region. They can hit detector components.

The neutron-induced background is subdivided into three categories : hadron-cluster background, upstream-π^0 background, and CV-η background.

The hadron-cluster background is caused by a halo-neutron directly hitting the calorimeter. The neutron makes a primary hadronic shower and then a neutron produced in the shower makes another

Table 2.1: Main decay modes of K_L and their branching fractions [15].

decay mode	branching fraction
$K_L \to \pi^{\pm} e^{\mp} \nu_e$	$40.55 \pm 0.11\%$
$K_L \to \pi^{\pm} \mu^{\mp} \nu_\mu$	$27.04 \pm 0.07\%$
$K_L \to 3\pi^0$	$19.52 \pm 0.12\%$
$K_L \to \pi^+ \pi^- \pi^0$	$12.54 \pm 0.05\%$
$K_L \to \pi^+ \pi^-$	$(1.967 \pm 0.010) \times 10^{-3}$
$K_L \to 2\pi^0$	$(8.64 \pm 0.06) \times 10^{-4}$
$K_L \to 2\gamma$	$(5.47 \pm 0.04) \times 10^{-4}$

hadronic shower after traveling inside the calorimeter. These two separated hadronic showers mimic the two photon clusters from the $\pi^0 \to 2\gamma$ decay.

The upstream-π^0 background is caused by a halo-neutron hitting a veto counter located at the upstream edge of the decay volume, generating a π^0. Basically, $Z_{\rm vtx}$ of such events is calculated to be around the z position of the counter, but if the energy of the photons are mis-reconstructed to be smaller, the $Z_{\rm vtx}$ is shifted downstream into the signal region.

The CV-η background is caused by a halo-neutron hitting the charged particle veto counter ("Charged particle counter" in Fig. 2.1) that we call CV. The neutron hits CV and produces an η meson. The η decays to two photons and they hit the calorimeter. Because these two photons are reconstructed using the π^0 mass hypothesis, the reconstructed $Z_{\rm vtx}$ is pushed upstream into the signal region.

2.1.2.3 Main Backgrounds in the 2013 Run Data

In the 2013 run data analysis [10], the dominant background source was the hadron-cluster background: 0.18 events were expected out of 0.34 in total.

The next largest contribution was the upstream-π^0 background and the number of background events in the signal region was estimated to be 0.06 events[*2].

The number of $K_L \to \pi^+ \pi^- \pi^0$ background events was small (0.002), but it is because we raised the lower P_t bound of the signal region to 150 MeV/c to avoid the $K_L \to \pi^+ \pi^- \pi^0$ background events distribute in low P_t region at the expense of signal acceptance loss.

The hardware upgrades we conducted before the 2015 run to deal with these backgrounds are summarized in Sec. 2.2.4.13.

2.1.3 Branching Fraction and Single Event Sensitivity of $K_L \to \pi^0 \nu\overline{\nu}$

The branching fraction of the $K_L \to \pi^0 \nu\overline{\nu}$ decay can be measured with the number of observed signal events, $N_{\rm sig}$, as

$$\mathcal{B}(K_L \to \pi^0 \nu\overline{\nu}) = \frac{N_{\rm sig}}{N_{\rm decay}\ A_{\rm sig}}, \tag{2.3}$$

where $N_{\rm decay}$ is the number of K_L decays in the decay volume and $A_{\rm sig}$ represents the signal acceptance. The $N_{\rm decay}$ can be measured with the $K_L \to 2\pi^0$ decay. Using the number of reconstructed $K_L \to 2\pi^0$ events after imposing specific cuts, $N_{\rm norm}$, and the acceptance for the cuts, $A_{\rm norm}$, we obtain $N_{\rm decay}$ as

$$N_{\rm decay} = \frac{N_{\rm norm}}{\mathcal{B}(K_L \to 2\pi^0)\ A_{\rm norm}}. \tag{2.4}$$

[*2] The residual 0.10 events are the contributions from the K_L decay backgrounds.

The branching fraction of $K_L \to \pi^0\nu\overline{\nu}$ is obtained as

$$\mathcal{B}(K_L \to \pi^0\nu\overline{\nu}) = \frac{N_{\rm sig}}{N_{\rm norm}} \frac{A_{\rm norm}}{A_{\rm sig}} \mathcal{B}(K_L \to 2\pi^0). \tag{2.5}$$

The single event sensitivity (SES) is defined as the corresponding branching fraction where one event is expected in an analysis. From Eq. 2.5, SES is calculated as

$$\text{SES} = \frac{1}{N_{\rm norm}} \frac{A_{\rm norm}}{A_{\rm sig}} \mathcal{B}(K_L \to 2\pi^0). \tag{2.6}$$

By taking the ratio of the number of events of signal and normalization modes, we expect the cancellation of systematic uncertainties in their acceptances in common, such as detector responses, decay probability, geometrical acceptance, the accumulated number of protons on target (POT), and trigger efficiency. The reason why we use the $K_L \to 2\pi^0$ decay for the normalization is that the kinematics of π^0's are relatively similar to that of the $K_L \to \pi^0\nu\overline{\nu}$ decay among possible candidate decays, $K_L \to 3\pi^0$, $K_L \to 2\pi^0$, and $K_L \to 2\gamma$, whose final states are composed of only photons[*3].

2.1.4 Accidental Signal Loss

Because the absence of extra activities in the KOTO detector is required in the signal identification, accidental hits on detector components coincident with the π^0 decay cause a signal loss named "*accidental signal loss*". The accidental signal loss becomes larger with a higher counting rate and longer coincidence timing window (hereinafter referred to as "*veto window*") in detector components. The accidental signal loss L can be written as

$$L = 1 - P(k = 0; \lambda = RT) \tag{2.7}$$
$$= 1 - e^{-RT}, \tag{2.8}$$

where $P(k;\lambda)$ represents the Poisson probability function of observing k events when the average number of events is λ, R and T are the counting rate and the width of veto window of a counter, respectively.

2.2 Experimental Facility and Apparatus

2.2.1 J-PARC Accelerator

The KOTO experiment is conducted at the Japan Proton Accelerator Research Complex (J-PARC) [47], in Tokai Village, Ibaraki Prefecture, Japan. A bird's-eye view of J-PARC is shown in Fig. 2.4. The accelerator chain of J-PARC is composed of three accelerators: the Linac [48, 49], the 3-GeV Rapid Cycling Synchrotron (RCS) [50], and the Main Ring (MR) [51].

At the Linac, negative hydrogen ions, H^-, from an ion source are accelerated up to 400 MeV. The electrons of the accelerated H^- ions are stripped off by passing through a foil and the resultant protons are injected into RCS. This scheme enables effective beam injection on RCS with small beam loss. The RCS accelerates two bunches of the proton beam up to 3 GeV at the repetition rate of 25 Hz. The beam is then provided to both the Material and Life Science Experimental Facility (MLF) and MR. Two beam bunches are injected into MR four times and then those eight bunches are accelerated to 30 GeV. The accelerated beam is extracted to the Hadron Experimental Facility through the hadron beamline with the slow-extraction technique, in which the beam is extracted with a duration of 2 seconds. The reason why we use the slowly extracted beam is to reduce the instantaneous rate of particles coming into detectors so as to avoid event pileups. In 2015, the beam was extracted with a

[*3] Reconstruction of the normalization modes is performed by measuring all the photons in the final states with the CsI calorimeter.

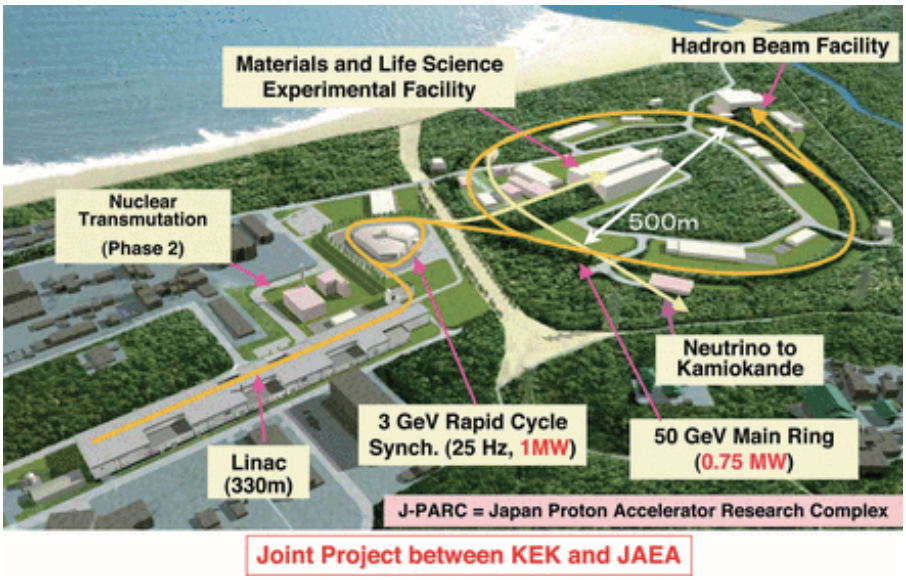

Figure 2.4: Bird's-eye view of J-PARC (quoted from Ref. [47]).

duration of 2 seconds as a "*spill*" every 5.52 - 6.0 seconds[*4]. The number of protons per spill was (3 - 5) $\times 10^{13}$ for the beam power of 24 kW to 42 kW.

The beam intensity should ideally be flat during spills, but actually it had some time structures. The beam structure, localization of the beam particles in time domain, causes high instantaneous counting rates in the KOTO detector components and thus makes the accidental signal loss described in Sec. 2.1.4 larger. The dominant structure called "*spike*" is caused by the ripple noise in the power supply of the MR magnets. The structures called "*Transverse-RF*" and "*Exciter*" are periodical structures due to the radio frequency field applied in MR to mitigate the spike structure and the frequencies are 47.47 MHz and 252.5 kHz, respectively. The first order effects of the structure is factorized by "*spill duty factor*" defined as

$$\frac{\left\{\int_0^T I(t)dt\right\}^2}{\int_0^T dt \cdot \int_0^T I^2(t)dt}, \tag{2.9}$$

where $I(t)$ is the spill intensity as a function of time t and T is the time range where the spill duty factor is computed. In case of the ideal flat beam, the duty factor is 100%, whereas the typical value was 40 - 50 % in 2015. Note that because of the finite sampling rate of the intensity monitor, effects from rapid structures like Transverse-RF and Exciter structures were not taken into account in the spill duty factor.

2.2.2 Hadron Experimental Facility

The KOTO's experimental area is located in the Hadron Experimental Facility (HEF) in J-PARC. The layout of HEF is shown in Fig. 2.5 and Fig. 2.6.

A 30-GeV proton beam extracted from MR is transported through the beam-switching yard (SY) to a gold production target ("T1 target" in Fig. 2.6) in HEF. The structure of the target is shown in Fig. 2.7. Two 66-mm-long gold blocks are bonded on a copper block with a water cooling pass embedded in. The two target blocks enable quick and remote replacement of the target in case of minor troubles. The horizontal (vertical) size of the gold targets is 15 mm (11 mm), whereas that of the beam is 2.5 mm (1 mm) in RMS. About 50% of the primary protons interact in the target,

[*4] The cycle time was 6.0 seconds at the beginning of 2015 and it was shortened to 5.52 seconds after the summer.

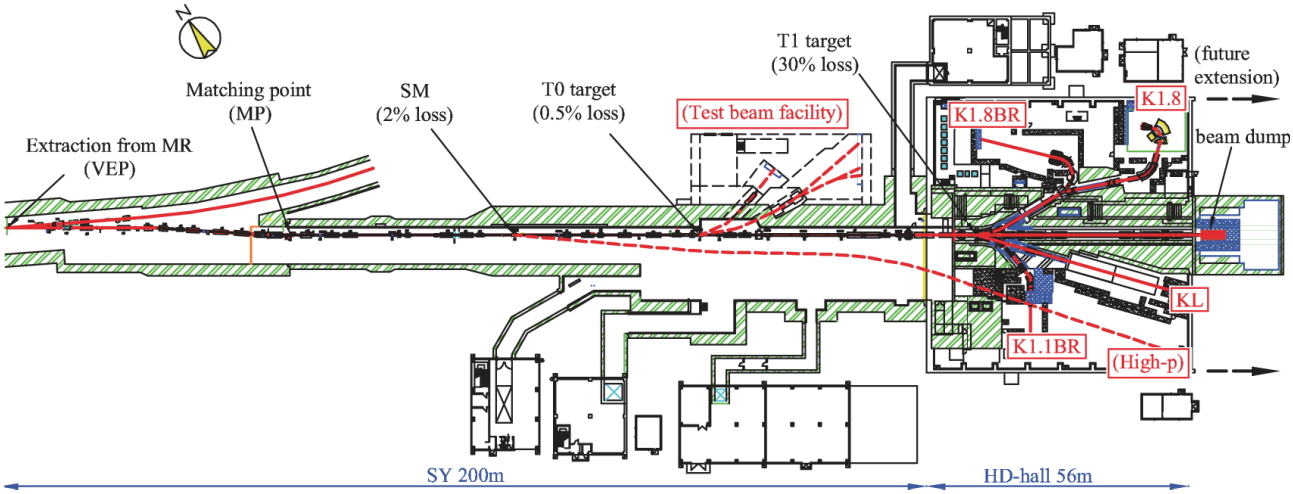

Figure 2.5: Layout of HEF including beam-switching yard region (quoted from Ref. [52]).

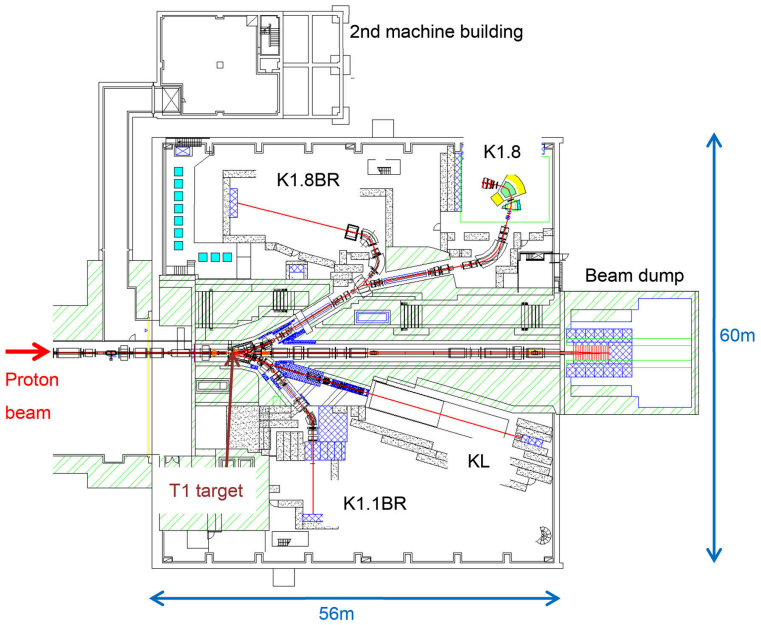

Figure 2.6: Layout of HEF (quoted from Ref. [53]). The region indicated as "KL" is the KOTO's experimental area.

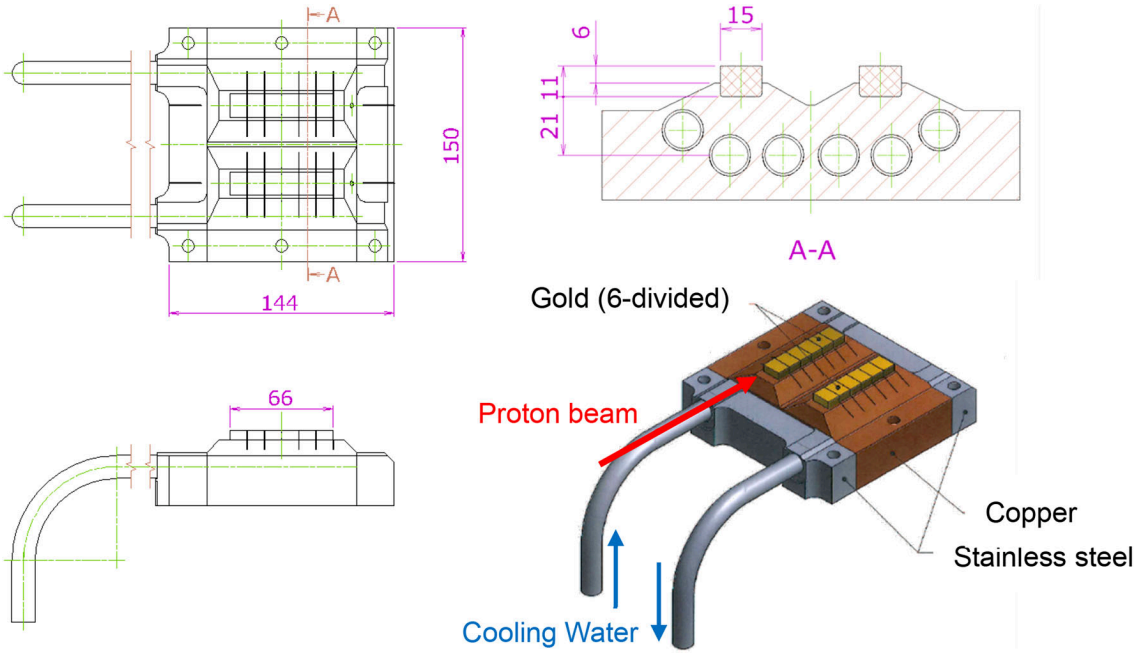

Figure 2.7: Structural drawings of the T1 production target (quoted from Ref. [53]).

and the secondary particles produced in the target are transported to experimental areas and used for experiments.

2.2.3 KL Beamline

For the KOTO experiment, the narrowness of the transverse beam width is an essential requirement. Since π^0's are reconstructed assuming their decay vertex to be on the beam axis, finite beam width causes the uncertainties of the vertex position, P_t, and other kinematic variables. Hence the beam is collimated in the beamline. The narrow beam is also required to maintain the coverage of the in-beam veto counters small, since they have lower detection efficiency due to a severe environment. Another important requirement on the beam is that it contains less "*halo-neutrons*". The halo-neutrons are neutrons which are scattered in the beamline and distribute outside the nominal solid angle of the beam. The core beam in the nominal solid angle passes the KOTO detector through the beam hole around the beam axis. On the other hand, the halo-neutrons can hit the detector components and be background sources.

The neutral beamline for KOTO is called "*KL beamline*" [54]. The schematic view of the KL beamline is shown in Fig. 2.8. The beamline is 20-m-long and 16° away from the primary proton beam. It consists of vacuum pipes, a 7-cm-thick lead absorber to reduce photons, two collimators to shape the beam, a beam plug to stop the beam if necessary, and a sweeping magnet to eliminate charged particles. The end of the beamline, or the downstream end of the second collimator, corresponding to 20 meters away form the T1 target, is referred to as "*beam-exit*". The beam is collimated by the two collimators to a size of 8×8 cm^2 at the beam-exit. The length of the beamline is long enough that short-lived particles such as hyperons and K_s's decay out. Therefore the main components of the beam at the beam-exit are photons, neutrons, and K_L's. The mean K_L momentum is 2 GeV/c with the peak at 1.4 GeV/c and the flux is 4.2×10^7 K_L's per 2×10^{14} protons on target (POT) [55, 56, 57, 58]. The fluxes of neutrons (kinetic energy $>$ 100 MeV) and photons (energy $>$ 10 MeV) were estimated to be six and seven times larger than the K_L, respectively. The collimators are arranged so as to minimize the halo-neutron yield. The profile of the beam neutrons at the surface of the CsI calorimeter is shown in Fig. 2.9. The small tail components represent halo-neutrons.

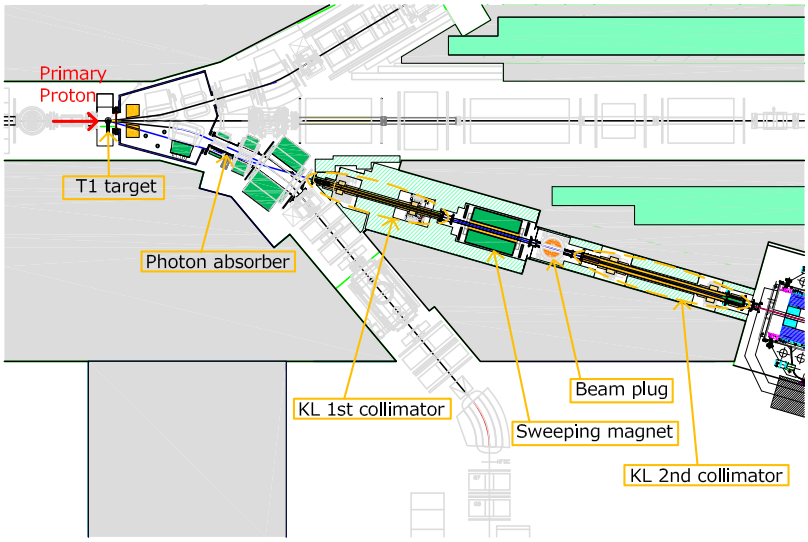

Figure 2.8: Schematic view of the KL beamline. A sweeping magnet and a beam plug are located between two collimators.

2.2.4 KOTO Detector

The schematic view of the KOTO detector is shown in Fig. 2.10. The origin of the z-axis is set at the upstream edge of Front Barrel (FB) and corresponds to 21.5 meters away from the T1 target[*5]. Most of the detector components are inside a vacuum vessel. The decay volume is kept in a vacuum of $\mathcal{O}(10^{-5})$ Pa in order to suppress π^0 productions by the interaction of beam neutrons and residual gas in the volume, which mimic the signal events. The decay region is separated from the detector region by thin films called "*Membranes*" in order to keep the high vacuum in the decay region avoiding outgas from detector components. The vacuum level of the detector region is 0.1 Pa.

Descriptions of detector components, the CsI Calorimeter and other veto counters, are written below. Updates from the setup of the first physics run in 2013 are summarized at the end of this section.

2.2.4.1 CsI Calorimeter (CSI)

The CsI electromagnetic calorimeter (CSI) is the main detector component of the KOTO detector. The schematic view and the picture of the CsI calorimeter are shown in Fig. 2.11. It consists of 2,716 un-doped CsI crystals read out by photomultiplier tubes (PMT's)[*6]. The crystal length along the z-axis is 50 cm and corresponds to $27X_0$. The 2,240 crystals have 2.5×2.5 cm^2 cross-section and occupy the central 1.2×1.2 m^2 region. The 476 crystals with 5×5 cm^2 cross-section surround the peripheral region. They are stacked inside a cylinder made of stainless-steel whose inner radius is 953 mm. The 15×15 cm^2 region at the center of the CsI calorimeter is an empty hole to let the beam particles pass through.

A PMT with a UV transmitting filter is attached to each crystal via a 4.6-mm-thick silicone disk, called cookie, for effective light transmission. The UV filter is used due to the following reason. The scintillation light emitted from the un-doped CsI crystal has two components. One is a fast component with the decay times of 10 ns and 36 ns, and the maximum light yield at the wavelength of 315 nm

[*5] 1.5 meters downstream from the beam-exit.

[*6] The CsI crystals and PMT's were previously used in the KTeV experiment [59, 60].

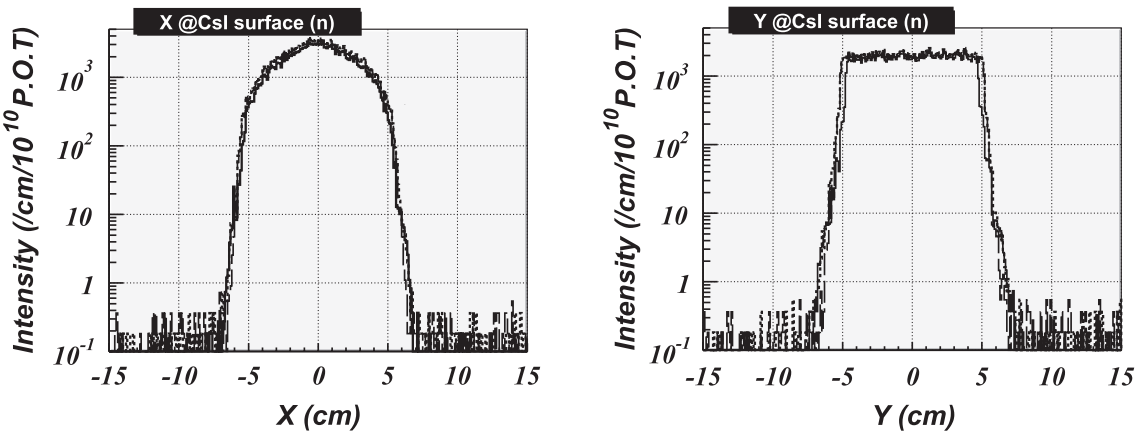

(a) Horizontal (x) beam profile.

(b) Vertical (y) beam profile.

Figure 2.9: Neutron profile at the surface of the CsI calorimeter (quoted from Ref. [54]).

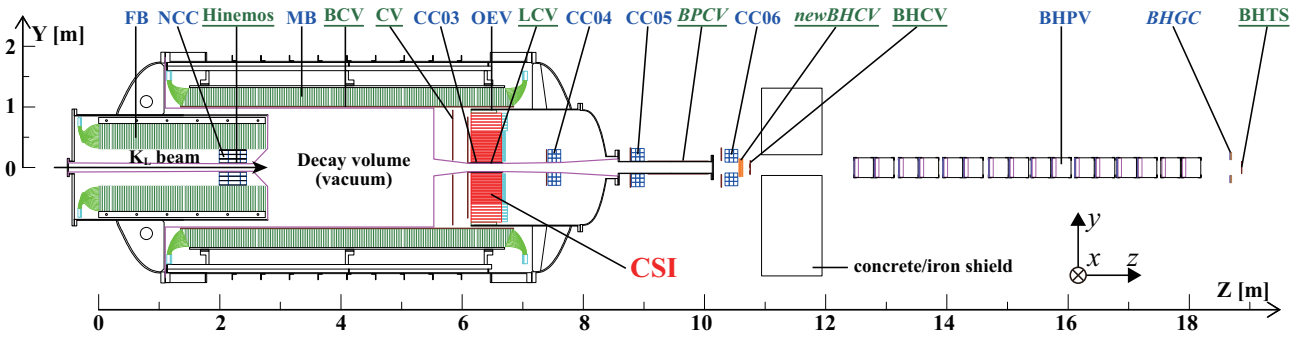

Figure 2.10: Sidecut view of the KOTO detector. The beam enters from the left. Detector components with their abbreviated names written in blue (in green and underlined) are photon (charged particle) veto counters. The Membranes are represented by magenta lines. BPCV, newBHCV, and BHGC are new counters installed after 2013. BHCV and BHTS were not used in the analysis. The origin of the z-axis, along with the beam direction, is the upstream edge of Front Barrel (FB) and x (horizontal) and y (vertical) axes are defined as in the right-handed coordinate system.

[61, 62]. The other is a slow component with the decay time around 1 μs and the maximum light yield at 480 nm [62, 61]. To reduce accidental pile-up effects from the slow component, we use the UV filter (Schott UG-11) with a near-zero transmission band in the wavelength range between 400 nm and 650 nm and a peak transmission of approximately 80% at 300 nm.

The CsI calorimeter has an excellent energy resolution σ_E of $\sigma_E/E = (0.99 \oplus 1.74/E)\%$, where $\oplus$ indicates a quadratic sum and E represents the energy of an incident electron in units of GeV [63].

Detailed descriptions of the CsI calorimeter can be found in Refs. [57, 58].

2.2.4.2 Charged Veto (CV)

The Charged Veto counter (CV) covers the front surface of CSI and serves to identify whether particles incident on CSI are charged particles or neutral particles. The CV is composed of two layers of 3-mm-thick and 69-mm-wide plastic-scintillator strips with wavelength-shifting (WLS) fibers embedded in the strips. The front (rear) layer is located 30 cm (5 cm) upstream of CSI.

The schematic view and the photographs of CV are shown in Fig. 2.12 and Fig. 2.13, respectively. The scintillator strips are aligned on a 0.8-mm-thick carbon fiber reinforced plastic (CFRP) plate. Scintillation light propagating in the fibers is detected by multi-pixel photon counters (MPPC's) attached to both ends of the fibers.

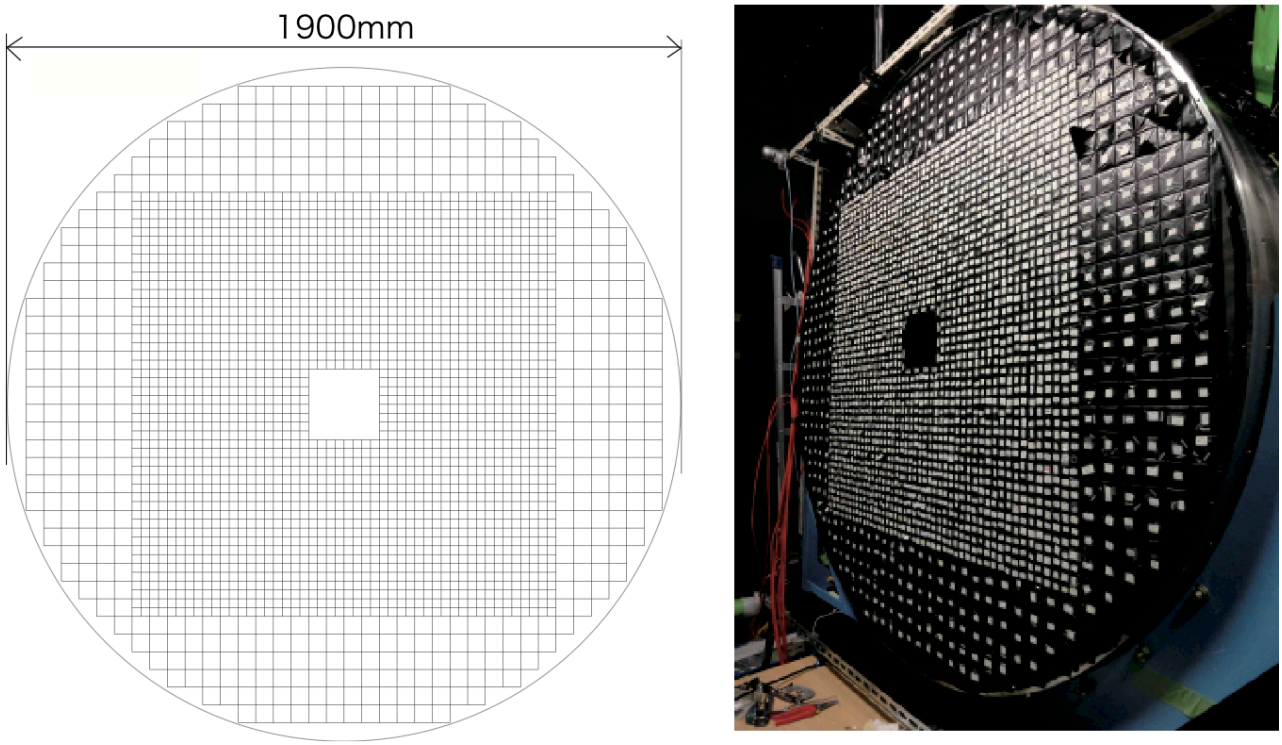

Figure 2.11: Schematic front view (left) and picture (right) of the CsI calorimeter (quoted from Ref. [57]).

Detailed descriptions of CV are found in Ref. [64].

2.2.4.3 Main Barrel (MB) and Front Barrel (FB)

The Main Barrel (MB) and the Front Barrel (FB) counters are photon veto counters surrounding the decay volume. The FB also covers the upstream region to veto K_L decays at upstream. They are lead-scintillator sandwich counters originally developed for the KEK E391a experiment.

The MB consists of 32 trapezoidal modules with a length of 5.5 meters arranged to surround cylindrical volume. The inner diameter is 2 meters. A cross-sectional view of MB and one of its modules are shown in Fig. 2.14. Each module consists of 45 layers of lead[*7] and 5-mm-thick plastic-scintillator sheets, and the total radiation length is $14.0X^0$. Scintillation light is read from both ends with PMTs via WLS fibers embedded in the scintillator sheets. Fibers from inner 15 layers and outer 30 layers of scintillator sheets are separately bundled to PMT's. The total number of readout channels of MB is 128.

The Front Barrel (FB) consists of 16 trapezoidal modules with a length of 2.75 meters. A cross-sectional view of FB and the constitutive module are shown in Fig. 2.15. Each module consists of 59 layers of 1.5-mm-thick lead and 5-mm-thick plastic-scintillator sheets, and the total radiation length is $16.5X^0$. Scintillation light is read from the upstream end with PMT's. Signals from inner 27 and outer 32 layers are read separately in a similar configuration as MB. The total number of readout channels of FB is 32.

Details of MB and FB are found in Ref. [65].

[*7] 1-mm-thick for inner 15 layers and 2-mm-thick for outer 30 layers.

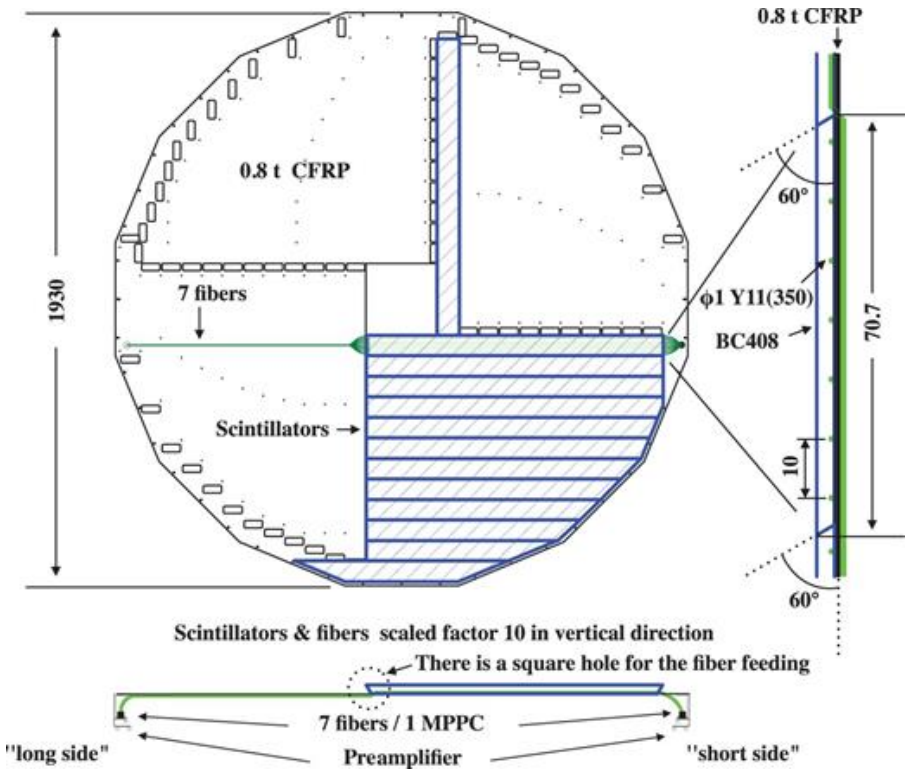

Figure 2.12: Schematic front view of the front layer of CV (quoted from Ref. [64]). The rear layer has a similar structure. It has a quadrant symmetry. Wavelength-shifting fibers are extended to MPPC's at the outer circumference.

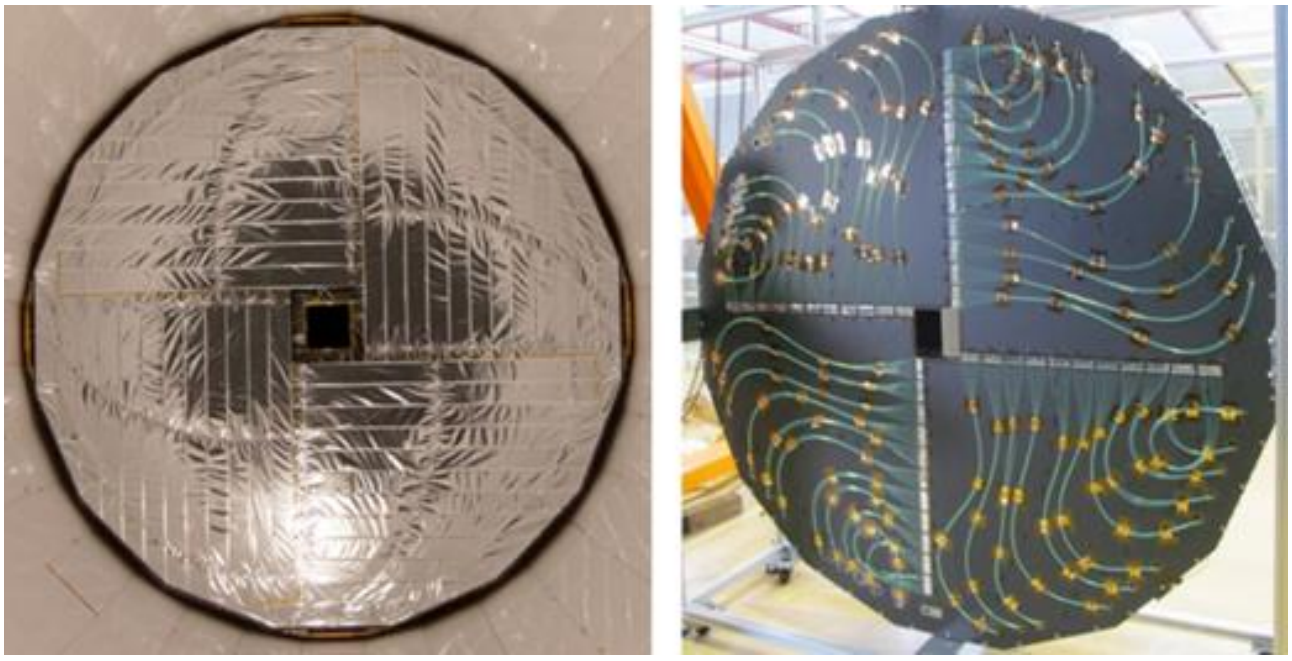

Figure 2.13: Photographs of CV layers (quoted from Ref. [64]). Left: an upstream view after installation in the KOTO detector system. Each scintillator strips is wrapped with an aluminized-mylar sheet. Right: a downstream view before installation. The black plane is a CFRP plate supporting the plastic-scintillator strips.

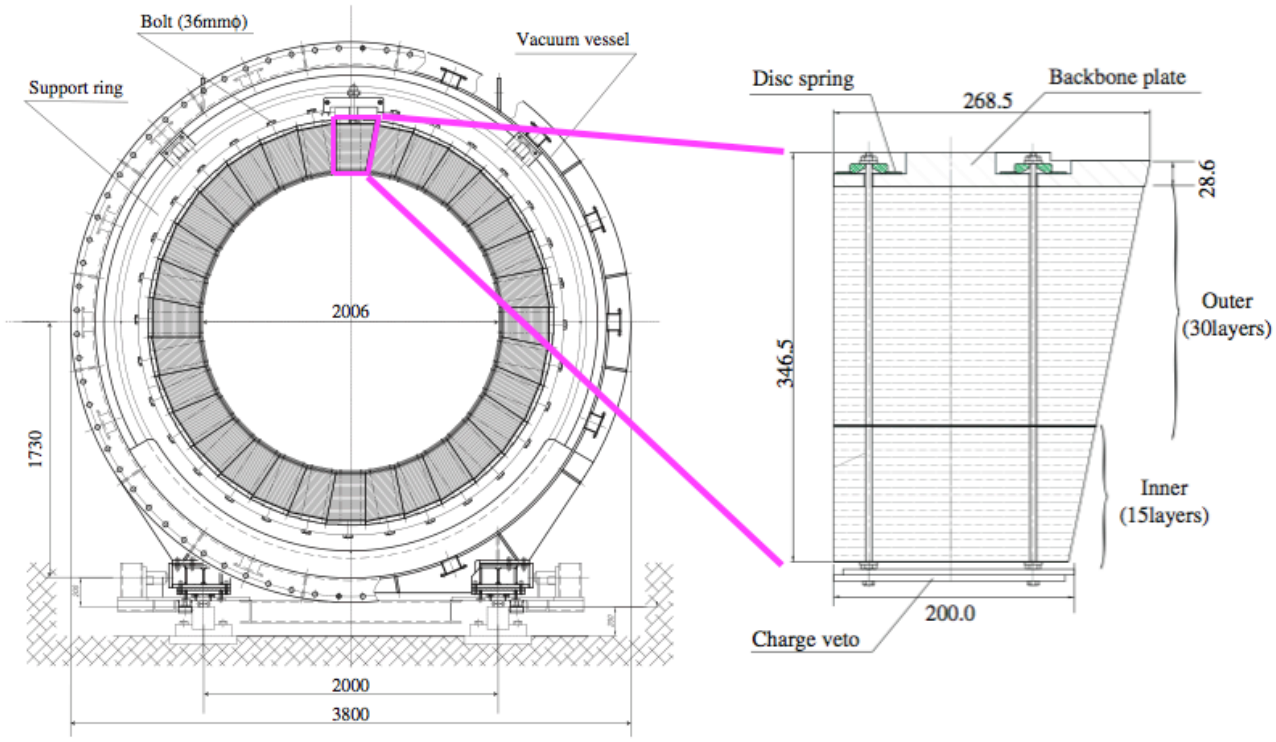

Figure 2.14: Cross-sectional views of MB and the vacuum vessel (left) and a MB module (right). The figures are quoted from Ref. [65]. Scales in the figures are in units of mm. The scintillator sheets attached inside the MB modules represented as "Charged veto" in the right figure are BCV.

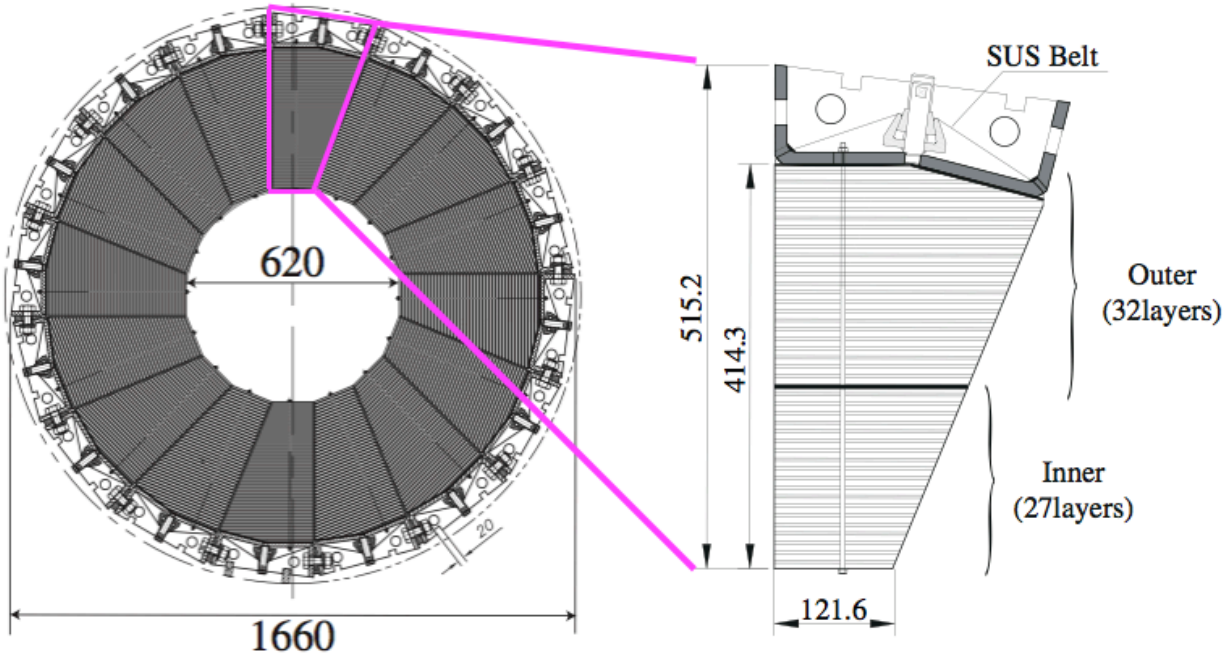

Figure 2.15: Cross-sectional views of FB (left) and a FB module (right). The figures are quoted from Ref. [65]. The lengths in the figures are in units of mm.

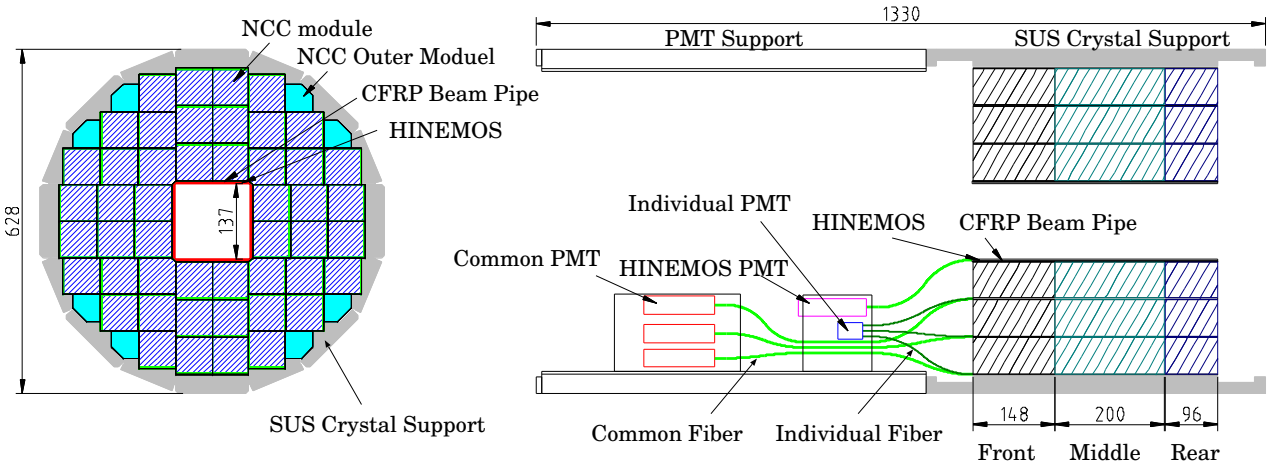

Figure 2.16: Schematic front (left) and side (right) views of NCC (quoted from Ref. [67]).

2.2.4.4 Barrel Charged Veto (BCV)

The Barrel Charged Veto (BCV) counter covers the inner surface of MB as shown in Fig. 2.14. It is composed of 32 plastic-scintillator sheets with a thickness of 10 mm where WLS fibers are embedded. The signal of each module is read from both ends of the WLS fibers by PMT's.

2.2.4.5 Neutron Collar Counter (NCC) and Hinemos

The Neutron Collar Counter (NCC) [66] is located inside FB and surrounds the K_L beam. It serves as an upstream boundary of the decay volume; decay products from K_L's which decay in the upstream of NCC are shielded. Another important role of NCC is to suppress the upstream-π^0 background, which is caused by halo-neutrons hitting the upstream boundary and producing π^0's. The full-activeness of NCC (mentioned later) suppresses this background by detecting the secondary particles associated with the π^0 production.

The NCC is a fully-active counter made of un-doped CsI crystals and consists of 48 inner modules and 8 outer modules. Figure 2.16 is a schematic view of NCC. The eight modules with pentagonal shapes located around the outer circumference are the outer modules and the others are the inner modules. The signal from the outer modules is read out with a PMT attached on the crystal. WLS fibers are used for the readout of the inner modules.

The NCC has a beam-hole at its center, which is made with a 2-mm-thick CFRP pipe. The inner surface of the CFRP pipe is covered by a charged particle veto counter named Hinemos. The Hinemos is made of plastic-scintillator sheets and WLS fibers. It vetoes the events with π^0's produced in NCC or the CFRP pipe by detecting associated particles.

2.2.4.6 Collar Counter 3 (CC03) and Liner Charged Veto (LCV)

The Collar Counter 3 (CC03) covers the inner surface of the CsI calorimeter beam-hole. They veto events in which K_L's decay near the CsI calorimeter. Figure 2.17 shows the positional relation with the CsI calorimeter, and Fig. 2.18 shows the closeup view around the beam-hole. The CC03 is composed of 16 un-doped CsI crystals with a rectangular cross-section of 45.5×18 mm^2 and a length of 500 mm, equipped with two PMT's for each. The CC03 fills the gap between the CsI calorimeter and a 4.5-mm-thick CFRP beam-pipe supporting the beam-hole structure.

The inner surface of the beam-pipe is covered by the Liner Charged Veto (LCV) counter to detect charged particles before they hit the beam-pipe. The LCV consists of four plastic-scintillator sheets with WLS fibers embedded.

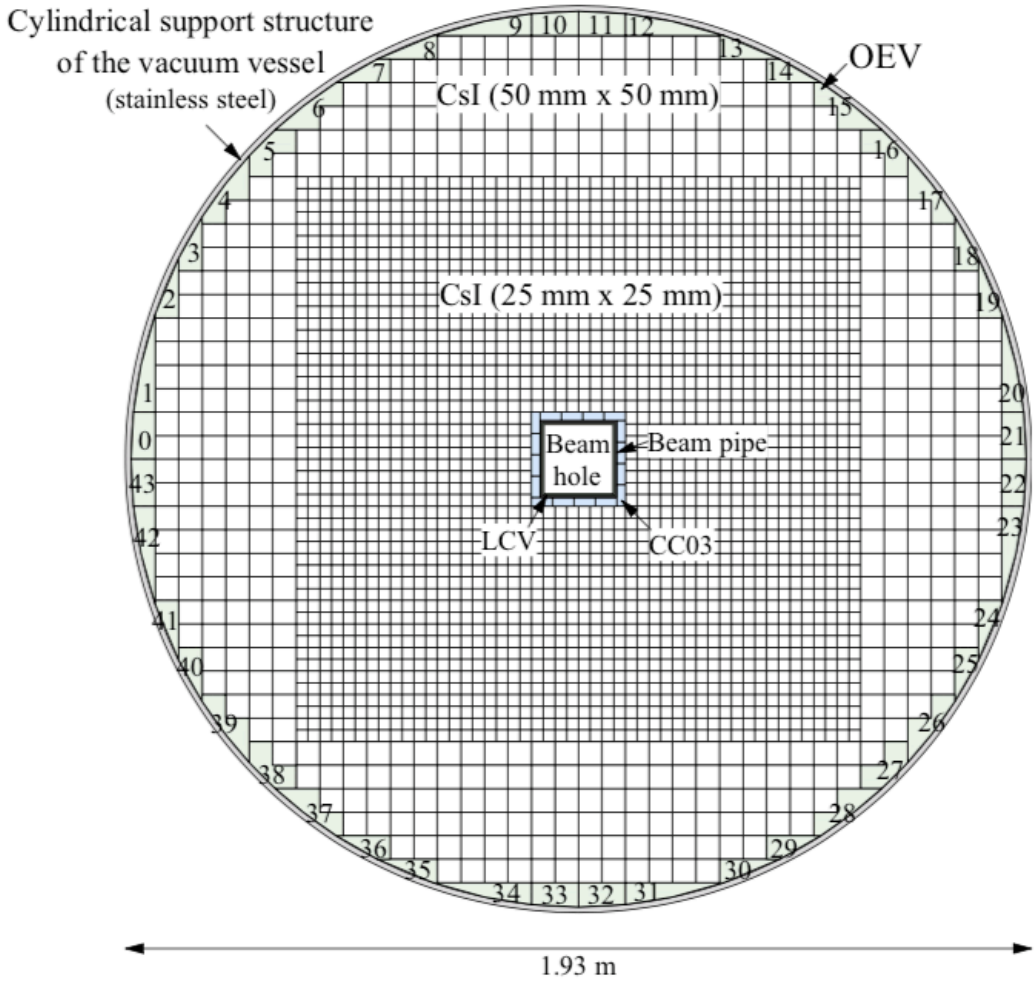

Figure 2.17: CsI calorimeter and veto counters covering inside and outside of the calorimeter (quoted from Ref. [68]).

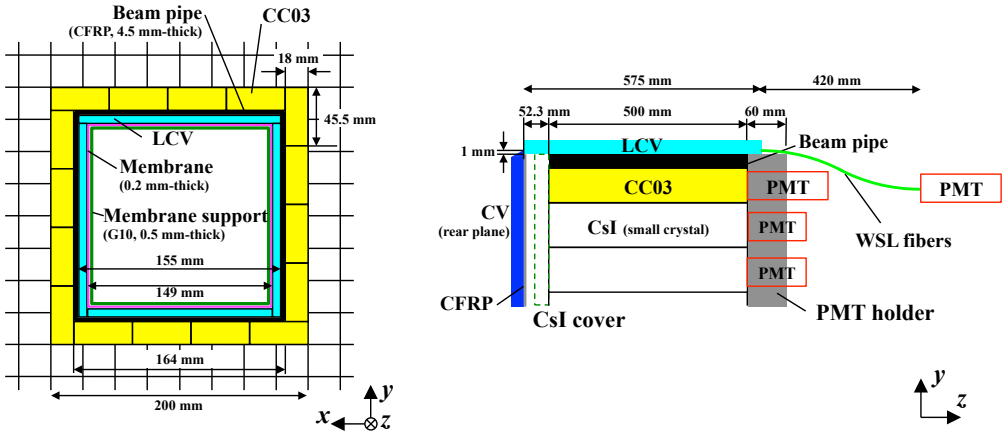

Figure 2.18: Closeup front (left) and side (right) views of the beam-hole of CSI (quoted from Ref. [67]).

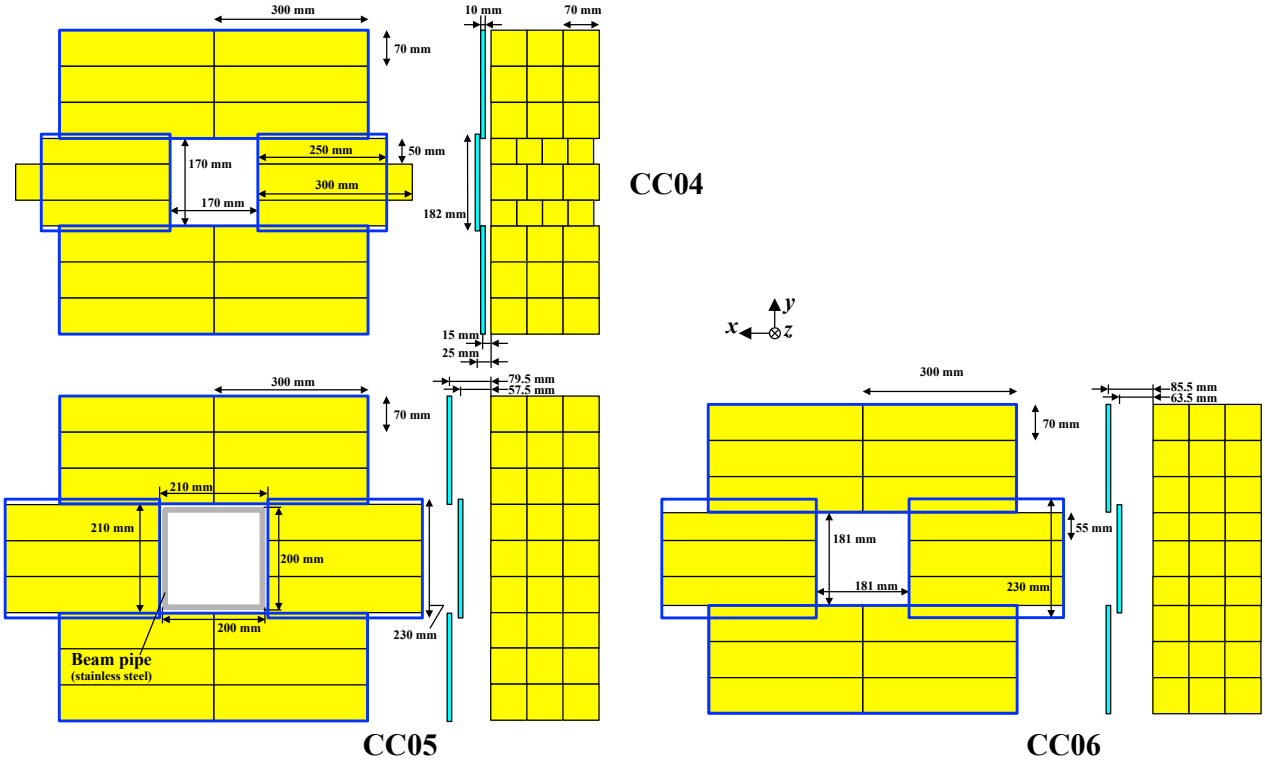

Figure 2.19: Configuration of CC04 (left top), CC05 (left bottom), and CC06(right bottom). The figures are quoted from Ref. [67]. In each counter, the left figure shows the upstream view and the right one shows the side view. The yellow boxes indicate CsI crystals and the blue lines or cyan boxes indicate plastic-scintillators.

2.2.4.7 Outer Edge Veto (OEV)

The Outer Edge Veto (OEV) counter covers the outer edge of CSI filling the gap between CSI and the SUS cylinder as shown in Fig. 2.17 to reject photons entering the outer edge region of CSI. The OEV is composed of 44 modules of lead-scintillator sandwich counters. The signals are read by PMT's via WLS fibers embedded in the plastic-scintillator sheets.

Details of OEV are found in Ref. [68].

2.2.4.8 Collar Counter 4, 5, and 6 (CC04, CC05, and CC06)

The Collar Counters named CC04, CC05, and CC06 are located in the downstream region surrounding the K_L beam to detect photons and charged particles escaping through the CSI beam-hole. They have the similar configuration as shown in Fig 2.19: pairs of a photon counter made of un-doped CsI crystals and a charged particle counter made of plastic-scintillators. The plastic-scintillators are located just in front of the CsI crystals. The CC04 is located in the vacuum vessel while CC05 and CC06 are located outside the vacuum.

2.2.4.9 Beam Pipe Charged Veto (BPCV)

The Beam Pipe Charged Veto (BPCV) counter is located between CC05 and CC06 along the downstream beam pipe to detect charged particles. Figure 2.20 shows the positional relation among them. The main role of the BPCV is to suppress the background from the $K_L \to \pi^+\pi^-\pi^0$ decay. This background is caused dominantly by the absorption of charged pions in the downstream beam pipe. We used the downstream beam pipe made with a 5-mm-thick SUS square pipe in the 2013 run and replaced

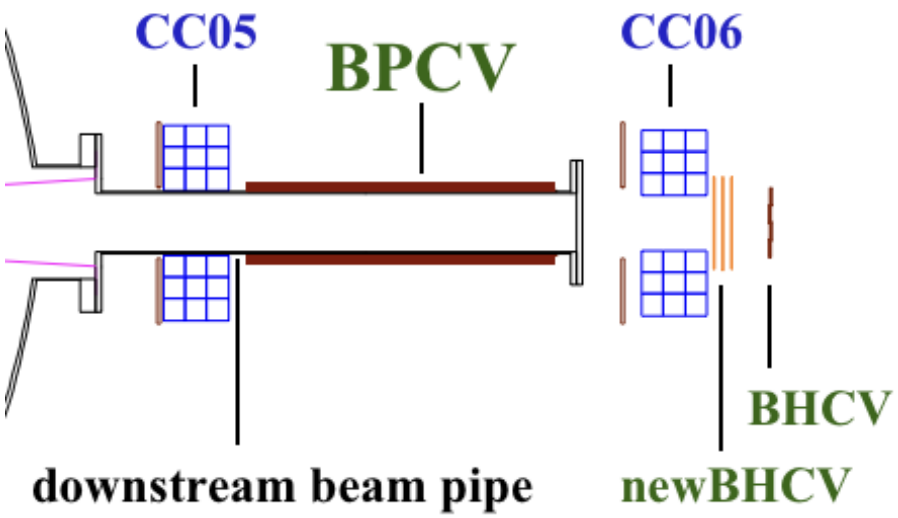

Figure 2.20: Schematic view of a downstream part of the KOTO detector.

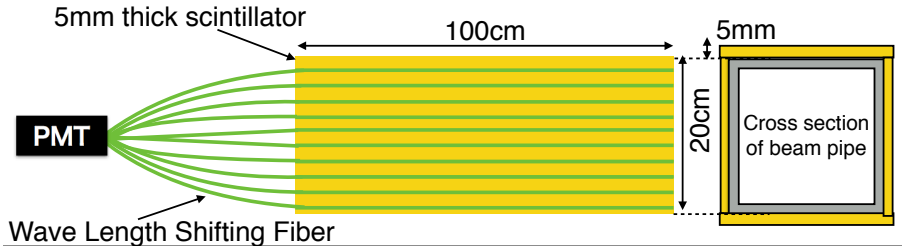

Figure 2.21: Schematic view of BPCV (quoted from Ref. [69]). The gray square in the right figure (cross-sectional view) represents the downstream beam pipe.

it with a 5-mm-thick aluminum pipe before the 2015 run to reduce the absorption. The BPCV is effective to suppress such background events further by detecting secondary charged particles associated with the interactions.

The BPCV is composed of four plastic-scintillator sheets with WLS fibers embedded in the sheets. A schematic view of BPCV is shown in Fig. 2.21.

The BPCV was installed after the first physics run in 2013.

2.2.4.10 Beam Hole Charged Veto (BHCV) and newBHCV

The Beam Hole Charged Veto (BHCV) counter covers the downstream in-beam region to detect charged-particles passing through the beam-hole. This counter should be insensitive to neutral particles because it is exposed to a high flux of photons and neutrons in the K_L beam. In the first physics run, BHCV was composed of eight pairs of a 3-mm-thick plastic-scintillator sheet and a PMT as shown in Fig. 2.22, but it suffered from a high rate of accidental hits with neutrons. The hit rate was 8.4 MHz with a 24 kW beam in 2013 and it caused gain instability of the PMT's.

We installed three layers of multi-wire proportional chambers (MWPC) as "newBHCV"[*8] before the 2015 run. In the 2015 run, we operated both BHCV and newBHCV for redundancy, though we did not use BHCV for the physics data analysis.

[*8] The newBHCV was developed by the author of this thesis, Kota Nakagiri [70, 71].

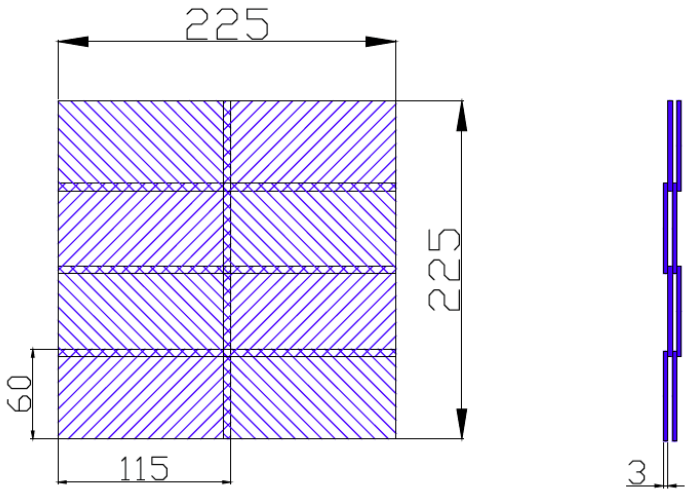

Figure 2.22: Schematic front (left) and side (right) views of BHCV used in 2013 (quoted from Ref. [69]).

Figure 2.23 shows the structure of a newBHCV chamber. Three chambers were stacked along the beam direction. Gold-plated 30-cm-long tungsten wires of 50-μm in diameter are used as anode wires. The 160 wires are strung with a spacing of 1.8 mm so that they cover an approximately 30×30 cm^2 region. Ten wires are ganged and read out as a channel.

One of the features of newBHCV is the thin gap, 1.4 mm, between the anode wires and cathode planes. This thin gap enables the fast removal of ions produced in a gas multiplication process and reduces a space charge effect. It makes the chamber tolerant to high rate condition.

Another feature of newBHCV is that it is a low-mass counter; it contains a small amount of material so that an interaction rate with beam-contained photons and neutrons is expected to decrease. To reduce the amount of material, we use graphite-coated polyimide films with a thickness of 50 μm for the cathode planes, which is located in-beam region. The cathode plane, however, could be distorted by the pressure difference between inside and outside of the sensitive volume of the chamber due to its weakness of mechanical strength. Hence, to reduce the pressure difference, we let gas flow to both inside and outside of the sensitive volume sequentially as shown in Fig. 2.24. The buffer region and outside air are bounded by a 12-μm-thick aluminized-mylar. Thanks to this low-mass feature, the hit rate in newBHCV was reduced by a factor of 3 compared with BHCV.

The chamber is filled with mixed gas of Tetrafluoromethane (CF_4) and n-Pentane with a mixing ratio of 55:45. Generally, wire chambers have a relatively large time jitter because of the drift time of electrons from their ionized points to the amplified region. We chose the CF_4 gas, which is known as "fast gas" in which electron drift velocity is fast, and mixed the n-Pentane gas as a quencher to stabilize the operation.

2.2.4.11 Beam Hole Photon Veto (BHPV)

The Beam Hole Photon Veto (BHPV) counter is placed in the downstream region of the KOTO detector system to detect photons passing through the beam hole. The BHPV is insensitive to neutrons contained in the K_L beam.

The BHPV consists of multiple modules of lead-aerogel Cherenkov counters placed along the beam axis. A schematic view of the module is shown in Fig. 2.25. Each module is composed of a lead converter, an aerogel radiator, light-collecting mirrors, and PMT's. Figure 2.26 shows the layout of BHPV with full 25 modules, the total converter thickness of which corresponds to $10X_0$. In the 2013 run, only 12 modules ($\sim 4X_0$) were installed. After the 2013 run, four modules were added and 16 modules ($\sim 6.2X_0$) were used in the 2015 run. Modules are going to be added as needed in the future.

Detailed descriptions of BHPV are in Ref. [72].

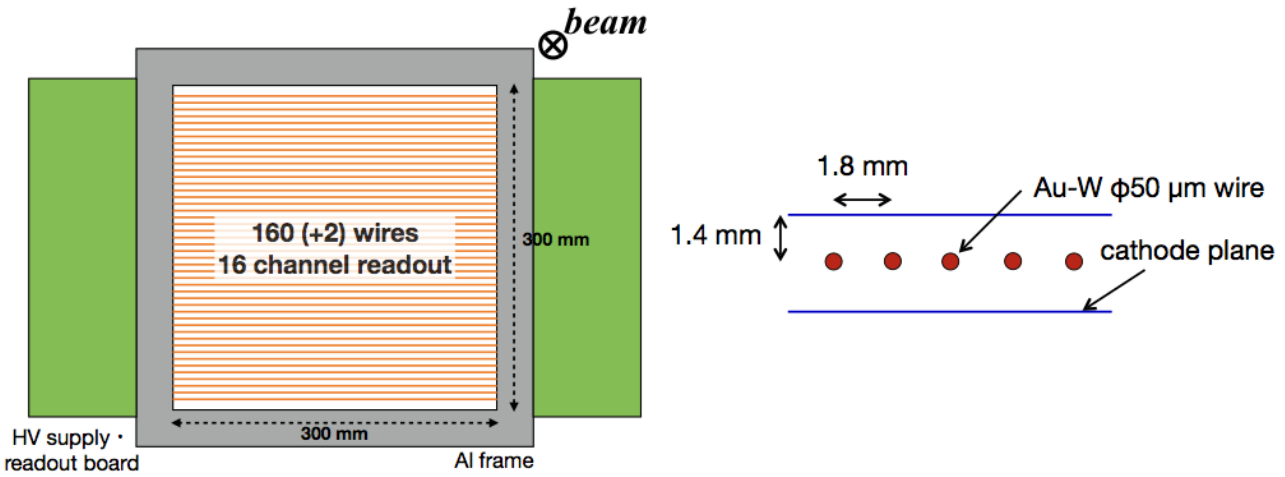

Figure 2.23: Schematic view of a newBHCV module (left) and its cell structure.

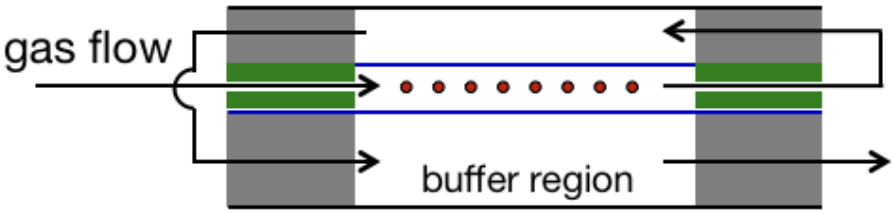

Figure 2.24: Schematic view of the gas flow path of newBHCV. The gas flows to the sensitive volume (the central region with wires) and then sequentially to the buffer regions (upper and lower regions) so that the pressure there is the same as that of the sensitive volume.

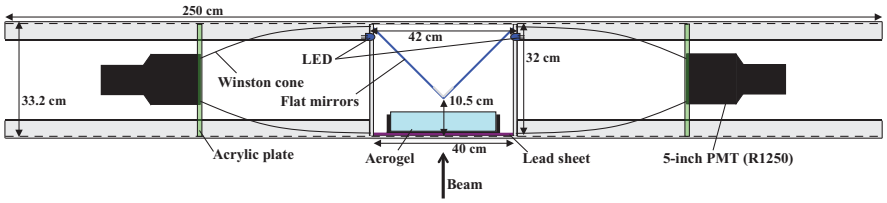

Figure 2.25: Schematic view of a BHPV module (quoted from Ref. [72]).

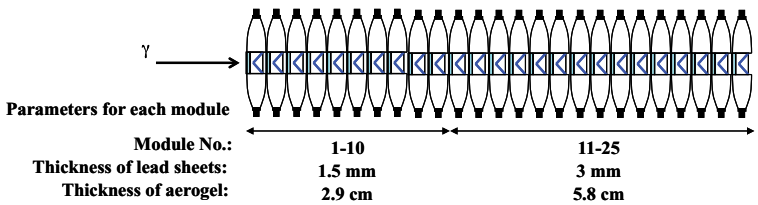

Figure 2.26: Layout of BHPV (quoted from Ref. [72]). The thickness of each lead converter and aerogel radiator is optimized with taking the photon efficiency and neutron blindness into account.

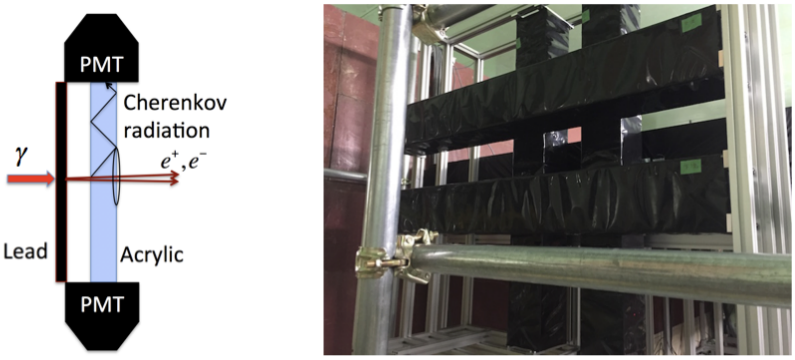

Figure 2.27: Left: Schematic view of a BHGC module (quoted from Ref. [73]). Right: a picture of BHGC viewed from downstream (quoted from Ref. [74]).

2.2.4.12 Beam Hole Guard Counter (BHGC)

The Beam Hole Guard Counter is located in the most downstream part of the KOTO detector system or just behind BHPV to detect photons passing through the BHPV edge region. The BHGC is composed of four modules of lead-acrylic Cherenkov counters arranged in parallel crosses as shown in Fig. 2.27. Each module consists of a 9.6-mm-thick lead converter and 10-mm-thick acrylic radiator with a size of 500×120 mm^2.

This counter was newly installed after the first physics run in 2013.

Details of BHGC are found in Refs. [73, 74].

2.2.4.13 Summary of the Detector Upgrades from the 2013 run

From the 2013 run, we newly installed BPCV, newBHCV, and BHGC. Additional four modules were installed for BHPV. The Hinemos, which had been already installed since the 2013 run but not used in the analysis, is used in the 2015 run analysis. On the other hand, BHCV were kept in the KOTO detector system in 2015 but it is not used in the $K_L \to \pi^0\nu\overline{\nu}$ analysis.

We replaced the downstream beam pipe made of SUS with the low-mass one made of aluminum to reduce the $K_L \to \pi^+\pi^-\pi^0$ background events.

We replaced the upstream vacuum window, which separates vacuum regions of the beamline and the KOTO detector[*9] and was made of a 125-μm-thick polyimide film located at $z = -500$ mm, with a 12.5-μm-thick polyimide film to reduce the amount of material which scatters particles in the beam.

We developed a beam profile monitor [75] for better alignment of the collimators to minimize the halo-neutron yield. In the 2015 run, we monitored the beam profile and aligned the collimators before the beam time.

2.2.5 Data Acquisition System

To ensure good performance in event reconstruction with the CsI calorimeter and to resolve overlapping pulses in the veto counters, signals from all the detector components are recorded with 125-MHz or 500-MHz sampling analog-to-digital converter (ADC) modules. In the KOTO data acquisition (DAQ) system, we adopted a pipeline readout system [76, 77] to eliminate dead time caused by trigger decision time.

The ADC modules were custom-built for the KOTO experiment. A large part of detector components, or all except for BHCV, newBHCV, BHPV, and BHGC, use the 125-MHz ADC modules. The 125-MHz ADC modules [78] have a 14-bit dynamic range for the energy measurement over the range

[*9] Some powdery materials were observed inside the vacuum region of the line vacuum. The upstream vacuum window was placed to prevent it from entering into the detector region.

of three orders of magnitude, $\mathcal{O}(1\text{ MeV})$ to $\mathcal{O}(1\text{ GeV})$. Because the raw waveform from the detector components is too narrow to be recorded with 125-MHz sampling, a ten-pole Bessel filter is used to widen and form the waveform of a Gaussian shape with $\sigma = 27$ ns [79]. The detector components with high hit rates, BHCV, newBHCV, BHPV, and BHGC, use the 500-MHz ADC modules with 12-bit dynamic range without shaping filters [80], which reduces pulse overlapping. The recorded time range for each event and each channel is 512 ns, which corresponds to 64 (256) samples in the case of 125-MHz (500-MHz) sampling.

The trigger scheme in KOTO mainly consists of two stages of trigger decisions.

The first stage called "*Level 1 (Lv1) trigger*" is issued based on the total energy deposit in each detector component. The sum of waveforms of all the channels in a detector component is used for the trigger decision. When the summed-up waveform has a peak with the peak height exceeding a given threshold, a signal, called "*Et signal*", is generated. The Lv1 trigger is formed by taking the coincidence or anti-coincidence of Et signals from detector components.

Once the Lv1 trigger is issued, the waveform information in the 512-ns time window of all the channels is sent to the "*Level 2 (Lv2) trigger*" system, which is the second stage of the KOTO trigger scheme. In the Lv2 trigger, the center of energy deposition (COE) of the CsI calorimeter is calculated to be used for the trigger decision. The distance of the COE position from the center of the calorimeter, R_{COE}, is utilized to suppress trigger rate from the $K_L \to 3\pi^0$ decay, which tends to have small R_{COE} value, while the $K_L \to \pi^0\nu\overline{\nu}$ signal event tends to have large R_{COE} due to the missing energy carried away by neutrinos. When R_{COE} is larger than a given threshold, the event is accepted and the Lv2 trigger is issued.

Events passing the Lv2 trigger decision are transferred to a computing farm for event building and data collection. The events are saved in temporary local disk storage and then transferred to permanent tape storage at KEK Computer Research Center in Tsukuba.

In the 2015 run, the Lv2 trigger was the bottleneck and the limited buffer size available in the Lv2 trigger caused the dead time of the DAQ system. To mitigate the dead time, in the middle of the 2015 run, we implemented bit-packing lossless data compression inside the ADC modules [77] which reduced the data packet size without losing any information.

Detailed descriptions of the DAQ system are found in Refs. [76, 77, 69].

Chapter 3

Data Taking

We define "physics run" as data taking with the purpose of collecting a $K_L \to \pi^0\nu\overline{\nu}$ sample. We performed several kinds of data taking other than the physics run to calibrate detectors and to understand backgrounds. In this chapter, we explain the trigger settings (Sec. 3.1) and types of data taken in 2015 (Sec. 3.2 and Sec. 3.3). The beam and DAQ conditions in 2015 are also explained in Sec. 3.4.

3.1 Trigger Conditions in Physics Run

We took data with various trigger conditions to collect data for several purposes simultaneously. The maximum number of events taken in a spill was approximately 8000-9000 limited by the buffer size of the L2 trigger system. We managed the trigger rates to be within the limit by adjusting the Et signal thresholds of each detector components or by pre-scaling triggered events. The main trigger to collect the $K_L \to \pi^0\nu\overline{\nu}$ sample was "Physics trigger" explained in Sec. 3.1.1. The purposes and conditions of the triggers used in the physics run are explained in the following sections.

3.1.1 Physics Trigger

The physics trigger was used to collect the $K_L \to \pi^0\nu\overline{\nu}$ sample. The Lv1 trigger decision was made by requiring the CSI Et signal and absence of Et signals (online veto) from MB, CV, NCC, and CC03. The threshold for the CSI Et signal was set to 550 MeV and the raw trigger rate was approximately 400 k events per spill at 42 kW beam intensity, and veto by MB, CV, NCC, and CC03 reduced the L1 trigger rate to 35 k events per spill. In the Lv2 trigger, R_{COE} was required to exceed 160 mm and it reduced the L2 trigger rate by 30%.

3.1.2 Normalization Trigger

The purpose of the Normalization trigger was to collect the $K_L \to 3\pi^0$, $K_L \to 2\pi^0$, and $K_L \to 2\gamma$ samples. In the normalization modes analysis described in Sec. 6.2, we reconstruct these decays with the events in which all the photons in the final state hit the CsI calorimeter. In such events, there should be no activities in veto counters, and R_{COE} should be small because there is no missing energy. For these reasons, in the Normalization trigger, we adopted the same Lv1 trigger condition as in the Physics trigger and imposed no COE selection in the Lv2 trigger. In order to suppress the trigger rate, we applied a pre-scaling factor of 30 for this trigger.

3.1.3 Minimum-Bias Trigger

The Minimum-Bias trigger was used to collect data free from the trigger biases from the online veto decisions. Only the CSI Et signal was required and a pre-scaling factor of 300 was applied to reduce the trigger rate.

3.1.4 Calibration Trigger

The Calibration trigger was used to collect the $K_L \to 3\pi^0$ sample which is used for the energy calibration of the CsI calorimeter. In this trigger, we used the Et signal information of subdivided twelve regions (Fig. 3.1) of the CsI calorimeter (sub-Et signal). The sub-Et signal of each region was issued when the energy sum in the region exceeded 120 MeV. If four or more sub-Et signals were generated, the Calibration trigger was issued. A pre-scaling factor of 10 was applied to this trigger.

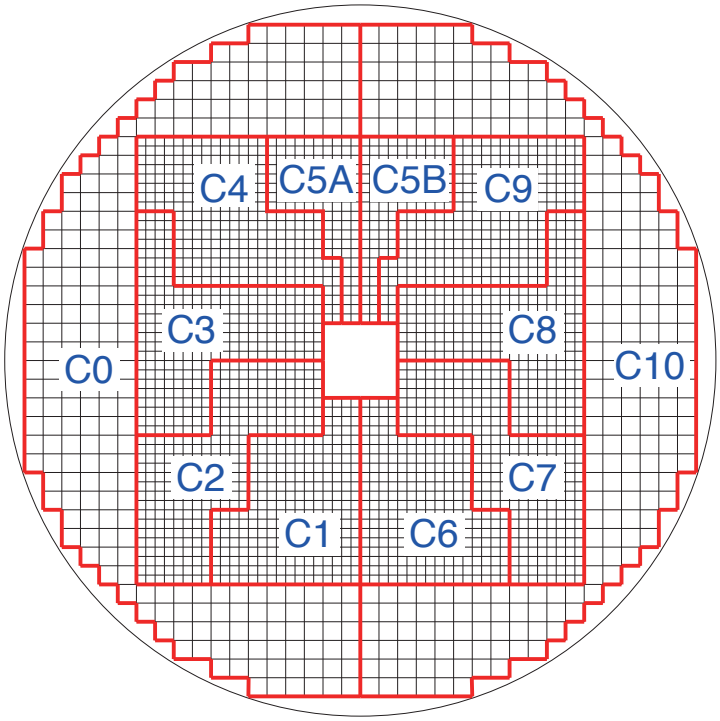

Figure 3.1: Segmented twelve regions of the CsI calorimeter for the Calibration trigger (quoted from Ref. [57]).

3.1.5 Clock Trigger

This Clock trigger and also TMON, LED, and Laser triggers are categorized as "external trigger", which do not use any information from detector components.

The Clock trigger was issued by 10 Hz periodic clock signal to take random trigger data. Clock trigger data were utilized to monitor the detector condition and the counting rates in detector components during a beam spill.

3.1.6 TMON Trigger

The TMON trigger was generated from the signals of the target monitor (TMON). The TMON consisted of a series of plastic scintillators and located in 50° direction from the primary beamline and is used to monitor the yields of secondary particles from the target.

TMON trigger was used to collect events with accidental activities related to the beam. The TMON trigger rate, as well as the Physics trigger rate, is proportional to the beam intensity, which has time structures. Thus the data taken with TMON trigger ("TMON data") reproduced the accidental activities where the Physics trigger was likely to be issued. We took the TMON data simultaneously with the Physics trigger data to reproduce the accidental activities in simulation as described in Sec. 5.5.

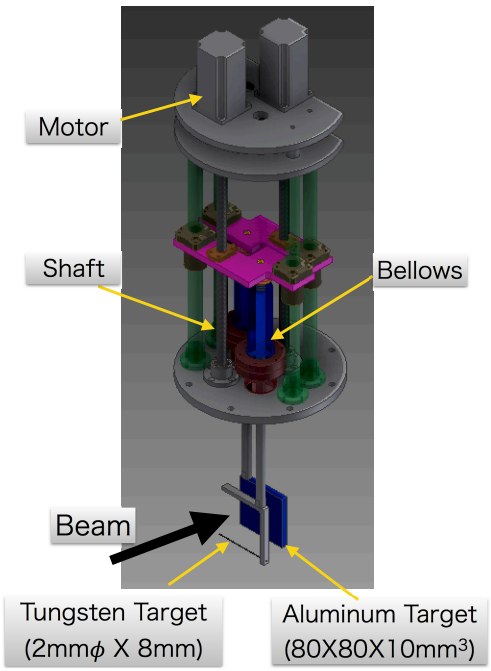

Figure 3.2: Schematic view of the Z0 target and its driving device. The aluminum target and the tungsten target can be moved along the vertical direction independently. The tungsten target was not used in the data taking in 2015.

3.1.7 LED Trigger and Laser Trigger

For the calibration purpose, light from laser or LED is distributed to almost all the modules of detector components. The laser and LED were flashed in 5 and 10 Hz, respectively. The LED trigger and Laser trigger were issued synchronously with their flash timing.

3.1.8 Cosmic Ray Trigger

In order to monitor the stability of the detector components especially for CSI, we collected cosmic ray data during the off-spill time. Cosmic ray trigger was issued based on the Et signals from CSI, NCC, and OEV.

3.2 Special Run for the Control Sample of the Hadron Cluster Background (Z0 Al run)

We performed special runs named "*Z0 Al run*" to collect a control sample for the hadron-cluster background: events in which a neutron directly hits the CsI calorimeter and produces two hadronic showers consecutively. In this run, we inserted a 10-mm-thick aluminum plate with the size of 80 × 80 mm^2 ("*Z0 target*"[*1]) as a scattering source of the beam-core neutrons. Figure 3.2 shows the schematic view of the Z0 target and its driving device to move the target. It was installed at $z = -639$ mm, just upstream of the KOTO detector. The Z0 target was inserted only when this special run was performed and was moved out in the rest of the time.

Some of the scattered neutrons due to the Z0 target hit the CsI calorimeter directly and made hadron-cluster events. We collected such events and used them as a control sample to study the hadron-cluster background.

In the data taking, we used Physics trigger with a pre-scaling factor of 9 to 12 depending on beam intensity, since the total trigger rate was approximately 10 times higher than that of the physics run to take a $K_L \to \pi^0\nu\bar{\nu}$ sample. We also used the Clock, TMON, LED, Laser, and Cosmic Ray triggers, mixed with the Physics trigger.

[*1] The Z0 target was named after its position close to $z = 0$ in the KOTO coordinate system, although the accurate position was $z = -643$ mm.

Table 3.1: Summary of the duration of each Run in the 2015 run.

operation cycle (Run)	period
Run 62	Apr. 24th ∼ May 7th
Run 63	Jun. 5th ∼ Jun. 26th
Run 64	Oct. 15th ∼ Nov. 12th
Run 65	Nov. 14th ∼ Dec. 18th

3.3 Calibration Runs

3.3.1 Cosmic Ray Run

In order to calibrate detector components, we took cosmic ray data before and after the beam time. The triggers were issued based on the Et signals from CSI, MB, NCC, OEV, CC04, CC05, and CC06. We used these data to calibrate CSI, FB, NCC, Hinemos, MB, BCV, CC03, LCV, OEV, CC04, CC05, and CC06.

3.3.2 Beam Muon Run

In the beam muon run, the beam plug in the beamline (Fig. 2.8) was closed to stop beam particles. High momentum muons can penetrate the beam plug and enter the KOTO detector. We performed the beam muon run to calibrate detector components using these muons which penetrate the detector components. The trigger setting was composed of BHCV Et signal and coincidence of Et signals of NCC and CC04, CC05, and CC06. We used these data to calibrate CC04, CC05, CC06, BHCV, BHPV, and BHGC.

3.3.3 BPCV Calibration Run

The BPCV calibration run was performed to calibrate BPCV with penetrating charged particles from the decay of K_L's. To collect such events, we required Et signal of CC06 which was located just downstream of BPCV.

3.3.4 Aluminum Target Run

In the aluminum target run, we inserted a 5-mm-thick aluminum plate ("*Al target*") 100 mm in diameter into beam-core region just downstream of FB ($z \sim 2800$ mm). Beam-core neutrons interacted with the Al target and generate π^0's. We collected such events to calibrate the CsI calorimeter since Z_{vtx} of such a π^0 is known and a product of energies of two photons are obtained from Eq. 2.2.

The trigger condition was similar to that of the special run described in Sec. 3.2.

3.4 Summary of the Beam and DAQ Conditions in the 2015 Run

In 2015, we took data over four operation cycles of the J-PARC MR, which are expressed as "*Run*"s[*2]: Run 62 to Run 65. The periods of those Runs are summarized in Table 3.1.

We subdivided the 2015 run data into nine periods (hereinafter referred to as "*run-periods*") based on the accelerator operation cycle (Run 62 to Run 65) and beam power (24kW to 42kW). They are summarized in Table 3.2. The spill cycle time, the time interval of spills, was 6.0 sec in Run 62 and Run 63, and 5.52 sec in Run 64 and Run 65, while the spill length of 2 sec was not changed.

In the following subsections, we describe some topics occurred during the 2015 run.

[*2] The Run number is incremented when the ion source of the accelerator is replaced.

Table 3.2: Summary of the subdivided run periods in the 2015 run.

	Run	beam power	spill cycle	accumulated POT
Period-1	Run 62	24 kW	6.0 sec	7.70×10^{17}
Period-2	Run 62	27 kW	6.0 sec	1.25×10^{18}
Period-3	Run 63	27 kW	6.0 sec	6.18×10^{17}
Period-4	Run 63	29 kW	6.0 sec	7.05×10^{17}
Period-5	Run 63	32 kW	6.0 sec	2.26×10^{18}
Period-6	Run 64	32 kW	5.52 sec	8.40×10^{17}
Period-7	Run 64	39 kW	5.52 sec	2.75×10^{18}
Period-8	Run 65	39 kW	5.52 sec	2.93×10^{18}
Period-9	Run 65	42 kW	5.52 sec	9.80×10^{18}

3.4.1 DAQ Upgrade : Data compression

As described in Sec. 2.2.5, the Lv2 trigger was the bottleneck of the DAQ system, and it caused a dead time fraction of 30% at maximum. From the Period-6, the loss-less data compression inside the ADC modules was implemented and the dead time was mitigated and became smaller by approximately 10%. After the implementation, for example in Period-9, the dead time fraction was 17%.

3.4.2 Exciter Setting with Narrow Bandwidth in Run63.

During Period-4 and Period-5, the setting of an accelerator parameter "Exciter RF bandwidth" was changed. The Exciter RF was, as mentioned in Sec. 2.2.1, an RF with the central frequency of 252.5 kHz used in MR to mitigate the spike structure of the beam. Originally, the bandwidth of the Exciter RF was set to be ±62.5 kHz and, to tune the beam, it was narrowed to ±3.75 kHz during the periods[*3]. Due to the narrow bandwidth of the Exciter RF, a large 252.5 kHz periodic beam structure was induced and it caused a high instantaneous counting rate, which resulted in the worst accidental loss among all the run-periods. This beam structure caused a large difference of accidental activities in detectors within a ~ 4 μs period: a factor four difference at maximum. The setting was put back to the original one from the Period-6.

We found that the timing of the 512-ns event window collected with the TMON trigger was shifted by approximately 2 μs from the appropriate timing due to the delay time in the trigger system during the Period-1 to Period-5. Because 2 μs corresponds to the half of the 252.5 kHz structure, and TMON trigger was mainly issued in the "peak" timing of the structure, the event window recorded by the trigger was on the "valley" of the structure. In Period-4 and Period-5, the TMON data were useless to reproduce the accidental activities of the detector in the simulations because the 252.5 kHz structure was large due to the Exciter setting. Treatment for these run-periods is explained in Sec. 5.5. Before Period-6, we shifted the timing of the event window for the TMON trigger by 2 μs.

[*3] The duty factor provided from the accelerator group was indeed improved by this tuning. However, it is insensitive to the beam structure induced by the Exciter RF because of the finite sampling rate of the intensity monitor used to calculate the duty factor.

Chapter 4

Event Reconstruction

In this chapter, we explain the methods to extract physical information from the recorded data.

As mentioned in Sec. 2.2.5, we recorded the waveforms of the signals from all the detector components in 512-ns event window with 125-MHz or 500-MHz sampling ADC's. For the first step, we extracted energy and time information of the activities in the detector components from the waveforms (Sec. 4.1). Then, using the energy and time information from each readout channel of the CsI calorimeter, we reconstructed photons, π^0's, and K_L's (Sec. 4.2). Information of the veto counters were also reconstructed, and variables used for the veto decisions were calculated (Sec. 4.3).

4.1 Energy and Timing Reconstruction from Waveform

This section explains how to extract the energy and timing information from the waveforms. The energy deposition and hit time are simply referred to as "energy" and "time" (or "timing"), respectively in this thesis.

4.1.1 CsI Calorimeter

The waveform of the signals from the CsI crystals was recorded with 125-MHz digitizers (ADC's) and 64 samples for each crystal were stored in an event.

4.1.1.1 Baseline

The baseline B of a waveform was given as an average of the first or last 10 samples, taking the one with a smaller standard deviation of the 10 samples.

4.1.1.2 Energy

First, integrated ADC counts I was calculated as a sum of ADC counts of the 64 samples with the baseline subtracted. Second, the energy calibration was performed based on I, and constants to scale I (calibration constants) were obtained for each channel. Finally, we obtained the energy by multiplying I and the constant. The calibration methods are found in Refs. [57, 81].

4.1.1.3 Timing

We calculated the pulse timing of each crystal as follows. Pulse timing $t_{\text{pulse}}^{\text{CF}}$ is defined as the timing when the rising edge of the pulse exceeds half of the maximum peak height of the pulse. We call this timing calculation method as constant fraction method. Figure 4.1 shows an example of a waveform and its constant fraction time. If we found two or more candidates, we selected the one closer to the peak.

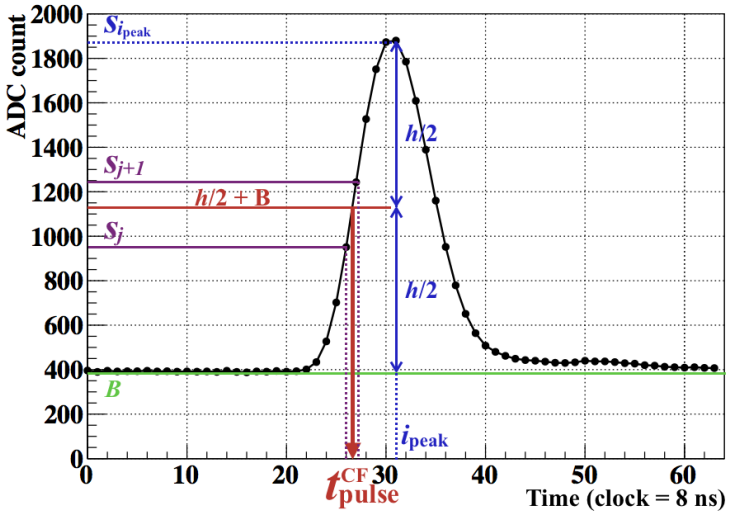

Figure 4.1: Waveform and its constant fraction time. The constant fraction time $t^{\mathrm{CF}}_{\mathrm{pulse}}$ is calculated as $t^{\mathrm{CF}}_{\mathrm{pulse}} \sim 27$ clock in this example.

The $t^{\mathrm{CF}}_{\mathrm{pulse}}$, in units of clock[*1], was converted into the unit of ns. The timing correction for each channel was then applied to align the timing of all the channels in the CsI calorimeter. The timing calibration methods are described in Ref.[57].

Considering the fact that $t^{\mathrm{CF}}_{\mathrm{pulse}}$ and the energy of the crystals had correlation due to the energy dependence of the pulse shape, we applied a timing correction Δt for crystals with large energy as

$$\Delta t(\mathrm{ns}) = \begin{cases} 0 & (e \leq 400 \text{ MeV}) \\ A_1(e-400) + A_2(e^2 - 400^2) & (e > 400 \text{ MeV}), \end{cases} \tag{4.1}$$

where e is the deposit energy in the crystal, and $A_1 = -1.325 \times 10^{-3}$ and $A_2 = 1.592 \times 10^{-6}$ are the parameters obtained by fitting the data [57].

4.1.2 Detector Components with 125-MHz Digitizers, other than CSI

For most of the veto counters, the signals were recorded with 125-MHz digitizers. The calculation methods of baseline and energy were almost the same as those of the CsI calorimeter.

4.1.2.1 Timing

The constant fraction time is susceptible to the pileup of pulses as shown in Fig 4.2; the pulse time might be shifted due to the pileup. If the timing of the veto counters was calculated wrongly, it might have caused the veto failure and consequently increase the background level. For this reason, instead of the constant fraction method, we used "the parabola interpolation method" for the veto counters. Compared to the constant fraction method, it had worse timing resolution but was less susceptible to the pileup[*2].

In the parabola interpolation method, for the first step, we smoothed the waveform by taking the moving average to mitigate the effect of local fluctuation due to noise. We then searched for local maximum points in the 64 samples (peak) with the ADC counts larger than the given threshold which was determined for each detector component. Using the three samples around the peaks, we calculated a parabola curve passing through those three points as shown in Fig. 4.3. If we found two or more

[*1] 1 clock = 8 ns.

[*2] As for the CsI calorimeter, the constant fraction method is used because the pulse pileup rarely occurs due to the high granularity of the constituent crystals.

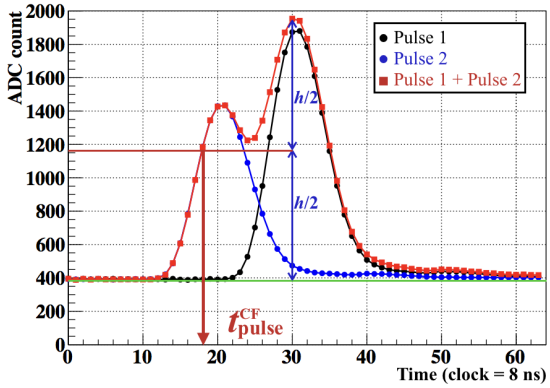

Figure 4.2: Timing shift of the constant fraction method due to the pulse pileup. Pulse 1 and Pulse 2 are merged and the time in this channel is calculated to be around 18-th clock.

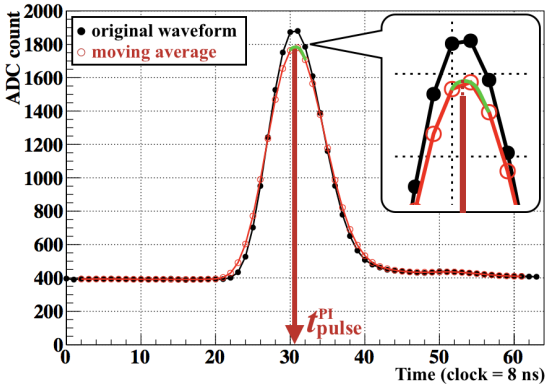

Figure 4.3: Timing calculation with the parabola interpolation method. The green line shows the parabola curve which passes through the three smoothed samples near the peak of the pulse.

peaks, we selected the one with its timing close to the typical hit timing of the detector component[*3]. The timing obtained by the procedure above was then converted into the units of ns. Relative timing differences between channels in a detector component were corrected, and they were aligned.

4.1.3 Detector Components with 500-MHz Digitizers

The waveforms from newBHCV, BHPV, and BHGC were recorded with 500-MHz digitizers and 256 samples for each channel were stored in one event data. Because of the high hit rate in these counters, we searched for multiple pulses (hits) in a window of 256 samples and calculated energy and timing information for each hit.

4.1.3.1 Baseline

The baseline was calculated as an average of the first or last 10 samples, just in the same manner as in the CSI case in Sec. 4.1.1.

4.1.3.2 Peak Finding

We searched for local maximum points in the 256-sample window. If the ADC counts of the points with the baseline subtraction exceeded the given threshold to discriminate pulses from noise fluctuations, such a local maximum was regarded as a peak.

4.1.3.3 Energy

The energy was calculated based on the summation of the ADC samples around the peak. The range of the samples to sum was determined for each detector component. The resulting values were multiplied by the calibration constant and converted into energy (for newBHCV) or the number of equivalent photons (for BHPV and BHGC).

4.1.3.4 Timing

The timing of each hit was calculated with the constant fraction methods described in Sec. 4.1.1.

[*3] Each veto counter has a typical hit time relative to the hit time in the CsI calorimeter due to K_L decay products associated with the particles which hit the CsI calorimeter.

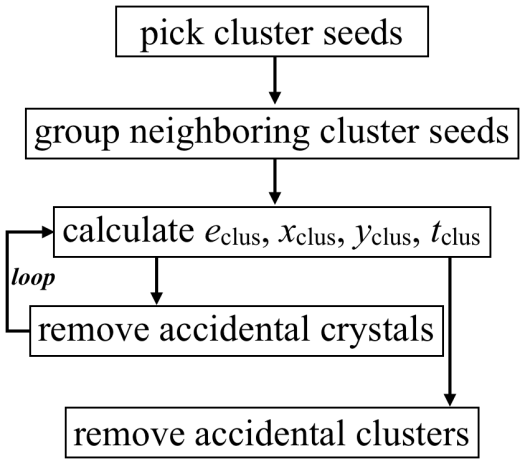

Figure 4.4: Workflow of the clustering. First, we group the hit crystals into clusters based on their positions. Then we remove the accidental hit crystals from the clusters using time information. Finally, we count the number of clusters removing accidental clusters.

4.2 Particle Reconstruction with the CsI Calorimeter

When a photon hits the CsI calorimeter, it generates an electromagnetic shower. The typical lateral spread of the shower is characterized by the Molière radius, which is 3.53 cm for CsI [15]. Considering the size of the CsI crystals, 2.5×2.5 cm^2 or 5×5 cm^2 in cross-section, the shower should spread out to multiple crystals. This group of crystals with deposit energies is called "*cluster*." Clusters regarded as photon candidates, and they were used to reconstruct π^0's and K_L's.

The clustering procedure, the photon-cluster selection, and π^0 and K_L reconstruction methods are described below. The detailed description of these reconstruction procedures is found in Ref. [57].

4.2.1 Clustering

The workflow of the clustering is shown in Fig. 4.4.

First, crystals with their energies larger than 3 MeV and with their hit time within a 150-ns time window were picked as "*cluster seeds.*"

Next, the cluster seeds within 71 mm of each other were grouped into a cluster as shown in Fig. 4.5. The clusters consisted of a single crystal are referred to as "*isolated hit crystals*" and they were not used for the reconstruction but used for the veto cut as described in Sec. 4.3.1.

For the third step, the energy ($e_{\rm clus}$), position of the center of energy ($x_{\rm clus}, y_{\rm clus}$), and timing ($t_{\rm clus}$) of each cluster were calculated as follows:

$$e_{\rm clus} = \sum_i^n e_i, \tag{4.2}$$

$$x_{\rm clus} = \frac{\sum_i^n x_i e_i}{\sum_i^n e_i}, \tag{4.3}$$

$$y_{\rm clus} = \frac{\sum_i^n y_i e_i}{\sum_i^n e_i}, \tag{4.4}$$

$$t_{\rm clus} = \frac{\sum_i^n t_i/\sigma_t^2}{\sum_i^n 1/\sigma_t^2}, \tag{4.5}$$

where n denotes the number of crystals contained in the cluster and e_i, x_i, y_i, and t_i represent the energy, x-position, y-position, and hit time of the i-th crystal, respectively. The σ_t is the timing resolution of each crystal as a function of energy, and it was measured to be $\sigma_t = 5/e_i \oplus 3.63/\sqrt{e_i} \oplus 0.13$ in the past beam test [58], where σ_t and e_i are in the units of ns and MeV, respectively.

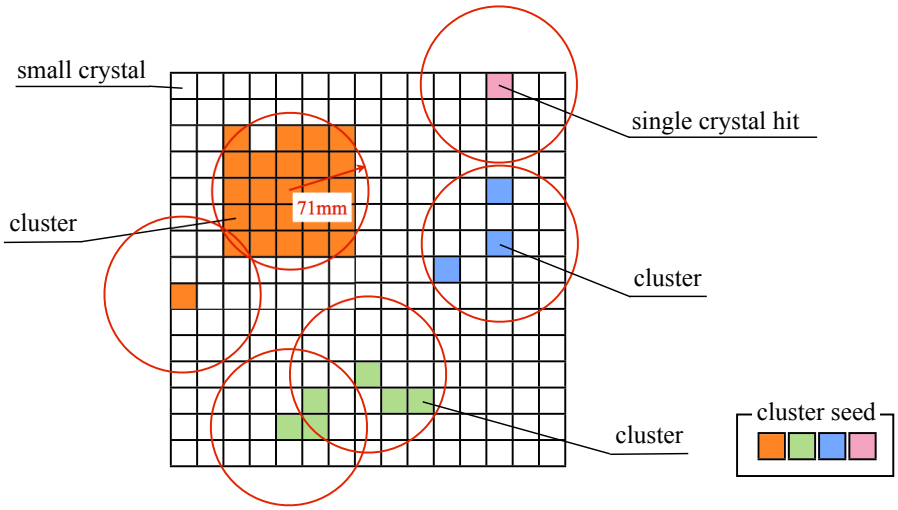

Figure 4.5: Example of the grouping of cluster seeds (quoted from Ref. [57]). Each box represents a small crystal and colored one denotes a cluster seed. The cluster seeds with the same color belong to the same cluster. The red circles with a radius of 71 mm represent the grouping region. There are three clusters (orange, green, blue) and one isolated hit crystal (magenta) in this figure.

Due to the wide timing window of 150 ns, the clusters might contain accidental hits, or hits unrelated to the shower of the cluster. For the fourth step, the contaminations of the accidental hits were removed. Figure 4.6 shows the distribution of the hit timing of each constitutive crystal relative to the cluster timing as a function of the crystal energy. The two red lines represent the spline interpolation of upper or lower edges of the 5σ allowed region of the timing difference distribution in each energy bin. For the crystals whose hit timings were outside the 5σ allowed region, the significance of the timing deviations defined as $|t_i - t_{\mathrm{clus}}|/\sigma_t$ were calculated and the crystal with the largest significance was removed from the cluster seeds. These removed crystals were used for the isolated crystal veto decision described in Sec. 4.3.1.1.

After the removal, the third step was processed again. The third and fourth steps were repeated until all the crystals were contained inside the 5σ allowed region.

For the last step, accidental clusters were, if any, removed. If the timing difference between the earliest and latest cluster time was larger than 30 ns, the cluster with the largest timing deviation from the average timing of all the clusters was removed. This process was repeated until all the clusters were contained within a 30 ns time window.

The clusters remaining after the above processes were used for the reconstruction of photon, π^0, and K_L. On the other hand, the removed clusters were used for the extra-cluster veto cut described in Sec. 4.3.1.2. The crystals which were not contained in any clusters were regarded as isolated hit crystals and used for the veto cut as described in Sec. 4.3.1.1.

4.2.2 Photon Reconstruction

Clusters with their energies larger than 20 MeV were defined as "*photon clusters.*"[*4] We reconstructed the energy of the photon and its hit position at the surface of the CsI calorimeter by correcting the information of the photon cluster as follows.

[*4] In the reconstruction scheme, we assume all the clusters are made by photons.

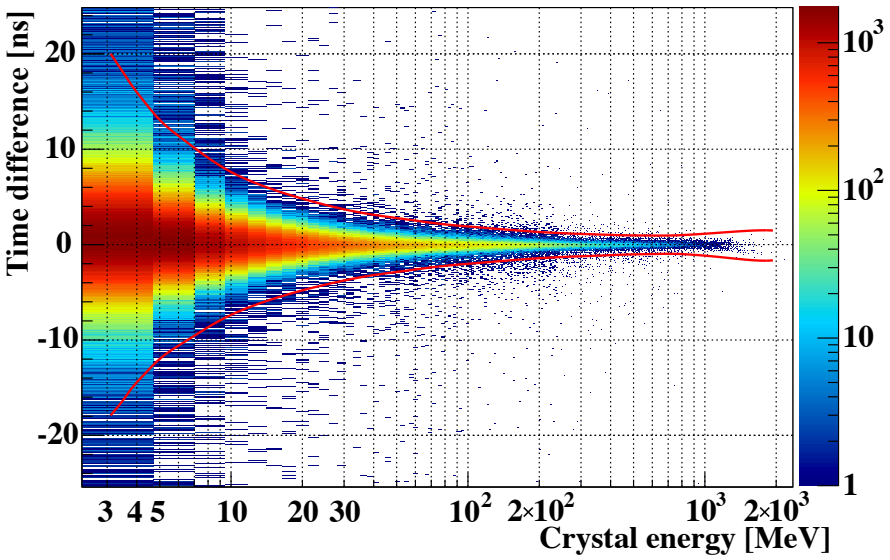

Figure 4.6: Distribution of the hit time of the crystals relative to the cluster time as a function of the energy of the crystals (quoted from Ref. [57]). Color represents the number of events in arbitrary units.

4.2.2.1 Energy Correction for Photon Clusters

The cluster energy calculated with Eq. 4.2 was usually smaller than the energy of the incident photon due to shower leakage, and the finite energy threshold of 3 MeV was used to pick the cluster seeds. The cluster energy was corrected with a correction map prepared by a simulation.

4.2.2.2 Position and Energy Correction with the Incident Angle of the Photon

Position and energy of a photon were corrected with the incident angle. To obtain the incident angle, we needed to know the decay vertex position of π^0 or K_L, or the generation point of the photon. Hence we reconstructed a π^0 (K_L) twice; we first reconstructed a π^0 (K_L) to obtain the approximate decay vertex and then applied the correction described below and reconstructed the π^0 (K_L) again. The π^0 (K_L) reconstruction is described in Sec. 4.2.3 (Sec. 4.2.4).

Here let $\theta_{\rm inc}$ and $\phi_{\rm inc}$ be the reconstructed polar and azimuthal angles of the momentum of a photon, respectively. The center of energy, $P_{\rm COE} = (x_{\rm clus}, y_{\rm clus})$, is deviated from the incident position of the photon on the surface of the CsI calorimeter, $P_{\rm inc} = (x_\gamma, y_\gamma)$, due to its incident angle. Figure 4.7 shows the conceptual view of this position shift. The $P_{\rm inc}$ is obtained as follows:

$$P_{\rm inc} = P_{\rm COE} - L_s v \sin\theta_{\rm inc}, \tag{4.6}$$

$$L_s/X_0 = p_0 + p_1 \ln(e_{\rm clus}), \tag{4.7}$$

where L_s is the distance between the incident position of a photon and the shower maximum position, $v = (\cos\phi_{\rm inc}, \sin\phi_{\rm inc})$ is the unit vector of the photon momentum in the x-y plane, $X_0 = 18.5$ mm is the radiation length of CsI, $e_{\rm clus}$ is the cluster energy in GeV, and $p_0 = 6.490$ and $p_1 = 0.993$ are the parameters obtained by a simulation.

The energy of the photon was re-corrected using the correction map with incident angle information.

4.2.3 π^0 Reconstruction

By using two photon clusters, we reconstructed a π^0 assuming the $\pi^0 \to 2\gamma$ decay. If we found more than two photon clusters in an event, we selected the two photons with the closest timing to each

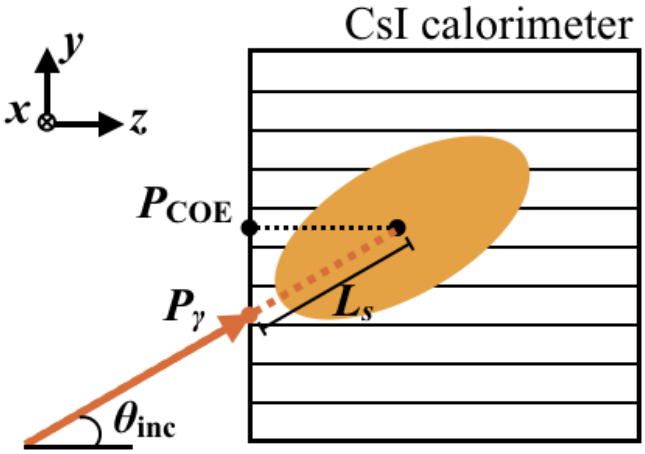

Figure 4.7: Conceptual view of the position shift due to the incident angle of the photon. The orange ellipse represents the shower propagation. The incident position of the photon is deviated from the center of energy of the cluster due to the shower depth and the incident angle.

other.

The kinematics of the $\pi^0 \to 2\gamma$ decay provides the opening angle of the two photons (θ) as

$$\cos\theta = 1 - \frac{M_{\pi^0}^2}{2E_1E_2}, \tag{4.8}$$

where M_{π^0} is the nominal π^0 mass and E_1 and E_2 are the energies of the photons. Assuming that the decay vertex was on the beam axis (z axis), we calculated the z position of the vertex ($Z_{\rm vtx}$) with the following equations :

$$(1-\cos^2\theta)dZ^4 + \left\{2\overrightarrow{r_1}\cdot\overrightarrow{r_2} - (r_1^2+r_2^2)\cos^2\theta\right\}dZ^2 + (\overrightarrow{r_1}\cdot\overrightarrow{r_2})^2 - r_1^2r_2^2\cos^2\theta = 0, \tag{4.9}$$

$$Z_{\rm vtx} = Z_{\rm CSI} - dZ, \tag{4.10}$$

where the two-dimensional vector $\overrightarrow{r_i} = (x_i, y_i)$ (i = 1,2) corresponds to the position of the i-th photon[*5] and $dZ(>0)$ represents the distance between the upstream surface of the CsI calorimeter ($Z_{\rm CSI}$ = 6148 mm) and $Z_{\rm vtx}$, as shown in Fig. 4.8. This equation of dZ^2 possibly has two real and positive solutions and consequently, dZ also has two possibilities. In this case, since we could not know which was the correct vertex, we discarded such events.

After reconstructing a π^0 decay vertex, we calculated the incident angle of the photons. We applied the corrections in Sec. 4.2.2.2 and then re-reconstructed a π^0 decay vertex with corrected energies and positions of the photons.

Following the second reconstruction, we calculated the kinematic variables described below.

Transverse Momentum P_t: The transverse momentum of the π^0 (P_t) was given by the following equation :

$$P_t = \left| \sum_i^2 \frac{E_i\overrightarrow{r_i}}{\sqrt{r_i^2+dZ^2}} \right|. \tag{4.11}$$

[*5] The center of energy of the cluster $(x_{\rm clus}, y_{\rm clus})$ is used in the first reconstruction and the corrected incident position of the photon (x_γ, y_γ) is used in the second reconstruction.

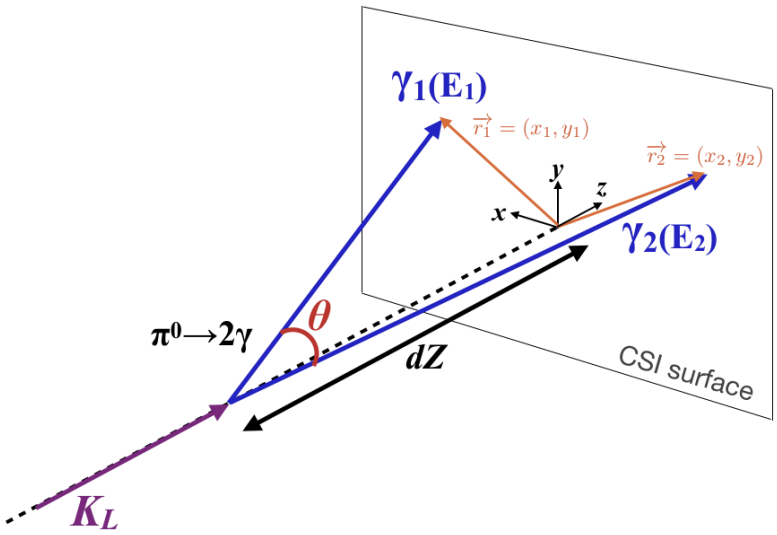

Figure 4.8: Reconstruction of the $\pi^0 \to 2\gamma$ decay with the CsI calorimeter.

Vertex Time $t_{\rm vtx}$: The vertex time of i-th photon, $t^i_{\rm vtx}$, was calculated with the cluster timing ($t^i_{\rm clus}$) and the time of flight of the photon :

$$t^i_{\rm vtx} = t^i_{\rm clus} - \sqrt{r_i^2 + dZ^2}/c, \tag{4.12}$$

where c is the speed of light.

Event Vertex Time $T_{\rm vtx}$: The event vertex time, $T_{\rm vtx}$, or the π^0 decay time, was calculated as a weighted average of the vertex times of the photons :

$$T_{\rm vtx} = \frac{\sum_i^2 t^i_{\rm vtx}/\sigma_t^2(E_i)}{\sum_i^2 1/\sigma_t^2(E_i)}, \tag{4.13}$$

where $\sigma_t(E) = 3.8/\sqrt{E} \oplus 0.19$ in ns represents the resolution of the vertex timing as a function of photon energy E in MeV.

After the reconstruction, we required the absence of extra photon clusters to eliminate accidental coincidence events. We calculated the vertex time (Eq. 4.12) of each cluster not used for the π^0 reconstruction, and if we found any clusters within ± 10 ns around $T_{\rm vtx}$, we discarded such an event.

The reconstruction of the $K_L \to 2\gamma$ decay was performed in the same way by substituting the K_L mass for the π^0 mass in the θ calculation in Eq. 4.8.

4.2.4 K_L Reconstruction

For normalization purpose, we reconstructed a K_L assuming the $K_L \to 2\pi^0 \to 4\gamma$ and $K_L \to 3\pi^0 \to 6\gamma$ decay chains. We first reconstructed π^0's and then reconstructed a K_L using the π^0's. As was done in Sec. 4.2.3, if we found more than N photon clusters in an event, where N is 4 (6) for the $K_L \to 2\pi^0$ ($K_L \to 3\pi^0$) reconstruction, we selected the N photons with the closest timings to each other.

There are 3 (15) possible combinations of 4 (6) photons forming 2 (3) π^0's. We reconstructed π^0's as in the first reconstruction of a π^0 in Sec. 4.2.3 for all the possible combinations. From 2 (3) π^0's information, the z position of the decay vertex $Z^{\rm K_L}_{\rm vtx}$ was calculated as follows :

$$Z^{\rm K_L}_{\rm vtx} = \frac{\sum_i^{N/2} Z^i_{\rm vtx}/\sigma_i^2}{\sum_i^{N/2} 1/\sigma_i^2}, \tag{4.14}$$

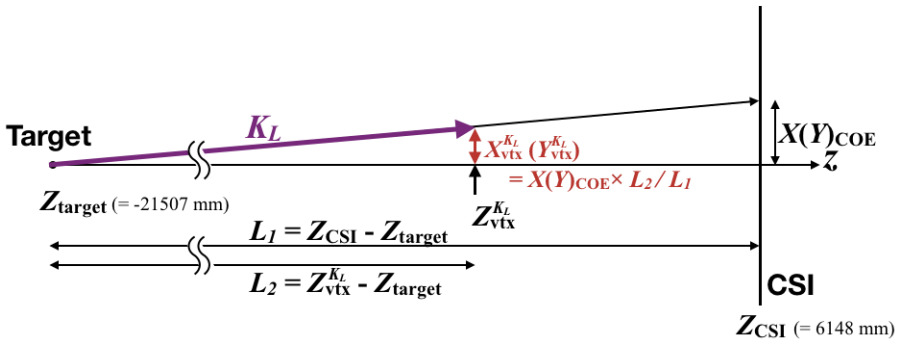

Figure 4.9: Schematic view of the $X^{K_L}_{\rm vtx}$ and $Y^{K_L}_{\rm vtx}$ calculation.

where σ_i represents the resolution of the reconstructed vertex position and $Z^i_{\rm vtx}$ represents the z position of the decay vertex of the i-th π^0. To evaluate the agreement of the vertexes of the π^0's, we defined variables "χ^2_z" and "$\Delta Z_{\rm vtx}$" as

$$\chi^2_z = \sum_i^{N/2} \frac{(Z^i_{\rm vtx} - Z^{\rm K_L}_{\rm vtx})}{\sigma_i^2}, \tag{4.15}$$

$$\Delta Z_{\rm vtx} = \max(|Z^i_{\rm vtx} - Z^j_{\rm vtx}|). \tag{4.16}$$

We adopted a combination with the smallest χ^2_z value among all the possibilities. The $\Delta Z_{\rm vtx}$ represents the maximum $Z_{\rm vtx}$ difference of π^0's and it was utilized for the event selection in the normalization modes analysis described in Sec. 6.2. Using the reconstructed $Z^{\rm K_L}_{\rm vtx}$ and the center of energy on the CsI calorimeter ($X_{\rm COE}$, $Y_{\rm COE}$), we obtained the x and y positions of the decay vertex ($X^{K_L}_{\rm vtx}$, $Y^{K_L}_{\rm vtx}$) as shown in Fig. 4.9 and the following equations :

$$X_{\rm COE} = \frac{\sum_i^N x_i E_i}{\sum_i^N Ei}, \tag{4.17}$$

$$Y_{\rm COE} = \frac{\sum_i^N y_i E_i}{\sum_i^N Ei}, \tag{4.18}$$

$$X^{K_L}_{\rm vtx} = \frac{Z^{\rm K_L}_{\rm vtx} - Z_{\rm target}}{Z_{\rm CSI} - Z_{\rm target}} X_{\rm COE}, \tag{4.19}$$

$$Y^{K_L}_{\rm vtx} = \frac{Z^{\rm K_L}_{\rm vtx} - Z_{\rm target}}{Z_{\rm CSI} - Z_{\rm target}} Y_{\rm COE}, \tag{4.20}$$

where x_i and y_i are the incident position and E_i is the energy of the i-th photon. By fixing the vertex position ($X^{K_L}_{\rm vtx}, Y^{K_L}_{\rm vtx}, Z^{K_L}_{\rm vtx}$), we re-reconstructed each π^0 kinematics without the π^0 mass constraint. Finally we reconstructed the K_L by summing up the four-momenta of the π^0's.

After the above reconstruction, as was done in the π^0 reconstruction, we applied the energy and position corrections in Sec. 4.2.2.2 to the photons and then re-reconstructed the K_L again.

The event vertex time, $T^{\rm K_L}_{\rm vtx}$, was then calculated as

$$T^{\rm K_L}_{\rm vtx} = \frac{\sum_i^{N/2} t^i_{\rm vtx}/\sigma_t^2(E_i)}{\sum_i^{N/2} 1/\sigma_t^2(E_i)}, \tag{4.21}$$

where the notations are the same as in Eq. 4.13. As was done in the π^0 reconstruction, we required that there were no extra photon clusters coincident with the K_L decay.

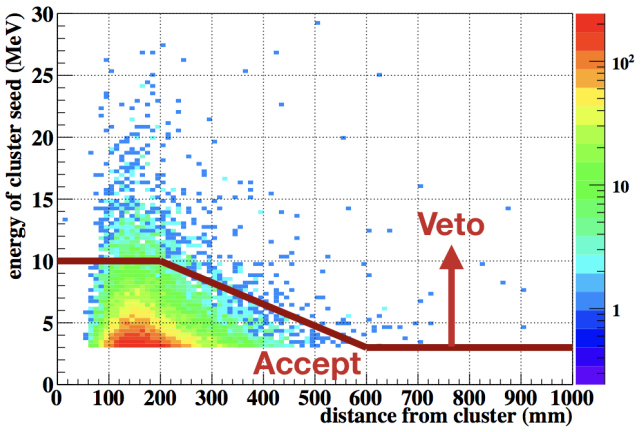

Figure 4.10: Energy and the distance from the closest cluster of the cluster seeds of $K_L \to \pi^0\nu\overline{\nu}$ events obtained by MC simulation (scatter plot). The veto energy threshold as a function of the energy of the cluster seed is shown by the red line.

4.3 Reconstruction of Veto Information

The veto decision was issued using energy and timing information of all the veto counters and extra activities in the CsI calorimeter. In this section, the veto criterion in each detector component is explained.

4.3.1 CsI Calorimeter

As mentioned in Sec. 4.2, isolated hit crystals and extra clusters which were not used for the π^0 or K_L reconstruction were utilized for veto decisions. The purpose of the veto cuts using the CsI calorimeter information was to reject the background events in which an extra photon associated with the reconstructed π^0/K_L decay hit the CsI calorimeter but was not detected as a photon cluster due to the photo-nuclear reaction in the shower propagation.

4.3.1.1 Isolated Hit Crystal Veto

If the hit time of isolated hit crystal was within ± 10 ns of the timing of photon clusters and the energy was larger than a given threshold, such an event was rejected. The veto energy threshold $E_{\rm thre}$ was determined as a function of distance from the closest cluster, d, based on the simulation and shown in the following equation and Fig. 4.10 :

$$E_{\rm thre} = \begin{cases} 10 \text{ MeV} & (d \leq 200 \text{ mm}) \\ (13.5 - 0.0175d) \text{ MeV} & (200 < d \leq 600 \text{ mm}) \\ 3 \text{ MeV} & (d > 600 \text{ mm}). \end{cases} \tag{4.22}$$

The threshold was set higher for the crystals with smaller d in order to reduce the signal loss due to the isolated hit crystals near the clusters made by the fluctuation of the shower propagation.

4.3.1.2 Extra-Cluster Veto

The vertex time of the extra clusters was calculated assuming the vertex of the reconstructed π^0/K_L. If it was within ± 10 ns from the event vertex time, such events were rejected.

4.3.2 Veto Counters

First, we define some basic variables for veto decision: module-energy, module-time, and module-veto-time.

The module-energy ($E_{\rm mod}$) and module-time ($t_{\rm mod}$) are the energy deposit and hit timing in a module of a veto counter, respectively. In the case of detector components with dual readout systems such as MB, BCV, CV, CC03, BHPV, BHGC, and parts of charged particle veto counters of CC04, CC05 and CC06, information of both channels was combined to calculate the module-energy and module-time.

The module-veto-time ($t_{\rm mod}^{\rm veto}$) was given as the relative module-time to the event vertex time ($T_{\rm vtx}$) with time-of-flight (TOF) correction (ΔTOF):

$$t_{\rm mod}^{\rm veto} = t_{\rm mod} - T_{\rm vtx} - \Delta{\rm TOF}. \tag{4.23}$$

The methods of the TOF correction were different among the veto counters.

The veto information of each veto counter is generally characterized by two variables :"*veto-energy*" and "*veto-time*". Among the hits with their module-veto-times within a given veto window, the hit with the largest module-energy was chosen. The module-energy and module-veto-time of the hit were defined as veto-energy and veto-time of the veto counter, respectively. In veto decision, when veto-energy exceeded a given veto threshold, such an event was vetoed.

The treatments for each type of veto counters are described in Appendix A. For veto counters with specific treatments, we briefly explain them in the following sections.

4.3.2.1 FB

For FB, the effect of miscalculation of timing due to overlapping pulses was not negligible with the timing calculation method used in this analysis because the probability of having overlapping pulses was large due to its low granularity of modules and single-end readout of the 2.7-m-long modules. To mitigate the effect, we adopted a special treatment for FBAR veto ("*FBAR wide window veto*") in addition to the normal veto decision described above. We set another wide veto window of 150 ns for FBAR to detect pulses with miscalculated timing[*6]. The energy threshold for this veto window was set to 30 MeV whereas that of normal FBAR veto was 1 MeV in the 2015 run analysis. This high energy threshold reduced the additional accidental loss to 3%.

4.3.2.2 newBHCV

As explained in Sec. 2.2.4, newBHCV was composed of three layers of chambers, and charged particles hitting newBHCV basically penetrated all the three layers. We took 2-out-of-3 logic for the veto decision: if there were hits in two or three layers, such an event was vetoed.

4.3.2.3 BHPV

For the veto decision of BHPV, we required the coincidence of consecutive three or more modules' hits in order to reduce the accidental veto effects from neutrons in the beam, because electromagnetic showers produced by photons developed in the forward direction while hadronic showers by neutrons tended to have more isotropic angular distribution in the shower development. Effects from low-energy photons in the beam were also suppressed by this requirement.

The algorithm to search for a hit-coincidence is described in Appendix A.7.

4.3.2.4 BHGC

For BHGC, we used the number of equivalent photons for a hit instead of module-energy. We reconstructed BHGC module hit information by merging the multiple-hit information of a pair of channels assigned for a module. If there were hits in both channels within $\pm$10 ns of timing, these hits were merged into one hit. For such a merged hit, the hit timing was given as an average of original hit

[*6] For normal FBAR veto, the width of the veto window was 51 ns in the 2015 run analysis, which was contained in the 150-ns window. The veto decisions of the normal veto and wide window veto were made independently.

timings and the number of equivalent photons was given as the sum of those of original hits. The timing and the number of equivalent photons of module hits were used to veto the event.

Chapter 5

Monte Carlo Simulation

In this chapter, we describe the Monte Carlo (MC) simulation used in this analysis. The purposes of the MC simulation are to estimate

- the signal acceptance for the $K_L \to \pi^0\nu\overline{\nu}$ and $K_L \to \pi^0 X^0$ decays
- the acceptance for the normalization mode decays, namely $K_L \to 3\pi^0$, $K_L \to 2\pi^0$, and $K_L \to 2\gamma$
- the background contributions.

The simulation was performed based on the GEANT4 toolkit [82, 83, 84] with the version 4.9.5p02.

In the following subsections, we describe the simulation processes in order. The generation and decay of K_L's are described in Sec. 5.1 and Sec. 5.2, and interactions in materials are described in Sec. 5.3. In Sec. 5.4 and Sec. 5.5, we describe detector responses and treatments of accidental activities in detector components to reproduce the real data.

5.1 K_L Generation

5.1.1 Momentum Spectrum

We generated K_L's with a given momentum spectrum which was obtained from past measurements at the KL beamline [58]. The obtained K_L momentum distribution at the beam exit is expressed with the following function:

$$f(p, \vec{a}) = \exp\left\{-\frac{(p-\mu)^2}{2(\sigma_0(1-(A+Sp)(p-\mu)))^2}\right\}, \tag{5.1}$$

where p is momentum in units of GeV/c and $\vec{a}^T = (\mu, \sigma_0, A, S)$ is a fit parameter vector [58][*1]. The parameters obtained by the fit are $\vec{a_0}^T = (1.420, 0.8102, -0.3014, 0.01709)$ and the spectrum is shown in Fig. 5.1.

5.1.2 Incident Position and Direction

We generated K_L's with the distributions of incident position and direction of K_L's given by a simple beam optical simulation based on the collimation lines by the collimators and the "target image". The target image was represented by the flux of secondaries obtained by an independent simulation with a 30 GeV proton beam and a gold target.

The target image and the collimation lines are shown in Fig. 5.2, and the resultant K_L incident position distribution at the beam exit are shown in Fig. 5.3.

The transverse momentum spectrum of the K_L at the beam exit is shown in Fig. 5.4.

[*1] The values of the parameters are slightly different from those in Ref. [58].

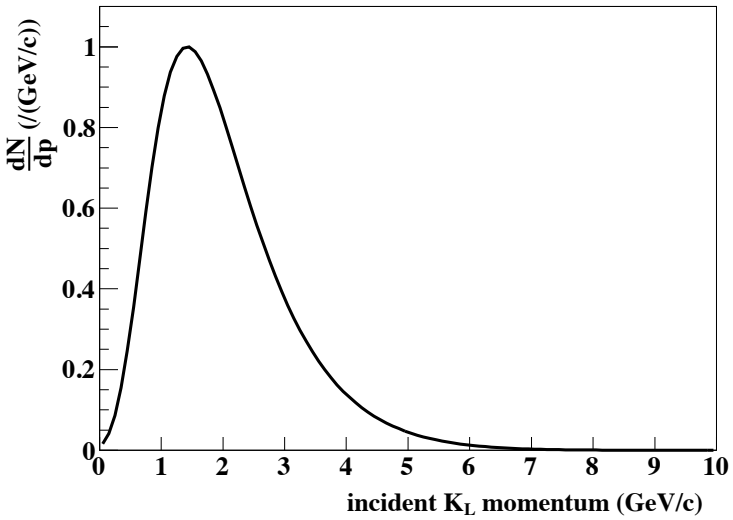

Figure 5.1: Momentum spectrum of the K_L at the beam exit.

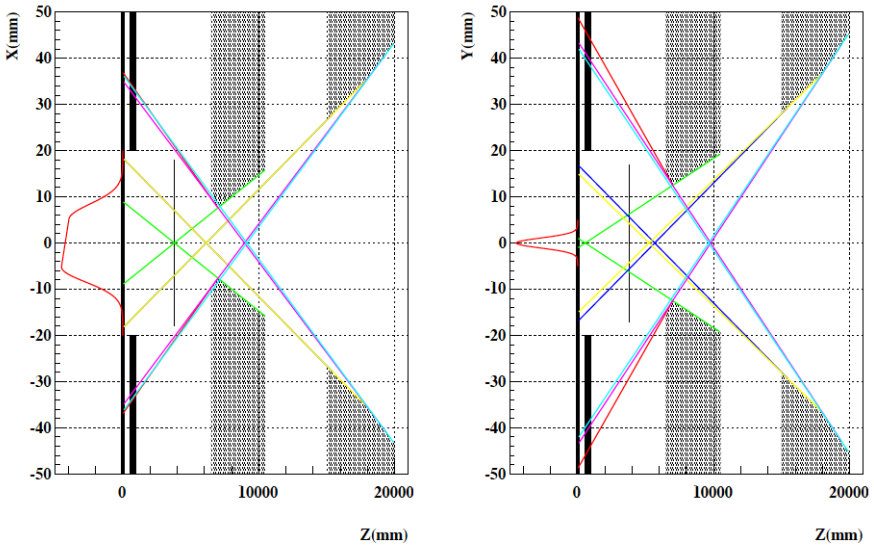

Figure 5.2: Target image (red lines drawn in the $Z < 0$ region) and collimation lines (colored straight lines) in X-Z (left) and Y-Z planes. The black shadows around $6500 < Z < 10500$ mm and $15000 < Z < 20000$ mm represent the 1st and 2nd collimators, respectively. In these figures, the origin of Z is the position of the target, so that the beam exit ($z = -1.5$ m in the KOTO detector coordinate system) corresponds to $Z = 20$ m.

5.2 Decay of K_L

The K_L decay was managed by the Geant4. In the decay process, kinematics of the daughter particles were calculated with the assumption of V-A interaction and the decay form factors were taken from Ref. [85]. We simulated and analyzed each K_L decay mode separately, and finally we combined their results by taking the branching fraction of each decay into account.

5.3 Interaction inside Detector Components

Interactions of particles inside the KOTO detector were also managed by the Geant4. The QGSP_BERT physics list in the Geant4 was adopted to handle the interactions.

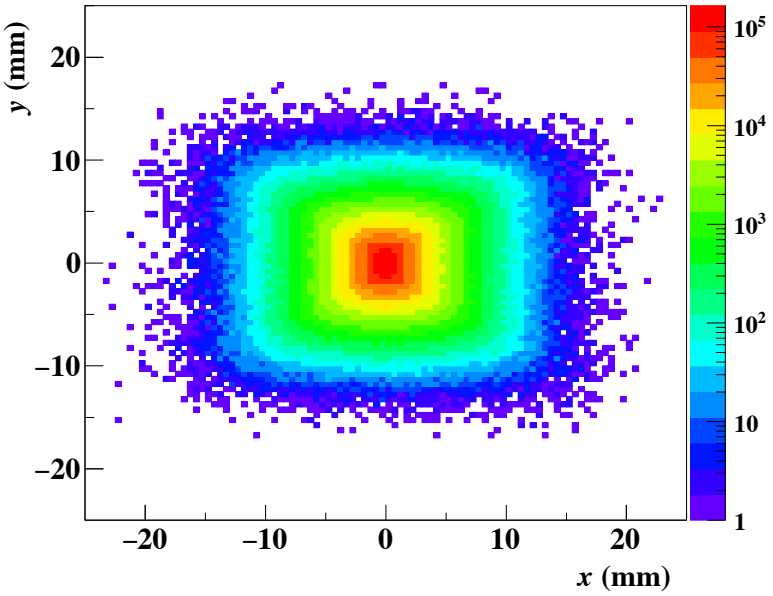

Figure 5.3: Distribution of the incident K_L position at the beam exit.

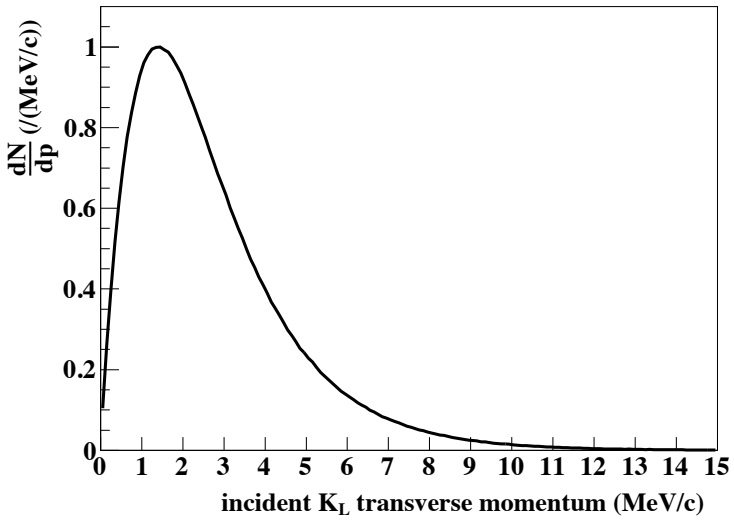

Figure 5.4: Transverse momentum spectrum of the K_L at the beam exit.

Interactions in materials were simulated step by step by tracking particle trajectories. Energy deposition in detector components in each step was recorded as five parameters: energy deposition e_i, interaction time t_i, interaction position x_i,y_i,z_i, where i indicate the step number. Based on these parameters, visible energy and timing in detector components were obtained as described in Sec. 5.4.

5.4 Detector Response

Based on the raw step information from the Geant4 output $(e_i, t_i, x_i, y_i, z_i)$, we calculated visible energy and timing information considering the detector response such as propagation time and attenuation of light, and photon statistics effect.

General procedures are mentioned in Sec. 5.4.3 and details for each detector component are found in Ref. [67]. As for BPCV and newBHCV, which were installed after 2013 run, procedures are described

in Sec. 5.4.2 and Sec. 5.4.3. BHGC was also a newly installed detector component, but we do not mention it here because the procedures are almost the same as that of BHPV.

5.4.1 General Procedures

For the first step, using the raw step information $(e_i, t_i, x_i, y_i, z_i)$, we calculated energy e'_i and time t'_i at the photosensors of the detector component.

As for timing, t'_i was calculated taking the propagation time into account. For some detector components, additional timing smearing was imposed.

As for energy, we calculated and smeared the energy by taking possible responses such as photon statistics effect, attenuation in propagation, and position dependence of light yield into account.

Next, using the (e'_i, t'_i), we generated a waveform. Each (e'_i, t'_i) was converted into 64 samples so as to match the data output with the following function,

$$f(t) = A \exp\left(-\frac{(t-t'_i)^2}{(\sigma_0 + a(t-t'_i))^2}\right), \tag{5.2}$$

where σ_0 and a are parameters given for each detector component, and A is determined so that the integral of $f(t)$ becomes e'_i. The waveform made for each step was summed up over all the steps to make a waveform of a readout signal.

5.4.2 Procedures for BPCV

As for timing correction, t'_i was obtained as follows:

$$t'_i = \frac{|z_{\mathrm{PMT}} - z_i|}{v^{\mathrm{prop.}}} + \mathrm{Gaussian}(\sigma_t = 2.02\ \mathrm{ns}), \tag{5.3}$$

where z_{PMT} represents the z position of the PMT used for BPCV, $v^{\mathrm{prop.}} = 173.7$ mm/ns represents the propagation velocity of light in the WLS fibers of BPCV, and $\mathrm{Gaussian}(\sigma_t = 2.02\ \mathrm{ns})$ represents a random additional time smearing given by a Gaussian distribution with the $\sigma = 2.02$ ns, which was obtained by a measurement with cosmic rays.

As for energy, we once converted energy e_i to the number of photons with the light yield of 6 p.e./MeV to consider the photon statistics effect. We obtained the number of photons assuming a Poisson distribution and then reconverted it to energy. Finally, we obtained e'_i after imposing additional smearing. The smearing was given by a Gaussian distribution whose σ was represented as follows:

$$\sigma = \begin{cases} 0.2001 & (N_p = 0) \\ 0.3501\sqrt{N_p} & (N_p > 0), \end{cases} \tag{5.4}$$

where N_p is the number of photons and the finite value of σ in the $N_P = 0$ case represents the effect of baseline fluctuation.

5.4.3 Procedures for newBHCV

As for newBHCV, the sum of energy deposit e_i in a gas volume corresponding to a readout channel, or a $300 \times 18 \times 2.8$ mm^3 volume, was regarded as an energy deposit in the channel without any correction.

The timing of the hit was obtained as the fastest hit (step) time in a channel with smearing by time jitter distribution, which was caused by the drift time of electrons. We prepared the time jitter distribution using the muon run data in which a muon penetrated newBHCV and 6 or more BHPV modules. By taking the timing difference between BHPV hit time and newBHCV hit time, we obtained the time jitter distribution as shown in Fig. 5.5[*2].

[*2] The timing resolution of BHPV was much better than the width of the time jitter distribution.

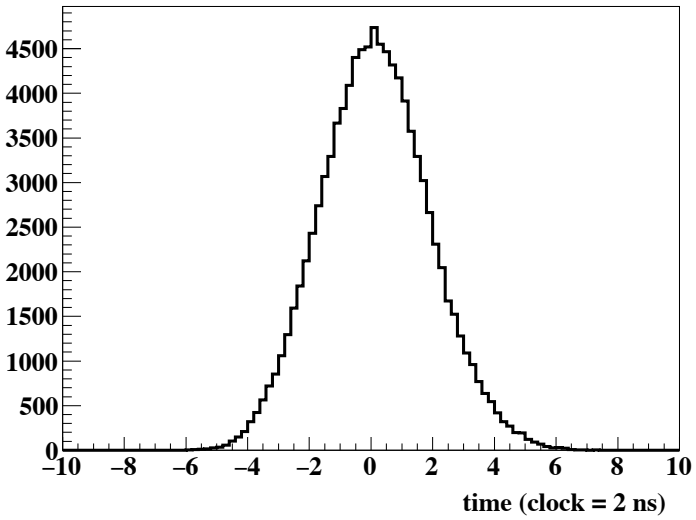

Figure 5.5: Distribution of the newBHCV time jitter.

5.5 Accidental Overlay

In order to reproduce the effect of miscalculation of timing due to noises or accidental activities in detector components, we overlaid waveforms of TMON-triggered data mentioned in Sec. 3.1.6 on the generated waveform. After the overlay procedure, we calculated the energy and timing information from the waveforms in the same manner as in data, as described in Sec. 4.1.

As described in Sec. 3.4.2, during the Period-4 and Period-5, the TMON data were not recorded properly due to the large beam structure and the incorrect timing window. Instead of using the TMON-triggered data taken in these run-periods, we adopted "multi-overlay method" in these run-periods based on the TMON data taken in the Period-3. In the multi-overlay methods, we overlaid TMON data on the simulation output twice for a part of events[*3] so that the accidental hit rates in detector components reproduced the data.

[*3] If we overlay TMON data twice for all the events, accidental hit rates in detector become twice higher than those obtained by the normal overlay procedure.

Chapter 6

Analysis of the $K_L \to \pi^0 \nu\overline{\nu}$ and $K_L \to \pi^0 X^0$ Searches

6.1 Overview

In this chapter, the analysis procedure to search for $K_L \to \pi^0 \nu\overline{\nu}$ and $K_L \to \pi^0 X^0$ decays, and their results are described. In the analysis of $K_L \to \pi^0 \nu\overline{\nu}$ and $K_L \to \pi^0 X^0$ searches, we adopted cut-based analysis. We imposed event selection criteria (cuts) on the data set based on the CsI calorimeter information and activities in the veto counters. We optimized the cuts to obtain larger signal acceptance and smaller background events. After all the cuts were imposed, remaining events in the signal region, which was defined on the P_t vs. $Z_{\rm vtx}$ plane, were regarded as the signal candidates. To avoid subjective biases in event selection, we performed the "blind analysis"; we determined all the cuts without examining events inside the signal region. In order to keep rooms for optimizing the signal region, we masked the region of $2900 < Z_{\rm vtx} < 5100$ mm and $120 < P_t < 260$ MeV/c during the analysis.

Since the final states of $K_L \to \pi^0 \nu\overline{\nu}$ and $K_L \to \pi^0 X^0$ are similar, we adopted the same cuts and signal region in both analyses. The cuts were optimized based on the $K_L \to \pi^0 \nu\overline{\nu}$ analysis. The difference from the $K_L \to \pi^0 \nu\overline{\nu}$ analysis is the estimation of the signal acceptance. The analysis of $K_L \to \pi^0 X^0$ is described later in this chapter.

The branching fraction ($\mathcal{B}_{\rm sig}$) and single event sensitivity (SES) of signal decays ($K_L \to \pi^0 \nu\overline{\nu}$ and $K_L \to \pi^0 X^0$) were normalized with the reference decay modes (normalization modes) which have well-measured branching fractions ($\mathcal{B}_{\rm norm}$) as:

$$\mathcal{B}_{\rm sig} = \frac{N_{\rm obs}/A_{\rm sig}}{pN_{\rm norm}/(A_{\rm norm}\ \mathcal{B}_{\rm norm})} \tag{6.1}$$

$$= \frac{N_{\rm obs}}{A_{\rm sig}}\ \frac{A_{\rm norm}\ \mathcal{B}_{\rm norm}}{pN_{\rm norm}}, \tag{6.2}$$

and

$$\mathrm{SES} = \frac{1}{A_{\rm sig}}\ \frac{A_{\rm norm}\ \mathcal{B}_{\rm norm}}{pN_{\rm norm}}, \tag{6.3}$$

where $A_{\rm sig}$ and $N_{\rm obs}$ ($A_{\rm norm}$ and $N_{\rm norm}$) are the acceptance and the number of observed events of the signal (normalization mode) decay, respectively, and p is the pre-scaling factor of 30 for the Normalization trigger.

The analysis is mainly composed of three parts: normalization modes analysis, signal acceptance estimation, and background estimation, which are related to each other. In the normalization mode analysis, we evaluated the number of collected K_L's by analyzing the normalization modes. We estimated the signal acceptance based on a simulation and then obtained the SES. In the background estimation, the number of background events was estimated for each source. Most of the estimations were based on simulations, whereas a data-driven approach was taken to estimate the hadron-cluster background.

Table 6.1: Summary of the statistics of each simulation sample used for the normalization modes analysis. The third column, "statistics", represents the number of generated K_L's at the beam exit which decay into a decay mode of interest. The fourth column, "N / $\mathcal{B}$", represents the statistics normalized with the branching fraction. These numbers correspond to the numbers of "normal" K_L's generated at the beam exit.

decay mode	branching fraction ($\mathcal{B}$)	statistics (N)	N / $\mathcal{B}$
$K_L \to 3\pi^0$	19.52%	1×10^9	5.12×10^9
$K_L \to 2\pi^0$	8.64×10^{-4}	1×10^9	1.16×10^{12}
$K_L \to 2\gamma$	5.47×10^{-4}	1×10^9	1.83×10^{12}

6.2 Normalization Mode Analysis

The normalization modes, namely the $K_L \to 3\pi^0$, $K_L \to 2\pi^0$, and $K_L \to 2\gamma$ decays were analyzed to obtain the number of collected K_L's ("K_L yield"). Actually, as described in Sec. 2.1.3, we normalized the sensitivity based on the results from the $K_L \to 2\pi^0$ decay analysis because the kinematics of π^0's are relatively similar to that of the $K_L \to \pi^0\nu\overline{\nu}$ decay, and systematic uncertainties of acceptances largely canceled. The other decays were used to cross-check the results.

The analysis was performed for each run-period separately.

6.2.1 Data Set

6.2.1.1 Data Sample

We used data taken with the Normalization trigger and Minimum-bias trigger. The pre-scaling factor of 30 (300) for the Normalization (Minimum-bias) trigger was used to scale the number of collected K_L's. In this analysis, the Normalization triggered data were mainly used since the statistics of the Normalization triggered data was approximately an order of magnitude larger than that of the Minimum-bias triggered data after imposing all the veto cuts.

6.2.1.2 Simulation Sample

The decay modes of $K_L \to 3\pi^0$, $K_L \to 2\pi^0$, and $K_L \to 2\gamma$ were simulated separately. We neglected the other K_L decay modes because their contaminations were found to be small in a past study [67]. The simulation statistics is summarized in Table 6.1. These simulation samples were prepared for each run-period.

6.2.2 Event Selection Criteria with CsI Calorimeter Information

We reconstructed K_L's as in Sec. 4.2. In order to purify the reconstructed events, we imposed some cuts on the reconstructed events. The cuts based on the CsI calorimeter information are summarized in this section and the veto cuts are summarized in Sec. 6.2.3.

All the cuts are summarized in Table 6.2 and each cut is explained below.

trigger timing : The short dead time of our trigger system possibly causes overlap of event windows, and one real event can be recorded twice as two different events. In order to eliminate such a double counting of an event, we required the average of the timing of clusters to be within ± 15 ns of the nominal trigger timing.

total energy: The total energy of photons were required to be larger than 650 MeV so that the effects from online Et trigger threshold of 550 MeV could be negligible.

Table 6.2: Summary of the selection criteria used in the normalization mode analysis.

selection	$K_L \to 3\pi^0$	$K_L \to 2\pi^0$	$K_L \to 2\gamma$
trigger timing		± 15 ns	
total energy		$E_{\rm tot} > 650$ MeV	
photon energy		$E_\gamma > 50$ MeV	
photon position		$\max(\lvert x\rvert, \lvert y\rvert) > 150$ mm	
		$R < 850$ mm	
two-photon distance		$d > 150$ mm	
$\Delta T_{\rm vtx}^{\rm K_L}$		$\Delta T_{\rm vtx}^{\rm K_L} < 3$ ns	
$Z_{\rm vtx}^{\rm K_L}$		$3000 < Z_{\rm vtx}^{\rm K_L} < 5000$ mm	
K_L P_t		$P_t < 50$ MeV/c	
K_L mass		± 15 MeV/c^2	–
χ^2_z		$\chi^2_z < 20$	–
$\Delta Z_{\rm vtx}$		$\Delta Z_{\rm vtx} < 400$ mm	–
π^0 mass	± 10 MeV/c^2	± 6 MeV/c^2	–
K_L pos. at beam exit	–	$\max(\lvert X\rvert, \lvert Y\rvert) < 50$ mm	–

photon energy: The energy of all the photons were required to be larger than 50 MeV to ensure the quality of photon reconstruction.

photon position: The hit positions of all the photons on the CsI calorimeter, x, y, and $R = \sqrt{x^2+y^2}$, should be inside the fiducial region of the CsI calorimeter, namely $\max(|x|, |y|) > 150$ mm and $R < 850$ mm.

two-photon distance: The clear separation of photons was required. The distances between all the possible pairs of photons were required to be larger than 150 mm.

$\Delta T_{\rm vtx}^{\rm K_L}$: The vertex time of photons should be consistent with each other. The maximum timing difference between the event vertex time $T_{\rm vtx}^{\rm K_L}$ (see Sec. 4.2.4) and vertex time of photons were required to be smaller than 3 ns. This requirement rejects the events formed by photons from accidental activities.

$Z_{\rm vtx}^{\rm K_L}$: The reconstructed z vertex position $Z_{\rm vtx}^{\rm K_L}$ was required to be inside the fiducial region of KOTO detector, $3000 < Z_{\rm vtx}^{\rm K_L} < 5000$ mm.

K_L P_t: The K_L's coming into the KOTO detector ideally have no transverse momentum P_t. To ensure that there were no missing particles, we required the P_t of the reconstructed K_L to be smaller than 50 MeV/c.

K_L mass: Invariant mass of photons was required to be close (± 15 MeV/c^2) to the nominal K_L mass of 497.614 MeV/c^2 [85]. This requirement reduces the contamination of mispairing events in the $K_L \to 3\pi^0$ and $K_L \to 2\pi^0$ analyses, and the contamination of the $K_L \to 3\pi^0$ decays in the $K_L \to 2\pi^0$ analysis. This selection was not used in the $K_L \to 2\gamma$ analysis, because K_L's were reconstructed by assuming the K_L mass.

χ^2_z: To ensure the consistency of π^0 vertexes, the χ^2_z defined in Eq. 4.15 was required to be less than 20 for the $K_L \to 3\pi^0$ and $K_L \to 2\pi^0$ candidates. Note that the number of degrees of freedom of χ^2_z is 2 (1) for the $K_L \to 3\pi^0$ ($K_L \to 2\pi^0$) candidates.

$\Delta Z_{\rm vtx}$: This selection was also imposed to ensure the consistency of π^0 vertexes. The $\Delta Z_{\rm vtx}$ defined in Eq. 4.16 was required to be less than 400 mm for the $K_L \to 3\pi^0$ and $K_L \to 2\pi^0$ candidates.

$\Delta\pi^0$ mass: In the $K_L \to 3\pi^0$ and $K_L \to 2\pi^0$ reconstruction, π^0's were re-reconstructed with a fixed vertex point and free invariant mass of two photons. The agreement with the nominal π^0 mass of 134.9766 MeV/c^2 [85] reflects the consistency of vertexes among π^0's. The deviation was required to be within ± 10 MeV/c^2 for the $K_L \to 3\pi^0$ analysis and 6 MeV/c^2 for the $K_L \to 2\pi^0$ analysis.

K_L position at beam exit: The (x, y) positions of K_L's at the beam exit $(X_{\rm exit}, Y_{\rm exit})$ were reconstructed with the center of energy of photons on the CsI calorimeter $(X_{\rm COE}, Y_{\rm COE})$ given in Eq. 4.17 and 4.18 as

$$X_{\rm exit} = \frac{Z_{\rm exit} - Z_{\rm target}}{Z_{\rm CSI} - Z_{\rm target}} X_{\rm COE}, \tag{6.4}$$

$$Y_{\rm exit} = \frac{Z_{\rm exit} - Z_{\rm target}}{Z_{\rm CSI} - Z_{\rm target}} Y_{\rm COE}, \tag{6.5}$$

$$\tag{6.6}$$

where $Z_{\rm exit}$, $Z_{\rm target}$, and $Z_{\rm CSI}$ are the z positions of the beam exit, the T1 target, and the upstream surface of the CsI calorimeter, respectively. In the $K_L \to 2\pi^0$ analysis, we required $(X_{\rm exit}, Y_{\rm exit})$ to be inside the beam core region, $\max(|X|, |Y|) < 50$ mm. This requirement rejected events with missing energy.

6.2.3 Veto Cuts

All the veto cuts used in the normalization modes analysis were the same as those in the $K_L \to \pi^0\nu\overline{\nu}$ analysis. The methods of veto decision are described in Sec. 4.3. The information of the veto window and veto energy threshold of each detector component are summarized in Table 6.3.

6.2.4 Distributions of kinematic Variables

6.2.4.1 $K_L \to 3\pi^0$ Decay

The $K_L \to 3\pi^0$ decay has a large branching fraction of 19.52% [15] and is almost free from backgrounds because there is no other natural mechanism to make six clusters on the CsI calorimeter.

The distributions of kinematic variables for the data set of Period-9 are shown in Fig. 6.1. In these plots, all the veto cuts and kinematic cuts except for the variable of interest are imposed. The purity of $K_L \to 3\pi^0$ event is almost 100% after all the cuts are imposed; contributions from the $K_L \to 2\pi^0$ and $K_L \to 2\gamma$ decays are negligibly small. The tail components of the K_L mass distribution, or six-photon invariant mass distribution in Fig. 6.1a are due to mispairing of photons forming a pion. A slight shift of the mass peak can be seen but we do not understand the cause of the shift. The edges of the reconstructed $Z_{\rm vtx}$ distribution (Fig. 6.1c) are determined by the detector position of NCC ($z = 1990 - 2440$ mm) and the CsI calorimeter ($z = 6148 - 6648$ mm). Except for the $\Delta T^{\rm K_L}_{\rm vtx}$ distribution (Fig. 6.1f), the simulations show good reproducibility of the data, which means we understand the properties of the K_L beam and the detector well. The discrepancies in the $\Delta T^{\rm K_L}_{\rm vtx}$ distribution tells us that we do not fully understand the timing response of the CsI calorimeter. In this analysis, in order to mitigate the effects of the efficiency difference between data and MC in the $\Delta T^{\rm K_L}_{\rm vtx}$ selection, we used a loose selection criterion of $\Delta T^{\rm K_L}_{\rm vtx} < 3$ ns.

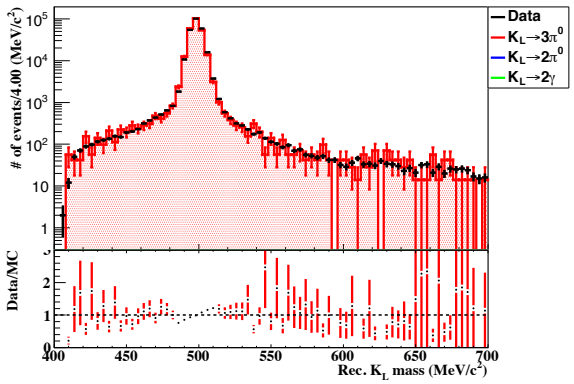

(a) K_L mass

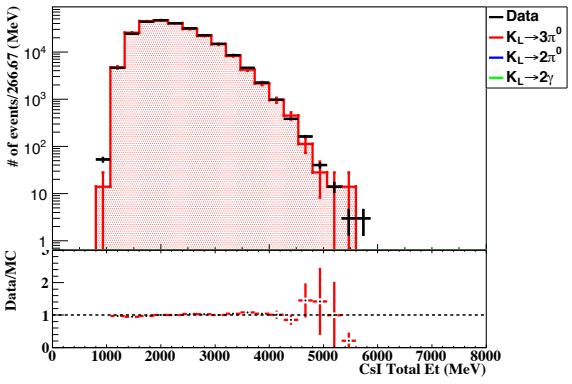

(b) total energy

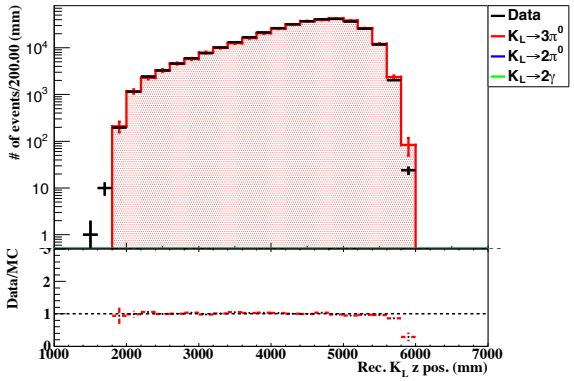

(c) K_L reconstructed $Z_{\rm vtx}$

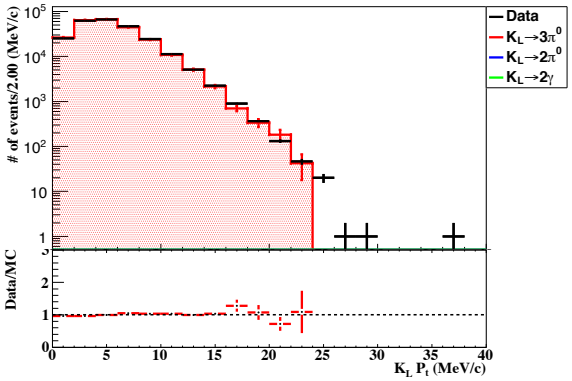

(d) K_L P_t

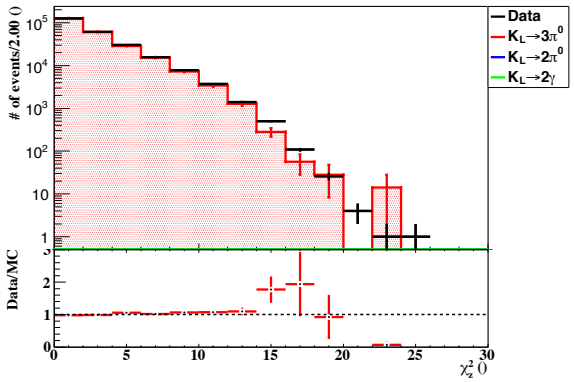

(e) χ^2_z

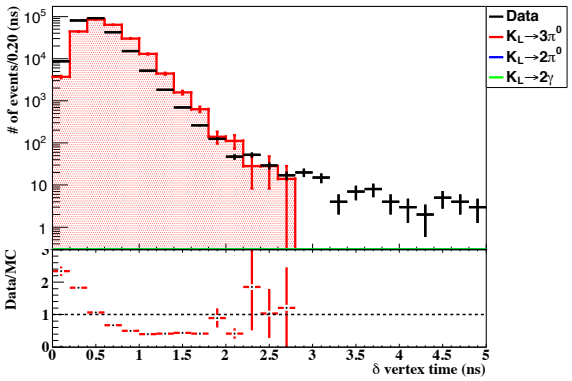

(f) $\Delta T^{\rm K_L}_{\rm vtx}$

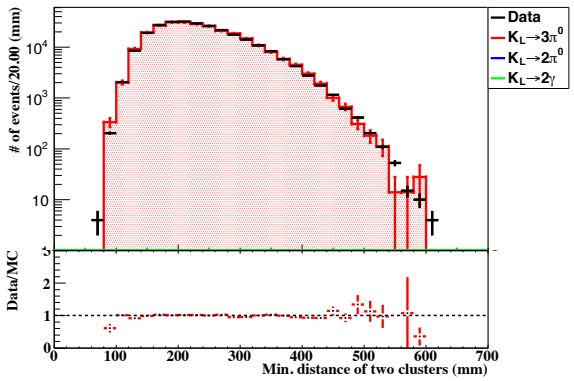

(g) two-photon distance

Figure 6.1: Distributions of the kinematic variables of reconstructed $K_L \to 3\pi^0$ events. Black points represent data and colored histograms represent MC simulations (stacked). The data/MC ratios are shown below each panel. The error bars represent the statistical errors.

Table 6.3: Veto window and veto energy threshold of each detector component. (*) The newBHCV adopted the 2-out-of-3 method and the energy threshold here is for the layer-veto-energy. (**) The BHPV veto was based on the number of consecutive hit modules and if it was three or more, such an event was vetoed. (***) The BHGC used the number of equivalent photons instead of energy for veto decision.

detector component	energy threshold	veto window
CSI (isolated hit crystal)	see Sec. 4.3.1	
CSI (extra-cluster)	see Sec. 4.3.1	
MB	1 MeV	60 ns
BCV	1 MeV	60 ns
CV	0.2 MeV	80 ns
CC03	3 MeV	60 ns
CC04, CC05, CC06 (CsI crystal)	3 MeV	30 ns
CC04, CC05, CC06 (plastic scintillator)	1 MeV	30 ns
OEV	1 MeV	20 ns
LCV	0.6 MeV	30 ns
BPCV	1 MeV	24 ns
FB	1 MeV	51 ns
FB (wide window)	30 MeV	150 ns
NCC	1 MeV	40 ns
Hinemos	1 MeV	60 ns
newBHCV	221 eV (*)	25 ns
BHPV	(**)	15 ns
BHGC	2.5 p.e.(***)	15 ns

6.2.4.2 $K_L \to 2\pi^0$ Decay

The $K_L \to 2\pi^0$ decay is most important among the three normalization modes because we normalized signal using the results from this decay mode. In this analysis, the main background is the $K_L \to 3\pi^0$ decay whose branching fraction is two hundred times larger than that of $K_L \to 2\pi^0$. It becomes a background event if two photons out of six are missed in the KOTO detector or two or more photons hitting the CsI calorimeter close to each other make a fused cluster. After all the veto cuts were imposed, the main component of the $K_L \to 3\pi^0$ contribution was caused by fused clusters, and most of it was eliminated by the K_L mass cut (Fig. 6.3e). The purity of the $K_L \to 2\pi^0$ events is 97% and the rest is the $K_L \to 3\pi^0$ contribution whose invariant mass of four photons was close to the nominal K_L mass by chance.

The distributions of all the kinematic variables used in the event selection (and "maximum photon energy" distribution in Fig. 6.2d) based on the data set of Period-9 are shown in Fig. 6.2 to Fig. 6.4. In these plots, all the veto cuts and kinematic cuts except for the variable of interest are imposed. The distributions show good agreements between data and MC, although discrepancies in $\Delta T_{\rm vtx}^{\rm K_L}$ distribution (Fig. 6.3b) and a slight peak shift in four-photon invariant mass distribution (Fig. 6.3e) are also seen as in the $K_L \to 3\pi^0$ analysis.

6.2.4.3 $K_L \to 2\gamma$ Decay

The $K_L \to 2\gamma$ events were reconstructed in the similar manner to the π^0 reconstruction because the final state has only 2 photons.

Data and MC distributions in $K_L \to 2\gamma$ events for the kinematic variables with the data set of Period-9 are shown in Fig. 6.5 with all the veto cuts and kinematic cuts imposed except for the variable of interest. The P_t distribution (Fig. 6.5c) is broader than that of the $K_L \to 3\pi^0$ (Fig. 6.1d)

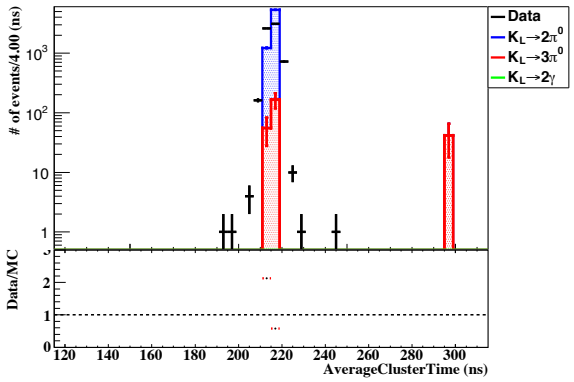

(a) trigger timing

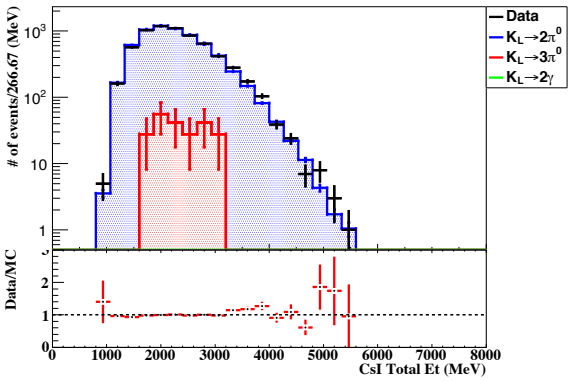

(b) total energy

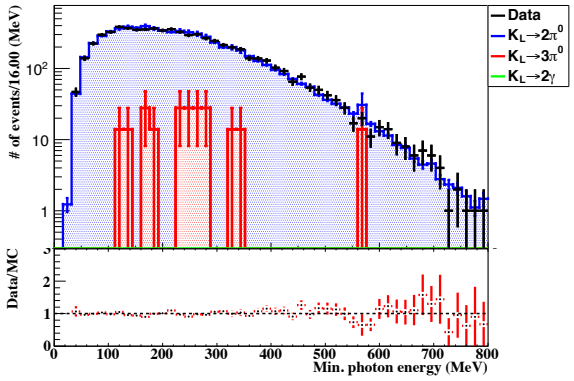

(c) minimum photon energy

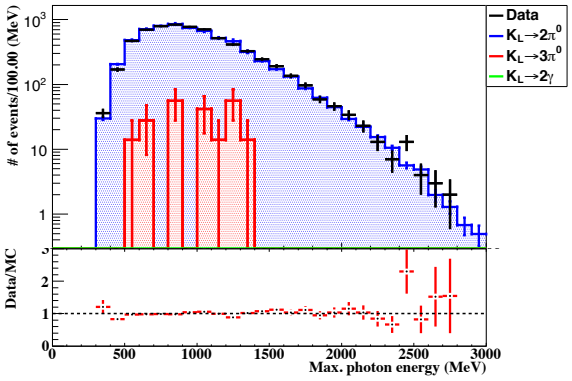

(d) maximum photon energy

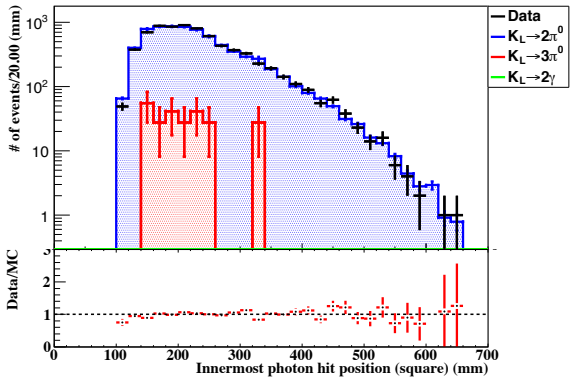

(e) photon position (inner xy)

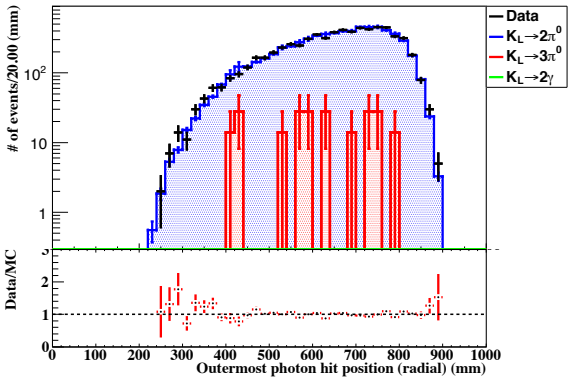

(f) photon position (outer R)

Figure 6.2: Distributions of the kinematic variables of reconstructed $K_L \to 2\pi^0$ events. Black points represent data and colored histograms represent MC simulations (stacked). The data/MC ratios are shown below each panel. The error bars represent the statistical errors.

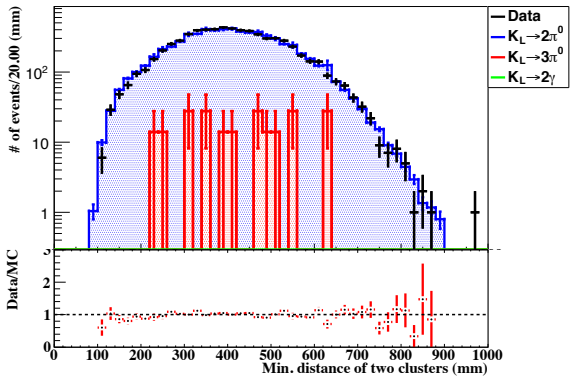

(a) two-photon distance

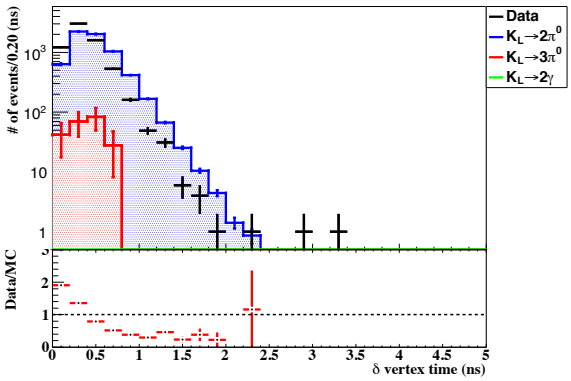

(b) $\Delta T_{\mathrm{vtx}}^{\mathrm{K_L}}$

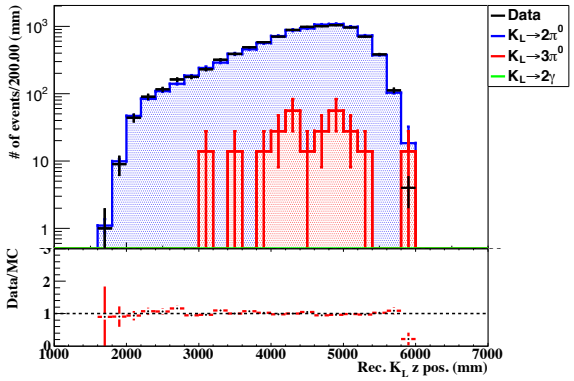

(c) $Z_{\mathrm{vtx}}^{\mathrm{K_L}}$

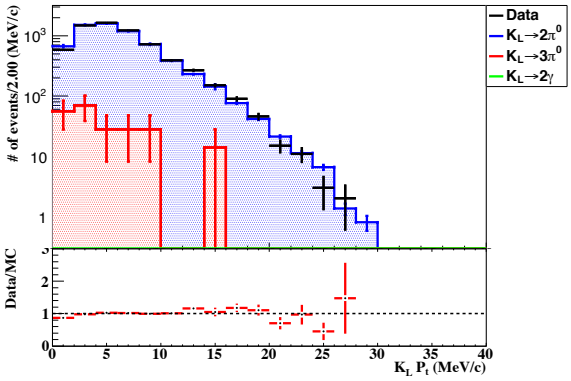

(d) K_L P_t

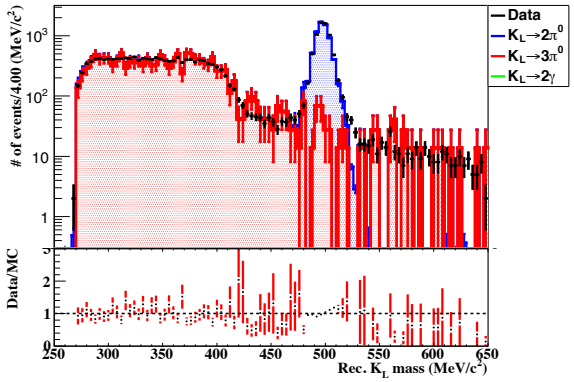

(e) K_L mass

Figure 6.3: Distributions of the kinematic variables of reconstructed $K_L \to 2\pi^0$ events. Black points represent data and colored histograms represent MC simulations (stacked). The data/MC ratios are shown below each panel. The error bars represent the statistical errors.

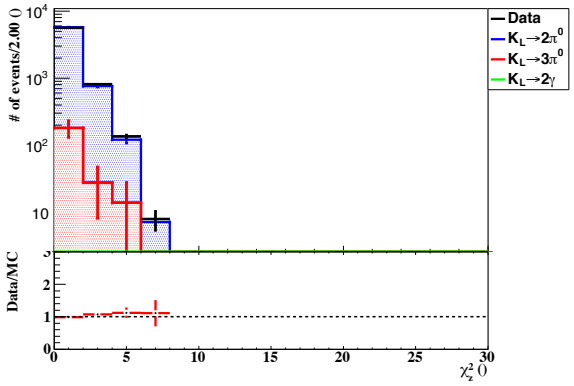

(a) χ^2_z

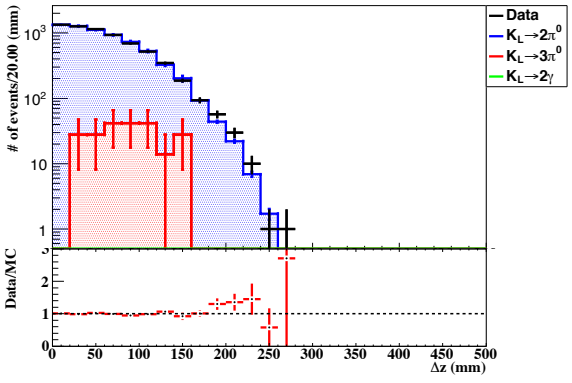

(b) $\Delta Z^{\mathrm{K_L}}_{\mathrm{vtx}}$

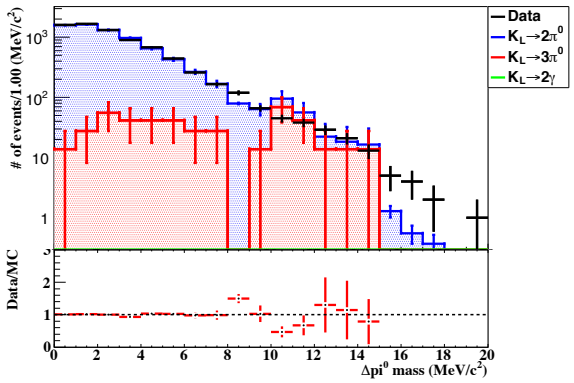

(c) $\Delta\pi^0$ mass

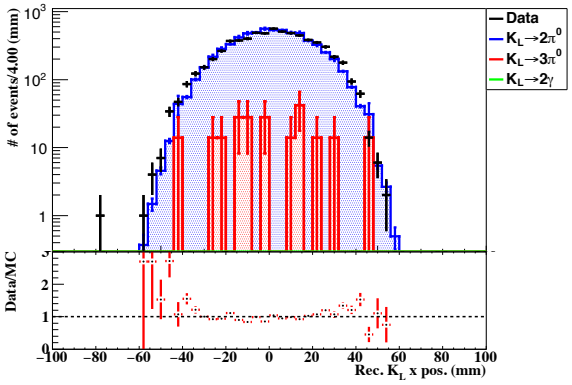

(d) K_L position at the beam exit (X)

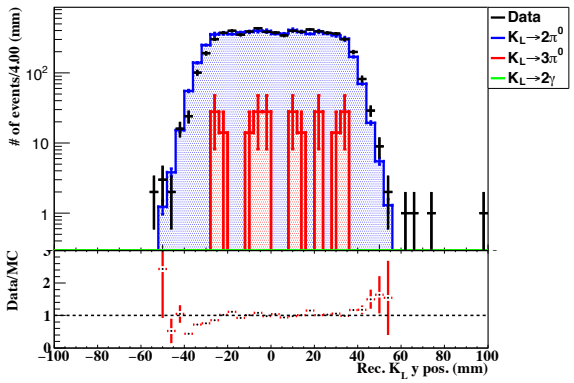

(e) K_L position at the beam exit (Y)

Figure 6.4: Distributions of the kinematic variables of reconstructed $K_L \to 2\pi^0$ events. Black points represent data and colored histograms represent MC simulations (stacked). The data/MC ratios are shown below each panel. The error bars represent the statistical errors.

Table 6.4: Summary of results from the $K_L \to 2\pi^0$ analysis. Acceptance for $A_{K_L\to 2\pi^0}$ includes the decay probability of K_L, which is approximately 3%.

run-period	$A_{K_L\to 2\pi^0}$	$N^{\rm Data}_{K_L\to 2\pi^0}$	N_{K_L} at the beam exit	K_L flux ($/2\times10^{14}$ POT)
Period-1	1.88×10^{-4}	7.50×10^{2}	1.39×10^{11}	$(3.60\pm0.13)\times10^{7}$
Period-2	1.80×10^{-4}	1.23×10^{3}	2.37×10^{11}	$(3.79\pm0.11)\times10^{7}$
Period-3	1.67×10^{-4}	5.49×10^{2}	1.15×10^{11}	$(3.71\pm0.16)\times10^{7}$
Period-4	1.03×10^{-4}	4.40×10^{2}	1.49×10^{11}	$(4.22\pm0.20)\times10^{7}$
Period-5	0.92×10^{-4}	1.31×10^{3}	4.95×10^{11}	$(4.39\pm0.13)\times10^{7}$
Period-6	1.41×10^{-4}	7.01×10^{2}	1.72×10^{11}	$(4.10\pm0.16)\times10^{7}$
Period-7	1.08×10^{-4}	1.80×10^{3}	5.82×10^{11}	$(4.23\pm0.10)\times10^{7}$
Period-8	1.10×10^{-4}	2.07×10^{3}	6.50×10^{11}	$(4.43\pm0.10)\times10^{7}$
Period-9	1.04×10^{-4}	6.39×10^{3}	2.14×10^{12}	$(4.36\pm0.07)\times10^{7}$
total	1.14×10^{-4}	1.52×10^{4}	4.68×10^{12}	4.27×10^{7}

and $K_L\to 2\pi^0$ (Fig. 6.3d) events since we reconstruct the $K_L\to 2\gamma$ events assuming the vertex on the beam axis, while the x and y positions of the decay vertex are obtained in the $K_L\to 3\pi^0$ and $K_L\to 2\pi^0$ event reconstruction. The deviation of K_L decay vertex position from the beam axis worsened the P_t resolution in the $K_L\to 2\gamma$ analysis. These distributions basically show good agreements between data and MC, except for the $\Delta T^{\rm K_L}_{\rm vtx}$ distribution (Fig. 6.5d), although there are small discrepancies in upstream region in the distribution of reconstructed $Z_{\rm vtx}$ (Fig. 6.5b) and in high P_t region in the K_L P_t distribution (Fig. 6.5c).

6.2.5 Results of the Normalization Modes Analysis

The acceptance for the $K_L\to 2\pi^0$ decay ($A_{K_L\to 2\pi^0}$) for the K_L's entering the KOTO detector and the purity in the reconstructed events were calculated with simulations. The number of reconstructed $K_L\to 2\pi^0$ decay events $N^{\rm Data}_{K_L\to 2\pi^0}$ is a product of the number of reconstructed events $N^{\rm Data}$ and purity : $N^{\rm Data}_{K_L\to 2\pi^0} = N^{\rm Data}\times purity$, where the purity was estimated with the simulation. The number of K_L's, N_{K_L}, and the flux (yield per the number of protons on target (POT)), Y, at the beam exit were then obtained as

$$N_{K_L} = \frac{N^{\rm Data}_{K_L\to 2\pi^0}}{\mathcal{B}(K_L\to 2\pi^0)\times A_{K_L\to 2\pi^0}} \tag{6.7}$$

and

$$Y = \frac{N^{\rm Data}_{K_L\to 2\pi^0}}{\mathcal{B}(K_L\to 2\pi^0)\times A_{K_L\to 2\pi^0}\times {\rm POT}}, \tag{6.8}$$

respectively. The same analyses were performed for the $K_L\to 3\pi^0$ and $K_L\to 2\gamma$ decays.

These results of the $K_L\to 2\pi^0$ analyses in each run-period are summarized in Table 6.4. The fluxes should be constant with run-period, or constant regardless of beam power, but they fluctuated between run-periods by 20% at maximum. The fluctuation was caused by an efficiency difference between data and MC in the veto cuts. We crosschecked the K_L fluxes using the $K_L\to 3\pi^0$ decay without any veto cuts. In this analysis, data taken with the Minimum-bias trigger were used to eliminate the online veto effects of MB, CV, NCC, and CC03. The fluxes were obtained as in Fig. 6.6 and they were stable within approximately 5%. That is why we concluded the cause of the flux fluctuation was the veto cuts. This fluctuation of flux is not serious in the estimation of SES because such effects are basically canceled out by taking the ratio of acceptances for $K_L\to 2\pi^0$ and $K_L\to\pi^0\nu\overline{\nu}$ as in Eq. 6.3.

The K_L fluxes derived from all the normalization modes in all the run-periods and the total K_L yields through the 2015 run calculated with three modes are shown in Fig. 6.7 and Fig. 6.8, respectively. The fluxes and yields obtained with the $K_L\to 2\gamma$ decay analysis seems to be approximately 5% lower

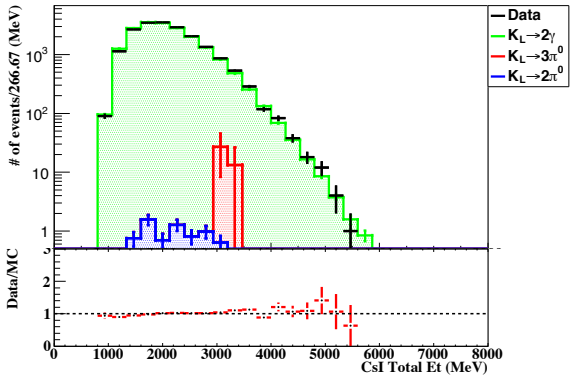

(a) total energy

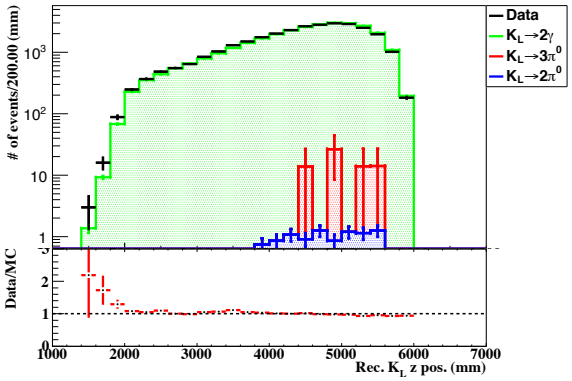

(b) K_L reconstructed $Z_{\rm vtx}$

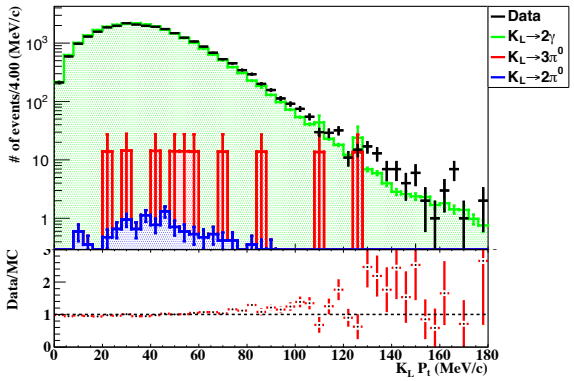

(c) K_L P_t

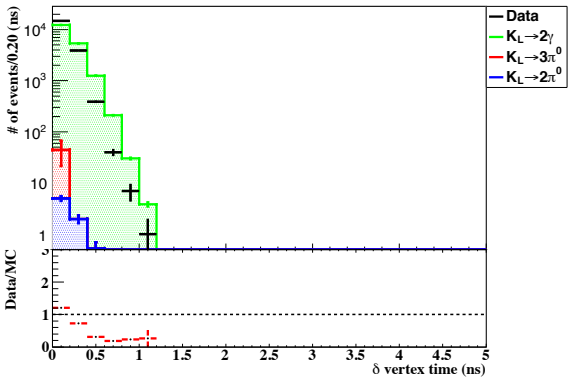

(d) $\Delta T^{\rm K_L}_{\rm vtx}$

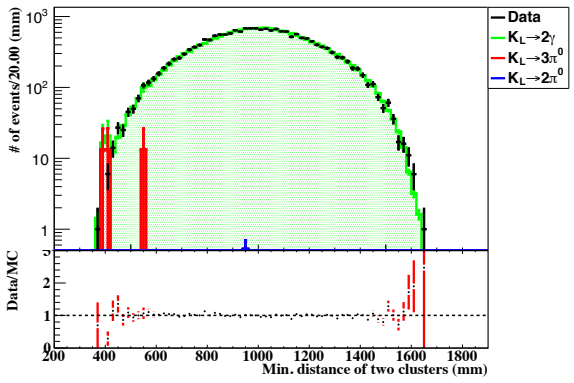

(e) two-photon distance

Figure 6.5: Distributions of the kinematic variables of reconstructed $K_L \to 2\gamma$ events. Black points represent data and colored histograms represent MC simulations (stacked). The data/MC ratios are shown below each panel. The error bars represent the statistical errors.

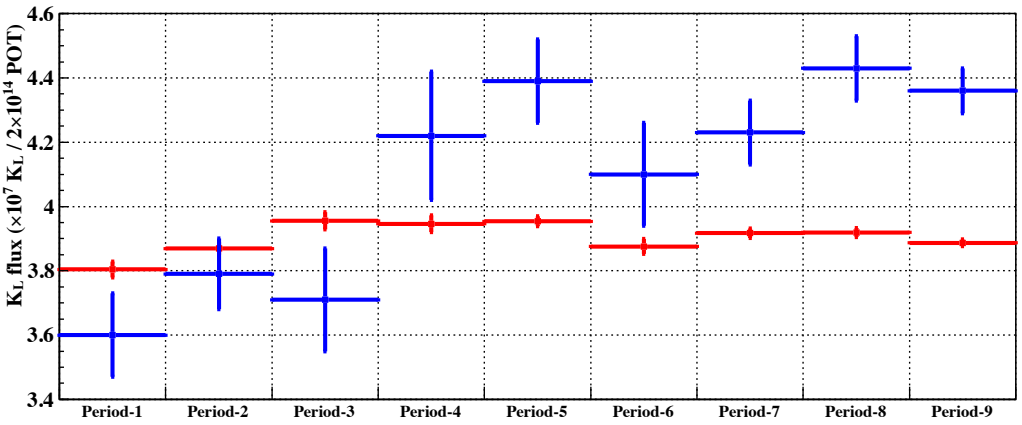

Figure 6.6: K_L fluxes obtained by the $K_L \to 3\pi^0$ analysis without veto cuts in each run-period (red points). The blue points represent the fluxes obtained with the $K_L \to 2\pi^0$ analysis. The error bars represent the statistical errors.

than that with the other modes for unknown reasons. We took this discrepancy into account in the evaluation of the systematic uncertainties of the single event sensitivity.

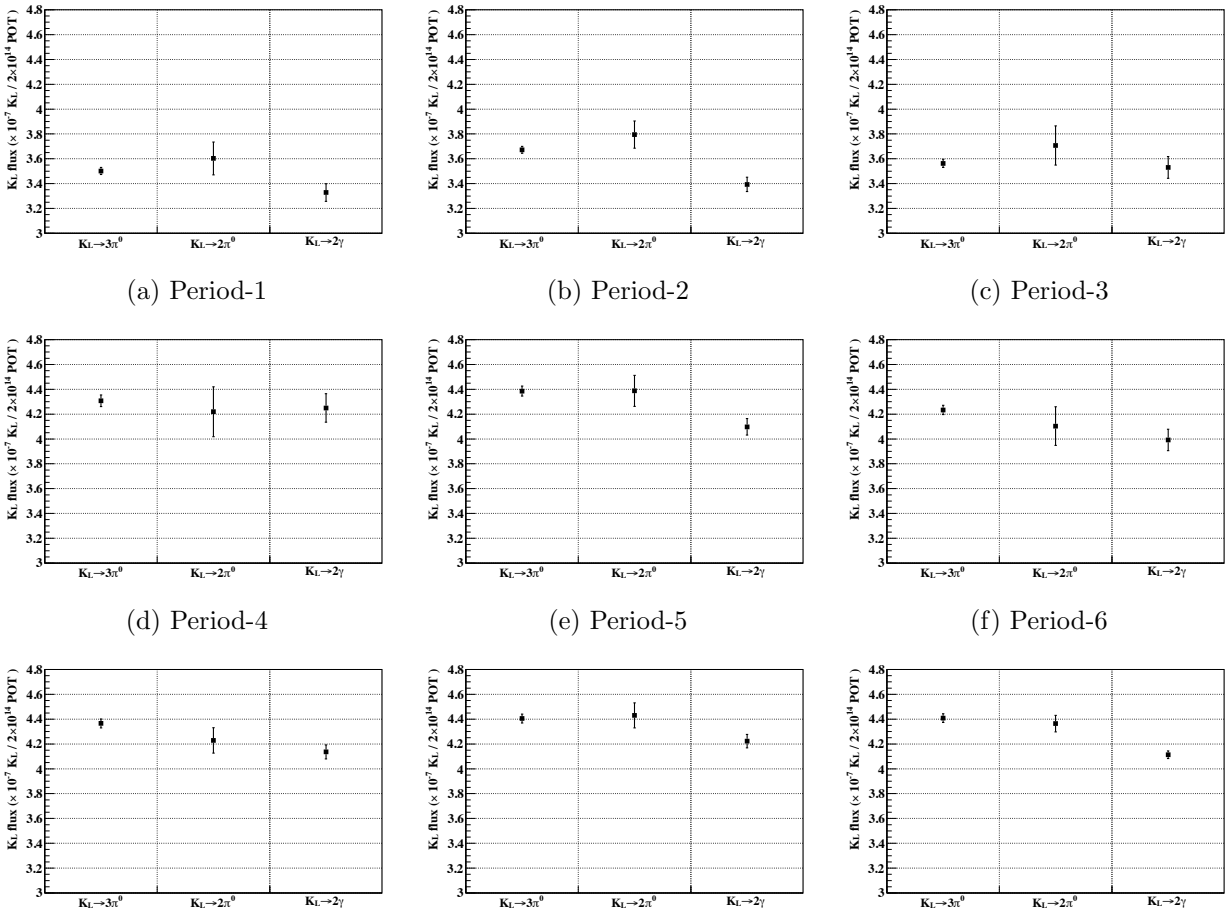

(a) Period-1 (b) Period-2 (c) Period-3

(d) Period-4 (e) Period-5 (f) Period-6

(g) Period-7 (h) Period-8 (i) Period-9

Figure 6.7: K_L fluxes measured with three normalization modes. Each panel corresponds to a run-period. The error bars represent the statistical errors.

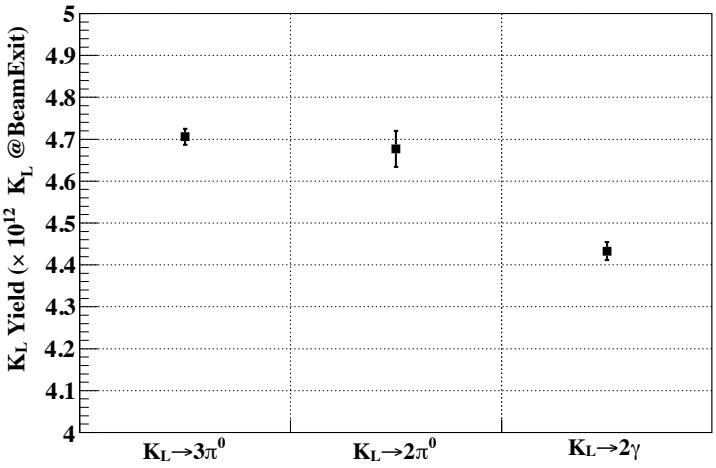

Figure 6.8: Total K_L yields at the beam exit through the 2015 run with three modes analysis. The error bars represent the statistical errors.

Table 6.5: Summary of the selection criteria for the $K_L \to \pi^0\nu\overline{\nu}$ and $K_L \to \pi^0 X^0$ event candidates.

category	selection name	selection criterion
trigger-related cuts	trigger timing	± 15 ns
	total energy	$E_{\rm tot} \geq 650$ MeV
	CSI Et trigger efficiency	(weighting for MC)
	COE	$R_{\rm COE} \geq 200$ mm
	COE trigger efficiency	(weighting for MC)
photon-selection cuts	photon energy	100 MeV $\leq E_\gamma \leq$ 2000 MeV
	photon position (inner)	$\max(\lvert x\rvert, \lvert y\rvert) \geq 150$ mm
	photon position (outer)	$R \leq 850$ mm
π^0 selection cuts	$\Delta T_{\rm vtx}$	$\Delta T_{\rm vtx} \leq 1$ ns
	cluster distance	≥ 300 mm
	energy ratio	$E_2/E_1 \geq 0.2$
	P_t/P_z-$Z_{\rm vtx}$, E-$Z_{\rm vtx}$	see Fig. 6.15
	projection angle	$\theta_{\rm proj.} \leq 150$
	$E \cdot \theta$	$E \cdot \theta \geq 2500$ MeV $\cdot$ deg
	dead channel	$d_{\rm dead} \geq 53$ mm
shape-related cuts	cluster size	$n_{\rm crystal} \geq 5$
	cluster RMS	$RMS_{\rm cluster} \geq 10$
	shape-χ^2	$\chi^2_{\rm shape} < 4.6$
	cluster shape NN	$o_{\rm SNN} > 0.8$
	theta-χ^2	$\chi^2_\theta < 4.5$
	eta-χ^2	$\chi^2_\eta > 17$
	pulse shape likelihood ratio	$R_{\gamma\gamma}^{\text{2-cluster}} > 0.1$

6.3 Selection Criteria and Acceptance for the Signal

In this section, we first explain event selection criteria (cuts) imposed on reconstructed events and then estimate the signal acceptance for the $K_L \to \pi^0\nu\overline{\nu}$ decay.

We estimated the signal acceptance by imposing all the cuts on $K_L \to \pi^0\nu\overline{\nu}$ MC samples. As for the pulse shape likelihood ratio cut explained later, we applied a weight factor of cut survival probability for each event as a function of energy because we could not reproduce the pulse shape of the CsI calorimeter in MC simulations. As for trigger efficiencies of CsI Et trigger (Lv1 trigger) and COE trigger (Lv2 trigger), we also used the weighting methods. The weight factors are given as a function of kinematical variables obtained with a data-driven approach.

The single event sensitivity for $K_L \to \pi^0\nu\overline{\nu}$ and its uncertainties are also described in this section.

6.3.1 Event Selection Criteria with CsI Calorimeter Information

Event selection criteria with the CsI calorimeter information are summarized in Table 6.5, and explained in order. We categorized these cuts into four groups: "*trigger-related cuts*", "*photon selection cuts*", "π^0 *kinematic cuts*", and "*shape-related cuts*".

6.3.1.1 Trigger-Related Cuts

trigger timing: We applied this cut to eliminate the double counting of an event as described in Sec. 6.2.2.

total energy and CSI Et trigger efficiency: Energy sum of two photons was required to exceed 650 MeV. Most of the bias from the CSI Et trigger (threshold: 550 MeV) was eliminated by this cut.

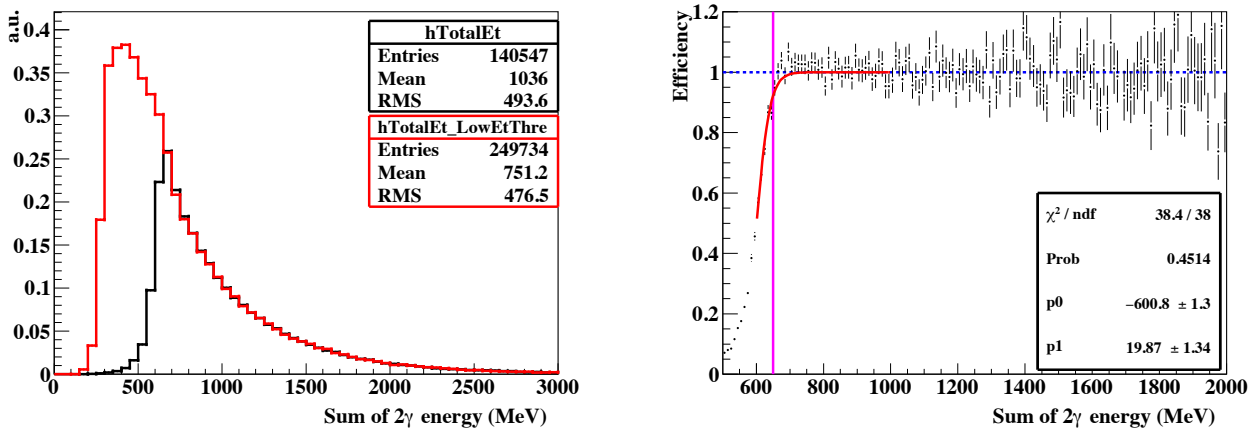

(a) (b)

Figure 6.9: (a) Distributions of energy sum of two photons obtained with a physics run data (black) and a low Et threshold run data (red). These histograms are normalized with the number of events with energy larger than 1000 MeV. (b) CSI Et trigger efficiency as a function of the sum of two photons' energies. The red line shows the fitted efficiency function and the magenta line represents the energy threshold of 650 MeV used in the total energy cut.

Even after imposing the total energy cut, we found a slight event loss due to the CSI Et trigger efficiency. Figure 6.9a shows the distributions of energy sum of two photons ($E_{\rm tot}$) in a normal physics run data and a special low threshold Et trigger run data (threshold: 250 MeV). By taking the ratio of each histogram bin and fitting the ratio plot as shown in Fig. 6.9b, we obtained the efficiency factor as a function of $E_{\rm tot}$:

$$\epsilon_{\rm Et}(E_{\rm tot}) = \frac{1}{1+\exp\{-(E_{\rm tot}+p_0)/p_1\}}, \tag{6.9}$$

where $p_0 = -601$ and $p_1 = 19.9$ are the fit parameters.

The efficiency for the $K_L \to \pi^0 \nu\overline{\nu}$ candidates was estimated to be 99.9%.

The distribution of total energy is shown in Fig. 6.12a.

COE and COE trigger efficiency: The center position of the energy of two photons were calculated and the distance from the beam axis, $R^{2\gamma}_{COE}$, was required to be larger than 200 mm, while the Lv2 trigger threshold was 165 mm. Even though most of the Lv2 trigger bias was eliminated with the above cut, there still was some trigger efficiency loss left. The $R^{2\gamma}_{\rm COE}$ used in the analysis was calculated with energies and x-y positions of two photons, whereas $R_{\rm COE}$ used in the Lv2 trigger was calculated with energies and positions of all the CsI crystals including the ones with off-timing hits. Hence accidental activities in the CsI calorimeter worsened the trigger efficiency.

We factorized the efficiency as a function of $R^{2\gamma}_{\rm COE}$ and $E_{2\gamma}/E_{\rm CSItot}$, where $E_{2\gamma}$ and $E_{\rm CSItot}$ are the energy sum of two photons and the energy sum over all the channels of the CsI calorimeter. Figure 6.10 shows the COE trigger efficiency as a function of $R^{2\gamma}_{\rm COE}$ in each $E_{2\gamma}/E_{\rm CSItot}$ region. Note that the energy correction for photons (see Sec. 4.2.2) allows $E_{2\gamma}$ and $E_{\rm CSItot}$ to be larger than 1. We obtained the COE trigger efficiency functions by fitting the efficiency histograms shown in the bottom panels of Fig. 6.10 with

$$\epsilon_{\rm COE}(R^{2\gamma}_{\rm COE}) = \frac{1}{1+\exp\{-(R^{2\gamma}_{\rm COE}+p_0)/p_1\}}, \tag{6.10}$$

where p_0 and p_1 are free parameters in the fit. The fitted functions and parameters are also shown in Fig. 6.10. We then obtained the efficiency factor as a function of $R^{2\gamma}_{\rm COE}$ and $E_{2\gamma}/E_{\rm CSItot}$ by interpolating the fitted functions. The resultant efficiency map is shown in Fig 6.11.

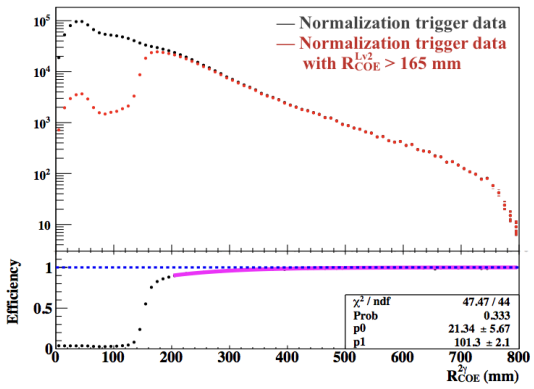

(a) $E_{2\gamma}/E_{\mathrm{CSItot}} > 0.9$

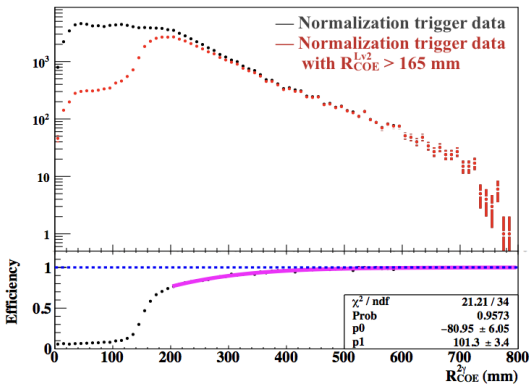

(b) $0.7 < E_{2\gamma}/E_{\mathrm{CSItot}} \leq 0.9$

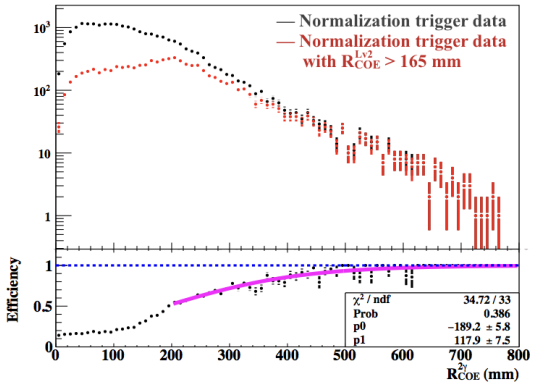

(c) $0.5 < E_{2\gamma}/E_{\mathrm{CSItot}} \leq 0.7$

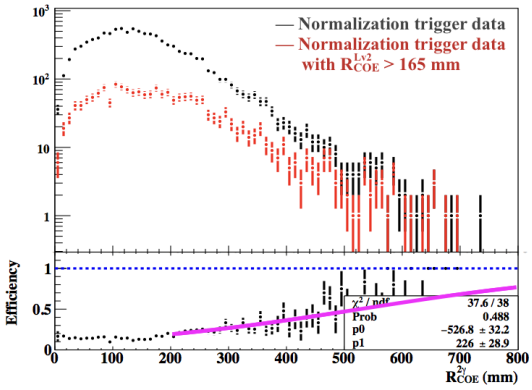

(d) $E_{2\gamma}/E_{\mathrm{CSItot}} \leq 0.5$

Figure 6.10: $R^{2\gamma}_{\mathrm{COE}}$ distributions with normalization trigger data before and after imposing the COE selection used in Lv2 trigger in each $E_{2\gamma}/E_{\mathrm{CSItot}}$ bin. Trigger efficiency obtained as the ratio of two histograms are shown below each panel. The magenta line represents the fitted function. The error bars represent the statistical errors.

The distribution of $R^{2\gamma}_{\mathrm{COE}}$ is shown in Fig. 6.12b.

6.3.1.2 Photon Selection Cuts

photon energy: We required the energy of each photon to exceed 100 MeV to ensure good reconstruction. We also avoided using unusually energetic photons, $E_\gamma > 2000$ MeV.

The distributions of the smaller E_γ and the larger E_γ are shown in Fig. 6.12c and Fig. 6.12d, respectively.

photon position (inner, outer): To ensure that electromagnetic showers were fully contained in the CsI calorimeter, we required both photons to hit within the fiducial region of the CsI calorimeter, $\max(|x|, |y|) > 150$ mm and $R = \sqrt{x^2 + y^2} < 850$ mm, where x and y are the hit positions of photons.

The distributions of inner photon position $\max(|x|, |y|)$ and outer photon position R are shown in Fig. 6.12e and Fig. 6.12f, respectively.

6.3.1.3 π^0 Kinematic Cuts

ΔT_{vtx}: We required the vertex time difference between two photons, ΔT_{vtx}, to satisfy $\Delta T_{\mathrm{vtx}} \leq 1$ ns. This selection eliminates the events which were made by the accidental coincidence of two clusters. It

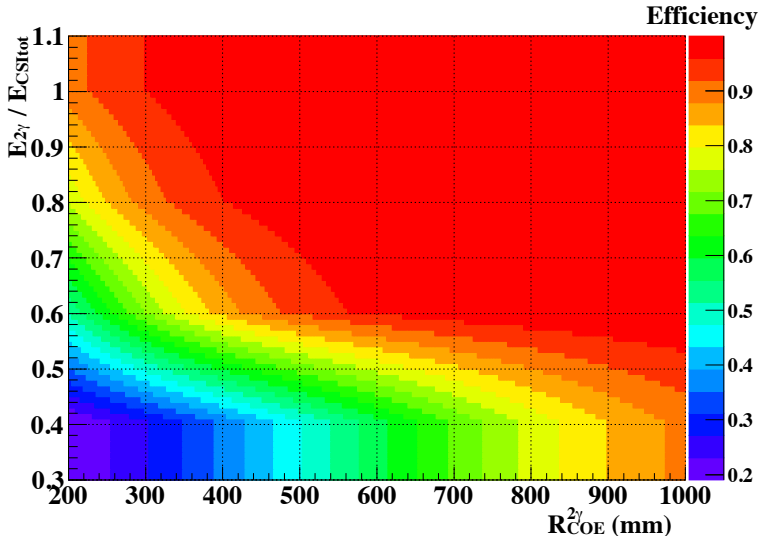

Figure 6.11: COE trigger efficiency map. The trigger efficiency is given as a function of $R^{2\gamma}_{\rm COE}$ and $E_{2\gamma}/E_{\rm CSItot}$.

was also effective to suppress the hadron-cluster background described in Sec. 2.1.2.2. The distributions of this variable are shown in Fig. 6.13a and Fig. 6.14a.

cluster distance: The distance between the two photons were required to be larger than 300 mm in the x-y plane to ensure a clean separation. The distribution of this variable is shown in Fig. 6.13b.

energy ratio: The energy ratio of two photons, E_2/E_1 ($E_1 > E_2$), was required to be larger than 0.2 to reduce the $K_L \to 2\pi^0$ background ("odd-pairing type" described in Sec. 6.4.1.2). This cut was also effective to eliminate the hadron-cluster background. The distributions of this variable are shown in Fig. 6.13c and Fig. 6.14b.

P_t/P_z-$Z_{\rm vtx}$, E-$Z_{\rm vtx}$: To select π^0's with plausible kinematics, we set allowed regions on P_t/P_z-$Z_{\rm vtx}$ and E-$Z_{\rm vtx}$ planes as shown in Fig. 6.15, where P_z and E are the longitudinal momentum and energy of the π^0, respectively.

projection angle: The opening angle of two photons projected in the x-y plane was required to be smaller than 150°. This cut eliminates the $K_L \to 2\gamma$ background, in which the photons are back-to-back and the angle is 180°. Figure. 6.16 shows the distribution of the projection angle in the $K_L \to \pi^0\nu\overline{\nu}$ and $K_L \to 2\gamma$ simulation sample. The distribution of this variable is also shown in Fig. 6.13d.

$E \cdot \theta$: The product of the energy and the angle between the beam axis and the momentum of a photon was required to be larger than 2500 MeV $\cdot$ deg. This cut is effective to reduce the odd-pairing type of the $K_L \to 2\pi^0$ background (described in Sec. 6.4.1.2). The distribution of this variable (smaller one of two photons) is shown in Fig. 6.17a.

dead channel: The photons' hit position were required to be more than 53 mm apart from dead channels. The distribution of this variable (smaller one of two photons) is shown in Fig. 6.17b.

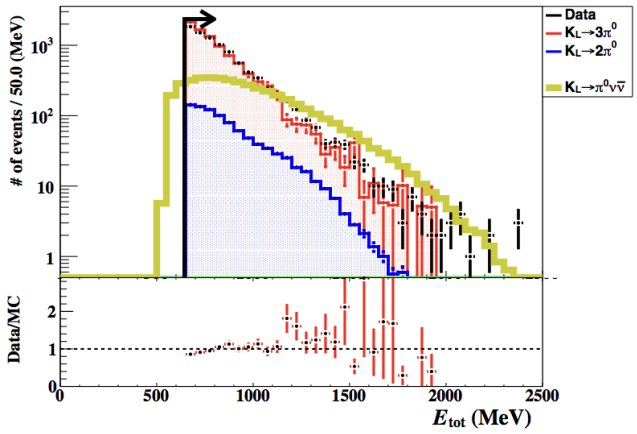

(a) total energy

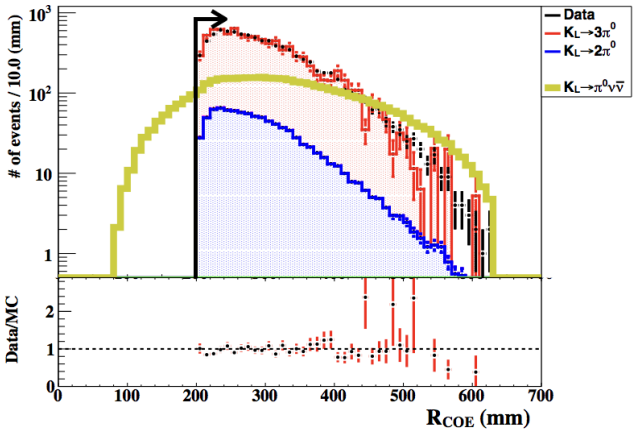

(b) COE

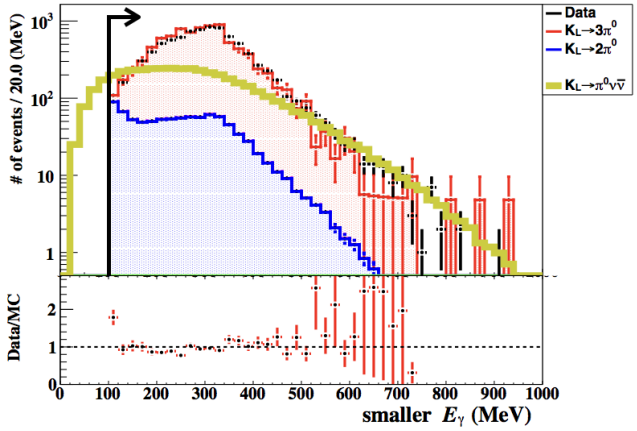

(c) photon energy (smaller)

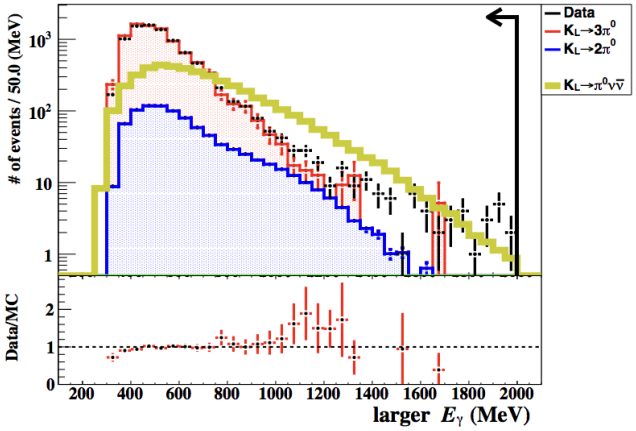

(d) photon energy (larger)

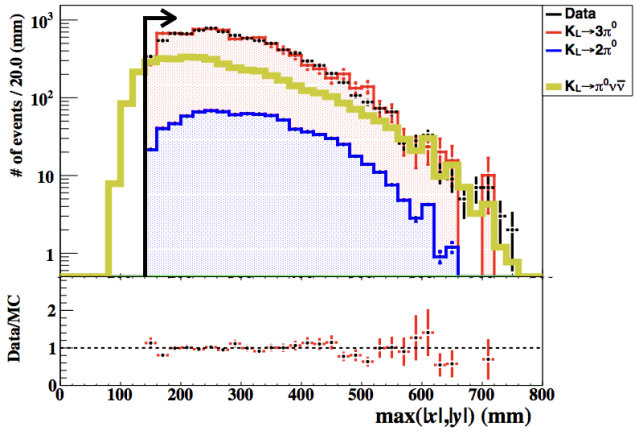

(e) photon position (inner)

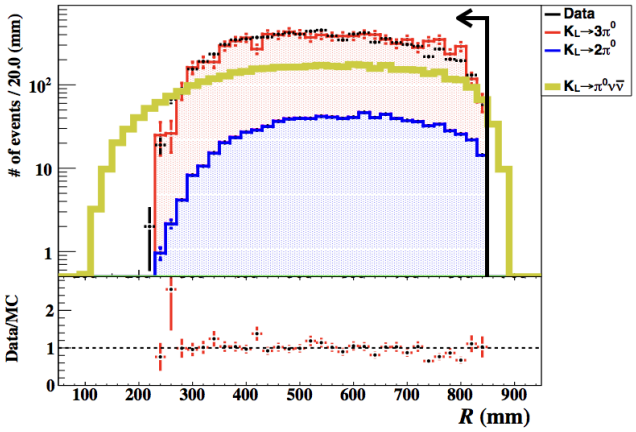

(f) photon position (outer)

Figure 6.12: Distributions of variables used for the trigger-related cuts and photon-selection cuts under a loose cut condition. $Z_{\mathrm{vtx}} > 2900$ mm is required to eliminate the contribution from the upstream-π^0 events. The black histograms represent the data and the red and blue ones represent the $K_L \to 3\pi^0$ (as stacked histograms) and $K_L \to 2\pi^0$ MC, respectively, which are normalized with the number of collected K_L's in the data. The yellow histograms represent the $K_L \to \pi^0\nu\overline{\nu}$ MC, whose vertical axis is in arbitrary units. All the trigger-related cuts and photon-selection cuts are applied on the data and the $K_L \to 3\pi^0$ and $K_L \to 2\pi^0$ MC, whereas they are not applied on the $K_L \to \pi^0\nu\overline{\nu}$ MC. In these plots, we used all the 2015 data including the events in the masked region. The black lines and arrows indicate the region accepted by the cuts. The data/MC ratios are shown below each panel. The error bars represent the statistical errors.

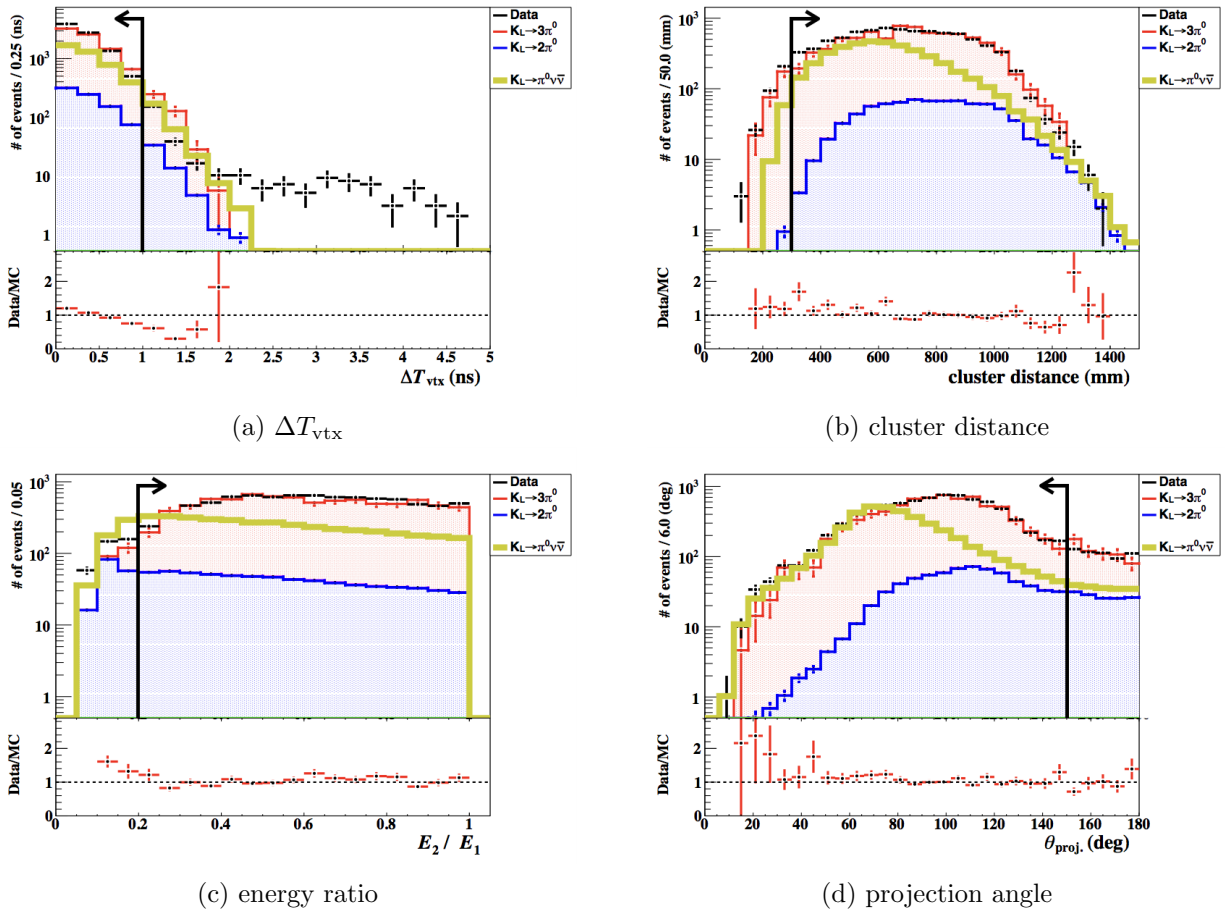

(a) $\Delta T_{\rm vtx}$

(b) cluster distance

(c) energy ratio

(d) projection angle

Figure 6.13: Distributions of variables used for the π^0 selection cuts under a loose cut condition. $Z_{\rm vtx} > 2900$ mm is required to eliminate the contribution from the upstream-π^0 events. The black histograms represent the data and the red and blue ones represent the $K_L \to 3\pi^0$ (as stacked histograms) and $K_L \to 2\pi^0$ MC, respectively, which are normalized with the number of collected K_L's in the data. The yellow histograms represent the $K_L \to \pi^0\nu\overline{\nu}$ MC, whose vertical axis is in arbitrary units. In these plots, we used all the 2015 data including the events in the masked region. The black lines and arrows indicate the region accepted by the cuts. The data/MC ratios are shown below each panel. The error bars represent the statistical errors.

6.3.1.4 Shape-Related Cuts

cluster size: Cluster size is defined as the number of constitutive crystals of the photon cluster. Hadronic showers made by neutrons tend to have a smaller cluster size due to larger dE/dx compared to electromagnetic showers. We required the cluster size of each photon to be 5 or more.

The cluster size distributions of $K_L \to \pi^0\nu\overline{\nu}$ MC sample and the hadron-cluster control sample mentioned in Sec. 3.2 are shown in Fig. 6.18a.

cluster RMS: Cluster RMS is defined as follows:

$$RMS_{\rm clus.} = \sqrt{\frac{\sum e_i r_i^2}{\sum e_i}}, \tag{6.11}$$

where e_i and r_i are energy and distance from the center of energy of the cluster of the i-th crystal in the cluster. We required $RMS_{\rm clus.} \geq 10$ mm to select well-spreading electromagnetic showers. The distribution of this variable is shown in Fig. 6.18b.

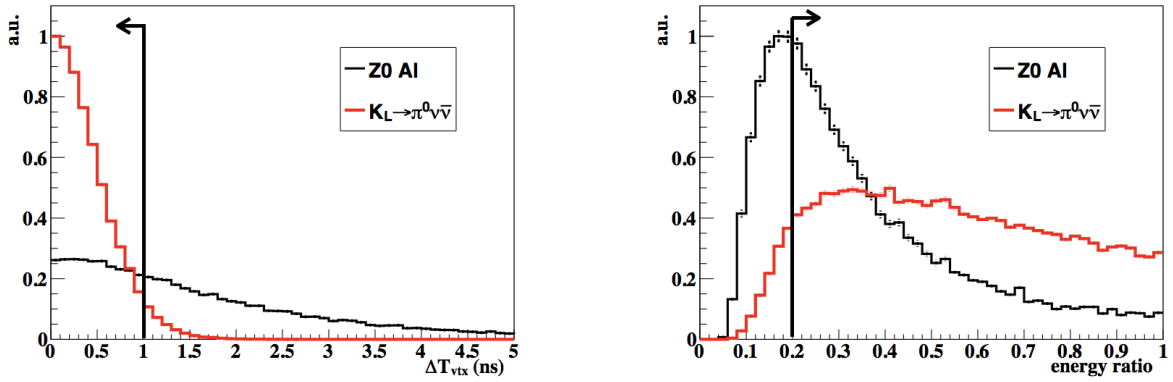

(a) $\Delta T_{\rm vtx}$ (b) energy ratio

Figure 6.14: Comparison of the $\Delta T_{\rm vtx}$ (left) and energy ratio (right) distributions between the Z0 Al data (the hadron-cluster events) and the $K_L \to \pi^0 \nu\overline{\nu}$ signal MC. The black lines and arrows indicate the region accepted by the cuts.

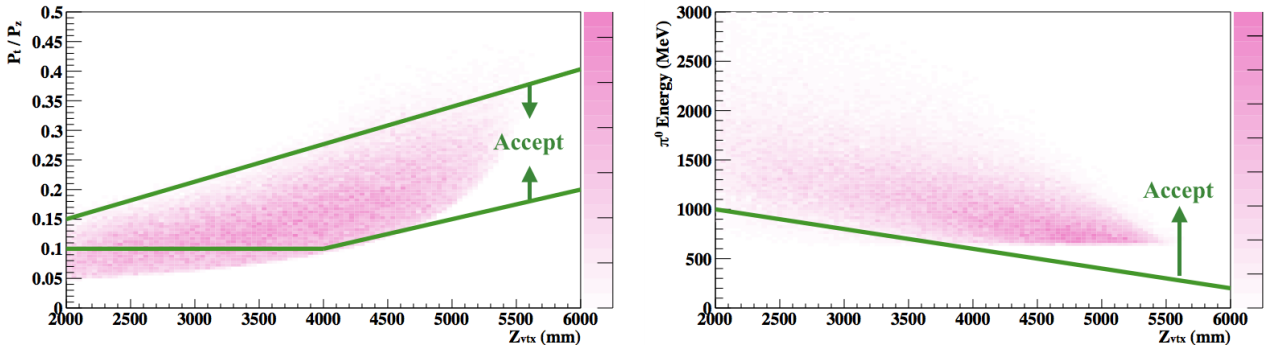

(a) P_t/P_z - $Z_{\rm vtx}$ (b) E_{π^0} - $Z_{\rm vtx}$

Figure 6.15: P_t/P_z-$Z_{\rm vtx}$ and E-$Z_{\rm vtx}$ selection. Distribution of the $K_L \to \pi^0 \nu\overline{\nu}$ events is shown with the accepted region bounded by green lines.

shape-χ^2: [*1] The shape-χ^2 evaluates the consistency of a shower shape with a template made by simulations. The templates were prepared with single photon simulations for various incident energies, angles, and positions. The $\chi^2_{\rm shape}$ is defined as follows:

$$\chi^2_{\rm shape} = \frac{1}{N} \sum_{i}^{27\times27} \left(\frac{e_i/E_\gamma - \mu_i}{\sigma_i} \right), \tag{6.12}$$

where E_γ is the energy of the photon, e_i is the energy of the i-th crystal, μ_i and σ_i are the expected mean and standard deviation of e_i/E_γ from a template, respectively. The summation is taken over 27×27 crystals around the center of the cluster.

This cut was originally developed to reduce the backgrounds caused by "fusion" cluster events, in which two photons hitting the CsI calorimeter close to each other are fused into a cluster. We found this cut was also greatly effective to reduce the hadron-cluster background events. The distribution of this variable is shown in Fig. 6.18c.

We required the $\chi^2_{\rm shape}$ to be less than 4.6 for each photon.

Detailed descriptions of the shape-χ^2 cut are found in Ref. [58].

[*1] This method was developed by K. Sato [58]

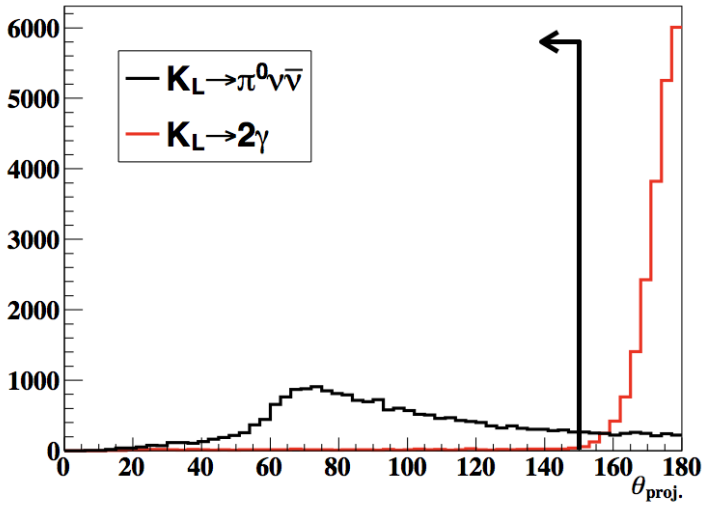

Figure 6.16: Projection angle distributions of simulated $K_L \to \pi^0 \nu\overline{\nu}$ and $K_L \to 2\gamma$ sample. The black line and arrow indicate the region accepted by the projection angle cut.

cluster shape NN: The cluster shape neural network (NN) cut was newly developed for the 2015 data analysis[*2] to eliminate the hadron-cluster background. As with the shape-χ^2 cut, this cut uses cluster shape information. The main difference from the shape-χ^2 is that the cluster shape NN cut uses timing information of the crystals in a cluster.

The neural network training was performed with the Z0 Al run data (see Sec. 3.2) for the hadronic shower sample and $K_L \to \pi^0 \nu\overline{\nu}$ MC for the electromagnetic shower sample.

The distribution of this variable is shown in Fig. 6.18d.

theta-χ^2: The theta-χ^2 method, which was newly developed for the 2015 data analysis[*3], evaluates the consistency of incident polar angle of photon obtained with two different methods: the π^0 reconstruction described in Sec. 4.2.3 and a neural network regression method. The neural network regression method uses the energy distribution in a cluster, the radial position of the photon, and the azimuthal angle of the photon obtained with the π^0 reconstruction as the input parameters, and was trained with simulated $K_L \to \pi^0 \nu\overline{\nu}$ events. The resolution of the obtained incident polar angle θ_{NN} was evaluated as shown in Fig. 6.19.

The consistency was quantified with χ^2_θ defined as

$$\chi^2_\theta = \frac{(\theta_{\rm rec} - \theta_{NN})^2}{\sigma^2_{\theta_{NN}}}, \tag{6.13}$$

where $\theta_{\rm rec}$ is the polar angle obtained with the π^0 reconstruction and $\sigma^2_{\theta_{NN}}$ is the angle resolution (in standard deviation) of θ_{NN}.

The distribution of this variable is shown in Fig. 6.18e. We required $\chi^2_\theta < 4.5$ for each photon.

eta-χ^2: We developed this cut to eliminate the CV-η background for the 2015 data analysis. Using the NN regression method in the theta-χ^2 cut, we evaluated the goodness of the assumption that two photons were produced at a common point on the CV front module. Details are described in Sec. 6.4.2.3.

We required the goodness of the CV-η assumption, χ^2_η, to be larger than 17.

[*2] This method was developed by Y. C. Tung [86]
[*3] This method was developed by Y. C. Tung [87]

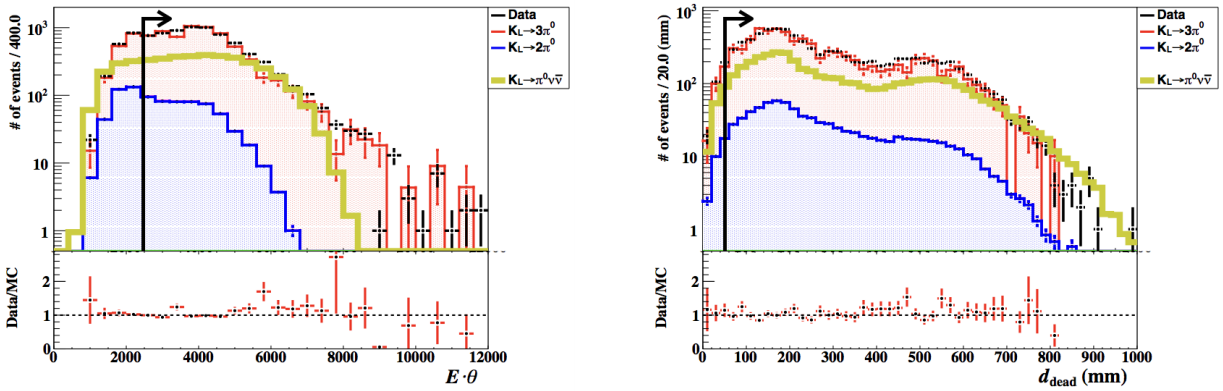

(a) $E \cdot \theta$

(b) dead channel

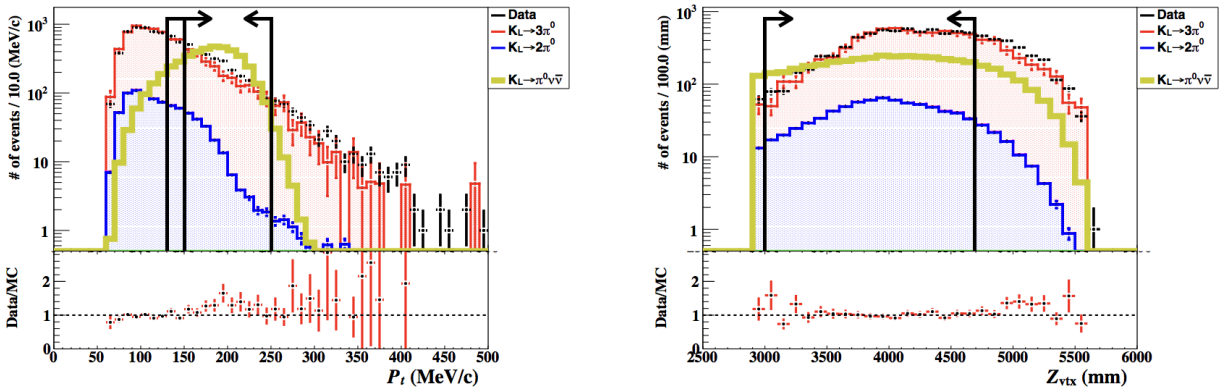

(c) P_t

(d) Z_{vtx}

Figure 6.17: Distributions of variables used for the π^0 selection cuts, P_t and Z_{vtx} under a loose cut condition. $Z_{\mathrm{vtx}} > 2900$ mm is required to eliminate the contribution from the upstream-π^0 events. The black histograms represent the data and the red and blue ones represent the $K_L \to 3\pi^0$ (as stacked histograms) and $K_L \to 2\pi^0$ MC, respectively, which are normalized with the number of collected K_L's in the data. The yellow histograms represent the $K_L \to \pi^0\nu\bar{\nu}$ MC, whose vertical axis is in arbitrary units. In these plots, we used all the 2015 data including the events in the masked region. The black lines and arrows indicate the region accepted by the cuts. The data/MC ratios are shown below each panel. The error bars represent the statistical errors.

pulse shape likelihood ratio: The pulse shape likelihood ratio cut was newly developed for the 2015 data analysis[*4]. This cut used waveforms of signals from the CsI calorimeter. We fitted the waveform with the following asymmetric Gaussian function:

$$A(t) = A \exp\left\{-\frac{(t-t_0)^2}{2\sigma(t)^2}\right\} + B, \tag{6.14}$$

where A, B, t_0 represent the peak height, baseline, and peak time of the waveform, respectively, and $\sigma(t) = \sigma_0 + a(t - t_0)$ represents the width of the waveform which depends on the timing difference from t_0.

The fitted σ_0 and a are compared with those for hadronic and electromagnetic shower values (template). The hadronic shower template was made from the Z0 Al run data and the electromagnetic shower template was made from $K_L \to 3\pi^0$ events. The templates were made as a function of pulse height, and an example is shown in Fig. 6.20. The likelihood for a crystal in a cluster L^{crystal} and for

[*4] This method was developed by Y. Sugiyama [69]

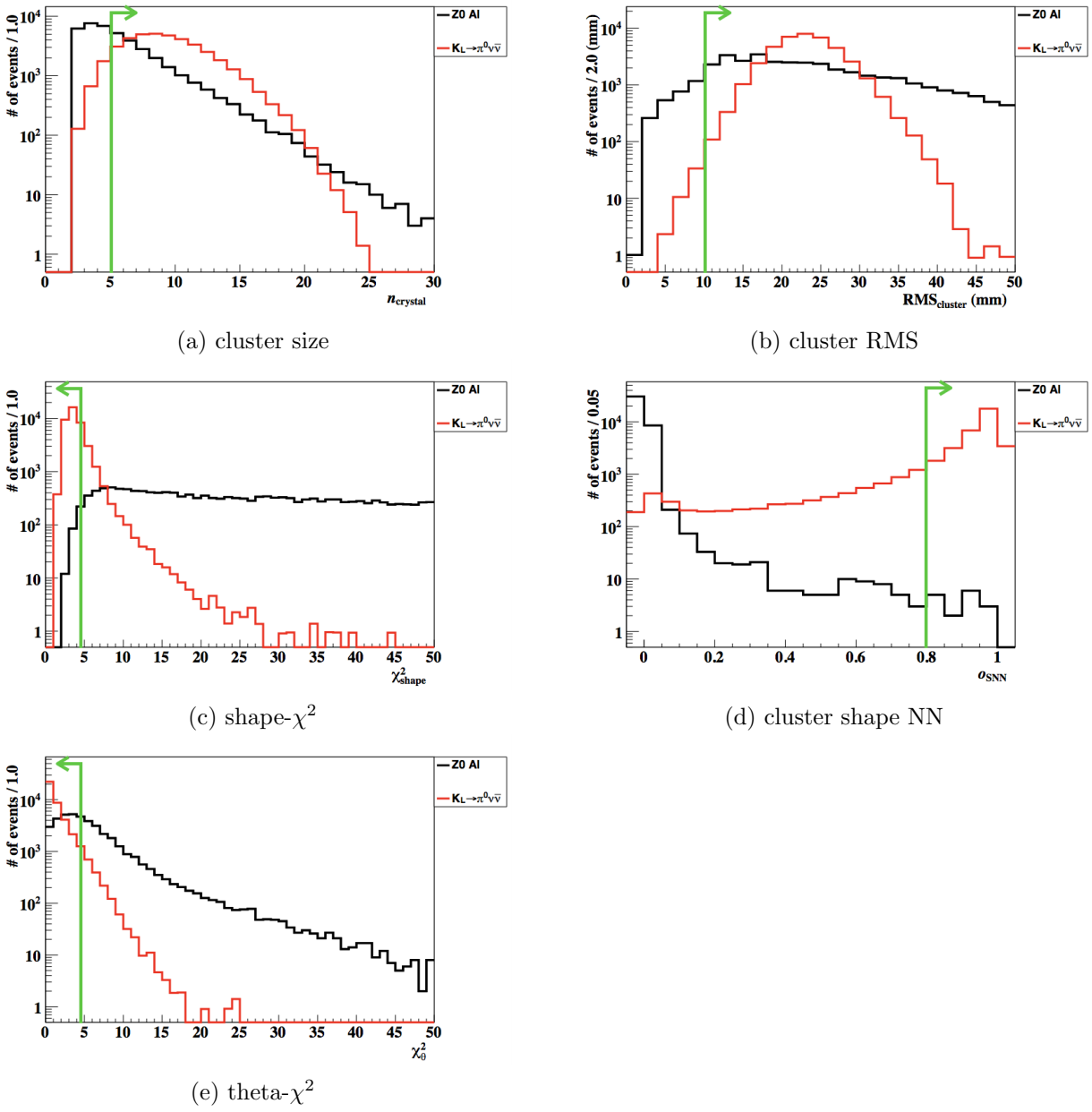

(a) cluster size

(b) cluster RMS

(c) shape-χ^2

(d) cluster shape NN

(e) theta-χ^2

Figure 6.18: Distributions of variables used for the shape-related cuts under a loose cut condition. $Z_{\rm vtx} > 2900$ mm is required to eliminate the contribution from the upstream-π^0 events. The black histograms represent the hadron-cluster control sample taken in the Z0 Al run and the red histograms represent the $K_L \to \pi^0 \nu\overline{\nu}$ MC. The green lines and arrows indicate the region accepted by the cuts.

a cluster $L^{\text{1-cluster}}$ were defined as follows:

$$L^{\text{crystal}} = \prod_{p}^{\sigma_0, a} \exp\left(-\frac{(p^{\text{meas.}} - p^{\text{exp.}}(H))^2}{2\sigma^2_{p^{\text{exp.}}(H)}}\right), \tag{6.15}$$

$$L^{\text{1-cluster}} = \prod_i L_i^{\text{crystal}}, \tag{6.16}$$

where p represents the parameters σ_0 and a, $p^{\text{meas.}}$ represents the parameters obtained by fitting the waveform of the crystal in the event, $p^{\text{exp.}}(H)$ and $\sigma_{p^{\text{exp.}}(H)}$ represent the mean and standard deviation of the template, respectively, as a function of peak height H. The likelihood for two cluster system is given by a product of $L^{\text{1-cluster}}$'s. The likelihoods are calculated for both hadronic and electromagnetic

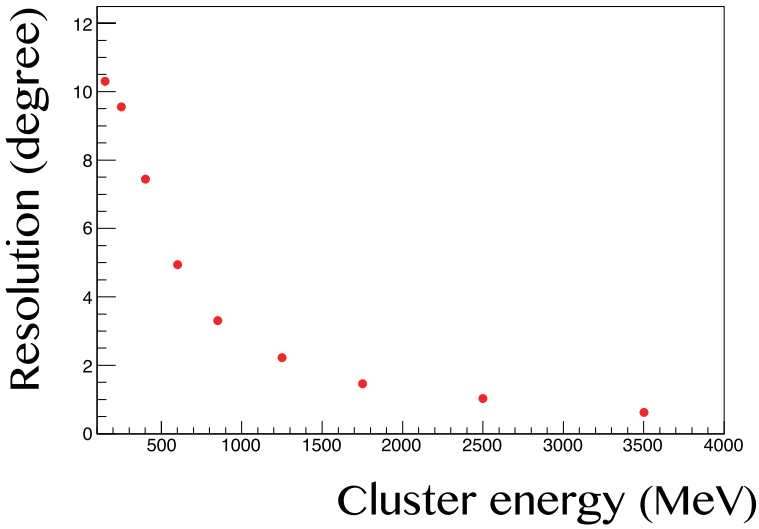

Figure 6.19: Resolution of θ_{NN} as a function of the energy of a photon. The vertical axis represents the resolution as a standard deviation. The figure is quoted from Ref. [87].

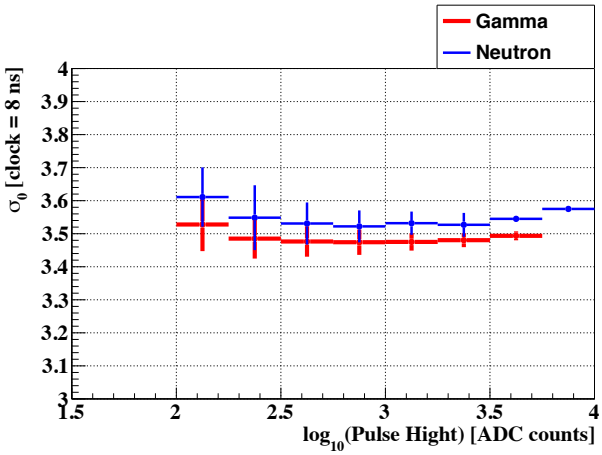

(a) Template of "a" parameter for a crystal (channel ID = 0) of the CsI calorimeter.

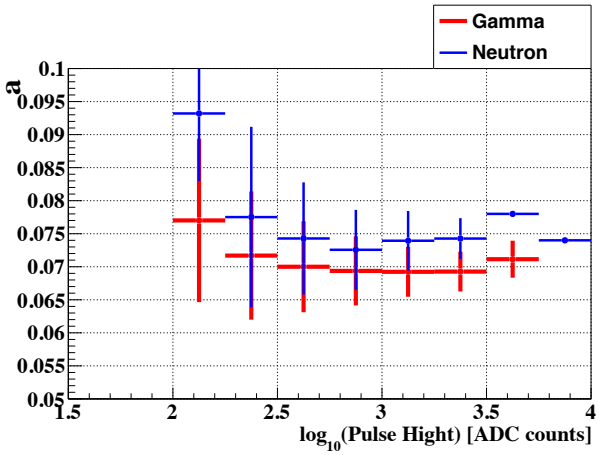

(b) Template of "σ_0" parameter for a crystal (channel ID = 0) of the CsI calorimeter.

Figure 6.20: Example of template parameters of "a" and "σ_0" used to calculate the pulse shape likelihood. Red and blue points represent the photon sample and hadron-cluster sample, respectively. The error bars represent the standard deviation of the parameters.

shower cases.

The likelihood ratio $R_{\gamma\gamma}^{\text{2-cluster}}$ is given as

$$R_{\gamma\gamma}^{\text{2-cluster}} = \frac{L_{\gamma\gamma}^{\text{2-cluster}}}{L_{\gamma\gamma}^{\text{2-cluster}} + L_{nn}^{\text{2-cluster}}}, \tag{6.17}$$

where $L_{\gamma\gamma}^{\text{2-cluster}}$ ($L_{nn}^{\text{2-cluster}}$) represents the likelihood for the assumption that the two showers are electromagnetic (hadronic) showers. We required $R_{\gamma\gamma}^{\text{2-cluster}} > 0.1$ for the signals. The $R_{\gamma\gamma}^{\text{2-cluster}}$ distributions of a π^0 sample obtained from a $K_L \to 2\pi^0$ sample and hadron-cluster control sample are shown in Fig. 6.21.

Detailed descriptions of the pulse shape likelihood ratio cut are found in Ref. [69].

In simulations, because we could not reproduce the pulse shape of the CsI calorimeter, we applied the efficiency factor on events as a function of energies of two photons. The efficiency map shown in

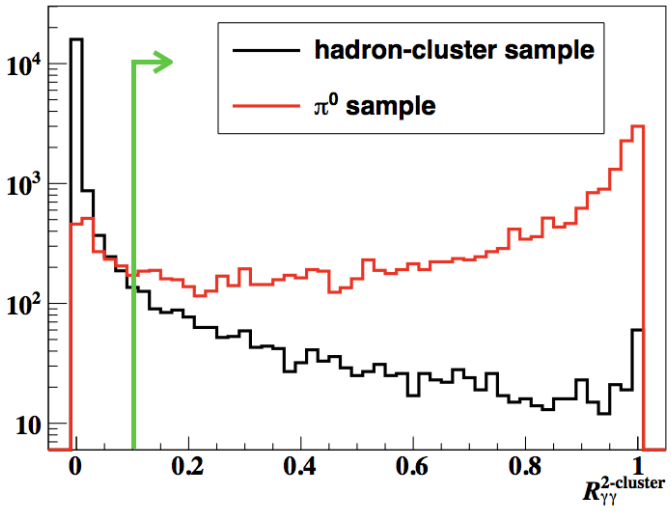

Figure 6.21: Distribution of the variable used for the pulse shape likelihood ratio cut. The black histogram represents the hadron-cluster control sample taken in the Z0 Al run and the red histogram represents a π^0 sample obtained with a $K_L \to 2\pi^0$ sample. The green lines and arrows indicate the accepted region by the cuts.

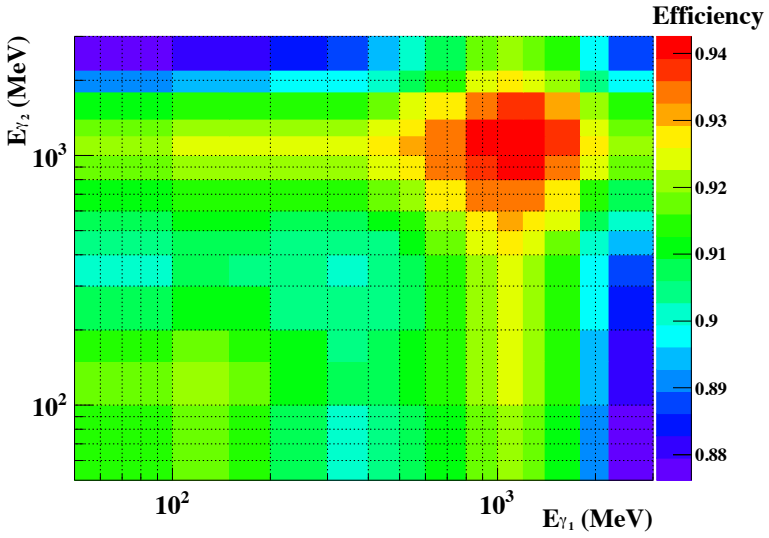

Figure 6.22: Efficiency map of the pulse shape likelihood ratio cut as a function of two photons' energies.

Fig. 6.22 was obtained with a π^0 sample from $K_L \to 3\pi^0$. The average acceptance for the $K_L \to \pi^0\nu\overline{\nu}$ signal events was estimated to be about 90%.

6.3.2 Veto Cuts

We required the absence of any particles other than a π^0 to identify the $K_L \to \pi^0\nu\overline{\nu}$ and $K_L \to \pi^0 X^0$ decays. Events were rejected if there were any extra hits in the veto counters or in the CsI calorimeter coincident with the π^0 decay. As described in Sec. 6.2.3, the same veto cut condition used in the normalization modes analysis were used for the $K_L \to \pi^0\nu\overline{\nu}$ and $K_L \to \pi^0 X^0$ selection.

Distributions of veto-energy and veto-time of MB and NCC under a loose cut condition are shown in Fig. 6.23. Peaks in the veto-time distributions of data are dominated by the hits of photons associated

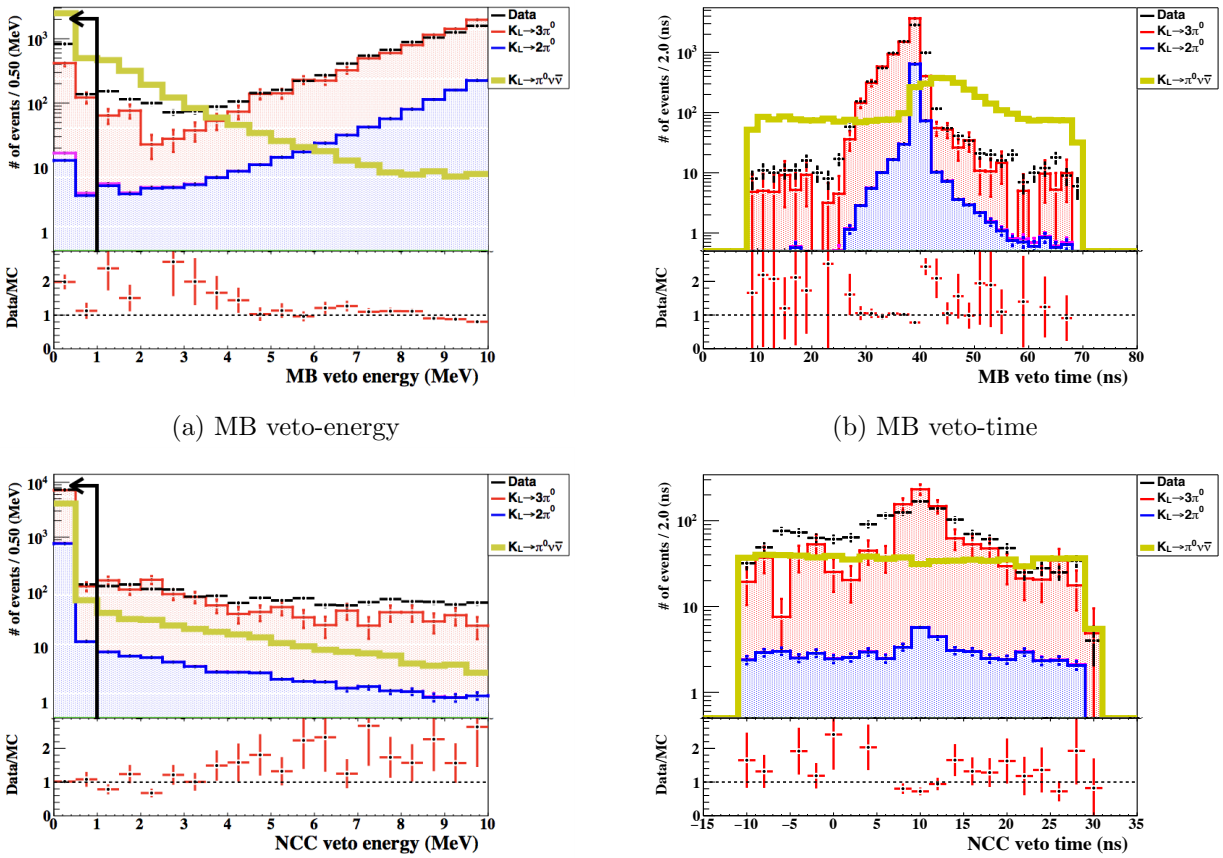

(a) MB veto-energy

(b) MB veto-time

(c) NCC veto-energy

(d) NCC veto-time

Figure 6.23: Distributions of variables used for the veto cuts. The black histograms represent the data and the red and blue ones represent the $K_L \to 3\pi^0$ (as a stacked histogram) and $K_L \to 2\pi^0$ MC, respectively, which are normalized with the number of collected K_L's in the data. The yellow histograms represent the $K_L \to \pi^0\nu\overline{\nu}$ MC, whose vertical axis is in arbitrary units. The black lines and arrows in veto-energy plots represent the veto energy thresholds. In the veto-timing plots, veto-energy larger than 1 MeV is required and only the events with the veto-time in the veto window are shown. The data/MC ratios are shown below each panel. The error bars represent the statistical errors.

with the two photons hitting the CsI calorimeter, whereas the tails are dominated by accidental activities. As for the $K_L \to \pi^0\nu\overline{\nu}$ events, activities in veto counters are due to accidental activities and shower leakage from the CsI calorimeter. A peak in MB veto-timing distribution represents the shower leakage events. Such a peak are not present for NCC since it is far from the CsI calorimeter.

6.3.3 Signal Region

We defined the signal region on the P_t-$Z_{\rm vtx}$ plane.

In considering the $Z_{\rm vtx}$ region, key components are the upstream-π^0 and hadron-cluster backgrounds. The upstream-π^0 events distribute around $Z_{\rm vtx} \sim 2500$ mm where NCC is located, while the hadron-cluster events distribute downstream. The $Z_{\rm vtx}$ distributions of the upstream-π^0 MC sample, the hadron-cluster control sample, and the $K_L \to \pi^0\nu\overline{\nu}$ MC sample are shown in Fig. 6.24. To suppress the background level while keeping the signal acceptance as large as possible, we determined the signal region to be $3000 < Z_{\rm vtx} < 4700$ mm.

As for the P_t selection, a key component is the $K_L \to \pi^+\pi^-\pi^0$ background. As shown in Fig. 6.25, the $K_L \to \pi^+\pi^-\pi^0$ events distribute in the low P_t region, and their P_t has a correlation with $Z_{\rm vtx}$ (Fig. 6.38). We determined the lower P_t boundary to avoid the $K_L \to \pi^+\pi^-\pi^0$ background as

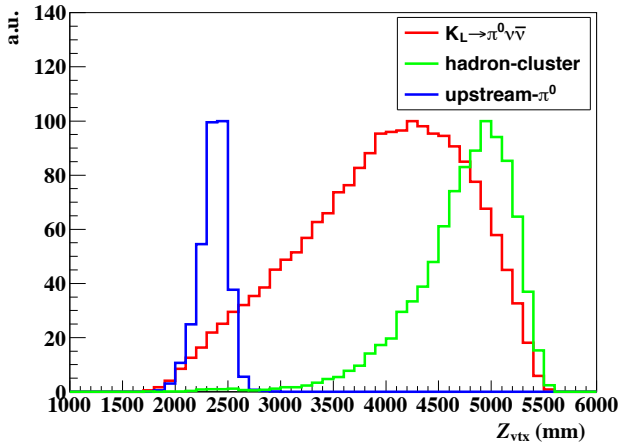

Figure 6.24: $Z_{\rm vtx}$ distributions of the $K_L \to \pi^0 \nu\overline{\nu}$ MC, hadron-cluster control sample, and upstream-π^0 MC.

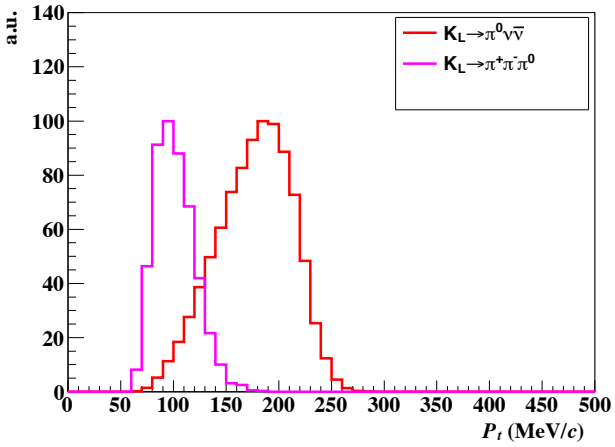

Figure 6.25: P_t distributions of the $K_L \to \pi^0 \nu\overline{\nu}$ and $K_L \to \pi^+ \pi^- \pi^0$ MC.

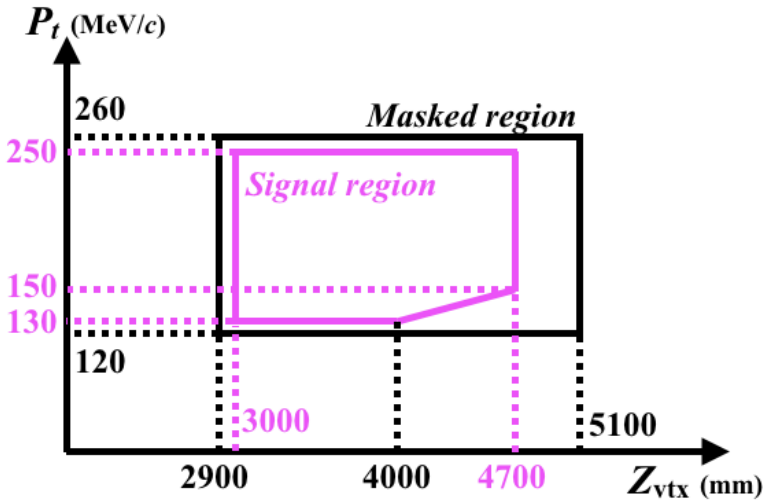

Figure 6.26: Definition of the signal region (surrounded by magenta lines) and the masked region (by black lines).

straight lines connecting $(Z_{\rm vtx}({\rm mm}), P_t({\rm MeV}/c)) = (3000, 130)$, $(4000, 130)$, and $(4700, 150)$. The upper boundary of 250 MeV/c was determined with the signal distribution.

Consequently, the signal region was determined as shown in Fig. 6.26.

The distribution of P_t and $Z_{\rm vtx}$ under a loose cut condition are shown in Fig. 6.17c and Fig. 6.17d. They are dominated by the $K_L \to 3\pi^0$ and $K_L \to 2\pi^0$ decays.

6.3.4 Data Reduction

We collected 4.3×10^9 events to search for the $K_L \to \pi^0 \nu\overline{\nu}$ and $K_L \to \pi^0 X^0$ decays in 2015. To select signal candidate events, we imposed a series of cuts explained in the previous sections. The data reduction by each cut category is summarized in Table 6.6. The veto cuts have a large reduction of three orders of magnitude, although the online veto is already imposed in the trigger stage.

Table 6.6: Data reduction in each of the selection criteria.

selection criteria	number of events
triggered events	4.31×10^9
two cluster selection	8.74×10^8
trigger-related cuts	2.50×10^8
photon selection cuts	1.75×10^8
π^0 kinematic cuts	3.59×10^7
veto cuts	3.83×10^4
shape-related cuts	347

Table 6.7: Summary of the signal acceptance for the $K_L \to \pi^0\nu\overline{\nu}$ decay and the single event sensitivity. The $A_{\rm sig}$ includes the decay probability of 3.18%.

run-period	$A_{\rm sig}$	N_{K_L} at the beam exit	SES
Period-1	2.80×10^{-4}	1.39×10^{11}	2.57×10^{-8}
Period-2	2.66×10^{-4}	2.37×10^{11}	1.58×10^{-8}
Period-3	2.39×10^{-4}	1.15×10^{11}	3.66×10^{-8}
Period-4	1.48×10^{-4}	1.49×10^{11}	4.55×10^{-8}
Period-5	1.31×10^{-4}	4.95×10^{11}	1.54×10^{-8}
Period-6	2.03×10^{-4}	1.72×10^{11}	2.86×10^{-8}
Period-7	1.57×10^{-4}	5.82×10^{11}	1.10×10^{-8}
Period-8	1.61×10^{-4}	6.50×10^{11}	9.58×10^{-9}
Period-9	1.52×10^{-4}	2.14×10^{12}	3.09×10^{-9}
total		4.68×10^{12}	1.30×10^{-9}

6.3.5 Signal Acceptance and Single Event Sensitivity

The signal acceptance ($A_{\rm sig}$) for the $K_L \to \pi^0\nu\overline{\nu}$ decay is obtained by imposing all the cuts and efficiency weights to the signal MC. The single event sensitivity (SES) is obtained as

$$\mathrm{SES} = \frac{1}{A_{\rm sig} \times (\text{the number of } K_L(N_{K_L}) \text{ at the beam exit})}. \tag{6.18}$$

The values of "N_{K_L} at the beam exit" are obtained from the normalization modes analysis summarized in Table. 6.4. The results of the signal acceptances and single event sensitivities for each run-period are summarized in Table. 6.7. Here, $A_{\rm sig}$ includes the K_L decay probability of 3.18% in $3000 < Z_{\rm vtx} < 4700$ mm. The breakdown of $A_{\rm sig}$ is shown in Fig. 6.27 and Table 6.8. The differences among run-periods are derived from the difference in acceptances of veto cuts, which depend on beam intensity. The smallness of acceptances in Period-4 and Period-5 reflects the bad beam condition due to the Exciter setting with narrow bandwidth mentioned in Sec. 3.4.2.

The single event sensitivity for the $K_L \to \pi^0\nu\overline{\nu}$ decay with the whole 2015 data is obtained as $(1.30 \pm 0.01_{\rm stat.}) \times 10^{-9}$, where the error is derived from the number of reconstructed $K_L \to 2\pi^0$ events. This sensitivity is approximately an order of magnitude better than that of the E391a experiment [11] and the KOTO 2013 results [10].

6.3.6 Systematic Uncertainty of Single Event Sensitivity

We used MC simulations to evaluate the single event sensitivity for the $K_L \to \pi^0\nu\overline{\nu}$ decay. Hence the discrepancies between data and MC should be taken into account as systematic uncertainties. In considering the systematic uncertainty of the single event sensitivity, the ratio of acceptances for $K_L \to 2\pi^0$ and $K_L \to \pi^0\nu\overline{\nu}$, $A_{\rm norm}/A_{\rm sig}$, plays an essential role as shown in Eq. 6.3. By taking the ratio

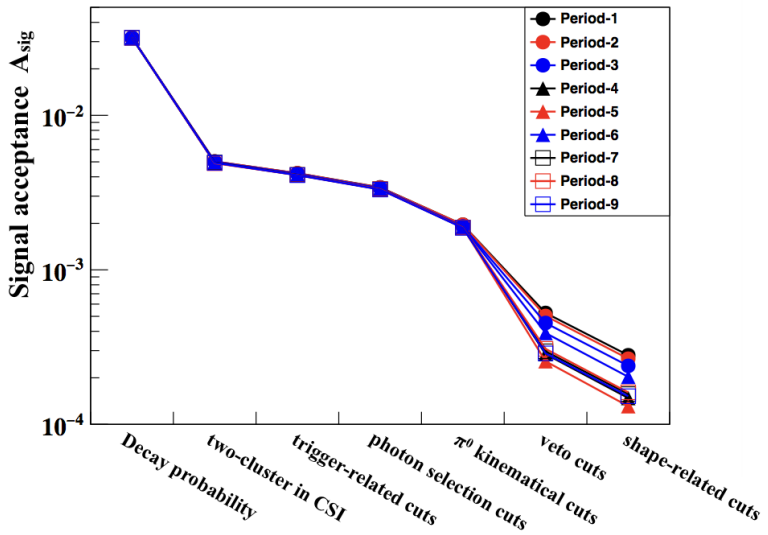

Figure 6.27: Breakdown of the signal acceptance in stages of cuts. Acceptances in each run-period are shown in different lines.

of acceptances, we expect that some uncertainties are canceled each other if they are common to both decays.

The acceptances can be broken down as follows:

$$A_{\rm norm} = A^{\rm norm}_{\rm geom.} \times A^{\rm norm}_{\rm trigger} \times A^{\rm norm}_{\gamma} \times A^{\rm norm}_{\rm kine.} \times A^{\rm norm}_{\rm veto}, \tag{6.19}$$

$$A_{\rm sig} = A^{\rm sig}_{\rm geom.} \times A^{\rm sig}_{\rm trigger} \times A^{\rm sig}_{\gamma} \times A^{\rm sig}_{\rm kine.} \times A^{\rm sig}_{\rm veto} \times A^{\rm sig}_{\rm shape}, \tag{6.20}$$

where $A_{\rm geom.}$ represents the geometrical acceptance, $A_{\rm trigger}$, A_{γ}, $A_{\rm kine.}$, $A_{\rm veto}$, and $A_{\rm shape}$ represent those for corresponding cuts. The uncertainties derived from these subdivided acceptances are described in the following sections.

In addition, we considered the statistical error of the $K_L \to \pi^0\nu\overline{\nu}$ MC (0.36%), the error of $K_L \to 2\pi^0$ purity in the normalization modes analysis (0.38%), and the error in the $K_L \to 2\pi^0$ branching fraction (0.69% [15]) as sources of the uncertainty. Inconsistency among K_L yields measured with three normalization modes (5.6%) was also added to the uncertainty.

The results of the estimation of systematic uncertainties of each source are summarized in Table 6.9. All the uncertainties were combined as their quadratic sum and it was found to be 11%. Consequently, the single event sensitivity for the $K_L \to \pi^0\nu\overline{\nu}$ decay with uncertainties is

$$(1.30 \pm 0.01_{\rm stat.} \pm 0.14_{\rm syst.}) \times 10^{-9}. \tag{6.21}$$

6.3.6.1 Uncertainty from Geometrical Acceptance

Here we define the geometrical acceptance as the probability that a K_L entering the detector from the beam exit decays within z range of $3000 < z < 4700$ mm and both ($K_L \to \pi^0\nu\overline{\nu}$) or all four ($K_L \to 2\pi^0$) photons from the π^0('s) hit the CsI calorimeter.

We considered the uncertainty of the geometrical acceptance arises from the deviation of the acceptance ratio $A^{\rm norm}_{\rm geom.}/A^{\rm sig}_{\rm geom.}$ when the actual K_L momentum spectrum was varied from one model.

As already described in Sec. 5.1.1, the K_L momentum spectrum used in MC is written as

$$f(p,\vec{a}) = \exp\left\{-\frac{(p-\mu)^2}{2(\sigma_0(1-(A+Sp)(p-\mu)))^2}\right\}, \tag{6.22}$$

Table 6.8: Breakdown of the signal acceptance in stages of cuts. The percentages in parentheses represent the relative acceptances to the previous (left) stage.

run-period	A_{decay}	$A_{\text{2-cluster}}$	A_{trigger}	A_{photon}	$A_{\pi^0\text{kine.}}$	A_{veto}	A_{shape}
Period-1	3.18%	5.03×10^{-3}	4.22×10^{-3}	3.42×10^{-3}	1.96×10^{-3}	5.26×10^{-4}	2.80×10^{-4}
		(15.8%)	(83.9%)	(81.0%)	(57.3%)	(26.8%)	(53.2%)
Period-2	3.18%	5.03×10^{-3}	4.22×10^{-3}	3.41×10^{-3}	1.96×10^{-3}	5.03×10^{-4}	2.66×10^{-4}
		(15.8%)	(83.9%)	(80.8%)	(57.5%)	(25.7%)	(52.9%)
Period-3	3.18%	5.00×10^{-3}	4.18×10^{-3}	3.38×10^{-3}	1.91×10^{-3}	4.53×10^{-4}	2.39×10^{-4}
		(15.7%)	(83.6%)	(80.9%)	(56.5%)	(23.7%)	(52.8%)
Period-4	3.18%	4.94×10^{-3}	4.12×10^{-3}	3.33×10^{-3}	1.88×10^{-3}	2.85×10^{-4}	1.48×10^{-4}
		(15.5%)	(83.4%)	(80.8%)	(56.5%)	(15.2%)	(51.9%)
Period-5	3.18%	4.93×10^{-3}	4.10×10^{-3}	3.32×10^{-3}	1.88×10^{-3}	2.56×10^{-4}	1.31×10^{-4}
		(15.5%)	(83.2%)	(81.0%)	(56.6%)	(13.6%)	(51.2%)
Period-6	3.18%	4.98×10^{-3}	4.16×10^{-3}	3.36×10^{-3}	1.90×10^{-3}	3.90×10^{-4}	2.03×10^{-4}
		(15.7%)	(83.5%)	(80.8%)	(56.5%)	(20.5%)	(52.1%)
Period-7	3.18%	4.95×10^{-3}	4.12×10^{-3}	3.33×10^{-3}	1.88×10^{-3}	2.97×10^{-4}	1.57×10^{-4}
		(15.6%)	(83.2%)	(80.8%)	(56.5%)	(15.8%)	(52.9%)
Period-8	3.18%	4.90×10^{-3}	4.11×10^{-3}	3.33×10^{-3}	1.88×10^{-3}	3.08×10^{-4}	1.61×10^{-4}
		(15.4%)	(83.9%)	(81.0%)	(56.5%)	(16.4%)	(52.3%)
Period-9	3.18%	4.93×10^{-3}	4.10×10^{-3}	3.31×10^{-3}	1.87×10^{-3}	2.88×10^{-4}	1.52×10^{-4}
		(15.5%)	(83.2%)	(80.7%)	(56.5%)	(15.4%)	(52.8%)

Table 6.9: Summary of relative systematic uncertainties in the single event sensitivity.

source	uncertainty [%]
trigger efficiency	1.9
photon selection cuts	0.81
kinematic cuts for $K_L \to \pi^0\nu\overline{\nu}$	5.1
veto cuts	3.7
shape-related cuts	5.1
$K_L \to \pi^0\nu\overline{\nu}$ MC statistics	0.36
K_L momentum spectrum	1.1
kinematic cuts for $K_L \to 2\pi^0$	2.7
$K_L \to 2\pi^0$ purity	0.38
$K_L \to 2\pi^0$ branching fraction	0.69
normalization modes inconsistency	5.6
total	11

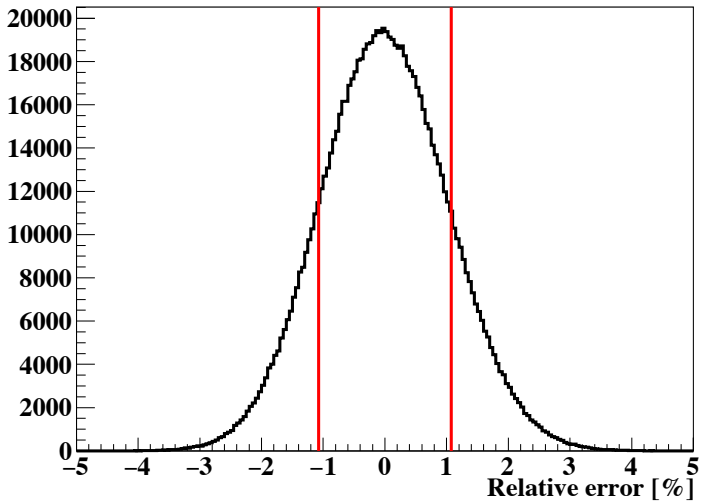

Figure 6.28: Relative deviation of geometrical acceptance ratio in various K_L momentum parameters. Red lines represent 1σ region in this distribution.

where p is momentum in units of GeV/c and $\vec{a}^T = (\mu, \sigma_0, A, S)$ is a parameter vector [58][*5]. The parameters used in simulations are $\vec{a_0}^T = (1.41991, 0.810237, -0.301413, 0.017092)$. The variance-covariance matrix V for the parameters (μ, σ_0, A, S) is given as follows [67]:

$$V = \begin{pmatrix} 0.0014402 & 0.000629142 & 0.00133248 & -0.000170238 \\ 0.000629142 & 0.00103403 & 0.00126643 & -0.000127379 \\ 0.00133248 & 0.00126643 & 0.00216038 & -0.000264671 \\ -0.000170238 & -0.000127379 & -0.000264671 & 0.000035702 \end{pmatrix}. \tag{6.23}$$

To calculate the change of the acceptance ratio, we varied the parameters from $\vec{a_0}$ with Gaussian by taking into account the correlation among the parameters represented by V.

In order to shorten the process time, we adopted "re-weighting method" instead of re-processing simulations with different K_L momentum spectrums. In the re-weighting method, we first prepared geometrical acceptances for $K_L \to \pi^0\nu\overline{\nu}$ and $K_L \to 2\pi^0$, $\rho^{\rm sig}_{\rm geom.}(p)$ and $\rho^{\rm norm}_{\rm geom.}(p)$, as a function of K_L momentum p with a simulation. The acceptance ratio with the momentum spectrum $f(p, \vec{a})$ is then given by

$$A^{\rm norm}_{\rm geom.}(\vec{a}) / A^{\rm sig}_{\rm geom.}(\vec{a}) = \frac{\int f(p, \vec{a}) \rho^{\rm norm}_{\rm geom.}(p) dp}{\int f(p, \vec{a}) \rho^{\rm sig}_{\rm geom.}(p) dp}. \tag{6.24}$$

The distribution of the relative deviation of the acceptance ratio with 10^6 trials with various $\vec{a}$ is shown in Fig. 6.28. The systematic uncertainty of 1.1% was obtained with $1\sigma = 68.27\%$ region in this distribution. This contribution is counted as "K_L momentum spectrum" in Table 6.9.

6.3.6.2 Uncertainty from the trigger-related cuts (trigger efficiency)

The uncertainties from total energy cut and COE cut were evaluated in the kinematic cuts category for technical reasons. As for trigger timing cut and CSI Et trigger efficiency, the cut acceptance and the efficiency are almost 100%, so that the effects on the systematic uncertainty are expected to be negligibly small. For the above reasons, here we consider only the COE trigger efficiency.

The COE trigger efficiency was not considered in the normalization modes analysis because the Normalization trigger does not utilize the COE trigger decision. We evaluated the uncertainty from the

[*5] The values of the parameters are slightly different from those in Ref. [58].

COE trigger efficiency by examining the agreement between data and MC using a validation sample: two-photon events outside the signal region taken with the Normalization trigger after applying loose selection cuts. The $R^{2\gamma}_{\rm COE}$ distributions before and after imposing COE trigger decision (for data) or COE efficiency weight (for MC) are shown in Fig. 6.29. The data and MC agree well both before and after imposing the COE cut or the efficiency weight. The efficiency of COE trigger decision for data ($\epsilon_{\rm data}$) was 89.6% and the efficiency obtained from COE efficiency weight for MC ($\epsilon_{\rm MC}$) was 91.3%. The discrepancy between data and MC, namely $\epsilon_{\rm MC}/\epsilon_{\rm data} - 1 = 1.9\%$, was counted as the systematic uncertainty from the COE trigger efficiency.

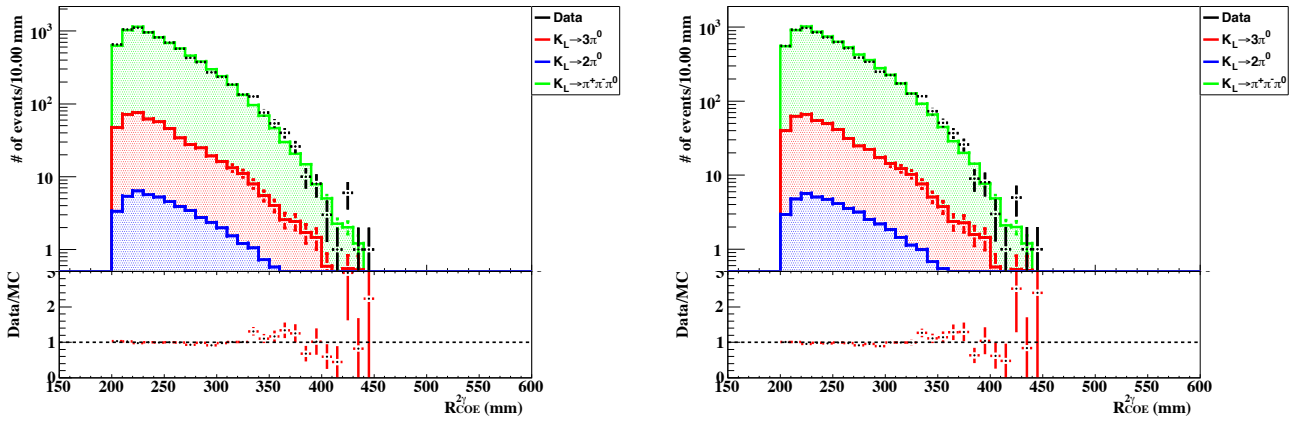

Figure 6.29: $R^{2\gamma}_{\rm COE}$ distributions of a validation sample before (left) and after (right) imposing the COE trigger decision. For MC, the COE efficiency is applied instead. Black points represent data and colored histograms represent MC. The data/MC ratios are shown below each panel. The error bars represent the statistical errors.

6.3.6.3 Uncertainty from the photon selection cuts

The uncertainty from the photon selection cuts was evaluated by using a validation π^0 sample which was made from a reconstructed $K_L \to 2\pi^0$ sample without the photon selection cuts imposed. The difference of cut acceptances between data and MC, $A^{i\text{-th cut}}_{\rm MC}/A^{i\text{-th cut}}_{\rm data} - 1$, was regarded as the uncertainty due to the i-th cut. The quadratic sum of the uncertainties of all the photon selection cuts was calculated to be 0.81%.

6.3.6.4 Uncertainty from the kinematic cuts

The uncertainties from the π^0 kinematic cuts for $K_L \to \pi^0\nu\overline{\nu}$ and K_L kinematic cuts for $K_L \to 2\pi^0$ were considered separately because they were completely different.

As for $K_L \to \pi^0\nu\overline{\nu}$, we estimated the uncertainty using a validation sample[*6] which was obtained from the reconstructed $K_L \to 2\pi^0$ sample. Using each pair of photons forming a π^0, we re-reconstructed a π^0 assuming the vertex to be on the beam axis as the same manner in the $K_L \to \pi^0\nu\overline{\nu}$ analysis. We compared the acceptances of each cut between data and MC, $A^{i\text{-th cut}}_{\rm data}$ and $A^{i\text{-th cut}}_{\rm MC}$ as shown in Fig. 6.30 and summarized in Table 6.10. Distributions of π^0 kinematic cut variables are also shown in Fig. 6.31 and Fig. 6.32. The largest discrepancy was in the $\Delta T_{\rm vtx}$ cut (Fig. 6.31a). We regarded $A^{i\text{-th cut}}_{\rm MC}/A^{i\text{-th cut}}_{\rm data} - 1$ as the uncertainty due to the i-th cut. By taking the quadratic sum over all the kinematic cuts and then averaging them over all the run-periods, the total uncertainty from the kinematic cuts for $K_L \to \pi^0\nu\overline{\nu}$ was 5.1%. Note that the uncertainty due to the selections for the signal region (requirements on P_t and $Z_{\rm vtx}$) and, as mentioned in Sec. 6.3.6.2, the total energy cut and COE cut were taken into account in this category.

[*6] Different from the validation sample used in Sec. 6.3.6.2.

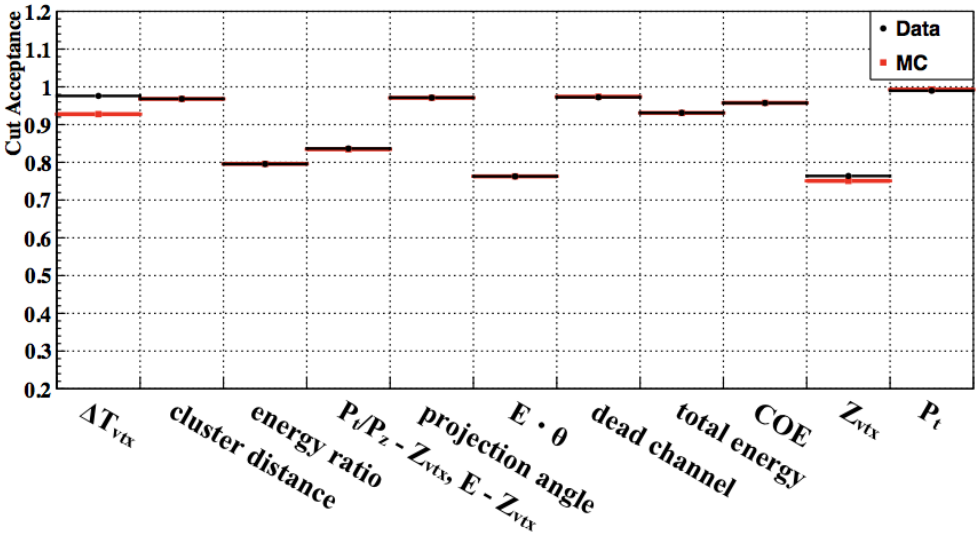

Figure 6.30: Acceptance of the π^0 kinematic cuts for the validation sample. Black and red points represent data and MC, respectively. This plot is based on the Period-9 data.

Table 6.10: Acceptance of the π^0 kinematic cuts for the validation sample. The values are based on the Period-9 data.

source	$A^{i\text{-th cut}}_{\text{data}}$	$A^{i\text{-th cut}}_{\text{MC}}$	$A^{i\text{-th cut}}_{\text{MC}}/A^{i\text{-th cut}}_{\text{data}} - 1$
ΔT_{vtx}	0.976	0.928	-4.95%
cluster distance	0.968	0.968	-0.03%
energy ratio	0.796	0.796	0.05%
P_t/P_z-Z_{vtx}, E-Z_{vtx}	0.837	0.835	-0.25%
projection angle	0.971	0.971	-0.04%
$E \cdot \theta$	0.763	0.763	0.01%
dead channel	0.972	0.974	0.16%
total energy	0.931	0.931	-0.03%
COE	0.957	0.958	0.04%
Z_{vtx}	0.769	0.751	-1.71%
P_t	0.990	0.993	0.32%
quadratic sum			5.3%

As for $K_L \to 2\pi^0$, the difference of cut acceptances between the data and MC was evaluated as systematic uncertainty. Here the cut acceptance ($A^{i\text{-th cut}}_{\text{MC(data)}}$) was defined for each cut with the fraction of remaining events after all the cuts were imposed, to those after all the cuts but other than the cut of interest were imposed. By taking the quadratic sum over all the kinematic cuts and then averaging them over all the run-periods, the total uncertainty from the kinematic cuts for $K_L \to 2\pi^0$ was 2.7%.

6.3.6.5 Uncertainty from the veto cuts

Here, we define the veto cut acceptance for each veto cut as the fraction of remaining events after all the veto cuts are imposed, to those after all the other veto cuts are imposed. The uncertainty from the veto cuts was evaluated by taking double ratio (DR) of veto cut acceptances between data and MC, and between $K_L \to 2\pi^0$ and $K_L \to 2\gamma$ as

$$DR^i = \frac{A^i_{K_L\to 2\pi^0\text{MC}}/A^i_{K_L\to 2\pi^0\text{Data}}}{A^i_{K_L\to 2\gamma\text{MC}}/A_{K_L\to 2\gamma\text{Data}}}, \tag{6.25}$$

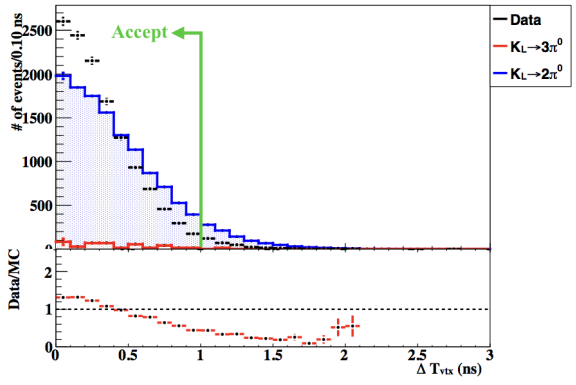

(a) ΔT_{vtx}

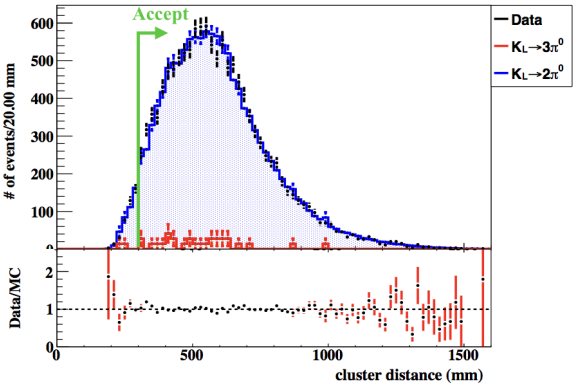

(b) cluster distance

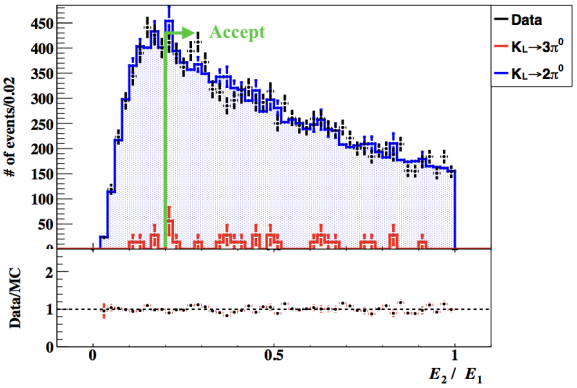

(c) energy ratio

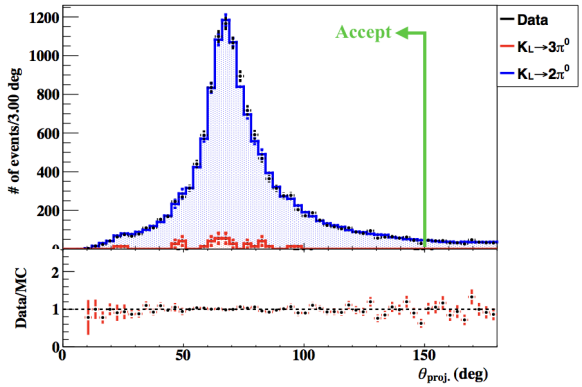

(d) projection angle

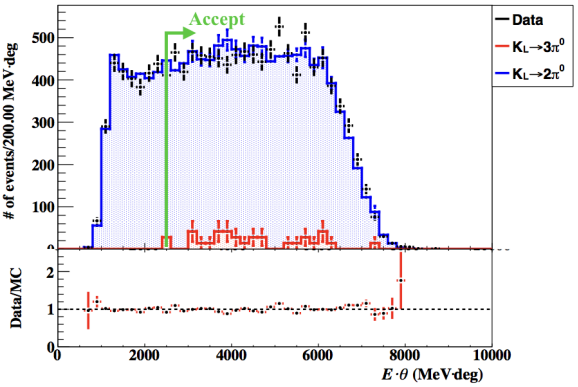

(e) $E \cdot \theta$

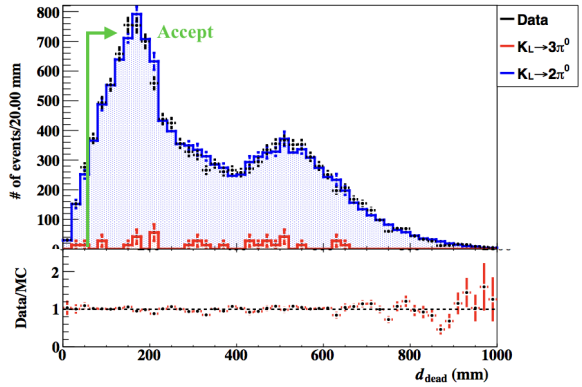

(f) dead channel

Figure 6.31: Distributions of π^0 kinematic cut variables of the validation sample. Black points represent data and red and blue histograms represent the contributions of the $K_L \to 3\pi^0$ and $K_L \to 2\pi^0$ events to the validation sample, respectively. Green line denotes the cut point of the cut. The data/MC ratios are shown below each panel. The error bars represent the statistical errors. This plot is based on the Period-9 data.

where i represents the i-th veto cut. The $K_L \to 2\gamma$ sample was used for emulating the $K_L \to \pi^0\nu\overline{\nu}$ decay since the decay has the same number of photons in the final state. The comparison between data and MC in $K_L \to 2\pi^0$ and $K_L \to 2\gamma$ samples, and the double ratio for each veto cut are shown in Fig. 6.33. By taking a quadratic sum of $DR^i - 1$ over all the veto cuts and by averaging the resultant quadratic sum over all the run-periods, we obtained the total uncertainty due to the veto cuts to be

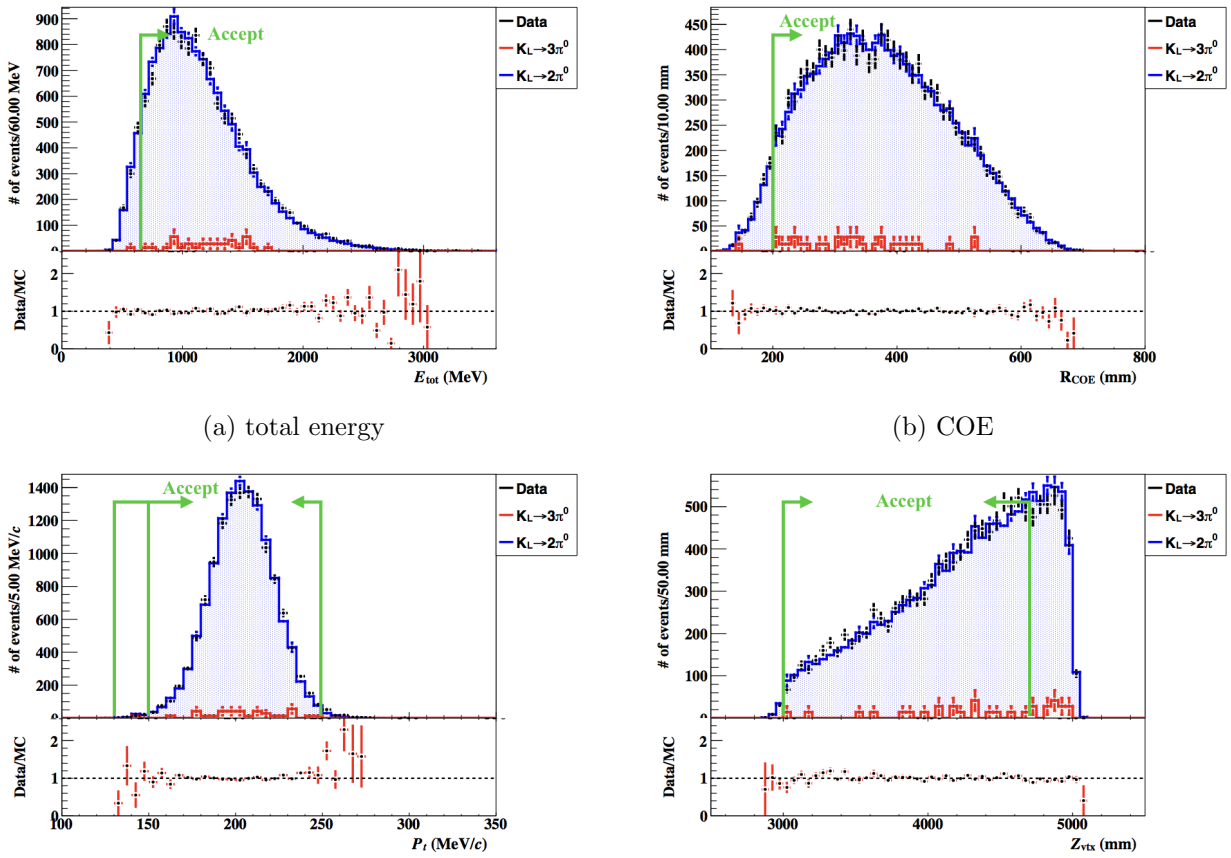

(a) total energy

(b) COE

(c) P_t

(d) Z_{vtx}

Figure 6.32: E_{tot}, R_{COE}, P_t, and Z_{vtx} distributions of the validation sample. Black points represent data and red and blue histograms represent the contributions of the $K_L \to 3\pi^0$ and $K_L \to 2\pi^0$ events to the validation sample, respectively. Green line denotes the cut point of the cut. The data/MC ratios are shown below each panel. The error bars represent the statistical errors. This plot is based on the Period-9 data.

3.7%.

6.3.6.6 Uncertainty from the shape-related cuts

The uncertainty from the shape-related cuts was estimated with the same method as for the kinematic cuts for $K_L \to \pi^0 \nu\overline{\nu}$, namely by using the validation sample from the $K_L \to 2\pi^0$ sample. As for the pulse shape likelihood ratio cut, the cut efficiency (for the data sample) and efficiency obtained by the efficiency map described in Sec. 6.3.1.4 (for the simulation sample) were compared. The comparison of each cut is shown in Fig. 6.34 and summarized in Table 6.11. Distributions of the cut variables are shown in Fig. 6.35. The total uncertainty from the shape-related cuts was 5.1%.

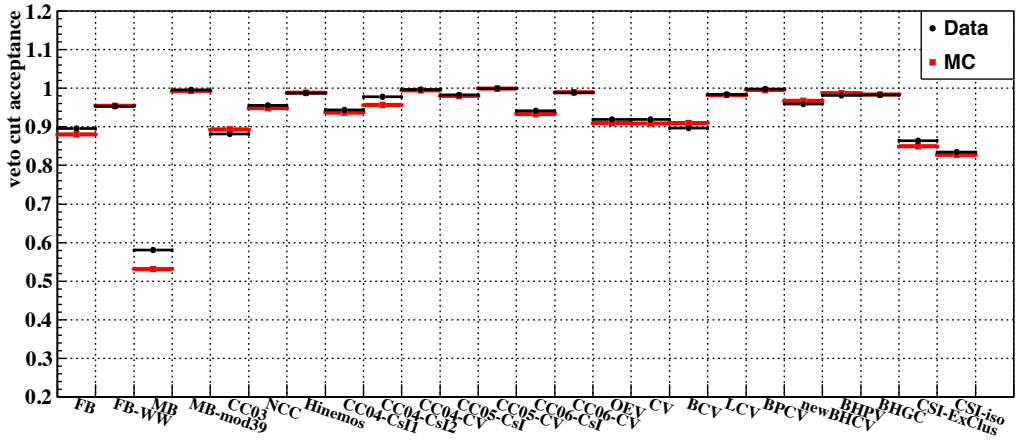

(a) Veto cut acceptance for the $K_L \to 2\pi^0$ sample

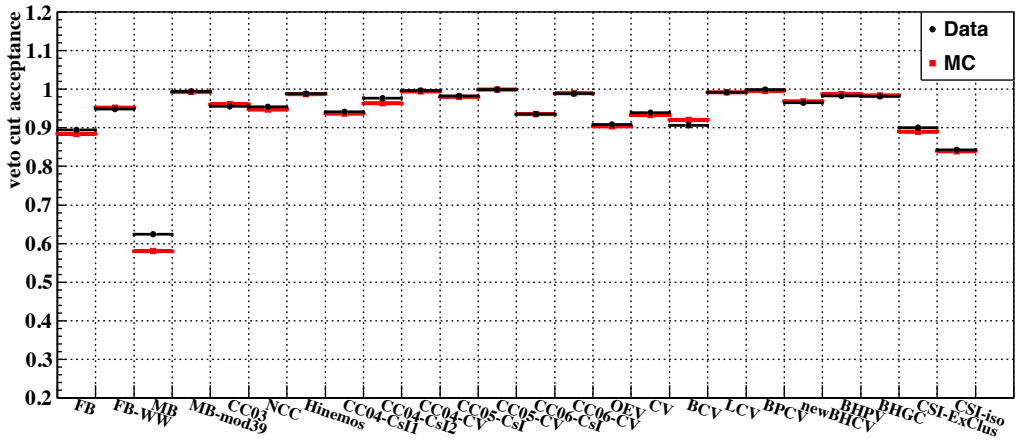

(b) Veto cut acceptance for the $K_L \to 2\gamma$ sample.

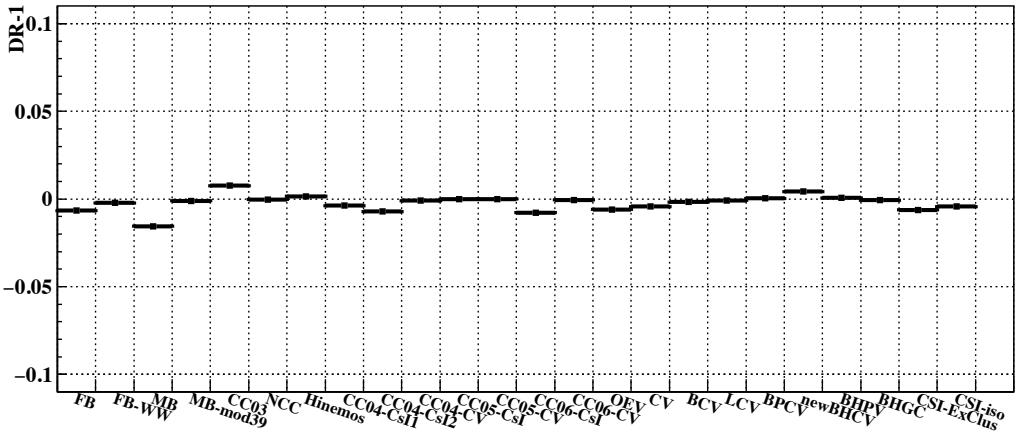

(c) Double ratio (subtracted by 1) of the veto cut acceptance.

Figure 6.33: The comparison of veto cut acceptances between data and MC in $K_L \to 2\pi^0$ and $K_L \to 2\gamma$ samples, and the double ratio for each veto cut. "FB-WW" represents the FB veto with a wide window, and "MB-mod39" represents the special veto treatment for MB module 39. "CC0X-CsI" and "CC0X-CV" represent the CsI and plastic scintillator modules of CC04-CC06, respectively. "CSI-ExClus" and "CSI-iso" represent the CSI extra-cluster veto and CSI isolated hit crystal veto, respectively. These plots are based on the Period-9 data.

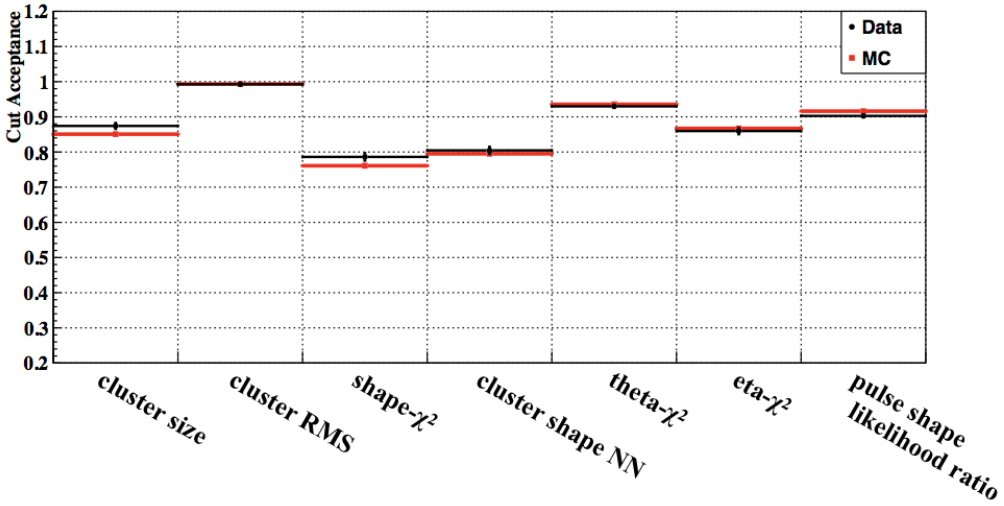

Figure 6.34: Cut acceptance of the shape-related cuts for the validation sample. Black and red points represent data and MC, respectively. This plot is based on the Period-9 data.

Table 6.11: Cut acceptance of the shape-related cuts for the validation sample. The values are based on the Period-9 data.

source	$A^{i\text{-th cut}}_{\text{data}}$	$A^{i\text{-th cut}}_{\text{MC}}$	$A^{i\text{-th cut}}_{\text{MC}}/A^{i\text{-th cut}}_{\text{data}} - 1$
cluster size	0.861	0.851	-1.07%
cluster RMS	0.994	0.993	-0.10%
shape-χ^2	0.791	0.755	-4.61%
cluster shape NN	0.784	0.774	-1.27%
theta-χ^2	0.934	0.936	0.23%
eta-χ^2	0.861	0.866	0.51%
pulse shape likelihood ratio	0.905	0.916	1.24%
quadratic sum			5.1%

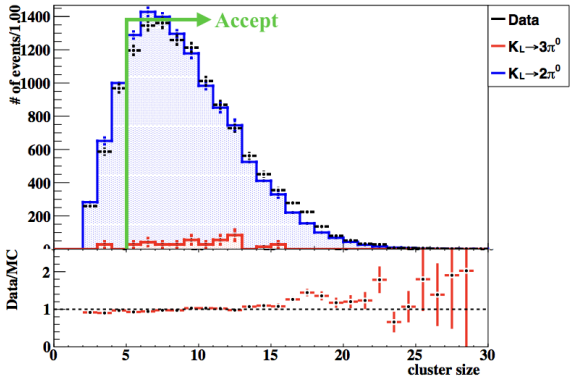

(a) cluster size

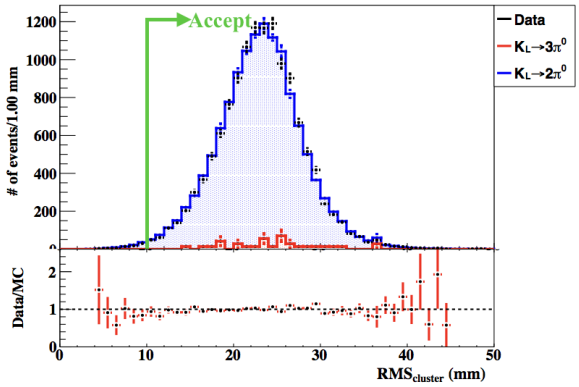

(b) cluster RMS

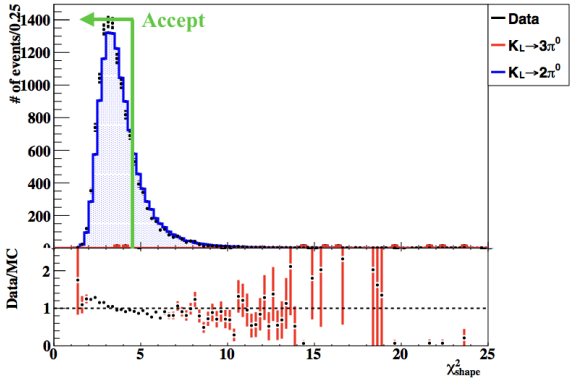

(c) shape-χ^2

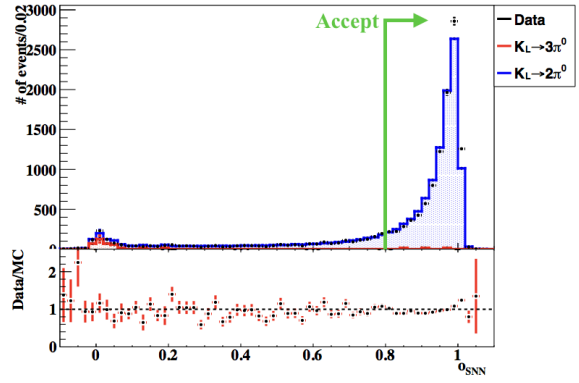

(d) o_{SNN}

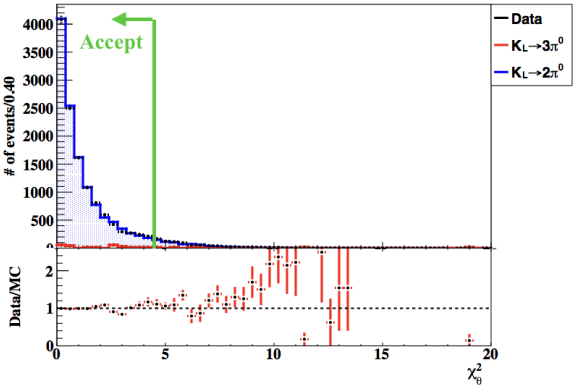

(e) theta-χ^2

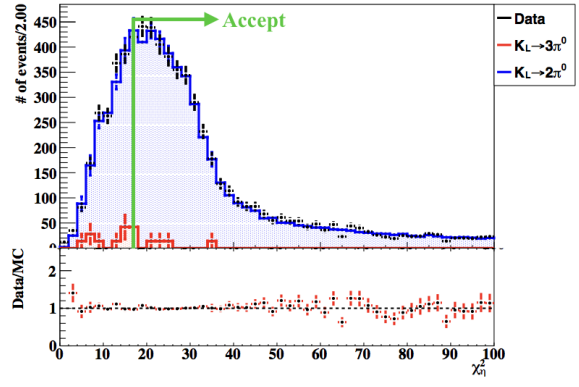

(f) eta-χ^2

Figure 6.35: Distributions of variables used in the shape-related cuts of the validation sample. Black points represent data and red and blue histograms represent the contributions of the $K_L \to 3\pi^0$ and $K_L \to 2\pi^0$ events to the validation sample. Green line denotes the cut point of each cut. The data/MC ratios are shown below each panel. The error bars represent the statistical errors. These plots are based on the Period-9 data.

Table 6.12: Summary of background estimation.

source		Number of events
K_L decay	$K_L \to \pi^+\pi^-\pi^0$	0.05 ± 0.02
	$K_L \to 2\pi^0$	0.02 ± 0.02
	other K_L decays	0.03 ± 0.01
neutron-induced	hadron-cluster	0.24 ± 0.17
	upstream-π^0	0.04 ± 0.03
	CV-η	0.04 ± 0.02
total		0.42 ± 0.18

6.4 Background estimation

This section describes how we estimated the number of background events. The estimation was performed while masking the data in the region $2900 < Z_{\rm vtx} < 5100$ mm and $120 < P_t < 260$ MeV/c to avoid human biases. The number of background events was estimated separately for each source and is described in the following sections. The results are summarized in Table 6.12. The total number of the background events in the signal region was 0.42 ± 0.18, and the dominant background source was the hadron-cluster background. The estimated number of background events in each region in the P_t-$Z_{\rm vtx}$ plane is shown in Fig. 6.36. The distribution of the data after applying all the cuts is also shown in this plot.

In the estimation, basically we evaluated the error with the statistics of the MC sample or the control sample. Systematic uncertainty was not taken into account in the estimation.

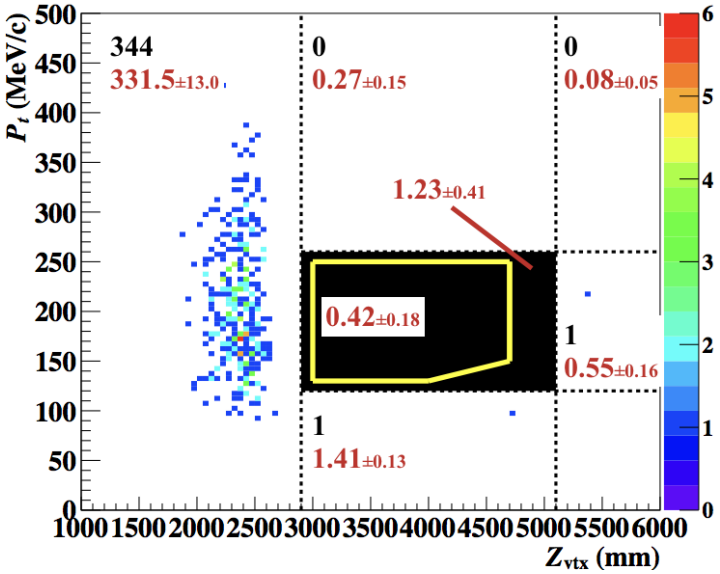

Figure 6.36: P_t-$Z_{\rm vtx}$ distribution of the 2015 run data with all the cuts imposed. The numbers in black (red) indicate the number of observed (estimated background) events in each region bounded by lines.

6.4.1 K_L Decay Background

The contributions from the K_L decay backgrounds were estimated based on simulations. We considered the contributions from the $K_L \to \pi^+\pi^-\pi^0$, $K_L \to 2\pi^0$, $K_L \to 2\gamma$, and $K_L \to 3\pi^0$ decays in this analysis. We neglected the other contributions such as the $K_L \to \pi^\pm e^\mp \nu_e$, $K_L \to \pi^\pm \mu^\mp \nu_\mu$, and $K_L \to \pi^+\pi^-$ decays because their contributions were small.

6.4.1.1 $K_L \to \pi^+\pi^-\pi^0$ Background

In the $K_L \to \pi^+\pi^-\pi^0$ background, the major mechanism was that two photons from a π^0 decay hit the CsI calorimeter and two charged pions $\pi^\pm$ escaped detection. Due to the small Q-value of the decay (83.5 MeV), charged pions tend to fly forward, passing through the beam hole of the CsI calorimeter. There were some non-active materials in the downstream of the CsI calorimeter such as the downstream beam pipe and a 0.5-mm-thick G10 pipe as a support structure for the Membranes (Membrane support) as shown in Fig. 6.37. If the charged pions were absorbed in the non-active materials, such an event can be a background event. The $K_L \to \pi^+\pi^-\pi^0$ background can be suppressed by the P_t requirement because the π^0 has a small P_t due to the kinematical limitation; the maximum π^0 momentum in K_L rest frame is 132 MeV/c. However, the reconstructed P_t can be larger than 132 MeV/c due to the finite energy and position resolution of the CsI calorimeter, and the finite beam size in x-y plane since we reconstruct a π^0 assuming that the decay vertex is on the beam axis.

By replacing the downstream beam pipe with the low-mass pipe and installing the new BPCV, the inefficiency to charged pions due to the absorption in the downstream beam pipe was suppressed by a factor of 20 compared with the 2013 run situation. This large suppression allowed us to extend the lower P_t bound of the signal region from 150 MeV/c in the 2013 run analysis. In this analysis, we set the lower P_t bounds as a function of $Z_{\rm vtx}$: 130 MeV/c in the region of $3000 < Z_{\rm vtx} < 4000$ mm, and varying linearly from 130 MeV/c to 150 MeV/c in the region of $4000 < Z_{\rm vtx} < 4700$ mm as shown in Fig. 6.38. This $Z_{\rm vtx}$-dependent P_t bound was adopted because of the $K_L \to \pi^+\pi^-\pi^0$ background populated in the lower right corner of the masked region. The correlation between P_t and $Z_{\rm vtx}$ of the background events is an effect of the finite beam size: the effect becomes larger as the decay vertex gets closer to the CsI calorimeter. Note that if we adopt the signal region with the constant lower P_t bound to be 130 MeV/c (150 MeV/c), the number of background events decreases by 0.04 events (increases by 0.04 events) while the signal acceptance decreases by 15% (increases by 3%).

Based on 4×10^{13} simulated $K_L \to \pi^+\pi^-\pi^0$ events, which corresponds to 68 times the statistics of the data, the number of background events in the signal region was estimated to be 0.05 ± 0.02 as shown in Fig. 6.38.

We checked the data reproducibility of the MC by removing the BPCV veto cut. As shown in Fig. 6.39, the data and MC showed good agreement in the low P_t region.

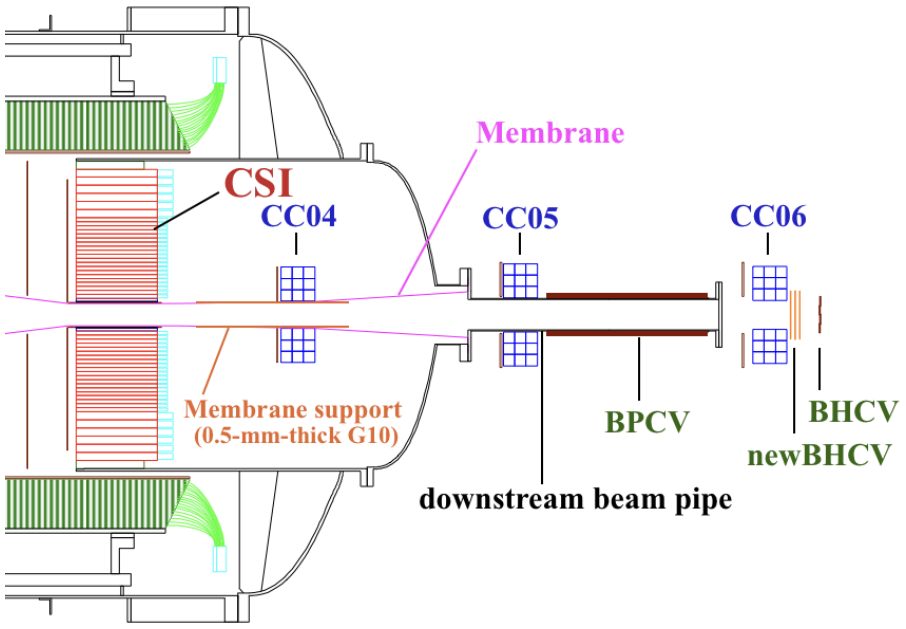

Figure 6.37: Downstream part of the KOTO detector.

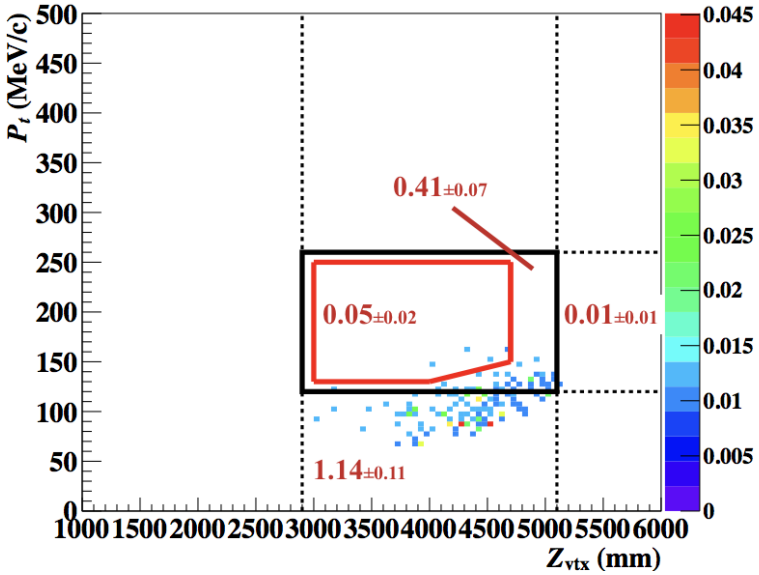

Figure 6.38: P_t-$Z_{\rm vtx}$ distribution of the simulated $K_L \to \pi^+\pi^-\pi^0$ background events. Numbers in red indicate the number of events in each region bounded by lines.

6.4.1.2 $K_L \to 2\pi^0$ Background

The mechanisms of the $K_L \to 2\pi^0$ background are categorized into three types: "even-pairing", "odd-pairing", and "fusion". In the even pairing-type, two photons from a π^0 decay are correctly reconstructed and the other two photons are not detected. In the odd-pairing type, two photons from different π^0 decays are reconstructed as a π^0 and the other photons are not detected. In this case, the π^0 decay vertex is not properly reconstructed and the kinematics of the reconstructed π^0 is wrong. The odd pairing events are therefore suppressed by the energy ratio and $E \cdot \theta$ cuts. As for the fusion type, three (or possibly four) photons hit the CsI calorimeter and two of them fuse into a single cluster because their hit positions are close to each other and the residual photon is not detected. The shape-χ^2 cut is effective to reduce this type of background because the shape of the fused cluster is different from that of a single photon cluster.

We estimated the contribution of the $K_L \to 2\pi^0$ background based on a simulation. The P_t-$Z_{\rm vtx}$ distribution of these background events is shown in Fig. 6.40. Based on 1.6×10^{11} simulated $K_L \to 2\pi^0$ events, which corresponds to 40 times higher statistics than the data, the number of background events in the signal region was estimated to be 0.02 ± 0.02.

The properties of the remaining twelve events after imposing all the cuts except for the P_t and $Z_{\rm vtx}$ requirements were examined. Eight events were the even-pairing events, two events were the odd-pairing events, and the residual two events were fusion events. We found that in four events photons disappeared around the outer edge of the CsI calorimeter. Figure 6.41 shows a schematic view and a photograph of the outer edge region of the CsI calorimeter. The non-active materials in the region caused the detection inefficiency of photons.

6.4.1.3 $K_L \to 2\gamma$ Background

The final state of the $K_L \to 2\gamma$ decay is only two photons, which is the same as that of the $K_L \to \pi^0\nu\overline{\nu}$ decay, but it can be distinguished from the signal decay with the kinematics: two photons are back-to-back in the x-y plane and the reconstructed π^0 from the two photons has ideally no P_t. However, if a K_L is scattered at the upstream vacuum window (mentioned in Sec. 2.2.4.13), a 12.5-μm-thick polyimide film located at $z = -500$ mm, and has a large transverse momentum, such a K_L decaying into two photons can be a background since the reconstructed π^0 has a finite P_t. Based on 2.5×10^{11}

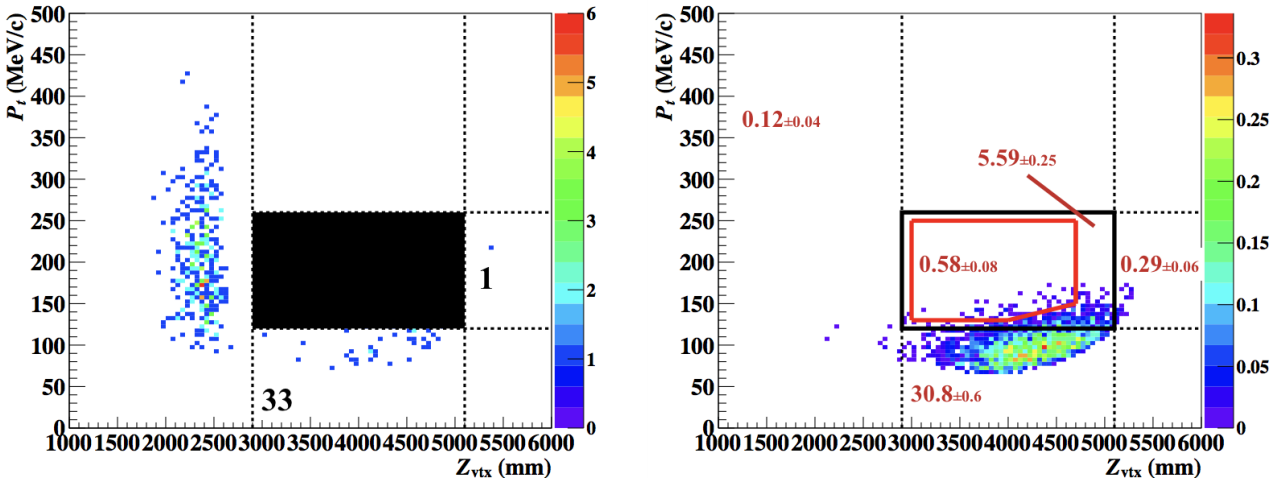

(a) Data (b) MC

Figure 6.39: P_t-Z_{vtx} distributions of the data and the $K_L \to \pi^+\pi^-\pi^0$ MC without imposing the BPCV veto cut. With this cut set, events in the low P_t region are dominated by the $K_L \to \pi^+\pi^-\pi^0$ events and other contributions are small. The numbers in black (red) in the data (MC) plot indicate the number of observed (estimated background) events in each region bounded by lines.

simulated $K_L \to 2\gamma$ events, which corresponds to 98 times higher statistics than the data, we estimated the number of background events in the signal region to be 0.02 ± 0.01. The P_t-Z_{vtx} distribution of the $K_L \to 2\gamma$ background events is shown in Fig. 6.42.

6.4.1.4 $K_L \to 3\pi^0$ Background

In the $K_L \to 3\pi^0$ decay, four photons are available to veto the event and thus this background is highly suppressed by the veto cuts. In this estimation, we considered the effect of the photon detection inefficiency caused by timing shifts in the veto counters due to pulse pileups. If another $K_L \to 3\pi^0$ decay occurs at almost the same timing as a $K_L \to 3\pi^0$ decay of interest, the pulse pileups can occur in multiple modules of the veto counters at the same time.

Due to the large branching fraction of the $K_L \to 3\pi^0$ decay, it was difficult to process all the simulation process with large enough statistics. To simulate this background in a practical time, we first simulated 2×10^{10} $K_L \to 3\pi^0$ decays without the accidental overlay process, and then repeated the accidental overlay process 3000 times with different TMON triggered events for each simulated event; consequently the effective statistics of the simulated events were 6×10^{13} $K_L \to 3\pi^0$ decays, which corresponds to 6.6 times higher statistics than data.

Based on this simulation, we estimated the number of the $K_L \to 3\pi^0$ background events in the signal region to be 0.01 ± 0.01. The P_t-Z_{vtx} distribution of the $K_L \to 3\pi^0$ background events is shown in Fig. 6.43.

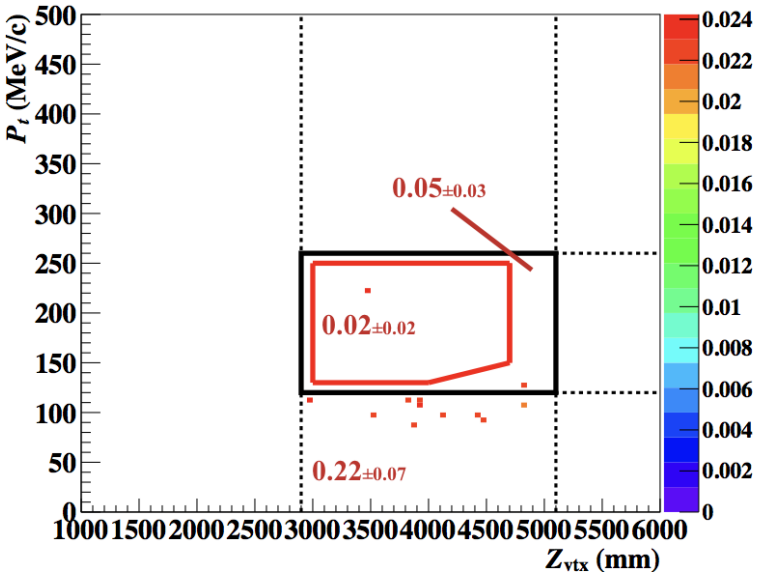

Figure 6.40: P_t-$Z_{\rm vtx}$ distribution of the simulated $K_L \to 2\pi^0$ background events. Numbers in red indicate the number of events in each region bounded by lines.

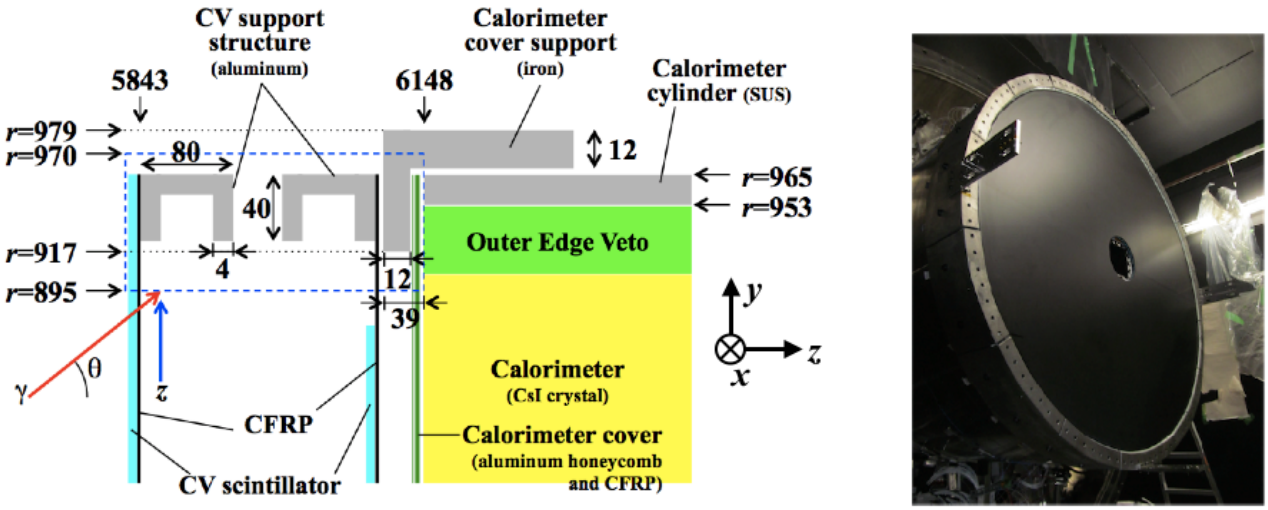

Figure 6.41: Schematic view of the calorimeter edge region (left) and photograph of the CsI calorimeter with the cover (right). The units of the numbers are mm. The figures are quoted from Ref. [67].

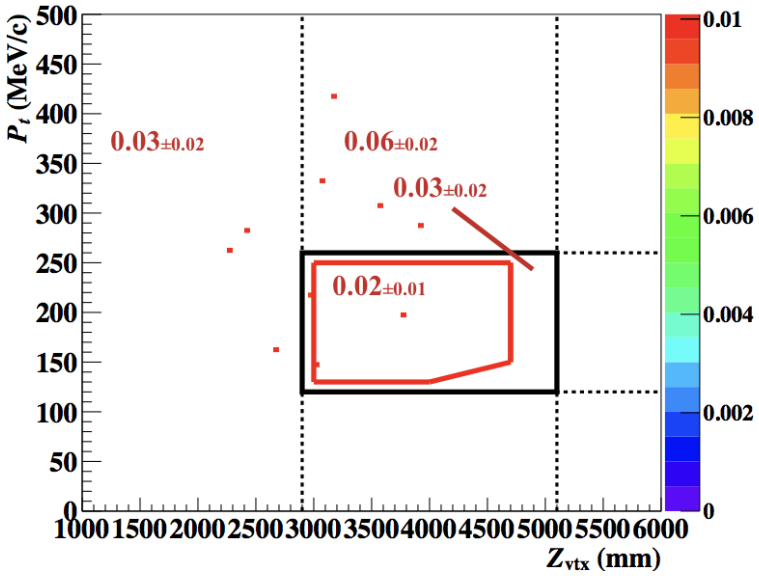

Figure 6.42: P_t-Z_{vtx} distribution of the $K_L \to 2\gamma$ background events. Numbers in red indicate the number of events in each region bounded by lines.

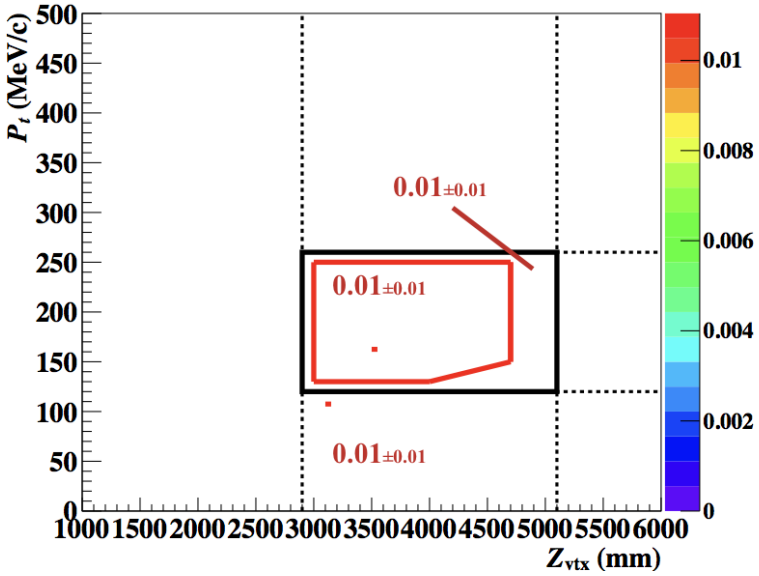

Figure 6.43: P_t-Z_{vtx} distribution of the $K_L \to 3\pi^0$ background events. Numbers in red indicate the number of events in each region bounded by lines.

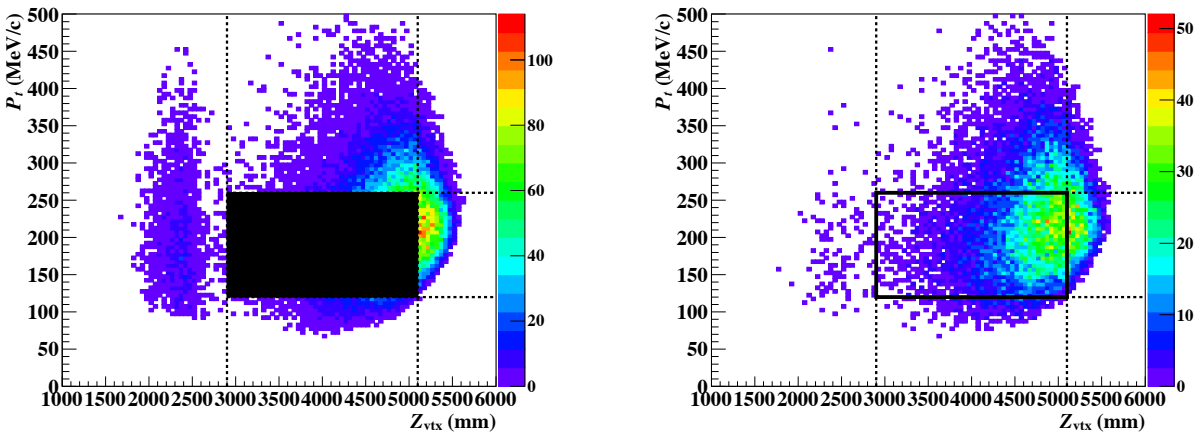

(a) data sample (b) control sample

Figure 6.44: P_t-$Z_{\rm vtx}$ distributions of the data (a) and the control sample taken in the Z0 Al run(b).

6.4.2 Neutron-Induced Background

Here we estimate the contributions from the hadron-cluster, upstream-π^0, CV-η, and CV-π^0 backgrounds.

6.4.2.1 Hadron-Cluster Background

The hadron-cluster background is caused by a halo-neutron directly hitting the CsI calorimeter. The neutron makes a primary hadronic shower and then another neutron produced in the shower makes another hadronic shower after traveling inside the calorimeter. These separated two hadronic showers mimic the two photon clusters from the $\pi^0 \to 2\gamma$ decay. If such a π^0 is reconstructed in the signal region by chance, it can be a background.

To eliminate this background, discrimination of electromagnetic showers from hadronic showers with the CsI calorimeter information is crucial. We developed some discrimination methods and they were categorized into two types: "cluster shape discrimination" and "pulse shape discrimination". All the shape-related cuts explained in Sec. 6.3.1.4 except for the pulse shape likelihood ratio cut are categorized into the cluster shape discrimination method. The pulse shape discrimination method (the pulse shape likelihood ratio cut) uses the waveform information of signals from each crystal in a cluster.

To study the hadron-cluster background, we took a data-driven approach; We used the control sample collected in the Z0 Al run explained in Sec. 3.2 to estimate the reduction power of cuts and the background yield. Here, we define a fraction of events which survive a cut as "reduction power" of the cut.

Figure 6.44 shows the P_t-$Z_{\rm vtx}$ distributions of the data and the control sample. In these plots, the trigger-related cuts, photon selection cuts, π^0 selection cuts, veto cuts, cluster size cut, and cluster RMS cut are imposed, though the threshold of the $\Delta T_{\rm vtx}$ cut is loosened to 2 ns, and some veto cuts are also loosened (this cut condition is hereinafter referred to as "*setup cut*"). The contributions from K_L decays are almost eliminated under this cut condition. Figure 6.45 and Fig. 6.46 show the comparison of the distributions of the kinematic variables and the variables used in the shape-related cuts, respectively. Good agreement between data and MC in these distributions validates the control sample.

Estimation of Background Rejection Power of the Shape-Related Cuts We estimated the reduction power of the shape-χ^2, cluster shape NN, and pulse shape likelihood ratio cuts with the

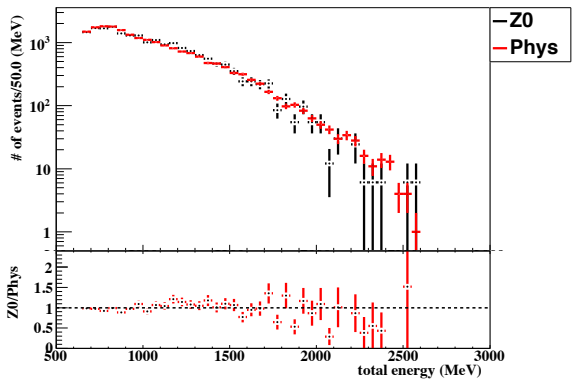

(a) total energy

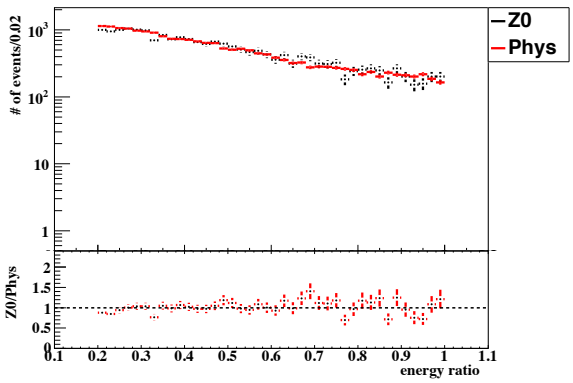

(b) energy ratio

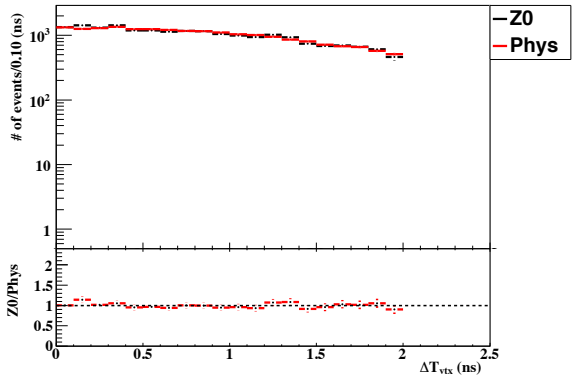

(c) ΔT_{vtx}

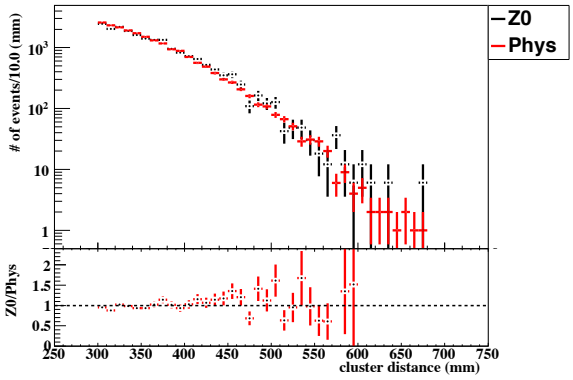

(d) cluster distance

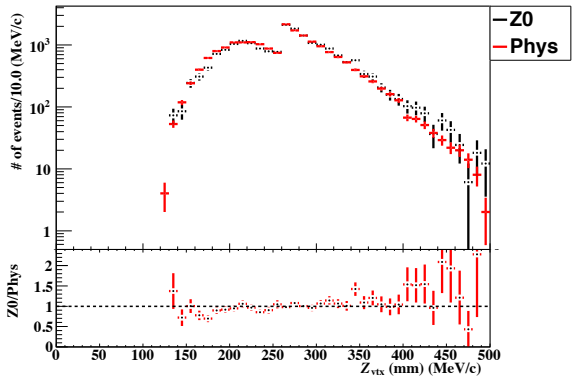

(e) P_t

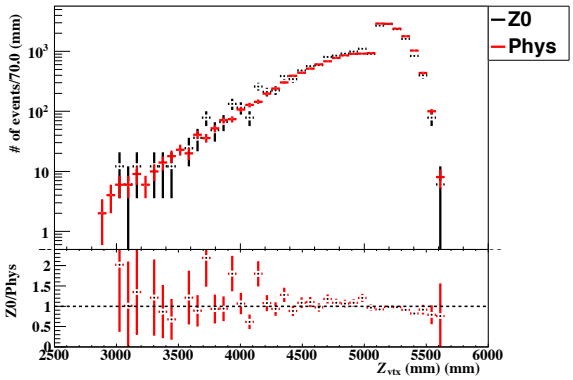

(f) Z_{vtx}

Figure 6.45: Distributions of the kinematic variables of the data and the control sample. Events in the region of $2900 < Z_{\mathrm{vtx}} < 6000$ mm and $120 < P_t < 500$ MeV/c, and outside the masked region ($2900 < Z_{\mathrm{vtx}} < 5100$ mm and $120 < P_t < 260$ MeV/c) are used. The gaps in the P_t and Z_{vtx} distributions are due to the masking. Black (Z0) and red (Phys) histograms represent the control sample and the data sample. The former histogram is normalized to the latter one using the number of total entries. The control sample / data ratios are shown below each panel. The error bars represent the statistical errors.

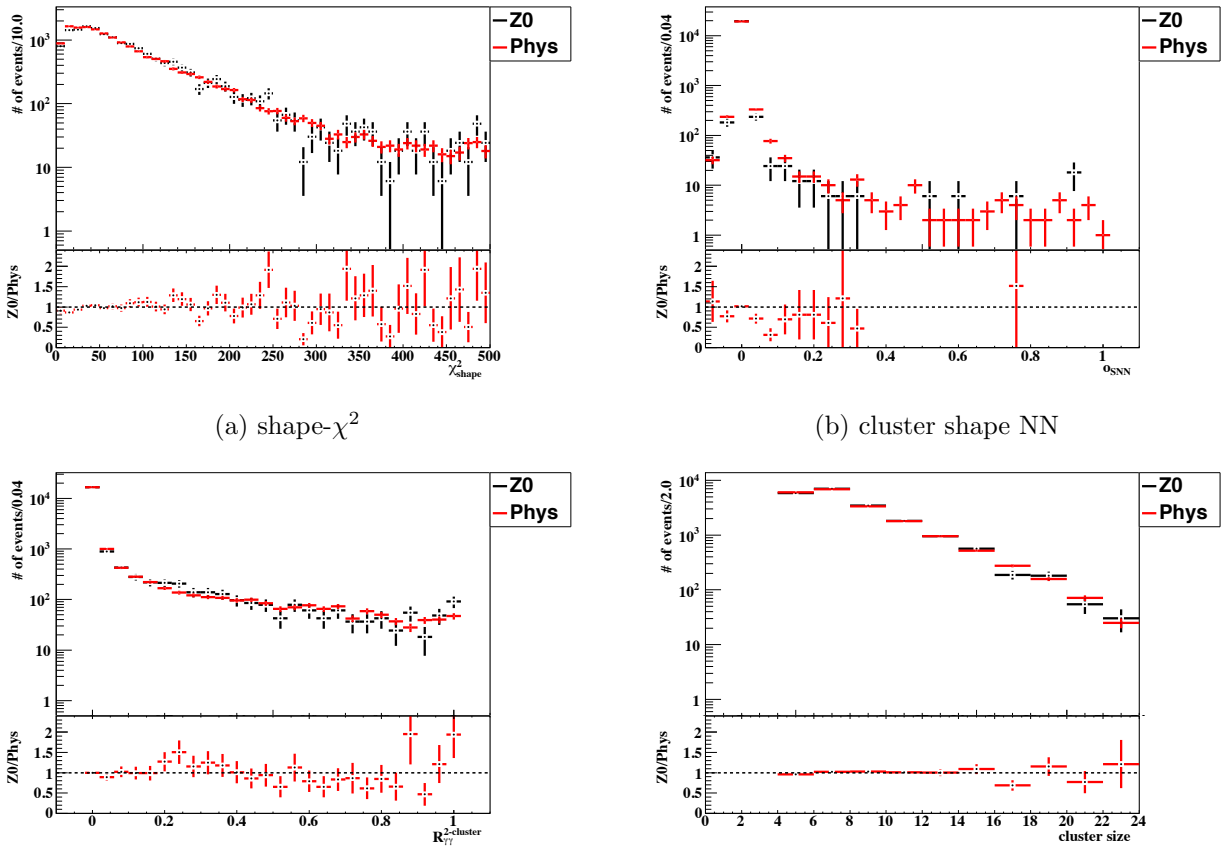

(a) shape-χ^2

(b) cluster shape NN

(c) pulse shape likelihood ratio

(d) cluster size

Figure 6.46: Distributions of the shape-related cuts' variables of the data and the control sample. Events in the region of $2900 < Z_{\rm vtx} < 6000$ mm and $120 < P_t < 500$ MeV/c, and outside the masked region ($2900 < Z_{\rm vtx} < 5100$ mm and $120 < P_t < 260$ MeV/c) are used. Black (Z0) and red (Phys) histograms represent the control sample and the data sample. The former histogram is normalized to the latter one using the number of total entries. The control sample / data ratios are shown below each panel. The error bars represent the statistical errors.

control sample under the setup cut condition[*7].

The reduction powers of the shape-χ^2, cluster shape NN, and pulse shape likelihood ratio cuts were evaluated as 2.8×10^{-3}, 5.9×10^{-4}, and 8.6×10^{-2}. respectively.

Figures 6.47a, 6.47b, and 6.47c show how the reduction power of one cut is affected by the change of other cuts. All the reduction curves of the shape-χ^2 are consistent regardless of the pulse shape likelihood ratio cut condition (Fig. 6.47a) so that we concluded these two cuts had no correlation. On the other hand, the reduction power of the cluster shape NN cut became larger under tighter shape-χ^2 cut condition (Fig. 6.47c). This indicates a strong correlation between these two cuts, which is natural because both of these cuts utilize cluster shape information. The cluster shape NN and pulse shape likelihood ratio cuts have a small correlation between them (Fig. 6.47b).

Due to the limited statistics of the control sample and large reduction power of those cuts, we adopted the "weighting method" to estimate the integrated reduction power of those three cuts. in this method, the reduction power of the shape-χ^2 cut after the cluster shape NN imposed (0.27 ± 0.13) and the combination of the cluster shape NN and pulse shape likelihood ratio cuts ($(2.1 \pm 1.1) \times 10^{-4}$) were estimated separately, and then they were multiplied to be integrated. Consequently, the reduction

[*7] As for the theta-χ^2 and eta-χ^2 cuts, since we found that they had no reduction power after the shape-χ^2 and cluster shape NN cuts imposed, we regarded the reduction power of the theta-χ^2 and eta-χ^2 cuts as 1.

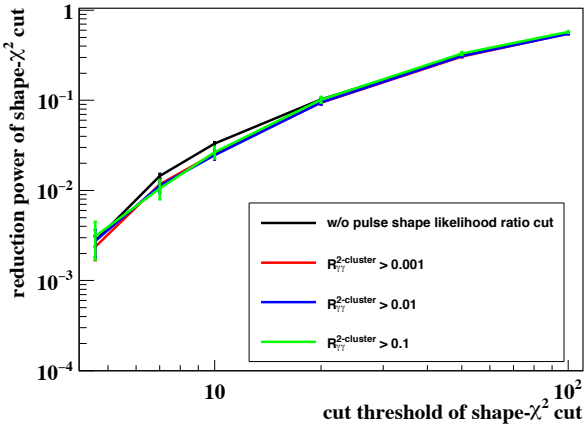

(a) Reduction power of shape-χ^2 cut as a function of its cut threshold under various pulse shape likelihood ratio cut conditions.

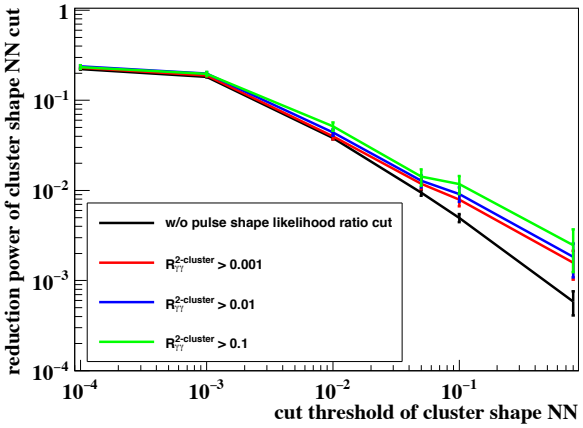

(b) Reduction power of cluster shape NN cut as a function of its cut threshold under various pulse shape likelihood ratio cut conditions.

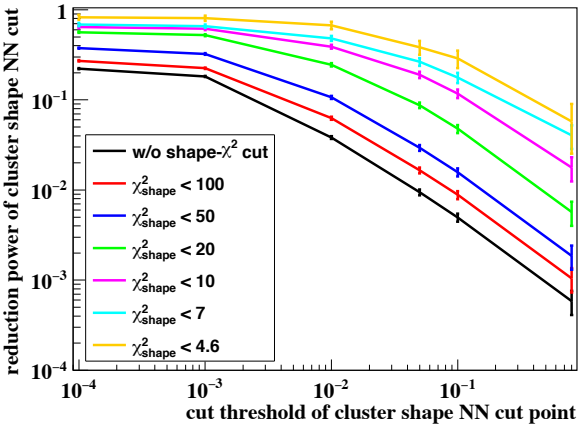

(c) Reduction power of cluster shape NN cut as a function of its cut threshold under various shape-χ^2 cut conditions.

Figure 6.47: Reduction curves of a cut under several cut conditions of another cut. If the two cuts have no correlation, all the curves should be consistent with each other.

power of those three cuts were estimated to be $(5.7 \pm 4.0) \times 10^{-5}$, where the error represents the statistical error. Note that this estimation is possibly an overestimate due to a few events level of kaon contamination in the control sample, which we were unable to subtract quantitatively from the estimation because of the limited statistics.

Normalization of Background Yield We normalized the background yield by comparing the number of events before imposing those three cuts in data and control sample. In order to avoid the contamination such as the upstream-π^0 events (described in Sec. 2.1.2.2 and Sec. 6.4.2.2) and the $K_L \to \pi^+\pi^-\pi^0$ events, we counted the events in the region $2900 < Z_{\text{vtx}} < 6000$ mm and $120 < P_t < 500$ MeV/c except for the masked region $2900 < Z_{\text{vtx}} < 5100$ mm and $120 < P_t < 260$ MeV/c.

By normalizing the control sample based on 1.60×10^3 events in the control sample and 1.28×10^4 events in the data, and then multiplying the reduction power of the three cuts, we obtained the estimated number of hadron-cluster background events in the signal region to be 0.24 ± 0.17. The estimated numbers of events around the signal region are shown in Fig. 6.48.

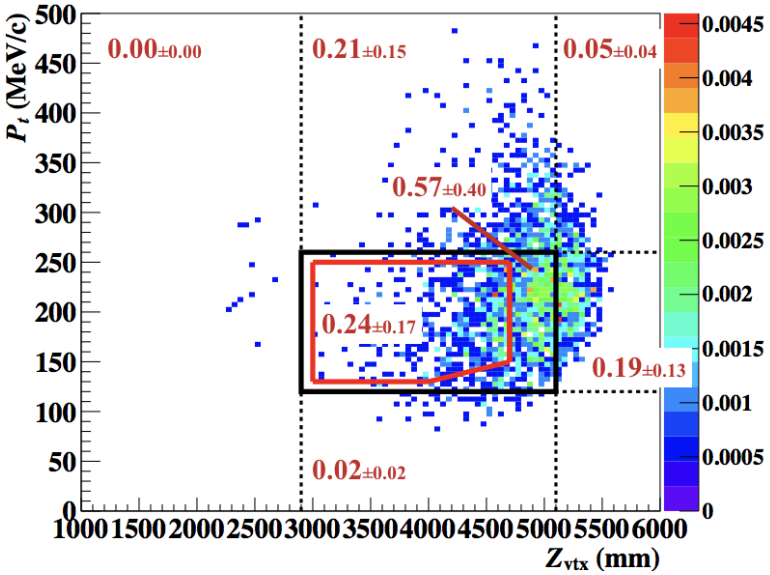

Figure 6.48: P_t-$Z_{\rm vtx}$ distribution of the hadron-cluster background events. The numbers in red indicate the number of events in each region bounded by lines.

6.4.2.2 Upstream-π^0 Background

The upstream-π^0 background is caused by a π^0 production by a halo-neutron hitting NCC, which is located at the upstream edge of the decay volume, $z \sim 2500$ mm. Basically, the $Z_{\rm vtx}$ of such events are calculated to be around $z \sim 2500$ mm, but if the energy of the photons is mis-reconstructed to be smaller due to the photo-nuclear interaction of the photons in the CsI calorimeter, the $Z_{\rm vtx}$ is shifted downstream into the signal region.

We simulated this background and normalized the yield by comparing the number of events with $Z_{\rm vtx} < 2900$ mm in the data and the simulation sample under a loose cut condition. In this cut condition, we applied the trigger-related cuts and photon selection cuts to ensure the quality of the sample, most of the veto cuts and π^0 selection cuts to eliminate K_L decay contamination, and the cluster size, cluster RMS, shape-χ^2, and cluster shape NN cuts to eliminate the contamination of the hadron-cluster events. The P_t-$Z_{\rm vtx}$ distributions of the data and simulation under the loose cut condition are shown in Fig. 6.49. Based on the 739 events in data and 3.2×10^4 events in MC, we obtained the normalization factor of 2.3×10^{-2}. Kinematical distributions of these events used for the normalization were examined as shown in Fig. 6.50, and they indicated good agreements between the data and MC.

The P_t-$Z_{\rm vtx}$ distributions of the upstream-π^0 background events after imposing all the cuts are shown in Fig. 6.51. The number of background events in the signal region was estimated to be 0.04 ± 0.03 based on the 2 remaining events in the simulation. In one event, one photon energy was measured correctly and the other photon caused a photo-nuclear interaction in the CsI calorimeter, and the photon energy was mis-measured. In the other event, one photon from a π^0 and an associated neutron made two clusters.

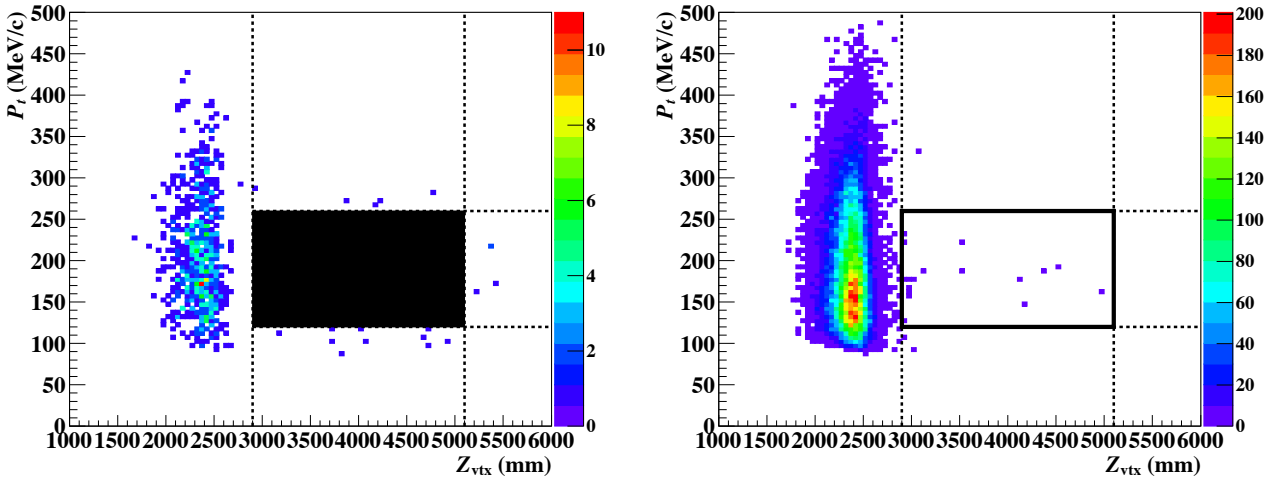

(a) data (b) MC

Figure 6.49: P_t-Z_{vtx} distributions of the data and the upstream-π^0 simulation sample with the loose cut condition. Events with $Z_{\mathrm{vtx}} < 2900$ mm were used for the normalization.

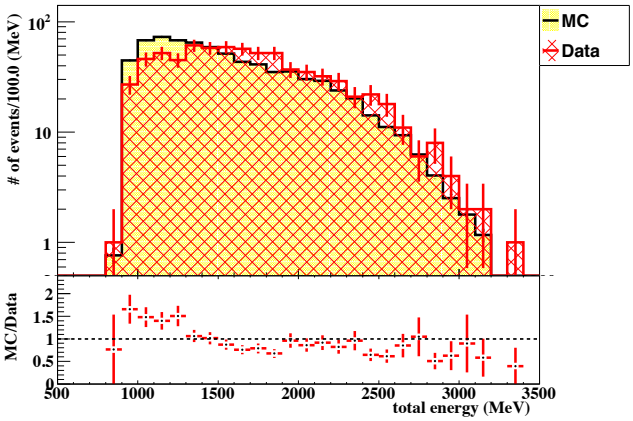

(a) total energy

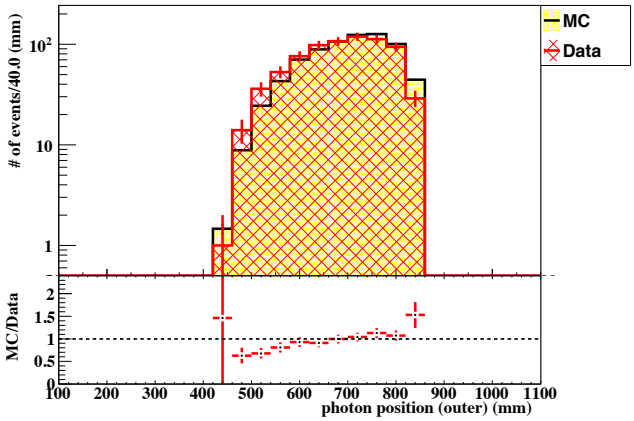

(b) photon position (outer)

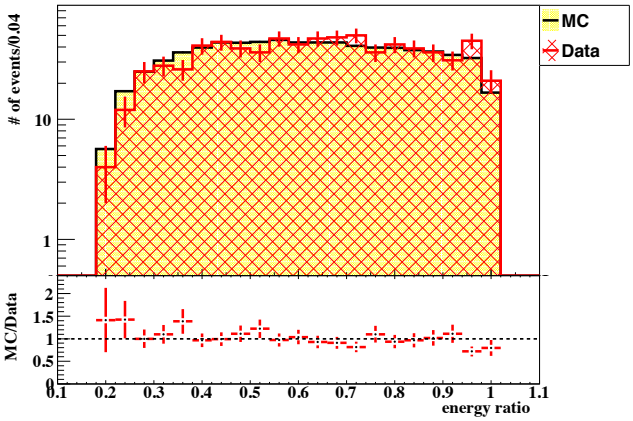

(c) energy ratio

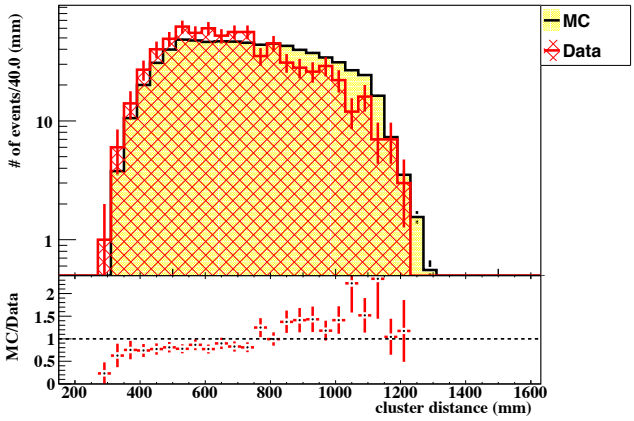

(d) cluster distance

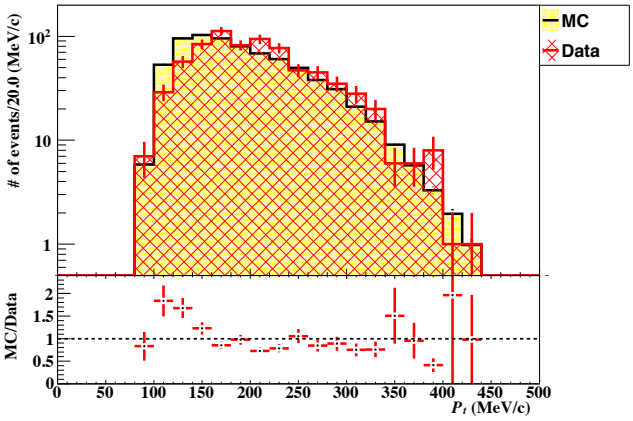

(e) P_t

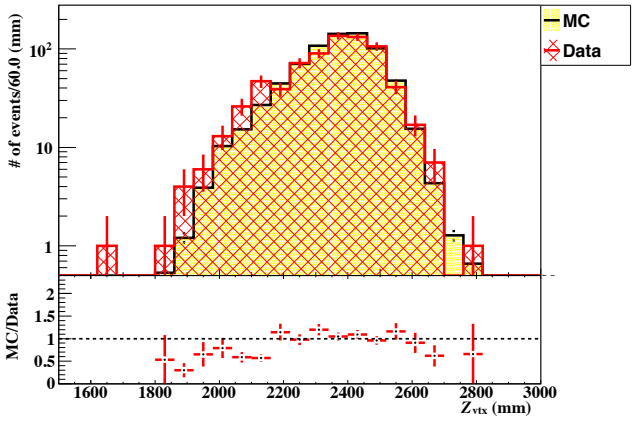

(f) Z_{vtx}

Figure 6.50: Distributions of kinematic variables of the data and the upstream-π^0 simulation sample used for the normalization. Red and yellow histograms represent the data and MC, respectively. The error bars represent the statistical errors.

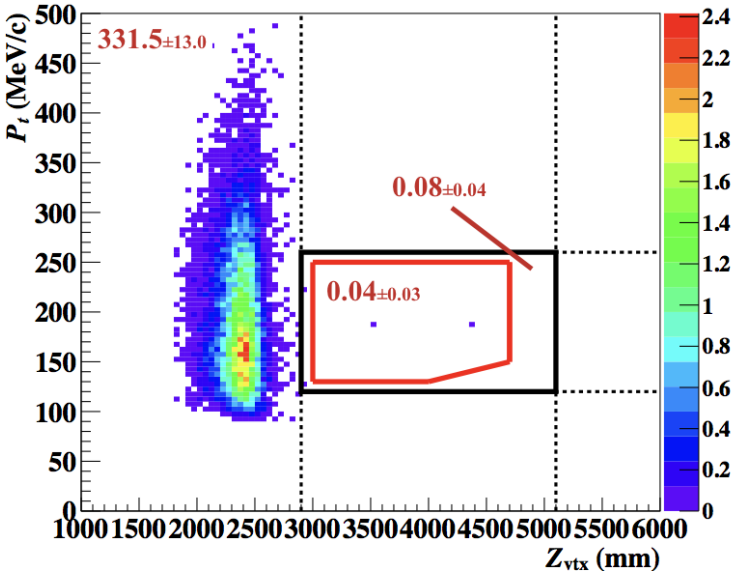

Figure 6.51: P_t-Z_{vtx} distributions of the upstream-π^0 background events after all the cuts imposed. The numbers in red indicate the number of events in each region bounded by lines.

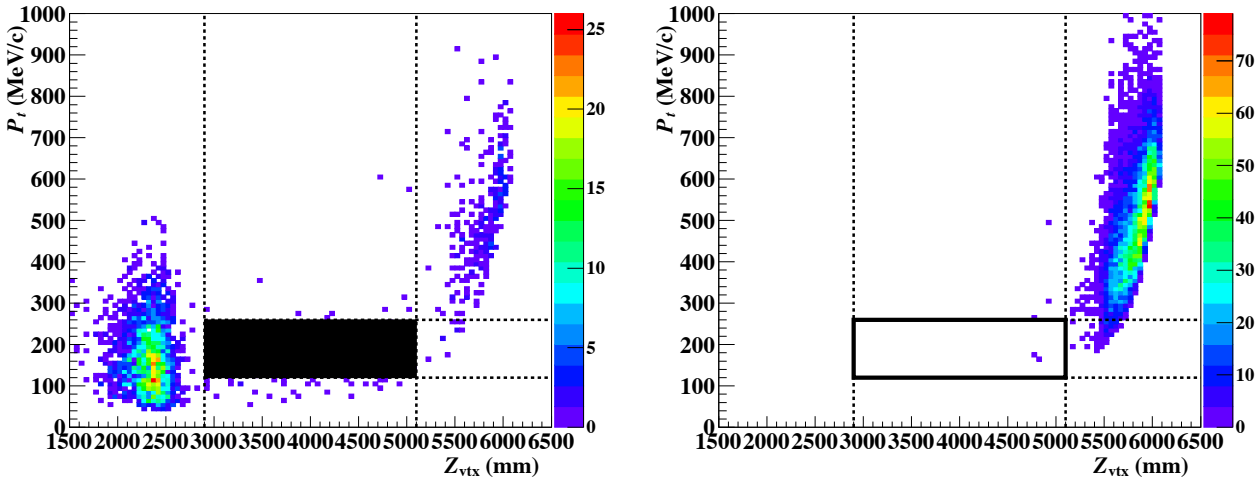

(a) data (b) MC

Figure 6.52: P_t-$Z_{\rm vtx}$ distributions of the data and the CV-π^0 simulation sample with the loose cut condition. Events with $Z_{\rm vtx} > 5100$ mm were used for the normalization.

6.4.2.3 CV-η, CV-π^0 Background

The CV-η background is caused by a halo-neutron hitting the CV. The neutron hits CV and produces an η meson which decays to two photons with a branching fraction of 39.4% [15]. A π^0 is reconstructed with these two photons hitting the CsI calorimeter, but the heavy mass of η ($M_\eta = 548$ MeV/c^2) pushes the reconstructed $Z_{\rm vtx}$ upstream into the signal region.

The CV-π^0 background is also caused by a halo-neutron hitting the CV. The neutron hits CV and produces a π^0. The reconstructed $Z_{\rm vtx}$ of such an event distributes in downstream ($Z_{\rm vtx} \sim$ 5500-6000 mm), but if a secondary particle associated with the π^0 production hits the CsI calorimeter near the hit positions of photons from the π^0 decay, the measured photon energy may increase and shifts the reconstructed $Z_{\rm vtx}$ upstream into the signal region.

The numbers of CV-η and CV-π^0 background events were estimated with simulations. The P_t-$Z_{\rm vtx}$ distribution of the CV-π^0 MC sample and data with a loose cut condition are shown in Fig. 6.52. In this cut condition, we applied the trigger-related cuts and photon selection cuts to ensure the quality of the sample, most of the veto cuts to eliminate K_L decay contamination, and the cluster size, cluster RMS, shape-χ^2, and cluster shape NN cuts to eliminate the contamination of the hadron-cluster events. We normalized the background yield by comparing the number of events with $Z_{\rm vtx} > 5100$ mm. Based on the 271 events in data and 8.5×10^3 events in MC, we obtained the normalization factor of 3.3×10^{-2}. Kinematical distributions of these events used for the normalization were examined as shown in Fig. 6.53 and they showed good agreements between the data and MC. We used the same normalization factor for the CV-η background.

The P_t-$Z_{\rm vtx}$ distributions of the CV-η and CV-π^0 background events after applying all the cuts except for the eta-χ^2 cut are shown in Fig. 6.54. For the CV-π^0 sample, no events remained in the signal region, and we set an upper limit for the CV-π^0 contribution as 0.08 at the 90% C.L. As for CV-η background, we found that it had a contribution of 0.27 events for the signal region. To suppress the background further, we developed the eta-χ^2 cut. In this cut, we evaluate the goodness of the assumption that two photons are generated at a common position in the CV front module using angle information from cluster shapes. Details of this cut are described below.

First, we calculated the opening angle of two photons with the kinematics (Eq. 4.8) assuming the invariant mass of two photons to be the mass of η. Using the hit positions of two photons on the CsI calorimeter and the opening angle, we obtained an allowed region where the decay vertex can be on the CV front module ($z = 5842$ mm). We call the possible vertex points in the allowed region as "η

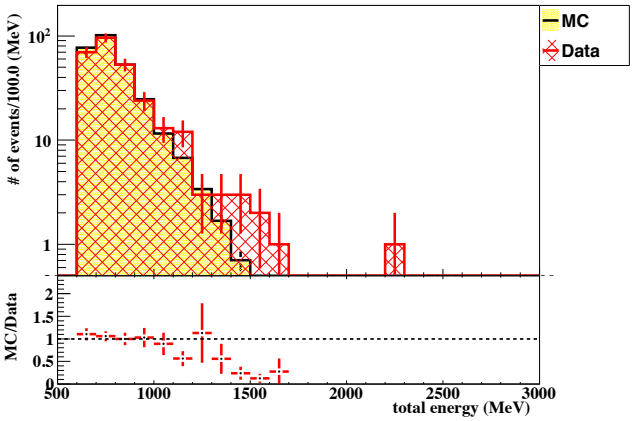

(a) total energy

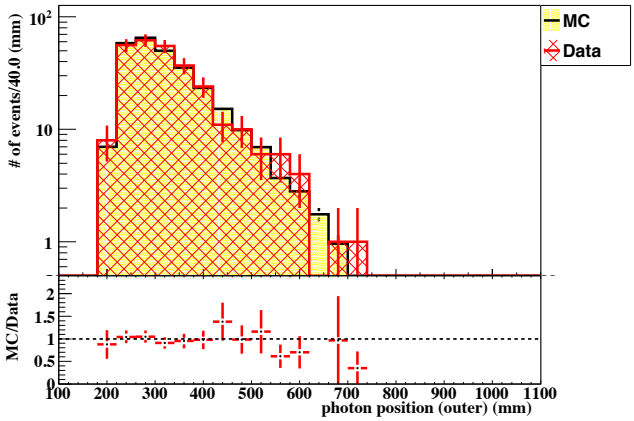

(b) photon position (outer)

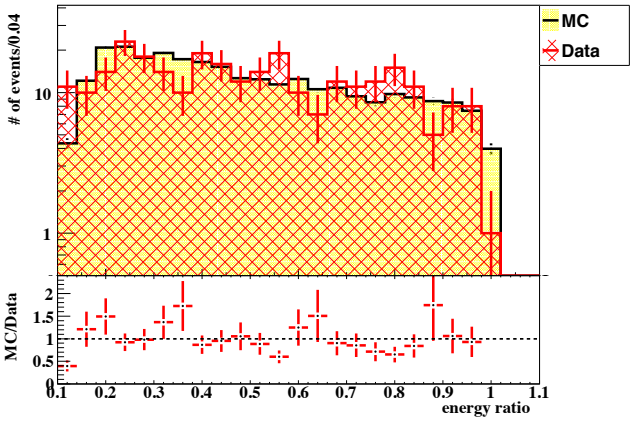

(c) energy ratio

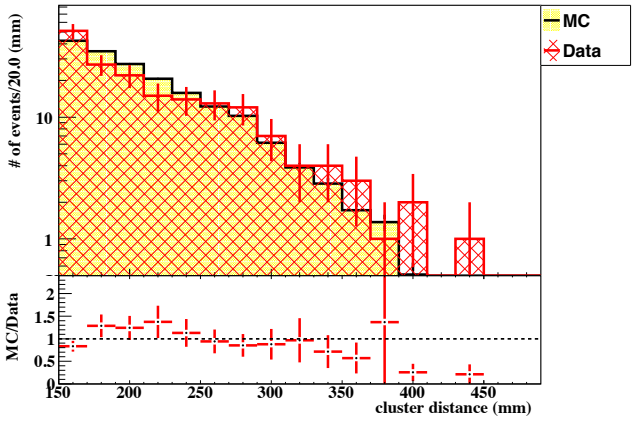

(d) cluster distance

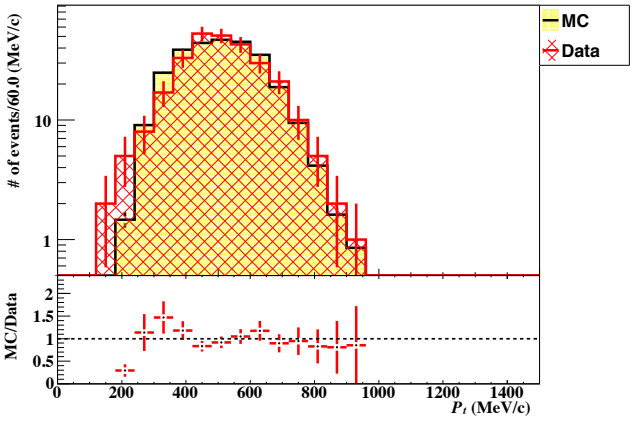

(e) P_t

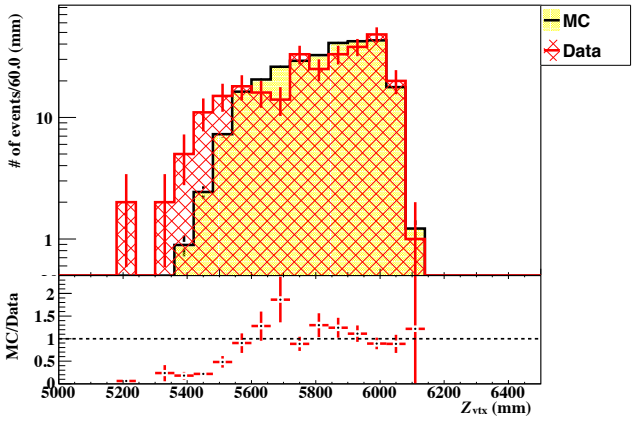

(f) Z_{vtx}

Figure 6.53: Distributions of kinematic variables of the data and the CV-π^0 simulation sample used for the normalization. Red and yellow histograms represent the data and MC, respectively. The error bars represent the statistical errors.

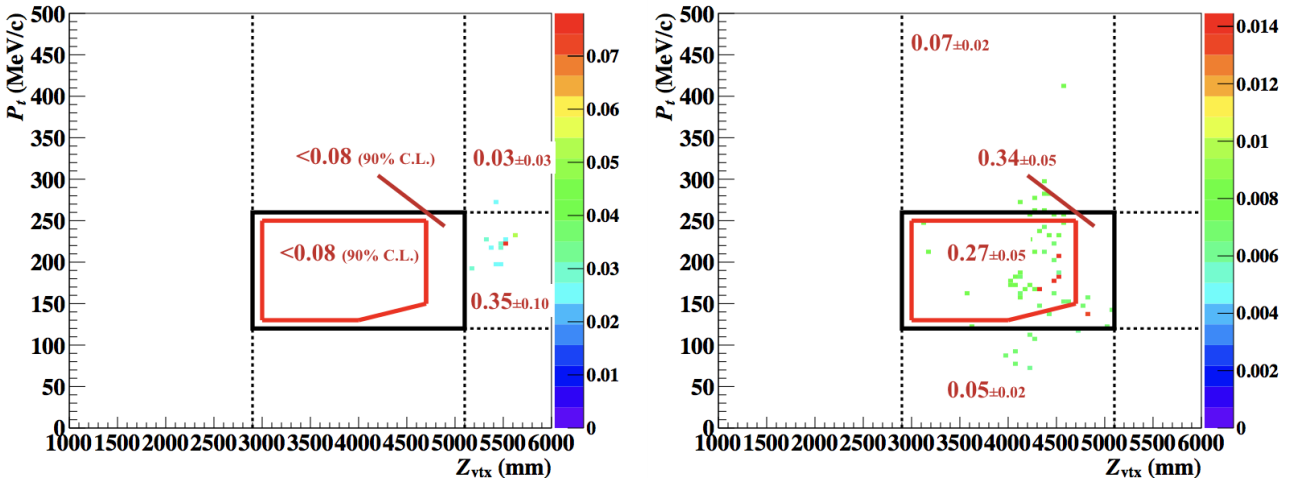

(a) CV-π^0 background (b) CV-η background

Figure 6.54: P_t-Z_{vtx} distributions of the CV-π^0 and CV-η events after all the cuts except for the eta-χ^2 cut imposed. The numbers in red indicate the number of events in each region bounded by lines.

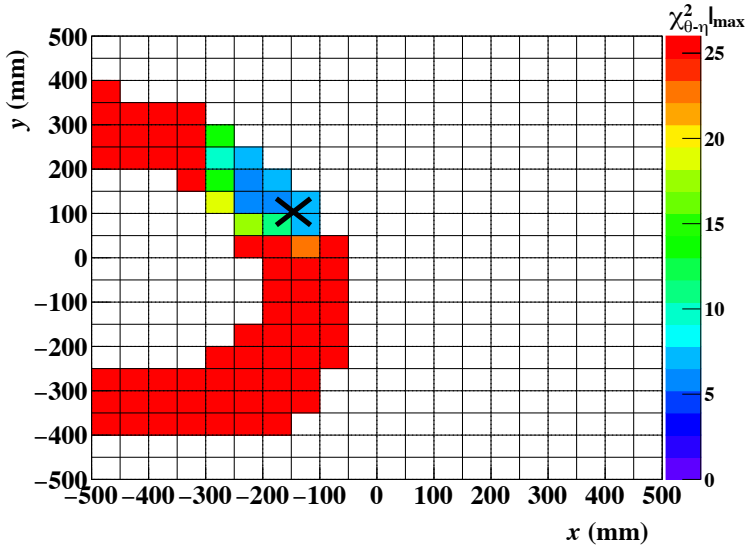

Figure 6.55: $\chi^2_{\theta\text{-}\eta}|_{\max}$ distributions of a CV-η event. The colored region represents the η vertex candidates. The black cross mark indicates decay position of η obtained from simulation record.

vertex candidates".

Next, for each η vertex candidate, we evaluated the consistency of the shower shapes of photons with the photons' incident angle using χ^2_θ defined in Eq. 6.13. The larger χ^2_θ of two photons is defined as $\chi^2_{\theta\text{-}\eta}|_{\max}$ for each η vertex candidate. An example of $\chi^2_{\theta\text{-}\eta}|_{\max}$ distribution of a CV-η event is shown in Fig. 6.55. Note that the $\chi^2_{\theta\text{-}\eta}|_{\max}$ became small if the cluster shapes of two photons were consistent with the assumption that those two photons were originated from the η vertex candidate.

Finally, the χ^2_η is given as the minimum $\chi^2_{\theta\text{-}\eta}|_{\max}$ among all the η vertex candidates.

The χ^2_η distributions of the $K_L \to \pi^0\nu\overline{\nu}$ signal and the CV-η background events are shown in Fig. 6.56. The signal acceptance and CV-η background reduction power as a function of eta-χ^2 cut threshold are shown in Fig. 6.57. Taking the signal acceptance and background rejection into account, we determined the cut point of χ^2_η to be 17. With this cut threshold, the signal acceptance and the number of background events in the signal region were 85% and 0.04 ± 0.02, respectively. The P_t-Z_{vtx}

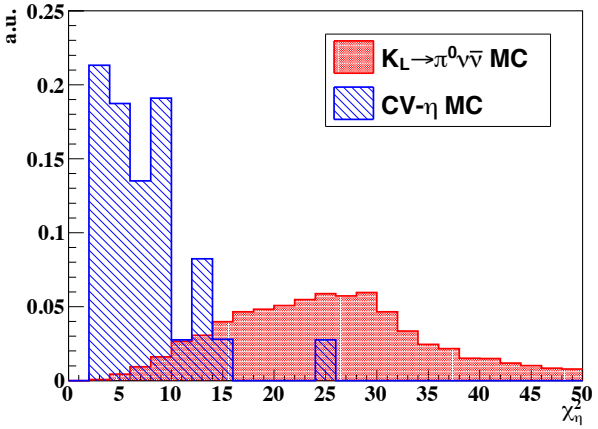

Figure 6.56: Distributions of of χ^2_η for the $K_L \to \pi^0\nu\bar{\nu}$ signal (red) and the CV-η background events (blue).

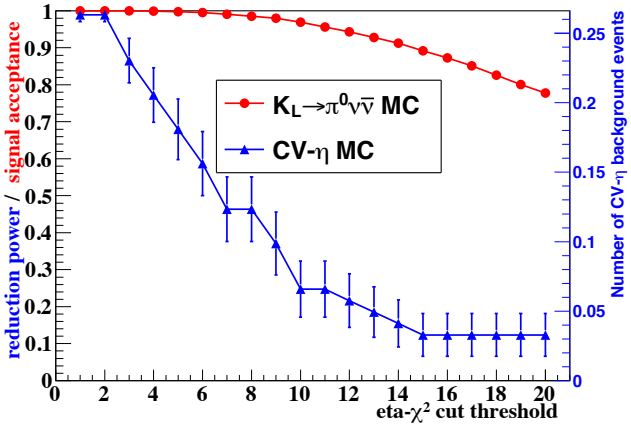

Figure 6.57: Signal acceptance (red) and CV-η background reduction power (blue) as a function of eta-χ^2 cut threshold. The right blue axis represents the corresponding number of CV-η background events for the blue graph.

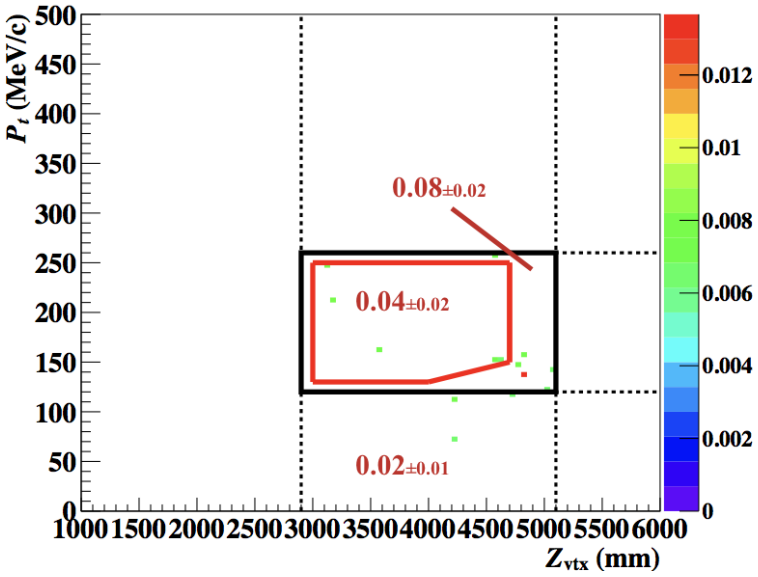

Figure 6.58: P_t-Z_{vtx} distributions of the CV-η events after all the cuts imposed. The numbers in red indicate the number of events in each region bounded by lines.

distribution of the CV-η background events after all the cuts imposed is shown in Fig. 6.58.

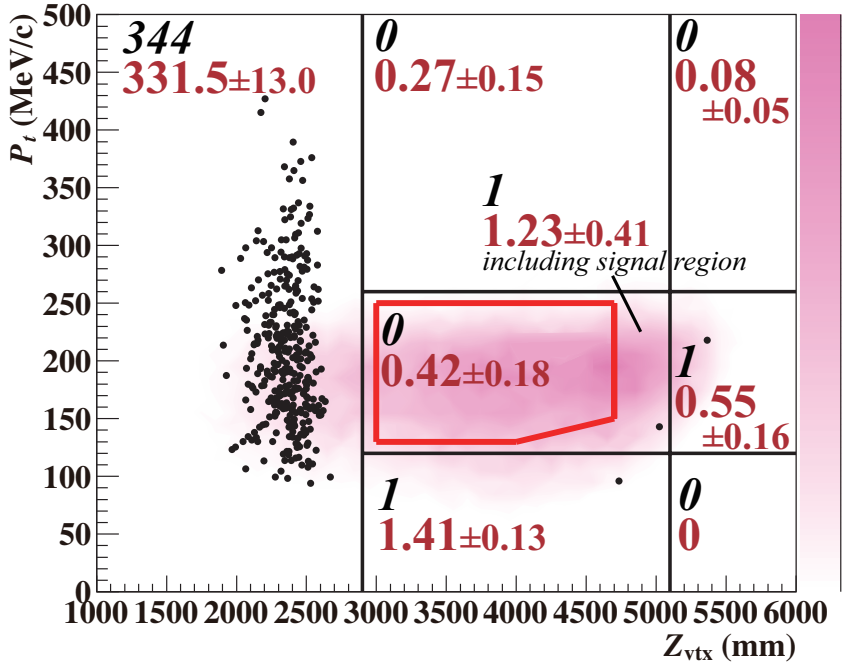

Figure 6.59: Reconstructed π^0 transverse momentum (P_t) versus π^0 decay vertex position ($Z_{\rm vtx}$) distribution of the events with all the cuts imposed. The region surrounded by red lines is the signal region. The black dots represent data points and the contour represents the $K_L \to \pi^0 \nu\overline{\nu}$ signal distribution derived from the simulation. The black italic (red regular) numbers indicate the numbers of observed (expected background) events for each region bounded by lines.

6.5 Results

6.5.1 Results of the $K_L \to \pi^0 \nu\overline{\nu}$ Search

After fixing all the selection criteria, we unblinded the masked region. As a result, no signal candidate events were observed in the signal region as shown in Fig. 6.59. From the Poisson statistics with uncertainties taken into account [88], we obtained an upper limit for the branching fraction of the $K_L \to \pi^0 \nu\overline{\nu}$ decay as 3.0×10^{-9} at the 90% C.L.

This result improved the previous best upper limit [11] by almost an order of magnitude.

6.5.2 Analysis and Results of the $K_L \to \pi^0 X^0$ Search

6.5.2.1 Signal Acceptance and Single Event Sensitivity for the $K_L \to \pi^0 X^0$ Decay

The signal acceptance for the $K_L \to \pi^0 X^0$ decay was obtained in a similar manner in $K_L \to \pi^0 \nu\overline{\nu}$. We prepared $K_L \to \pi^0 X^0$ simulation samples with several X^0 mass (m_{X^0}) hypotheses and estimated the signal acceptance for each m_{X^0} hypotheses.

The P_t-$Z_{\rm vtx}$ distributions of the $K_L \to \pi^0 X^0$ signal with $m_{X^0} = 135$ MeV/c^2 (mass of π^0) and $m_{X^0} = 260$ MeV/c^2 are shown in Fig. 6.60. The lower P_t threshold of the signal region limits the sensitivity for heavier X^0 since the signal distributes in the lower P_t region for heavier X^0 mass. The single event sensitivity for the $K_L \to \pi^0 X^0$ decay with the X^0 mass of 135 MeV/c^2 was obtained as $(1.01 \pm 0.01_{\rm stat.}) \times 10^{-9}$.

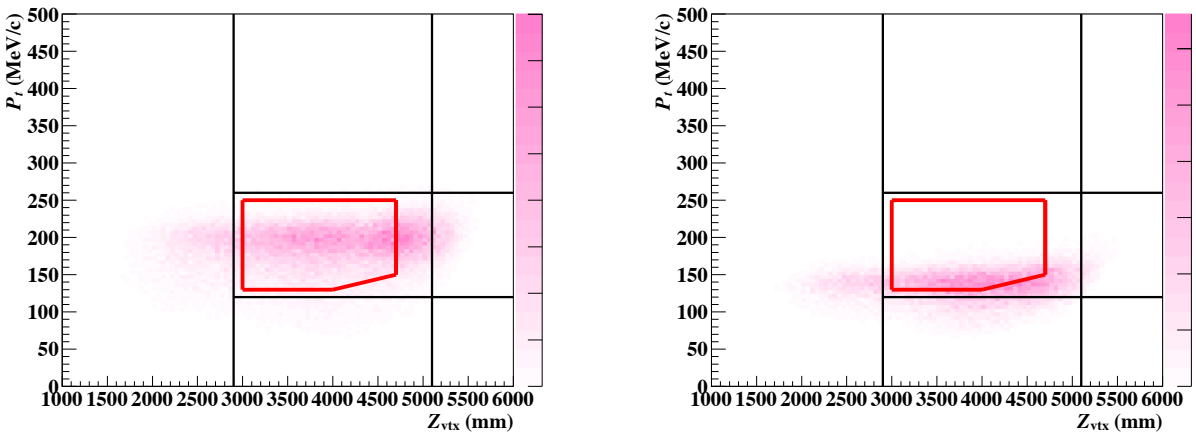

(a) $m_{X^0} = 135$ MeV/c^2 (b) $m_{X^0} = 260$ MeV/c^2

Figure 6.60: Reconstructed π^0 transverse momentum (P_t) versus π^0 decay vertex position ($Z_{\rm vtx}$) distributions of the $K_L \to \pi^0 X^0$ decay with different X^0 mass after all the cuts imposed. The region surrounded by red lines is the signal region and the contour represents the $K_L \to \pi^0 \nu\overline{\nu}$ signal distribution derived from the simulation.

6.5.2.2 Results of the $K_L \to \pi^0 X^0$ Search

Using the same systematic uncertainty for the single event sensitivity as in the $K_L \to \pi^0 \nu\overline{\nu}$ analysis (11%), we set an upper limit for the branching fraction of the $K_L \to \pi^0 X^0$ decay as a function of X^0 mass as shown in Fig. 6.61. The result for the $m_{X^0} = 135$ MeV/c^2 was 2.4×10^{-9} (90% C.L.) at the "loophole" of the indirect limit from the $K^+ \to \pi^+ X^0$ search [21] as described in Sec. 1.2.4. This result improved the previous best upper limit [10] by almost an order of magnitude. As shown in Fig. 6.62, this results gave the upper limit better than the indirect limit from the E949 experiment [21] in the heavy mass region, $m_{X^0} > 240$ MeV/c^2, where the sensitivity in the E949 experiment was limited due to the small momentum of π^+ derived from the decay of K^+ at rest.

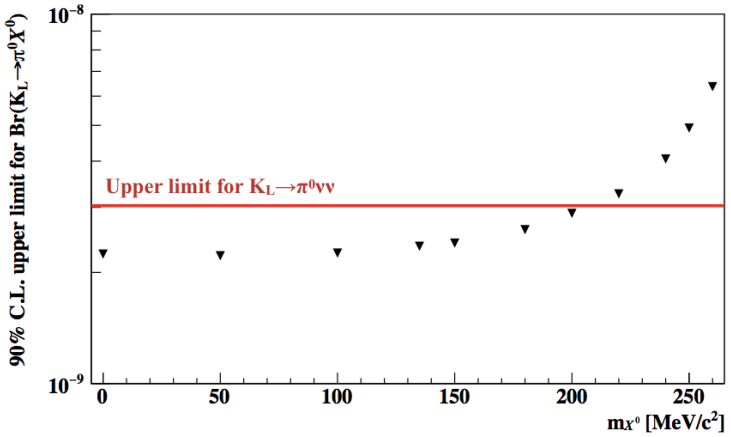

Figure 6.61: Upper limit at the 90% C.L. for the $K_L \to \pi^0 X^0$ branching fraction as a function of the X^0 mass. The limit for the $K_L \to \pi^0 \nu\overline{\nu}$ decay is shown with the red line for comparison.

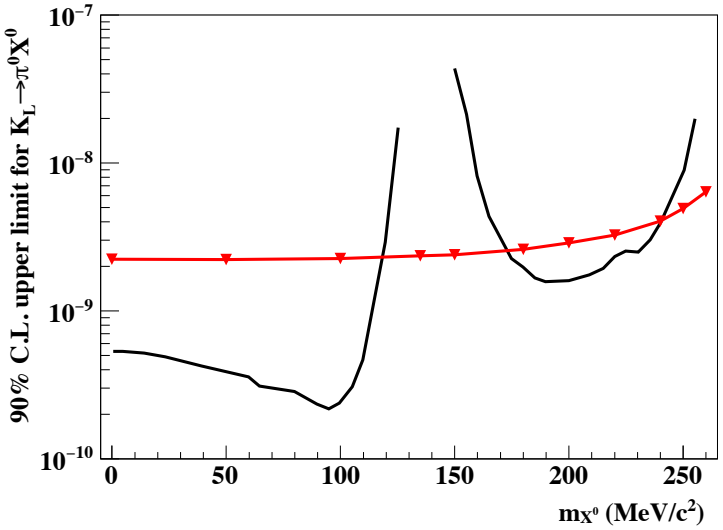

Figure 6.62: Comparison of the 90% C.L. upper limit for the $K_L \to \pi^0 X^0$ branching fraction between this measurement (red) and indirect limit from the E949 experiment (black) [21].

Chapter 7

Discussion

We achieved a significant improvement for the $K_L \to \pi^0 \nu\overline{\nu}$ and $K_L \to \pi^0 X^0$ search without no candidate events. To search for new physics beyond the SM, the search with the sensitivity approaching the SM sensitivity ($\sim 3 \times 10^{-11}$) is desired.

In this analysis, the expected number of background events was 0.42 in total. For the future search with better sensitivity, further background rejection is crucial.

Meanwhile, we also need to improve the signal acceptance. To achieve orders of magnitude improvement of the sensitivity in a practical time, we need higher beam intensity. Higher intensity of the beam, however, causes a higher accidental activity rate that induces a significant acceptance loss. J-PARC plans to improve the beam intensity up to 100 kW in several years. To get a benefit from the high-intensity beam, we need to reduce the accidental loss.

Here we discuss further background suppression and the recovery of the signal acceptance. The following is the review of ongoing efforts by the KOTO collaboration.

7.1 Further Background Suppression

7.1.1 Hadron-Cluster Background

The hadron-cluster background was the largest background in the 2015 data analysis and it was estimated to be 0.24 ± 0.17 events. Further suppression of this background is the most important subject of the KOTO experiment.

The hadron-cluster background is caused by the consecutive two hadronic showers originated from a halo-neutron directly hitting the CsI calorimeter. Due to the long interaction length of CsI for neutrons ($\sim$ 40 cm), interaction points of neutrons, or the start point of hadronic showers, tend to distribute broadly along the longitudinal (z) direction, whereas photons produce electromagnetic showers around the upstream surface of the CsI crystals due to the short radiation length for photons ($\sim$ 2 cm). Thus, if we know the longitudinal position of the interaction point, we can distinguish photons from neutrons.

We are upgrading the CsI calorimeter in the summer to winter of 2018 [89]. In this upgrade, we attach Multi-Pixel Photon Counters (MPPC's) on the upstream edges of the CsI crystals. With the both-end readout, we can obtain the longitudinal position of showers using the timing difference Δt between upstream and downstream signal timings. A study with a positron beam was performed and we obtained the timing resolution for Δt to be $\sigma_{\Delta t} = 0.4$ ns for the energy deposit larger than 600 MeV, which corresponds to the position resolution of $\sigma_z \sim 3$ cm. Figure 7.1 shows the distributions of Δt for the $K_L \to \pi^0 \nu\overline{\nu}$ signal and hadron-cluster background obtained by simulations. We achieved the background reduction power of 1/10 keeping the 90% signal acceptance [89].

In addition to the hardware upgrade, we are developing a new cluster shape discrimination [90] with deep learning techniques using a rich amount of the hadron-cluster control sample collected from 2016 to 2018. Although the performance is still under the estimation, we expect a factor of four

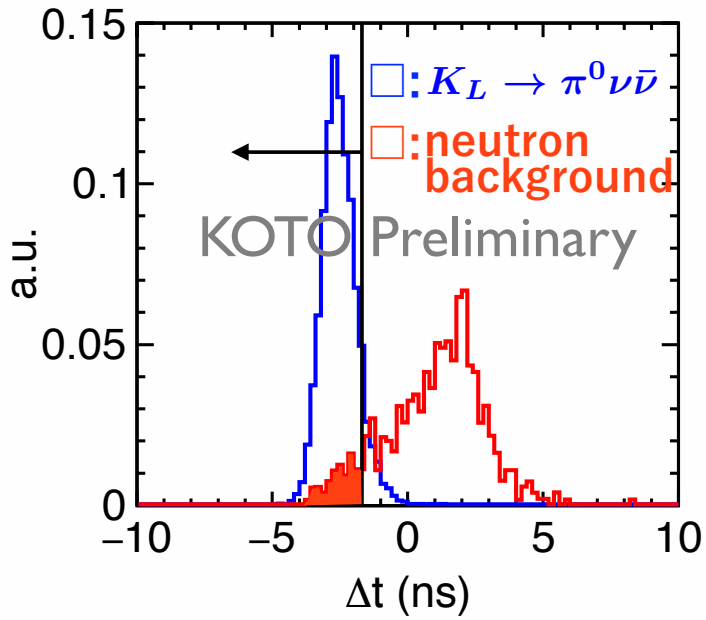

Figure 7.1: Distribution of the timing difference for simulations of $K_L \to \pi^0\nu\bar{\nu}$ (blue) and the hadron-cluster background (red). The black line represents the threshold of the Δt cut. The figure is quoted from Ref. [89].

improvement for the reduction power against the hadron-cluster background [90].

7.1.2 Upstream-π^0 background

As described in Sec. 6.4.2.2, half of the contributions from the upstream-π^0 background was a "photon + neutron event". This kind of events are expected to be suppressed by the methods to reduce the hadron-cluster background; reduction by a factor of three or more is anticipated for the photon + neutron events.

7.1.3 CV-η background

As for the CV-η background, we expect a factor two reduction in the data taken after 2015 because we moved the location of the support structure for the Membrane which was one of the η production sources after imposing all the cuts in the 2015 data analysis.

7.1.4 $K_L \to \pi^+\pi^-\pi^0$ Background

Among the K_L decay backgrounds, the largest contribution was the $K_L \to \pi^+\pi^-\pi^0$ background in the 2015 data analysis, which was estimated to be 0.05 ± 0.02 events. As described in Sec. 6.4.1.1, the $K_L \to \pi^+\pi^-\pi^0$ background was due to the absorption of charged pions in the non-active material downstream of the CsI calorimeter. Even after imposing the BPCV veto cut, we found that some events survived. Figure 7.2 shows the distribution of the endpoints of the charged pions in the remaining $K_L \to \pi^+\pi^-\pi^0$ simulated events after all the cuts imposed. The charged pions were absorbed in not only the downstream beam pipe but also in the G10 pipes which are placed inside the beam holes of the CsI calorimeter and CC04 to support the Membrane.

To detect these pions before they are absorbed, we plan to install a new detector component, which is called "Downstream Charged Veto (DCV)". The configuration of DCV is shown in Fig. 7.3. The DCV will be composed of two square pipes made of 5-mm-thick plastic scintillators (DCV1 and DCV2) and installed inside the high vacuum region. The G10 pipe inside the CC04 beam hole will be removed and the inside the CsI calorimeter beam hole will be shortened to reduce the amount of

non-active material. A simulation study shows that we can achieve the background reduction power of 1/50 with these upgrades [91]. These hardware upgrades will be completed by Feb. 2019.

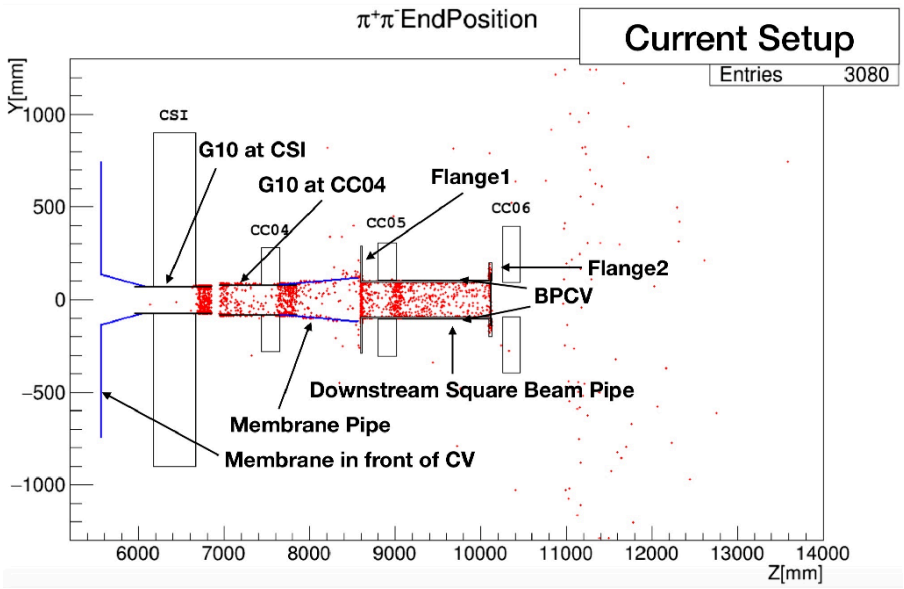

Figure 7.2: Cross-sectional view of the vanishment points of the charged pions in the $K_L \to \pi^+\pi^-\pi^0$ simulated events (red points). "Downstream Square Beam Pipe" indicates the downstream beam pipe. Even after BPCV veto cuts imposed, some charged pions are not detected when they hit the downstream beam pipe or G10 pipes. The figure is quoted from Ref. [91].

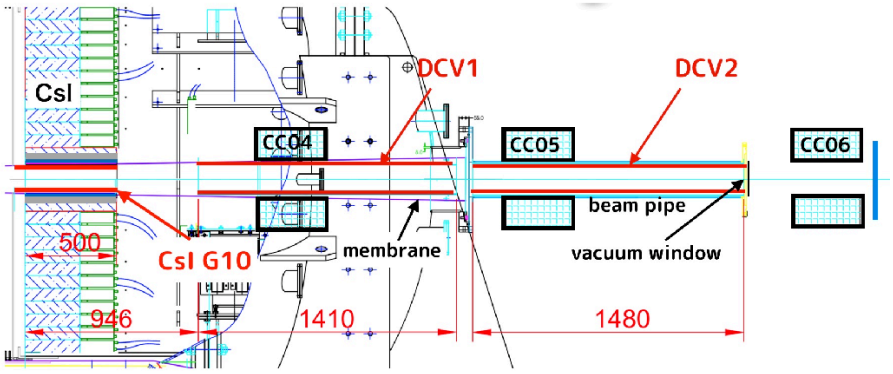

Figure 7.3: Configuration of a new detector component (DCV) to be placed inside the beam pipe. The DCV1 supports the membrane from the inside around CC04, while the DCV2 covers inside of the downstream beam pipe. The G10 pipe in the beam hole of the calorimeter will be shortened. The figure is quoted from Ref. [92].

7.1.5 $K_L \to 2\pi^0$ Background

To suppress the $K_L \to 2\pi^0$ background, we installed a new detector component, called "Inner Barrel (IB)" after the 2015 run. The IB is a barrel photon veto counter similar to MB. It is inserted inside MB to increase the total radiation length of the photon veto counters in the barrel region from $14.0X^0$ to $19X^0$. We expect the $K_L \to 2\pi^0$ background to be suppressed to 1/3, based on a simulation study [93].

In addition, we plan to replace the support structure of the CsI calorimeter cover ("Calorimeter

cover support" in Fig. 6.41) to reduce the amount of non-active material [94], which was one of the sources of photon detection inefficiency as mentioned in Sec. 6.4.1.2. We have not estimated the effects yet, but we expect that this upgrade, done in Dec. 2018, contributes to reducing the $K_L \to 2\pi^0$ background.

7.1.6 Summary of the Further Background Suppression

Taking the above prospects into account, even for the search with the sensitivity one order of magnitude better than the 2015 data analysis, we anticipate that the number of background events will be kept less than 1 event. Note that the above extrapolations are based on the 2015 run analysis with limited statistics of data and simulations, so that for further discussion appropriate amount of data / simulations expected to be corrected / generated in the next years are needed.

7.2 Acceptance Recovery

To identify the signal events, we need to veto events with any activities in the detector other than two photons from a π^0 decay. Acceptance loss due to accidental activities in the detector (accidental loss), for example due to another K_L decay and interaction with beam-halo particles, becomes larger with higher beam power. In the 2015 data analysis, we found that we lost 75% of the signal acceptance due to the accidental loss (with 42 kW beam intensity).

Let us consider a simple model of accidental loss due to a single veto counter. Assuming an accidental activity rate R and the width of the veto window T, The accidental loss is obtained as $1 - e^{-RT}$ with Poisson statistics. It tells us that we can mitigate the accidental loss by reducing accidental activity rate and shortening the veto window. Although we should consider multiple veto counters with different accidental rates and veto windows, and the correlation among them in the real situation, the basic thinking in this simplified model should hold.

We discuss the analysis update plan to shorten the veto window width of the veto counters, and the possible measures for the reduction of the accidental activity rate in the following sections.

7.2.1 Waveform Analysis for Timing Calculation

In the 2015 data analysis, we calculated veto timing based on the parabola interpolation method described in Sec. 4.1.2.1. With this method, however, the timing of a pulse can be wrongly reconstructed if it overlaps with another pulse as shown in Fig. 7.4a. Since this time shift causes veto failure, we used wide veto window: 60 ns for MB, 51 ns for FB, and 80 ns for CV, for example. If we can resolve the two pulses like Fig. 7.4a and obtain the correct time of the pulses, we can shorten the veto window and consequently reduce the accidental loss.

A new algorithm to fit waveforms with pulse shape template is now being developed [95]. Figure 7.4b shows an example of pulse finding with this algorithm. Two pulses are resolved and the timing of each pulse is obtained correctly.

Figure 7.5 shows the pulse resolving efficiency as a function of timing difference between two pulses. The new algorithm can separate two pulses with 20-30 ns shorter timing difference than the parabola interpolation method [95]. We anticipate that we can shorten the widths of the veto windows for FB, MB, NCC, and CV to 30-ns level.

7.2.2 Beam Structure

As described in Sec. 2.2.1, the time profile of our beam has the spike structure due to the ripple noise in the power supplies of the MR magnets. This spike structure enlarges the instantaneous rate of the beam particles. In the 2015 run, the typical value of the duty factor was 40-50%, and the instantaneous rate was effectively twice as high as that of the ideal flat beam.

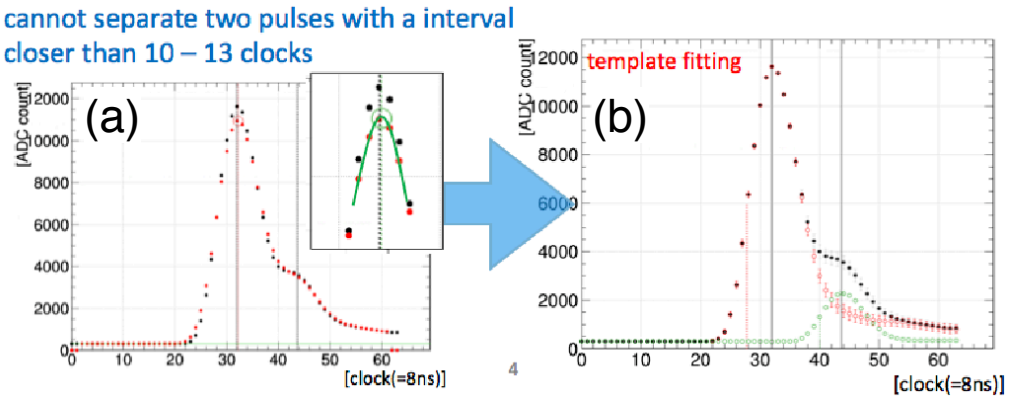

Figure 7.4: Example of pileup waveform. (a) the parabola interpolation method cannot separate two pulses, while (b) the new algorithm with pulse fitting finds two pulses (red and green dots) from a pileup waveform (black dots). The figures are quoted from Ref. [95].

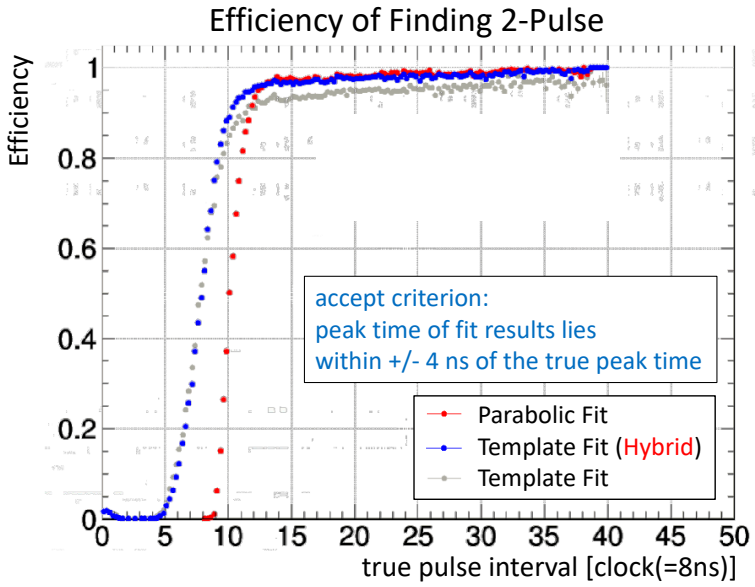

Figure 7.5: Pulse resolving efficiency as a function of the timing difference between two pulses. The red (blue) dots represent the results from the parabola interpolation method (new algorithm with pulse fitting). The figure is quoted from Ref. [95].

The J-PARC accelerator group plans to upgrade the power supplies for the MR magnets in 2021. In this upgrade, the ripple noise which induces the spike structure of the beam is expected to be substantially mitigated. We expect that this upgrade reduces the accidental activity rate effectively by half and thus helps to recover the signal acceptance.

7.2.3 Neutrons from the Primary Beamline

Accidental hit rates in FB, MV, NCC, and CC06 evaluated with TMON data with the beam plug (see Sec. 2.2.3) opened and closed are summarized in Table 7.1. Even with the beam plug closed, FB and MB still had high hit rates. The source of these activities was neutrons from the primary beamline as shown in Fig. 7.6.

To reduce the neutron flux, we plan to add a 20-cm-thick iron shield as shown in Fig. 7.7, which corresponds to 1.2 interaction length, before the data taking in 2020. Taking into account the effective

Table 7.1: Accidental hit rates with TMON data with the beam plug opened and closed taken in the Period-9 [96].

	energy threshold	hit rate (MHz)	
beam plug		open	close
FB	1 MeV	6.2	2.5
MB	1 MeV	5.6	3.4
NCC	1 MeV	5.2	0.7
CC06	3 MeV	4.7	0.1

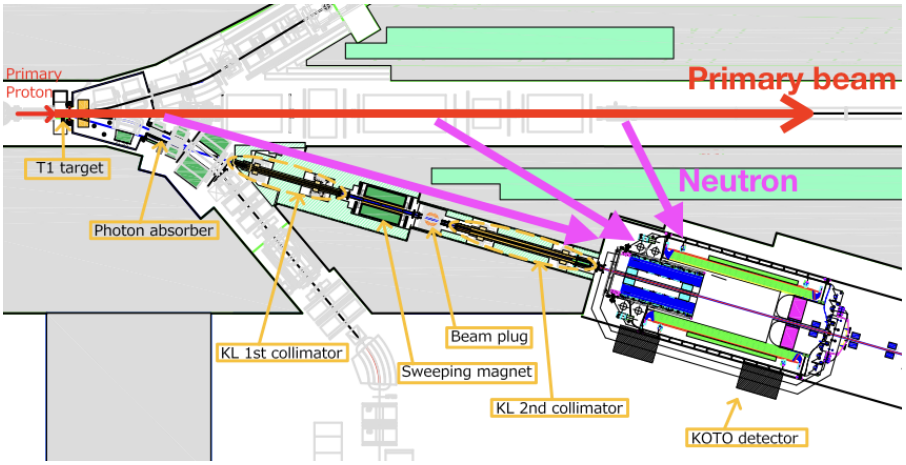

Figure 7.6: Schematic view of the neutron flux (magenta allows) comes from the primary beamline.

thickness of the iron shield, 2.5×20 cm[*1], due to the incident angle and energy distribution of the neutrons, we anticipate the neutron flux will be reduced to 5% of the current one.

[*1] The factor 2.5 is based on the empirical fact that a 30-cm-thick water shield (0.36 interaction length equivalent) installed in 2013 reduced the neutron flux by a factor of 0.4 ($= \exp(-0.36 \times 2.5)$).

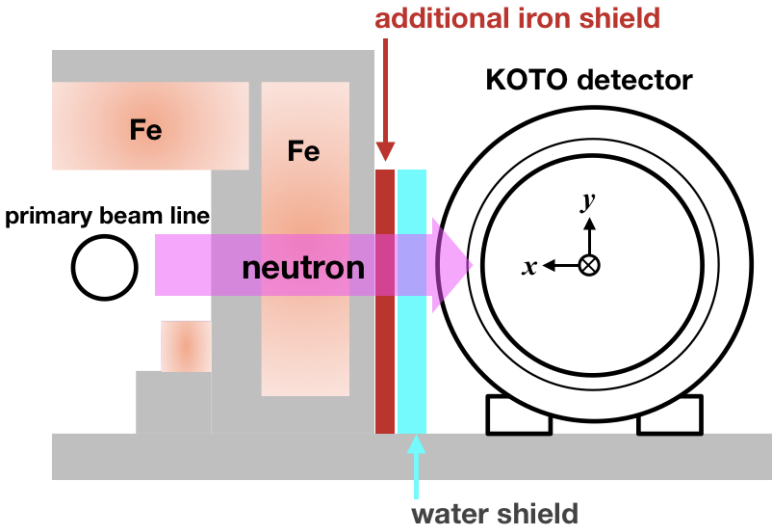

Figure 7.7: Cut-out view of the primary beamline and KOTO detector (quoted from Ref. [97]). The red rectangle represents the additional 20-cm-thick iron shield.

Chapter 8

Conclusion

We searched for the $K_L \to \pi^0 \nu\overline{\nu}$ and $K_L \to \pi^0 X^0$ decays with the KOTO 2015 data.

We developed new methods to suppress the "hadron-cluster background", which was the dominant background in the KOTO 2013 data analysis, by collecting and studying a large control sample. The number of the hadron-cluster background events was estimated to be 0.24 ± 0.17, which was the largest background in the 2015 data analysis. We found a new background source, "CV-η" background, which was not taken into account in the analysis of KOTO 2013 data, and developed a new method to eliminate this background.

With the single event sensitivity of $(1.30 \pm 0.01_{\text{stat.}} \pm 0.14_{\text{syst.}}) \times 10^{-9}$ for $K_L \to \pi^0 \nu\overline{\nu}$ and $(1.01 \pm 0.01_{\text{stat.}} \pm 0.11_{\text{syst.}}) \times 10^{-9}$ for $K_L \to \pi^0 X^0$ (with X^0 mass of 135 MeV/c^2), no signal candidate events were observed. The upper limits for the branching fraction of $K_L \to \pi^0 \nu\overline{\nu}$ and $K_L \to \pi^0 X^0$ were set as

$$\mathcal{B}(K_L \to \pi^0 \nu\overline{\nu}) < 3.0 \times 10^{-9}, \tag{8.1}$$

$$\mathcal{B}(K_L \to \pi^0 X^0) < 2.4 \times 10^{-9} \quad (m_{X^0} = 135 \text{ MeV}/c^2), \tag{8.2}$$

at the 90% C.L. These results improved the previous best upper limits by almost an order of magnitude.

In this analysis, I established the estimation method of the number of the hadron-cluster background events. I revealed that even with the newly developed analysis methods, the hadron-cluster background was still the dominant background. I also developed a new analysis method to eliminate the CV-η background. In addition, I performed the normalization modes analysis and the estimation of the signal acceptance developing new techniques to evaluate the trigger efficiencies and the cut efficiency of the pulse shape likelihood ratio cut for simulation samples. Through the $K_L \to 2\pi^0$ background analysis, I gave the knowledge of the sources of photon detection inefficiency, the non-active materials around the outer edge of the CsI calorimeter.

Future prospects for the background suppression and sensitivity recovery were also discussed. The new barrel photon counter installed in 2016 and detector upgrades ongoing in early 2019 are expected to reduce the background level. We also anticipate to improving the background rejection by improving analysis methods with a rich amount of hadron-cluster control sample taken from 2016 to 2018. To recover the signal acceptance, we are developing new timing calculation methods using waveform information to improve timing resolution by separating multi-pulses. The upgrade of the power supplies of the MR magnets improving the beam condition is also expected to greatly recover the signal acceptance.

We expect to achieve the sensitivity of 5×10^{-10} with the data taken by the end of 2018, and 1×10^{-10} with the data expected to be collected by the upgrade of the power supplies of the MR magnets in 2021. After that, by 2026, we anticipate to reaching the sensitivity of 3-5 $\times 10^{-11}$ to discover the $K_L \to \pi^0 \nu\overline{\nu}$ and $K_L \to \pi^0 X^0$ decays.

Appendix A

Details of Calculation of Veto Cut Variables

General treatments for the reconstruction of veto information are described in Sec. 4.3.2. Here, details of treatment for each veto counter are described.

A.1 MB and BCV

Treatments for MB and BCV were similar because both of them used both-end readout system. Let t_u and e_u (t_d and e_d) be the time and energy of upstream (downstream) readout channel of a module, respectively. The module-time was obtained by taking the average of t_u and t_d:

$$t_{\mathrm{mod}} = \frac{t_u + t_d}{2}. \tag{A.1}$$

Hit position z_{hit} of the particle which made the activity in the module was given by using the timing difference between upstream and downstream channels as

$$z_{\mathrm{hit}} = \frac{v_{\mathrm{prop}}}{2}(t_u - t_d), \tag{A.2}$$

where $v_{\mathrm{prop}} = 168.1$ mm/ns is the propagation velocity of light in MB and BCV modules, and the origin of z_{hit} is the center of MB and BCV ($z = z_0 = 4105$ mm). We then obtained the module-energy using e_u and e_d by correcting for a light attenuation as:

$$E_{\mathrm{mod}} = \frac{e_u}{\exp\left(\frac{-z_{\mathrm{hit}}}{\Lambda+\alpha z_{\mathrm{hit}}}\right)} + \frac{e_d}{\exp\left(\frac{z_{\mathrm{hit}}}{\Lambda-\alpha z_{\mathrm{hit}}}\right)}, \tag{A.3}$$

where $\Lambda = 4920.5$ mm and $\alpha = 0.495$ are attenuation parameters [57].

The TOF was calculated as

$$\Delta\mathrm{TOF} = \sqrt{\{(z_{\mathrm{hit}} + z_0) - Z_{\mathrm{vtx}}\}^2 + R^2}/c, \tag{A.4}$$

where R is the inner radius of the MB or BCV module and c is the speed of light.

A.2 CV

The module-energy was obtained as the sum of energies in the dual-end channels. The module-time was obtained as the mean of times in the dual-end channels.

The TOF was calculated as

$$\Delta\mathrm{TOF} = \sqrt{(z_{\mathrm{mod}} - Z_{\mathrm{vtx}})^2 + x_{\mathrm{mod}}^2 + y_{\mathrm{mod}}^2}/c, \tag{A.5}$$

where x_{mod} and y_{mod} (z_{mod}) are the positions of the center (upstream surface) of the module.

A.3 CC03

Each CC03 module was attached to a pair of PMT's. The module-energy and module-time are calculated as the mean of the two PMTs' information.

The TOF was calculated as

$$\Delta\text{TOF} = (z_{\text{CC03}} - Z_{\text{vtx}})/c, \tag{A.6}$$

where z_{CC03} is the z position of CC03.

A.4 CC04, CC05, and CC06

As for the charged particle veto counters (made of plastic-scintillator sheets) of CC04, CC05, and CC06, there were four modules and two of them had dual-end readout system. The module-energy and module-time of the modules with dual-end readout were obtained by taking the average of both channels. In the case of the other modules with single-end readout system, module-energy and module-time corresponded to the energy and time of the readout channel, respectively.

The TOF was calculated as

$$\Delta\text{TOF} = (z_{\text{det}} - Z_{\text{vtx}})/c, \tag{A.7}$$

where z_{det} is the z position of the detector component.

The veto decision was done separately in plastic-scintillator modules and in CsI modules[*1], which means veto-energy and veto-time were defined separately for each type of modules.

A.5 OEV, LCV, BPCV, FB, NCC, and Hinemos

For OEV, LCV, and BPCV, the TOF was calculated in the same way as CC04, CC05, and CC06 (Eq. A.7).

In the odd-pairing type $K_L \to 2\pi^0$ events (explained in) in which a K_L decay at upstream of NCC and the reconstructed Z_{vtx} is calculated wrongly, TOF correction based on Z_{vtx} information work wrongly and can cause veto failure. For this reason, for FB, NCC, and Hinemos which were located upstream of the CsI calorimeter, the TOF correction was applied as it canceled the TOF correction in the vertex time, namely TOF from Z_{vtx} to the CsI calorimeter:

$$\Delta\text{TOF} = (z_{\text{CSI}} - Z_{\text{vtx}})/c, \tag{A.8}$$

where z_{CSI} is the z position of the CsI calorimeter. As a result, effectively the module-veto-time of these veto counters are given simply as the timing difference between hit time in CSI and hit time in the module of the veto counter.

A.6 newBHCV

For newBHCV the module-energy and module-time were given from the energy and timing information of each readout channel as was done in other veto counters with single-end readout system and the TOF correction was given as in Eq. A.7.

As explained in Sec. 2.2.4, newBHCV was composed of three layers of chambers, and charged particles hitting newBHCV basically penetrated all the three layers. We define "*layer-veto-energy*" and "*layer-veto-time*" as the largest module-energy in a given veto window in a layer and its module-time, respectively. If two or three modules had the layer-veto-energy larger than a given energy threshold, such an event was vetoed (2-out-of-3 logic).

[*1] In the case of CsI modules of CC04, which were composed of two types of CsI crystals with different sizes, the two types were treated separately in the veto decision.

A.7 BHPV

For the veto decision of BHPV, we required the coincidence of consecutive three or more modules' hits in order to reduce the accidental veto effects from neutrons in the beam, because electromagnetic showers produced by photons develops to the forward direction while hadronic showers by neutrons tend to have more isotropic angular distribution in the shower development. Effects from low-energy beam-contained photons are also suppressed by this requirement.

The algorithm to search for a hit-coincidence is described below. First, in this algorithm, we used hits in BHPV channels with the number of equivalent photons larger than 2.5. We corrected the timing of the hits ($t_{\rm hit}$) to the time at the most upstream BHPV module ($t'_{\rm hit}$) assuming that the photon which made the activity came from upstream:

$$t'_{\rm hit} = t_{\rm hit} - (z_{\rm mod} - z_0)/c, \tag{A.9}$$

where z_0 and $z_{\rm mod}$ are z positions of the most upstream BHPV module and of the module in which the hit is recorded, respectively. Next, we picked a hit in a module and then searched the next downstream module for hits within $\pm$10 ns of the timing. If such hits existed, we searched the next-next consecutive module. Repeating this procedure until no hits were found in the consecutive module, we obtained the number of coincidence modules ($N_{\rm coin}$) and the coincidence time ($t_{\rm coin}$) as the average time of the coincident hits.

The above procedure to search for a hit-coincidence was iterated using the remaining hits until all the hits were assigned into coincidence groups. After searching for hit-coincidences, we made a veto decision based on $N_{\rm coin}$ and $t_{\rm coin}$ of each hit-coincidence. The "*veto-coincidence-time*" ($t^{\rm veto}_{\rm coin}$) was defined as

$$t^{\rm veto}_{\rm coin} = t_{\rm coin} - T_{\rm vtx} - (z_0 - Z_{\rm vtx})/c, \tag{A.10}$$

and veto-number-of-coincidence ($N^{\rm veto}_{\rm coin}$) was defined as the largest $N_{\rm coin}$ in the event with its $t^{\rm veto}_{\rm coin}$ within a given veto window. If $N^{\rm veto}_{\rm coin}$ was 3 or more, such an event was vetoed.

A.8 BHGC

For BHGC, we used the number of equivalent photons of hit instead of module-energy. We reconstructed BHGC module hit information by merging the multiple-hit information of a pair of channels assigned for a module. If there were hits in both channels within $\pm$10 ns of timing, these hits were merged into one hit. For such a merged hit, the hit timing was given as an average of original hit timings and the number of equivalent photons was given as the sum of those of original hits. The timing and the number of equivalent photons of module hits were used to veto the event.

We defined a variable $t^{\rm veto}_{\rm hit}$ for each hit in BHGC modules as

$$t^{\rm veto}_{\rm hit} = t_{\rm hit} - T_{\rm vtx} - (z_{\rm BHGC} - Z_{\rm vtx})/c, \tag{A.11}$$

where $z_{\rm BHGC}$ is the z position of BHGC. We also defined a variable called "*veto-$N_{p.e.}$*", which is similar to veto-energy, as the largest number of equivalent photons among all the hits in BHGC with their $t^{\rm veto}_{\rm hit}$ within a given veto window. If the veto-$N_{p.e.}$ was larger than 2.5, such an event was vetoed.

References

[1] A. D. Sakharov, Pisma Zh. Eksp. Teor. Fiz. 5 (1967) 32–35, [Usp. Fiz. Nauk161,no.5,61(1991)]. doi:10.1070/PU1991v034n05ABEH002497.

[2] J. H. Christenson *et al.*, Phys. Rev. Lett. 13 (1964) 138–140. doi:10.1103/PhysRevLett.13.138, [link].
URL https://link.aps.org/doi/10.1103/PhysRevLett.13.138

[3] N. Cabibbo, Phys. Rev. Lett. 10 (1963) 531–533. doi:10.1103/PhysRevLett.10.531, [link].
URL https://link.aps.org/doi/10.1103/PhysRevLett.10.531

[4] M. Kobayashi, T. Maskawa, Prog. Theor. Phys. 49 (2) (1973) 652–657. doi:10.1143/PTP.49.652, [link].
URL http://dx.doi.org/10.1143/PTP.49.652

[5] P. Huet, E. Sather, Phys. Rev. D 51 (1995) 379–394. doi:10.1103/PhysRevD.51.379, [link].
URL https://link.aps.org/doi/10.1103/PhysRevD.51.379

[6] L. S. Littenberg, Phys. Rev. D 39 (1989) 3322–3324. doi:10.1103/PhysRevD.39.3322, [link].
URL https://link.aps.org/doi/10.1103/PhysRevD.39.3322

[7] V. Cirigliano *et al.*, Rev. Mod. Phys. 84 (2012) 399–447, and references therein. doi:10.1103/RevModPhys.84.399, [link].
URL https://link.aps.org/doi/10.1103/RevModPhys.84.399

[8] J. Comfort et al., "Proposal for $K_L \to \pi^0 \nu\bar{\nu}$ Experiment at J-Parc" (2016), data last accessed February 14th, 2019 (https://j-parc.jp/researcher/Hadron/en/pac_0606/pdf/p14-Yamanaka.pdf).

[9] T. Yamanaka, Prog. Theor. Exp. Phys. 2012 (1) (2012) 02B006. doi:10.1093/ptep/pts057, [link].
URL http://dx.doi.org/10.1093/ptep/pts057

[10] J. K. Ahn et al., Prog. Theor. Exp. Phys. 2017 (2) (2017) 021C01. doi:10.1093/ptep/ptx001.

[11] J. K. Ahn *et al.*, Phys. Rev. D 81 (2010) 072004. doi:10.1103/PhysRevD.81.072004, [link].
URL https://link.aps.org/doi/10.1103/PhysRevD.81.072004

[12] K. Fuyuto, W.-S. Hou, M. Kohda, Phys. Rev. Lett. 114 (2015) 171802. doi:10.1103/PhysRevLett.114.171802, [link].
URL https://link.aps.org/doi/10.1103/PhysRevLett.114.171802

[13] K. Fuyuto, W.-S. Hou, M. Kohda, Phys. Rev. D 93 (2016) 054021. doi:10.1103/PhysRevD.93.054021, [link].
URL https://link.aps.org/doi/10.1103/PhysRevD.93.054021

[14] L. Wolfenstein, Phys. Rev. Lett. 51 (1983) 1945–1947. doi:10.1103/PhysRevLett.51.1945, [link].
URL https://link.aps.org/doi/10.1103/PhysRevLett.51.1945

[15] M. Tanabashi et al., Phys. Rev. D 98 (2018) 030001. doi:10.1103/PhysRevD.98.030001, [link].
URL https://link.aps.org/doi/10.1103/PhysRevD.98.030001

[16] K. Shiomi, Measurement of K_L^0 flux at the J-PARC neutral-kaon beam line for the $K_L^0 \to \pi^0\nu\bar{\nu}$ experiment, Ph.D. thesis, Kyoto University, data last accessed February 14th, 2019 (https://www-he.scphys.kyoto-u.ac.jp/theses/doctor/dt_shiomi.pdf) (2012).

[17] S. L. Glashow, J. Iliopoulos, L. Maiani, Phys. Rev. D 2 (1970) 1285–1292. doi:10.1103/PhysRevD.2.1285, [link].
URL https://link.aps.org/doi/10.1103/PhysRevD.2.1285

[18] A. J. Buras *et al.*, J. High Energy Phys. 2015 (11) (2015) 33. doi:10.1007/JHEP11(2015)033, [link].
URL https://doi.org/10.1007/JHEP11(2015)033

[19] Y. Grossman, Y. Nir, Phys. Lett. B 398 (1) (1997) 163 – 168. doi:10.1016/S0370-2693(97)00210-4, [link].
URL http://www.sciencedirect.com/science/article/pii/S0370269397002104

[20] W. J. Marciano, Z. Parsa, Phys. Rev. D 53 (1996) R1–R5. doi:10.1103/PhysRevD.53.R1, [link].
URL https://link.aps.org/doi/10.1103/PhysRevD.53.R1

[21] A. V. Artamonov et al., Phys. Rev. D 79 (2009) 092004. doi:10.1103/PhysRevD.79.092004, [link].
URL https://link.aps.org/doi/10.1103/PhysRevD.79.092004

[22] E. Cortina Gil et al.arXiv:1811.08508, [link].
URL https://arxiv.org/abs/1811.08508

[23] A. J. Buras, D. Buttazzo, R. Knegjens, J. High Energy Phys. 2015 (11) (2015) 166. doi:10.1007/JHEP11(2015)166, [link].
URL https://doi.org/10.1007/JHEP11(2015)166

[24] M. Tanimoto, K. Yamamoto, Prog. Theor. Exp. Phys. 2016 (12) (2016) 123B02. doi:10.1093/ptep/ptw160, [link].
URL http://dx.doi.org/10.1093/ptep/ptw160

[25] A. Crivellin *et al.*, Phys. Rev. D 96 (2017) 015023. doi:10.1103/PhysRevD.96.015023, [link].
URL https://link.aps.org/doi/10.1103/PhysRevD.96.015023

[26] M. Bordone *et al.*, Eur. Phys. J. C 77 (9) (2017) 618. doi:10.1140/epjc/s10052-017-5202-1, [link].
URL https://doi.org/10.1140/epjc/s10052-017-5202-1

[27] S. Fajfer, N. Košnik, L. V. Silva, Eur. Phys. J. C 78 (4) (2018) 275. doi:10.1140/epjc/s10052-018-5757-5, [link].
URL https://doi.org/10.1140/epjc/s10052-018-5757-5

[28] M. Endo *et al.*, J. High Energy Phys. 2018 (4) (2018) 19. doi:10.1007/JHEP04(2018)019, [link].
URL https://doi.org/10.1007/JHEP04(2018)019

[29] X.-G. He, G. Valencia, K. Wong, Eur. Phys. J. C 78 (6) (2018) 472. doi:10.1140/epjc/s10052-018-5964-0, [link].
URL https://doi.org/10.1140/epjc/s10052-018-5964-0

[30] C.-H. Chen, T. Nomura, J. High Energy Phys. 2018 (8) (2018) 145. doi:10.1007/JHEP08(2018)145, [link].
URL https://doi.org/10.1007/JHEP08(2018)145

[31] F. Ambrosino et al.arXiv:1901.03099.

[32] G. Isidori *et al.*, J. High Energy Phys. 2006 (08) (2006) 064–064. doi:10.1088/1126-6708/2006/08/064, [link].
URL https://doi.org/10.1088%2F1126-6708%2F2006%2F08%2F064

[33] M. Blanke *et al.*, Acta Phys. Polon. B41 (2010) 657–683. arXiv:0906.5454.

[34] A. J. Buras *et al.*, J. High Energy Phys. 2014 (11) (2014) 121. doi:10.1007/JHEP11(2014)121, [link].
URL https://doi.org/10.1007/JHEP11(2014)121

[35] A. J. Buras, F. De Fazio, J. Girrbach, J. High Energy Phys. 2013 (2) (2013) 116. doi:10.1007/JHEP02(2013)116, [link].
URL https://doi.org/10.1007/JHEP02(2013)116

[36] J. Brod, M. Gorbahn, Phys. Rev. D 82 (2010) 094026. doi:10.1103/PhysRevD.82.094026, [link].
URL https://link.aps.org/doi/10.1103/PhysRevD.82.094026

[37] M. Blanke, Acta Phys. Polon. B41 (2010) 127. arXiv:0904.2528, [link].
URL http://www.actaphys.uj.edu.pl/vol41/abs/v41p0127

[38] M. Blanke *et al.*, J. High Energy Phys. 2009 (03) (2009) 108–108. doi:10.1088/1126-6708/2009/03/108, [link].
URL https://doi.org/10.1088%2F1126-6708%2F2009%2F03%2F108

[39] F. Jegerlehner, A. Nyffeler, Physics Reports 477 (1) (2009) 1 – 110. doi:https://doi.org/10.1016/j.physrep.2009.04.003, [link].
URL http://www.sciencedirect.com/science/article/pii/S0370157309001306

[40] X. G. He *et al.*, Phys. Rev. D 43 (1991) R22–R24. doi:10.1103/PhysRevD.43.R22, [link].
URL https://link.aps.org/doi/10.1103/PhysRevD.43.R22

[41] G. Graham *et al.*, Phys. Lett. B 295 (1) (1992) 169 – 173. doi:10.1016/0370-2693(92)90107-F, [link].
URL http://www.sciencedirect.com/science/article/pii/037026939290107F

[42] M. Weaver *et al.*, Phys. Rev. Lett. 72 (1994) 3758–3761. doi:10.1103/PhysRevLett.72.3758, [link].
URL https://link.aps.org/doi/10.1103/PhysRevLett.72.3758

[43] J. Adams *et al.*, Phys. Lett. B 447 (3) (1999) 240 – 245. doi:10.1016/S0370-2693(98)01593-7, [link].
URL http://www.sciencedirect.com/science/article/pii/S0370269398015937

[44] A. Alavi-Harati *et al.*, Phys. Rev. D 61 (2000) 072006. doi:10.1103/PhysRevD.61.072006, [link].
URL https://link.aps.org/doi/10.1103/PhysRevD.61.072006

[45] J. K. Ahn *et al.*, Phys. Rev. D 74 (2006) 051105. doi:10.1103/PhysRevD.74.051105, [link].
URL https://link.aps.org/doi/10.1103/PhysRevD.74.051105

[46] J. K. Ahn *et al.*, Phys. Rev. Lett. 100 (2008) 201802. doi:10.1103/PhysRevLett.100.201802, [link].
URL https://link.aps.org/doi/10.1103/PhysRevLett.100.201802

[47] S. Nagamiya, Prog. Theor. Exp. Phys. 2012 (1) (2012) 02B001. doi:10.1093/ptep/pts025, [link].
URL http://dx.doi.org/10.1093/ptep/pts025

[48] M. Ikegami, Prog. Theor. Exp. Phys. 2012 (1) (2012) 02B002. doi:10.1093/ptep/pts019, [link].
URL http://dx.doi.org/10.1093/ptep/pts019

[49] K. Hasegawa, Comissioning of energy upgraded linac of J-PARC, in: Proceedings, 27th Linear Accelerator Conference, LINAC2014, no. TUIOB03, 2014, p. 417.
URL https://accelconf.web.cern.ch/accelconf/SRF2011/papers/tuiob03.pdf

[50] H. Hotchi *et al.*, Prog. Theor. Exp. Phys. 2012 (1) (2012) 02B003. doi:10.1093/ptep/pts021, [link].
URL http://dx.doi.org/10.1093/ptep/pts021

[51] T. Koseki *et al.*, Prog. Theor. Exp. Phys. 2012 (1) (2012) 02B004. doi:10.1093/ptep/pts071, [link].
URL http://dx.doi.org/10.1093/ptep/pts071

[52] K. Agari *et al.*, Prog. Theor. Exp. Phys. 2012 (1) (2012) 02B008. doi:10.1093/ptep/pts034, [link].
URL http://dx.doi.org/10.1093/ptep/pts034

[53] H. Takahashi *et al.*, J. Radioanal. Nucl. Chem. 305 (3) (2015) 803 – 809. doi:10.1007/s10967-015-3940-9.

[54] T. Shimogawa, Nucl. Instrum. Methods Phys. Res., Sect. A 623 (1) (2010) 585 – 587. doi:10.1016/j.nima.2010.03.078, [link].
URL http://www.sciencedirect.com/science/article/pii/S016890021000642X

[55] K. Shiomi *et al.*, Nucl. Instrum. Methods Phys. Res., Sect. A 664 (1) (2012) 264 – 271. doi:10.1016/j.nima.2011.11.010, [link].
URL http://www.sciencedirect.com/science/article/pii/S0168900211020444

[56] T. Masuda *et al.*, Prog. Theor. Exp. Phys. 2016 (1) (2016) 013C03. doi:10.1093/ptep/ptv171, [link].
URL http://dx.doi.org/10.1093/ptep/ptv171

[57] T. Masuda, Development and Experimental Study of the KOTO Detector System using Three K_L Neutral Decay Modes, Ph.D. thesis, Kyoto University, data last accessed February 14th, 2019 (https://www-he.scphys.kyoto-u.ac.jp/theses/doctor/taka_dt.pdf) (2014).

[58] K. Sato, Measurement of the csi calorimeter performance and k_l momentum spectrum for the j-parc koto experiment, Ph.D. thesis, Osaka University, data last accessed February 14th, 2019 (http://osksn2.hep.sci.osaka-u.ac.jp/theses/doctor/2015/dt_sato.pdf) (2015).

[59] R. E. Ray, The KTeV pure CsI calorimeter, in: Calorimetry in high-energy physics. Proceedings, 5th International Conference, Brookhaven, Upton, USA, September 25 - October 1, 1994, Vol. C940925, 1994, pp. 110–115.
URL http://lss.fnal.gov/archive/1994/conf/Conf-94-418.pdf

[60] Y. Yanagida, H. Yoshimoto, Reusing KTeV CsI crystals for J-PARC KOTO experiment, in: Proceedings, International Conference on Kaon (KAON09): Tsukuba, Japan, June 9-12, 2009, Vol. KAON09, 2009, p. 021. doi:10.22323/1.083.0021.

[61] S. Kubota *et al.*, Nucl. Instrum. Methods Phys. Res., Sect. A 268 (1) (1988) 275 – 277. doi:10.1016/0168-9002(88)90619-5, [link].
URL http://www.sciencedirect.com/science/article/pii/0168900288906195

[62] A. Alavi-Harati *et al.*, Phys. Rev. D 67 (2003) 012005, see in Sec.C.2 *The CsI calorimeter*. doi:10.1103/PhysRevD.67.012005, [link].
URL https://link.aps.org/doi/10.1103/PhysRevD.67.012005

[63] K. Sato *et al.*, JPS Conf. Proc. 8 (2015) 024007. doi:10.7566/JPSCP.8.024007.

[64] D. Naito *et al.*, Prog. Theor. Exp. Phys. 2016 (2) (2016) 023C01. doi:10.1093/ptep/ptv191, [link].
URL http://dx.doi.org/10.1093/ptep/ptv191

[65] Y. Tajima *et al.*, Nucl. Instrum. Methods Phys. Res., Sect. A 592 (3) (2008) 261 – 272. doi:10.1016/j.nima.2008.04.080, [link].
URL http://www.sciencedirect.com/science/article/pii/S0168900208006505

[66] N. Kawasaki, PoS KAON13 (2013) 040. doi:10.22323/1.181.0040.

[67] Y. Maeda, Search for the decay $k_l \to \pi^0\nu\bar{\nu}$ with a neutron-insensitive gev-energy photon detector, Ph.D. thesis, Kyoto University, data last accessed February 14th, 2019 (https://www-he.scphys.kyoto-u.ac.jp/theses/doctor/dt_maeda.pdf) (2016).

[68] T. Matsumura *et al.*, Nucl. Instrum. Methods Phys. Res., Sect. A 795 (2015) 19 – 31. doi:10.1016/j.nima.2015.05.036, [link].
URL http://www.sciencedirect.com/science/article/pii/S0168900215006762

[69] Y. Sugiyama, Pulse shape discrimination method to suppress neutron-induced background in the j-parc koto experiment, Ph.D. thesis, Osaka University, data last accessed February 14th, 2019 (http://osksn2.hep.sci.osaka-u.ac.jp/theses/doctor/2016/dt_sugiyama.pdf) (2016).

[70] K. Nakagiri *et al.*, JPS Conf. Proc. 8 (2015) 024004. doi:10.7566/JPSCP.8.024004.

[71] K. Nakagiri, PoS FPCP2015 (2015) 081. doi:10.22323/1.248.0081.

[72] Y. Maeda *et al.*, Prog. Theor. Exp. Phys. 2015 (6) (2015) 063H01. doi:10.1093/ptep/ptv074, [link].
URL http://dx.doi.org/10.1093/ptep/ptv074

[73] S. Shinohara, PoS FPCP2015 (2015) 079. doi:10.22323/1.248.0079.

[74] S. Shinohara, J. Phys. Conf. Ser. 800 (1) (2017) 012044. doi:10.1088/1742-6596/800/1/012044, [link].
URL http://stacks.iop.org/1742-6596/800/i=1/a=012044

[75] T. Matsumura *et al.*, Nucl. Instrum. Methods Phys. Res., Sect. A 885 (2018) 91 – 97. doi:10.1016/j.nima.2017.12.019, [link].
URL http://www.sciencedirect.com/science/article/pii/S0168900217313736

[76] Y. Sugiyama *et al.*, IEEE Trans. Nucl. Sci. 62 (3) (2015) 1115–1121. doi:10.1109/TNS.2015.2417312.

[77] S. Su *et al.*, IEEE Trans. Nucl. Sci. 64 (6) (2017) 1338–1345. doi:10.1109/TNS.2017.2694040.

[78] M. Bogdan, J. Genat, Y. Wah, Custom daq module for timing and energy measurements for j-parc e14, in: Proceedings of the 16th IEEE-NPSS Real Time Conference, Beijing, 2009, 2009, pp. 443–445. doi:10.1109/RTC.2009.5321611.

[79] E. Iwai, Csi calorimeter for the j-parc koto experiment, Ph.D. thesis, Osaka University, data last accessed February 14th, 2019 (http://osksn2.hep.sci.osaka-u.ac.jp/theses/doctor/2012/dt_iwai.pdf) (2012).

[80] M. Bogdan, J. Genat, Y. Wah, Custom 12-bit, 500mhz adc/data processing module for the koto experiment at j-parc, in: Proceedings of the 17th IEEE-NPSS Real Time Conference, Lisbon, 2010, 2010, pp. 1–2. doi:10.1109/RTC.2010.5750452.

[81] L. Jong-won, Energy Calibration Method for the KOTO CsI Calorimeter, Ph.D. thesis, Osaka University, data last accessed February 14th, 2019 (http://osksn2.hep.sci.osaka-u.ac.jp/theses/doctor/2014/dt_jwlee.pdf) (2014).

[82] S. Agostinelli et al., Nucl. Instrum. Methods Phys. Res., Sect. A 506 (3) (2003) 250 – 303. doi:10.1016/S0168-9002(03)01368-8, [link].
URL http://www.sciencedirect.com/science/article/pii/S0168900203013688

[83] J. Allison et al., IEEE Trans. Nucl. Sci. 53 (1) (2006) 270–278. doi:10.1109/TNS.2006.869826.

[84] J. Allison et al., Nucl. Instrum. Methods Phys. Res., Sect. A 835 (2016) 186 – 225. doi:10.1016/j.nima.2016.06.125, [link].
URL http://www.sciencedirect.com/science/article/pii/S0168900216306957

[85] K. A. Olive et al., Chin. Phys. C38 (2014) 090001. doi:10.1088/1674-1137/38/9/090001.

[86] Y. C. Tung, presentation in KOTO weekly meeting (2016).

[87] Y. C. Tung, presentation in KOTO weekly meeting (2016).

[88] R. D. Cousins, V. L. Highland, Nucl. Instrum. Methods Phys. Res., Sect. A 320 (1) (1992) 331 – 335. doi:10.1016/0168-9002(92)90794-5, [link].
URL http://www.sciencedirect.com/science/article/pii/0168900292907945

[89] K. Kotera, Four dimensional calorimetry with both-side readout of the CsI calorimeter in the $K_L \to \pi^0\nu\bar{\nu}$ search, proceedings for ICHEP 2018, to be published.

[90] Y. C. Tung, presentation in the KOTO collaboration meeting on Jun. 14th, 2018.

[91] H. Kim, presentation in the KOTO collaboration meeting on Jun. 14th, 2018.

[92] G. Y. Lim, presentation in KOTO weekly meeting (2018).

[93] R. Murayama, New cylindrical gamma-veto detector for the J-PARC KOTO experiment, Ph.D. thesis, Osaka University, data last accessed February 14th, 2019 (http://osksn2.hep.sci.osaka-u.ac.jp/theses/doctor/2017/dt_murayama.pdf) (2017).

[94] T. Yamanaka, presentation in the KOTO collaboration meeting on Dec. 15th, 2018.

[95] I. Kamiji, presentation in the KOTO collaboration meeting on Jun. 13th, 2018.

[96] I. Kamiji, private communication.

[97] T. Yamanaka, presentation in the KOTO internal meeting on Oct. 21st, 2018.